Ph. D. Thesis

Top-Tagging with Shower Deconstruction and Search for Single Production of Vector-Like Quarks at ATLAS

School of Physics and Astronomy
College of Science and Engineering

Submitted in fulfilment of the requirements for the degree of Doctor in Philosophy at the University of Glasgow

September 2015

Abstract

The identification of high-p_{T} top quarks is an essential ingredient of many searches for new physics. This thesis presents, for the first time, the performance of shower deconstruction, a new top-tagging algorithm, using data collected with the ATLAS detector at the LHC. The distribution of the shower deconstruction observable, the likelihood ratio χ_{SD}, is shown to be very well modelled by modern Monte Carlo generators, and is compared to several other algorithms and jet substructure observables. Shower deconstruction is shown to have the best quark- and gluon-jet background rejection over a wide range of signal efficiency.

Vector-like quarks are a feature of several new physics models. As they do not gain their mass from a Yukawa coupling, they are still allowed by constraints set by Higgs production cross section measurements. These, so-called, fermionic-partners can play a role similar to that of bosonic-partners in supersymmetric models, providing a solution for the naturalness problem. This thesis presents the first dedicated search for single production of vector-like quarks, using data collected with the ATLAS detector, introducing novel strategies for separating signal from background. This work extends the exclusion limits from production of pairs of vector-like quarks, from 700 GeV to 950 GeV, for suitably large vector-like quarks couplings. Also, exclusion limits on the coupling versus vector-like quark mass space are presented for the first time.

Large-R jet triggers are first introduced in ATLAS during Run 1 to cover topologies where these jets play a predominant role. In this thesis, several performance metrics of these triggers are presented, using data collected with the ATLAS detector, highlighting their advantages over standard jet triggers. Also, an example of how these triggers can be combined to lepton triggers to increase the efficiency of a search for new physics is shown.

Acknowledgements

This thesis is the result of a collaborative effort within the Glasgow PPE group and the ATLAS collaboration.

To my supervisor, Tony Doyle, I would like to thank him for his constant support and encouragement, and for the freedom I was given to choose what to make my research on. I am particularly grateful to James Ferrando and Jiahang Zhong, for sharing their experience and ideas, and for all the valuable discussions. To them, and to all the people in Glasgow and the IPPP I collaborated with: Danilo Ferreira de Lima, Deepak Kar, Andrea Knue, Cristina Oropeza Barrera and Michael Spannowsky, I would like to express my appreciation for the patience shown towards my lack of it.

The three year long stay at CERN seems so brief now, and there are far too many people I am grateful to for all that I learnt from them. I can only state how much I value those who sat with me in R1 for a chat, and how much I benefited from all the meetings, workshops etc. To Diane Cinca and Graeme Stewart, thank you for the nice working atmosphere.

To all who contributed to the shower deconstruction ATLAS approval process, Jon Butterworth, Daniel Froidevaux, Dag Gillberg, David Miller and Emily Thompson thank you for the discussions. I learnt a lot from you all. To the vector-like quark search editorial board, Ben Cooper, Joe Haley, Thibault Guillemin and Wolfgang Wagner, thank you for the interest shown and the time devoted. I can only hope that you will be pleased with the results.

Thanks to my wife, Yuliya, and to my parents and family for everything.

Declaration

I declare that, except where explicit reference is made to the contribution of others, that this dissertation is the result of my own research work in the Experimental Particle Physics group of the School of Physics and Astronomy in the University of Glasgow. It has not been submitted for any other degree at the University of Glasgow or any other institution.

Chapter 3 contains the results from my ATLAS authorship qualification task on evaluating large-R jet trigger performance. In addition, it includes the implementation I made of these triggers into the $t\bar{t}$-resonances search [1]. Chapter 4 is a continuation of Ref. [2], in which I was the main analyst and co-editor. The analysis strategy used in Chapter 5 is derived from Ref. [3]. I am a co-author of this work, where I contributed to the event simulation and analysis, the strategy design and the paper edition. The BoostedSLUtils package, written for the processing of the datasets used in Chapter 4 and Chapter 5 is the result of my own work. I am the main analyst and co-editor of the search presented in Chapter 5.

Nicolas Gilberto Gutierrez Ortiz

Contents

Chapter 1

Theoretical background

1.1 The Standard Model

The Standard Model (SM) of particle physics, *the most successful theory ever* [4] describes the particles, and their interactions, composing all the matter and forces that have been observed yet.

Figure 1.1 shows its constituents: bosons (integer spin quantum number), such as those mediating the electromagnetic (γ), nuclear weak (W,Z) and strong (g) forces, and the Higgs boson, responsible for the masses of the SM particles; fermions (half-integer spin quantum number), divided into quarks and leptons, forming the matter particles.

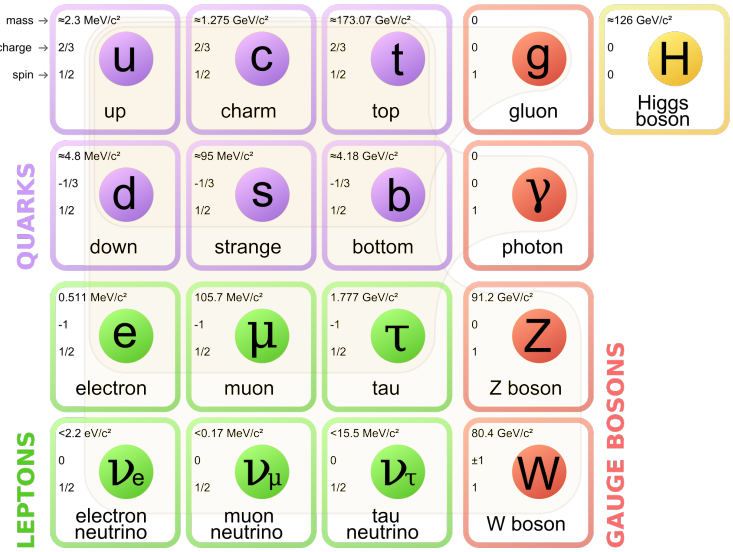

Figure 1.1: The Standard Model is a triumph of modern physics. With this handful of particles shown here, we can explain all of the matter we have encountered, from atoms to entire galaxies. Taken from Ref. [5].

The up and down quarks are the building blocks of protons and neutrons, while the other quarks have only been directly observed in particle colliders and cosmic rays. From the electrically charged leptons, electrons are found orbiting the atom nuclei, while muons and taus are present in cosmic rays, and produced in particle colliders. The neutral leptons (*neutrinos*) interact only through the nuclear weak force, making them nearly impossible to capture, through their interaction with matter.

In this thesis, in particular in Chapter 5, an extension of the SM is examined. This extension follows the same underlying principles defining the mathematical description of the SM, attempting to stay in harmony with all previous observations, while solving some of the open issues with the SM. Therefore, these mathematical principles, as well as the most relevant open issues are introduced below.

Gauge theories: the SM is a renormalisable gauge theory that builds on the quantum field theory [6–10] theoretical framework. In a gauge theory, interactions between fields result from imposing invariance under group transformations to the *Lagrangian* of a system, which represents its dynamics. For instance, starting from the Dirac free particle Lagrangian

$$\mathcal{L}_\psi = \bar{\psi}\left(i\not{\partial} - m\right)\psi \tag{1.1}$$

that under a local gauge transformation on the Dirac field $\psi \to \psi' = \exp\left[-i\alpha(x)\right]\psi$ transforms as

$$\mathcal{L}_\psi \to \mathcal{L}'_\psi = \mathcal{L}_\psi + \bar{\psi}\gamma_\mu\psi(\partial^\mu\alpha) \tag{1.2}$$

and is therefore not invariant under rotations on the phase angle of the field, transformations corresponding the gauge group U(1). The introduction of the gauge field A_μ, transforming under U(1) as

$$A_\mu \to A'_\mu = A_\mu + \frac{1}{e}\partial_\mu\alpha \tag{1.3}$$

where e corresponds to the elementary charge, and the introduction of the covariant derivative $D_\mu \equiv \partial_\mu + ieA_\mu$ in the free particle Lagrangian $\mathcal{L}_\psi = \bar{\psi}\left(i\not{D} - m\right)\psi$ restores gauge invariance

$$\begin{aligned}\mathcal{L}_\psi \to \mathcal{L}'_\psi &= \bar{\psi}'\left[(i\not{\partial} - e\not{A}') - m\right] \\ &= \mathcal{L}_\psi - e\bar{\psi}\gamma_\mu\psi A^\mu.\end{aligned} \tag{1.4}$$

Here, the requirement of invariance under local gauge transformations has naturally introduced the coupling of the electron field (ψ) to the electromagnetic field (A). This follows Noether's theorem, where the invariance under U(1) lead to a conserved current proportional to $\bar{\psi}\gamma_\mu\psi$. The complete Lagrangian describing Quantum Electrodynamics is given by

$$\mathcal{L}_{\text{QED}} = \bar{\psi}\left(i\not{D} - m\right)\psi - \frac{1}{4}F_{\mu\nu}F^{\mu\nu} \tag{1.5}$$

where the electromagnetic tensor $F_{\mu\nu}$ in the last term of the Right Hand Side (RHS) of Eq. 1.5, given by the free field Lagrangian, is invariant under Eq. 1.3. This Lagrangian is therefore invariant under U(1) transformations.

The SM electroweak Lagrangian is based on the $\text{SU}(2)_L\times\text{U}(1)_Y$ gauge group. Here, $\text{U}(1)_Y$ is associated to the leptonic hypercharge (Y) and $\text{SU}(2)_L$ to the weak isospin (T_3), both associated to the electromagnetic charge Q as

$$Q = T_3 + \frac{1}{2}Y. \tag{1.6}$$

Invariance under this gauge group requires four gauge bosons: (W^1,W^2,W^3), a triplet associated with the generators of SU(2), and B, a neutral field related to $\text{U}(1)_Y$. Figure 1.2 shows the hypercharge and weak isospin number associated to quarks, leptons and electroweak gauge bosons.

Fermionic mass and chirality: in the SM fermions are chiral, i.e. right- and left-handed fermions transform differently under $\text{SU}(2)_L\times\text{U}(1)_Y$. Left-handed fermions form an isospin doublet ($I = \frac{1}{2}$) while right-handed fermions form a singlet ($I = 0$), transforming as

$$\begin{aligned}\psi_L \to \psi'_L &= e^{i\alpha(x)T + i\beta(x)Y}\psi_L \\ \psi_R \to \psi'_R &= e^{i\beta(x)Y}\psi_R.\end{aligned} \tag{1.7}$$

The mass term for a fermion in the SM Lagrangian would have the form $m_f\bar{\psi}\psi$, that can be decomposed in helicity states

$$\begin{aligned}m_f\bar{\psi}\psi &= m_f\left(\bar{\psi}_R + \bar{\psi}_L\right)\left(\psi_L + \psi_R\right) \\ &= \left[\bar{\psi}_R\psi_L + \bar{\psi}_L\psi_R\right]\end{aligned} \tag{1.8}$$

which is not invariant under the gauge transformations in Eq. 1.7. This is of particular relevance to this thesis, as for new fermions from any

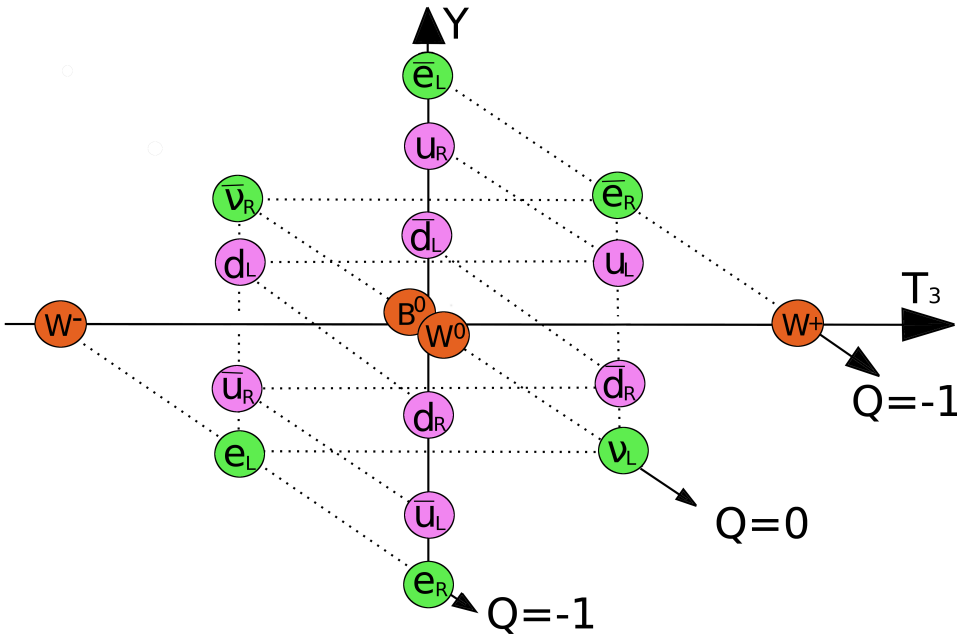

Figure 1.2: Hypercharge (Y) and weak isospin assignment to leptons, quarks and electroweak gauge bosons. The electric charge (Q) is constant along the diagonal lines as indicated in this figure.

SM extension with identical transformation rules under $\mathrm{SU}(2)_L \times \mathrm{U}(1)_Y$ for their left- and right-handed components, this fermion mass term is allowed.

In the SM fermions gain their masses from the Yukawa coupling to the Higgs doublet field, that is,

$$\mathcal{L}_{\mathrm{fermion-mass}} \propto \lambda_f \left[\bar{\psi_L}\phi\psi_R + \bar{\psi_R}\phi\psi_L\right] \tag{1.9}$$

where λ_f is known as the Yukawa coupling. Fermions acquire a finite mass if ϕ has a non-zero expectation value

$$\phi_0 = \begin{pmatrix} 0 \\ h \end{pmatrix}. \tag{1.10}$$

Gauge boson mass and mixing: the kinetical term of the scalar field Lagrangian $\mathcal{L}_{\mathrm{kine-scalar}} = (D^\mu\phi)^\dagger (D_\mu\phi)$, where the covariant derivative for $\mathrm{SU}(2)_L \times \mathrm{U}(1)_Y$ is given by

$$D_\mu = \partial_\mu + ig\frac{1}{2}\vec{\tau}W_\mu + ig'\frac{1}{2}YB_\mu \tag{1.11}$$

with $\vec{\tau}$ being the $\mathrm{SU}(2)_L$ generators corresponding to the three Pauli

matrices, and where g and g' are the coupling constants associated to the groups $\mathrm{SU}(2)_L$ and $\mathrm{U}(1)_Y$ respectively, can be expanded in three terms: two proportional to vh and h^2 respectively, where v corresponds to the vacuum expectation value, resulting in the interactions between the gauge bosons and the Higgs, and a term proportional to v^2, giving masses to the gauge bosons. This last term is given by

$$\begin{aligned}(D_\mu\phi) &\propto \left[g\left(\tau_1 W_1 + \tau_2 W_2 + \tau_3 W_3\right)\right]\begin{pmatrix}0\\ v\end{pmatrix}\\ &\propto \begin{pmatrix} g\left(W_1 - iW_2\right)\\ -gW_3 + g' Y_{\phi_0} B_\mu\end{pmatrix}\end{aligned} \tag{1.12}$$

times its hermitian conjugate, resulting in

$$\left(D^\mu\phi\right)^\dagger \left(D_\mu\phi\right) \propto v^2\left[g^2\left(W_1^2 + W_2^2\right) + \left(-gW_3 + g' Y_{\phi_0} B_\mu\right)^2\right]. \tag{1.13}$$

This can be rewritten in terms of physical gauge bosons. For the neutral bosons, the last term on the RHS of Eq. 1.13 can be rewritten as

$$\left(-gW_3 + g' Y_{\phi_0} B_\mu\right)^2 = \left(W_3, B_\mu\right)\begin{pmatrix} g^2 & -gg' Y_{\phi_0}\\ -gg' Y_{\phi_0} & g'^2\end{pmatrix} \tag{1.14}$$

where only if $Y_{\phi_0} \neq 0$ the W_3 and B_μ fields mix, and if $Y_{\phi_0} = \pm 1$ the matrix's determinant vanishes, resulting in a massless physical gauge boson. For $Y_{\phi_0} = 1$, the two eigenvectors of the mixing matrix, with eigenvalues $\lambda = 0$ and $\lambda = \left(g^2 + g'^2\right)$ respectively, are

$$\begin{aligned}\text{photon}(\gamma)\ A_\mu &= \frac{1}{g^2 + g'^2}\left(g' W_3 + g B_\mu\right)\\ \mathrm{Z} - \text{boson}(Z)\ Z_\mu &= \frac{1}{g^2 + g'^2}\left(g W_3 - g' B_\mu\right)\end{aligned} \tag{1.15}$$

and therefore

$$\left(-gW^3 + g' Y_{\phi_0} B_\mu\right)^2 = \left(g^2 + g'^2\right) Z_\mu^2 + 0 \cdot A_\mu^2. \tag{1.16}$$

For the charged bosons, in the first term on the RHS of Eq. 1.13 W_1 and W_2 can be rewritten in terms of W_+ and W_- using

$$W^\pm = \frac{1}{\sqrt{2}}\left(W_1 \mp i W_2\right) \tag{1.17}$$

and therefore,

$$g^2\left(W_1^2 + W_2^2\right) = g^2 W^{+2} + g^2 W^{-2}. \tag{1.18}$$

In the example above, the masses of the physical gauge bosons are a result of the mixing between gauge bosons after electroweak symmetry breaking. This concept is of particular relevance to this thesis, as in some extensions of the SM interactions between new particles and the SM are often a result of mixing between these two sectors, following the same principles discussed above.

Renormalisability: renormalisation is a procedure under which infinities are systematically removed, making calculations possible at any order in perturbation theory. Infinities can arise from additional loops in a Feynman diagram. For instance, the electron-positron scattering process as illustrated in Figure 1.3 (a) up to one order in α, would include a divergent loop in the next term in the perturbation expansion ($\mathcal{O}(\alpha^2)$), as illustrated in Figure 1.3 (b). Each loop involves one integral over four-momentum, and each particle contributes a factor of inverse four-momentum. Hence a diagram such as the one in Figure 1.3 (b) has an integral that goes as momentum squared, diverging when integrating to infinity.

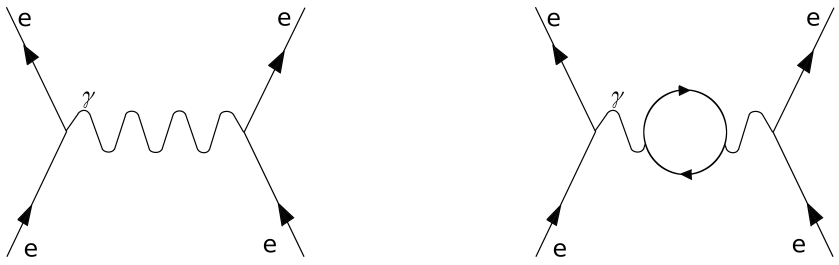

(a) (b)

Figure 1.3: Illustration of processes contribution to electron scattering at leading order (a) and at next-to-leading order (b).

The renormalisation of an observable starts with the regularisation, where integrals are parametrised in terms of a regulator, with an energy scale cut-off Λ. Renormalised observables are then rewritten in terms of this cut-off scale, such that

$$\alpha\left(\Lambda\right) \xrightarrow{\Lambda\to\infty} \alpha \tag{1.19}$$

meaning that renormalised quantities depend on the energy, or equivalently, the length scale of an experiment or measurement. This feature has been observed for the electron electric charge, the strong interaction coupling among others, and is formally described by the renormalisation group [11].

All the operators on the SM Lagrangian are renormalisable, and therefore many of its extensions follow this by adding only renormalisable terms. This, however, is not necessarily the case of effective Lagrangians, expected to describe certain phenomena only up to some scale. In these cases, the cut-off scale can correspond to some real physical quantity, such as the scale at which new physics is expected. Parameter calculation in these cases is also possible, often by performing an expansion in inverse powers of Λ, resulting in predictions with approximate accuracy to finite order in Λ. This is of particular relevance to this thesis, as in Chapter 5 both renormalisable and non-renormalisable extensions of the standard model are tested, the latter including terms not present in the former, representing additional real physics interactions.

Naturalness problem: calculating the Higgs mass at some energy scale Λ amount to calculating the corrections from its couplings to SM fermions and bosons

$$m_h = m_h^{\text{bare}} + \delta m_h^{\text{fermions}} + \delta m_h^{W/Z} + \delta m_h^{\text{Higgs}} + \dots \tag{1.20}$$

which corresponds at next-to-leading order to the illustration in Figure 1.4. Given its large mass, the correction from the top-quark is large

$$\left(\delta m_h^2\right)^{top} \propto \lambda_t^2 \Lambda^2 \tag{1.21}$$

which is in conflict with the observation.This is the naturalness problem: why those seemingly uncorrelated terms in Eq. 1.20, that can be as large as Λ^2, add to the observed relatively flat scaling of m_h^2 with Λ? An elegant solution to this problem is the existence of some additional symmetry protecting the mass of the Higgs. Two typical approaches to this are outlined below.

A possible solution is the existence of a boson-fermion symmetry or *SUperSYmmetry* (SUSY) [12–21], where given that fermion and boson corrections enter Eq. 1.20 with opposite sign quadratic divergences vanish,

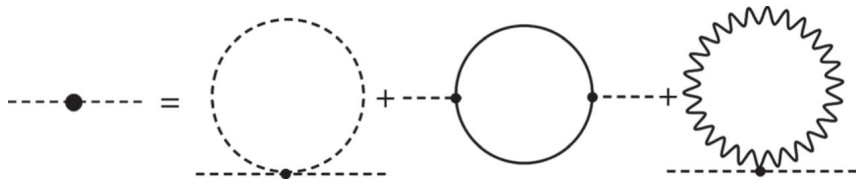

Figure 1.4: One-loop corrections to the Higgs mass. The three diagrams are quadratically divergent and make the Higgs mass highly UV-sensitive.

leaving corrections of the order $\ln\left(\frac{\Lambda}{m_{\mathrm{SUSY-partner}}}\right)$

$$\left(\delta m_h^2\right)^{top} \propto \left(m_{\mathrm{top}}^2 - m_{\mathrm{SUSY-partner}}^2\right) \ln\left(\frac{\Lambda}{m_{\mathrm{SUSY-partner}}}\right) \tag{1.22}$$

Another possibility is that the Higgs boson is a bound state. Composite Higgs Models (CHMs) [22–29] include a new strong force from a global symmetry, where the Higgs is a pseudo (massive) Nambu-Goldstone (NG) boson. This idea is inspired by the description, at the energy scale where the strong interaction coupling becomes large, of light scalars, such as pions, as quark bound states without problems of naturalness. The two-quark description of the strong interaction at this energy scale contains only two doublets

$$\begin{pmatrix} u_L \\ d_L \end{pmatrix}, \begin{pmatrix} u_R \\ d_R \end{pmatrix} \tag{1.23}$$

where the global symmetry $\mathrm{SU}(2)_L \times \mathrm{SU}(2)_R$ is broken by the quark condensate ($\langle q\bar{q} \rangle \neq 0$)

$$\mathrm{SU}(2)_L \times \mathrm{SU}(2)_R \rightarrow \mathrm{SU}(2)_{\mathrm{isospin}} \tag{1.24}$$

results in three massless NG bosons (π^+,π^-,π^0), eventually gaining mass from the quark mass ($m_\pi^2 \propto m_q$). In this description, pions are the lightest pseudo NG bosons, separated by a large gap ($m_\pi \approx 100$ MeV) to the next bound state ($m_\rho \approx 1$ GeV). Analogously, for a composite Higgs, this large mass gap could explain the absence of new bound states in experimental observations. A particularly interesting prediction of CHMs, within the scope of this work, is the existence of multiplets of new heavy fermions, controlling naturalness, similarly to the bosonic-partners in SUSY. This is further discussed in Section 1.2.

1.2 Vector-like quarks

Contrary to the SM fermions, the colour and electroweak quantum numbers of the left- and right-handed components of the Vector-Like Quarks (VLQs) are identical. Therefore, terms such as $m_Q\bar{Q}Q$ are allowed by electroweak gauge symmetry. VLQs have spawned considerable phenomenological literature in recent years, see for example Refs. [30–34]. VLQs are coloured fermions, and hence, they can be produced in pairs through QCD interactions, as illustrated in Figure 1.5 (a).

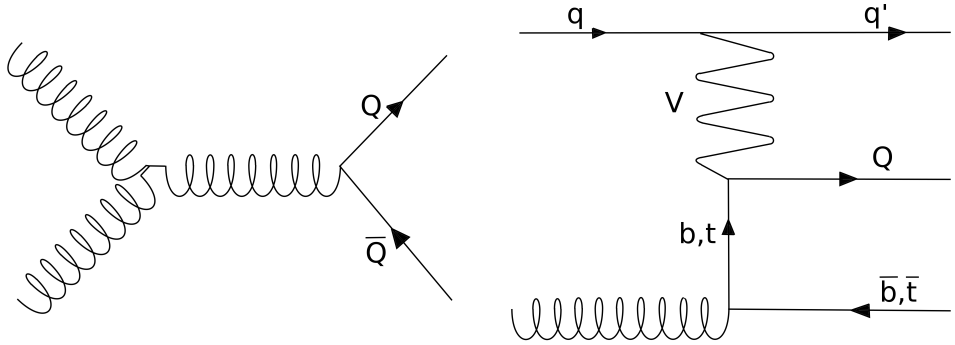

Figure 1.5: A representative diagram illustrating the production of pairs of (a) and a single (b) VLQ, where V corresponds to the SM $W^{\pm}$- or Z-boson.

Both ATLAS and CMS have performed searches for production of VLQ pairs [35, 36]. Figure 1.6 illustrates the range of the current observed limits for a vector-like top (T), with charge 2/3. This is shown in the space of the possible decay modes. For a SU(2) singlet, these limits reach between 700 to 750 GeV. The limits on $T \to Wb$ could also be interpreted in terms of a vector-like Y, with charge $-4/3$ and therefore BR($Y \to Wb$) = 100%.

VLQs can also be singly produced through their interaction to SM gauge bosons and heavy quarks. Some models also predict interactions with light quarks. This is, however, out of the scope of this thesis. For a vector-like T, this production process is analogous to t-channel single top production, as illustrated in Figure 1.5 (b), where the top quark is produced in association with a light- and a heavy-quark. For VLQs, this channel has the caveat of its dependence on the formulation of the QVb and QVt vertices, however, its production cross section can exceed that of pair production [31, 34]. This is a fundamental motivation for the work in Chapter 5, therefore, two approaches for the interpretation of single production of VLQs and their consequences on the production cross-sections are discussed below.

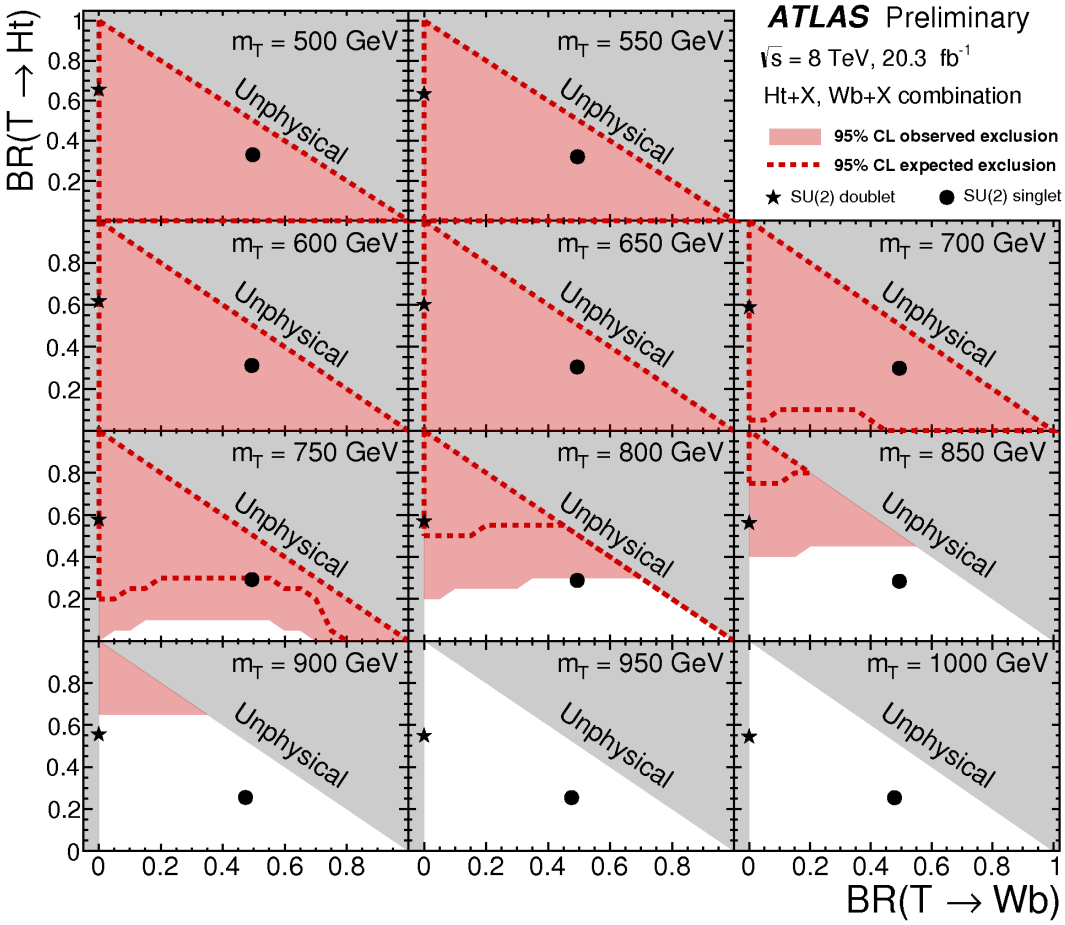

Figure 1.6: Observed (red filled area) and expected (red dashed line) 95% CL exclusion in the plane of BR($T \to Wb$) versus BR($T \to Ht$) from the combination of the $T\bar{T} \to Wb+X$ and $T\bar{T} \to Ht+X$ searches, for different values of the vector-like T quark mass. The grey (dark shaded) area corresponds to the unphysical region where the sum of branching ratios exceeds unity. Example branching ratio values for the weak-isospin singlet and doublet cases are shown as plain circle and star symbols respectively. Figure taken from Ref. [36]. The VLQ pair-production cross section for each value of the VLQ mass is taken from Ref. [34]. This is shown in Figure 1.8.

Fermionic partners in CHMs: there are several theoretical works involving CHMs and fermionic partners [22–29]. In this work, the focus is on the non-renormalisable effective Lagrangian description presented in Refs. [31, 37], where the Higgs is the pseudo-NG boson of the SO(5)/SO(4) coset. The SO(5) symmetry is broken by terms like

$$\lambda_L q_L \mathcal{O}_R \tag{1.25}$$

where $\mathcal{O}_R$ is a right-handed composite operator that after symmetry breaking becomes ht_L, hence recovering the top-Yukawa coupling. The Lagrangian, and therefore the possible interactions, depends on the choice of the representations of SO(4), controlling the new fermion (Ψ) multiplets, and of SO(5), controlling the operators of the Lagrangian. In this work, the focus is on the $\mathbf{M1}_5$ model, where only a new fermion singlet (T) is introduced, and where the elementary (non-composite) q_L are embedded in

$$\left(Q_L^5\right) = \begin{pmatrix} ib_L \\ b_L \\ it_L \\ -t_L \\ 0 \end{pmatrix}. \tag{1.26}$$

For this model, the interactions involving new fermions are

$$\mathcal{L}^{\mathbf{M1}_5} \supset i\bar{\Psi} i\not{D}\Psi - M_\Psi \bar{\Psi}\Psi \quad + yf \left(\bar{Q}_L^5\right)^I U_{I5} \Psi_R + yc_2 f \left(\bar{Q}_L^5\right)^I U_{I5} t_R + \text{h.c.} \tag{1.27}$$

where U is the 5x5 NG boson matrix, the mixing between composite and elementary states is controlled by the Yukawa coupling y, the interactions of t_R are controlled by the $\mathcal{O}(1)$ parameter c_2, and f is the scale of the symmetry breaking of the new strong sector. From the three parameters (M_Ψ, y, c_2), one is fixed by the top-Yukawa coupling, leaving the mass of the VLQ and the coupling c_2 as free parameters.

The trilinear couplings on Eq. 1.27 contribute to the single production of VLQs, and are therefore written explicitly below

$$\mathcal{L}^{\mathbf{M1}_5} \supset \frac{y}{\sqrt{2}} \left(\rho + i\phi^0\right) \bar{T}_R t_L + y\phi^+ \bar{T}_R b_L \tag{1.28}$$

where $y \sim y_t/c_2$. Since the mass of the new fermions is expected to

be considerably larger than the mass of the electroweak bosons, the equivalence theorem is used here to describe the interactions in terms of the Goldstone fields. Following the equivalence theorem, the longitudinal components of the Z and $W^{\pm}$ bosons are described by the neutral (ϕ^0) and charged ($\phi^{\pm}$) fields, and ρ represents the coupling to the Higgs. Then, from Eq. 1.28, is noted that T couples to all the SM bosons. Also, that it is produced with either an associated b- or t-quark and that its Branching Ratios (BR) to the different decay modes are $\mathrm{BR}(T \to Zt) \approx \mathrm{BR}(T \to Ht) \approx \frac{1}{2}\mathrm{BR}(T \to Wb) \approx 0.25$.

Figure 1.7 summarises the consequences of Eq.1.28 for singly produced T. Here, the production with an associated b-quark (Tb) is larger than with an associated t-quark (Tt). This is understood both in terms of kinematics and of the $\sqrt{2}$ factor. Also here, Tb production dominates over pair production over most of the mass range. The work in Chapter 5 concentrates in searching for Tb production.

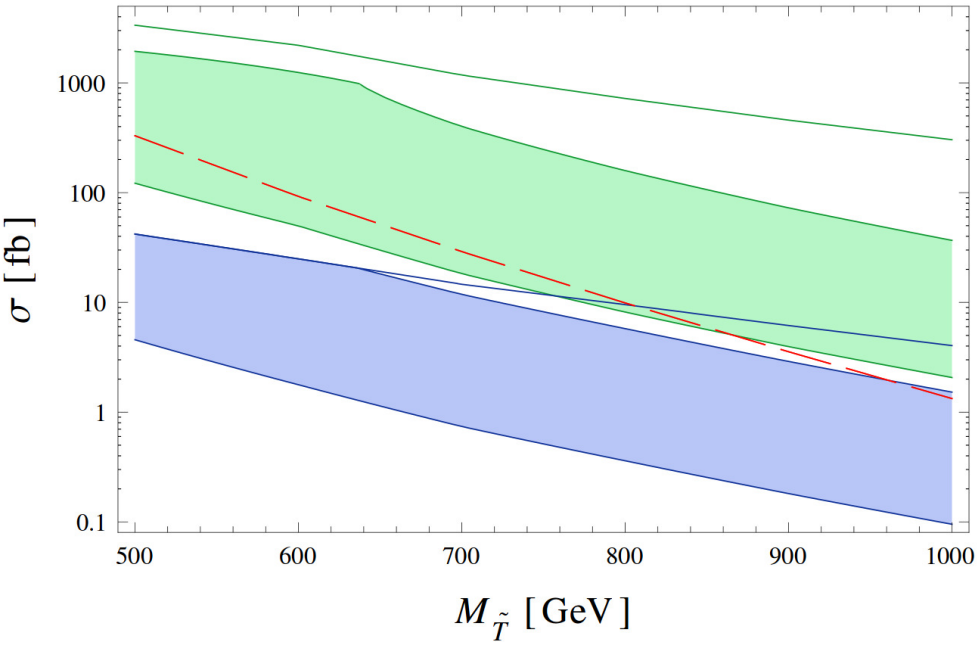

Figure 1.7: Cross sections for the different production mechanisms of T in the model $\mathbf{M1}_5$. Red dashed: pair production; green line: Tb production with the maximal allowed coupling, green band: Tb production for $0.5 < c_2 < 2$; blue line: Tt production for the maximal allowed coupling, blue band: Tt production for $0.5 < c_2 < 2$. Figure taken from Ref. [31].

VLQ via renormalisable couplings: the approach followed in Ref. [34] considers all possible gauge invariant multiplets that can mix with the SM via renormalisable couplings [38, 39]. These multiplets are

$$\begin{aligned} &\text{(singlets) } T_{L,R},\ B_{L,R} \\ &\text{(doublets) } (X\ T)_{L,R},\ (T\ B)_{L,R},\ (B\ Y)_{L,R} \\ &\text{(triplets) } (X\ T\ B)_{L,R},\ (T\ B\ Y)_{L,R}. \end{aligned} \tag{1.29}$$

In this work the focus is on the simplest case (singlet) and on the charge 2/3 VLQ T. Then, the Lagrangians controlling the production and decay of single T are

$$\begin{aligned} \mathcal{L}_W &\propto \sin\theta_L \bar{T}\gamma^\mu P_L b W^+_\mu + \text{h.c.} \\ \mathcal{L}_Z &\propto \sin\theta_L \cos\theta_L \bar{t}\gamma^\mu P_L T Z_\mu + \text{h.c.} \\ \mathcal{L}_H &\propto \frac{m_t}{m_T}\sin\theta_L \cos\theta_L \bar{t} P_L T H + \sin\theta_R \cos\theta_R \bar{t} P_R T H + \text{h.c} \end{aligned} \tag{1.30}$$

where $P_{L,R}$ are the left- and right-handed operators. From Eq. 1.30 is noted that the production with either an associated b- or t-quark is possible. Also, the decay to Wb, studied in Chapter 5, is favoured by at least an extra cosine, present in the Ht and Zt channels. Ref. [34] presents a complete derivation of the BRs. These show a dependency on m_T that should be taken into account for an accurate interpretation of results. However, the $\text{BR}(T \to Zt) \approx \text{BR}(T \to Ht) \approx \frac{1}{2}\text{BR}(T \to Wb) \approx 0.25$ rule holds approximately.

Figure 1.8 summarises the maximum expected single production cross sections. Here, the production with an associated b-quark (Tb) is larger than with an associated t-quark (Tt). Also here, Tb production dominates over pair production for m_T above 600 GeV. Compared with Ref. [31], the T production cross section shown here is about one order in magnitude smaller (see Figure 1.7). This is understood in terms of the higher-dimension operators allowed in Ref. [31], forbidden by the renormalisation requirement made to all terms in Ref. [34].

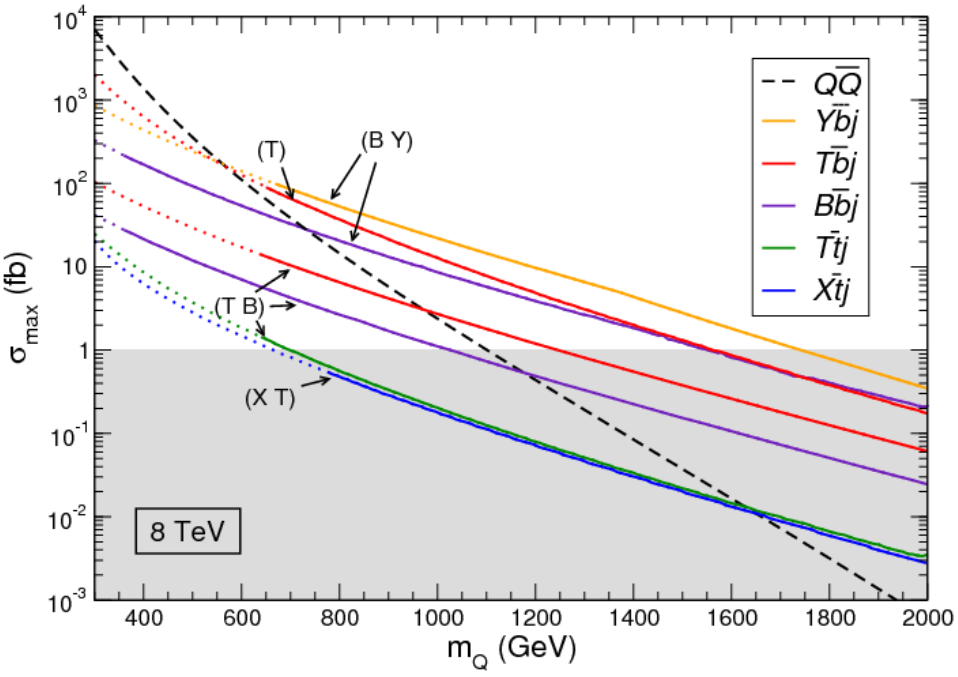

Figure 1.8: Maximum single VLQ production cross sections at t he LHC with 8 TeV, for selected quark multiplets. The dotted part of the lines indicate the range of masses already excluded by direct searches. Figure taken from Ref. [34].

1.3 Jet production and clustering

Jets play an important role in the final states that are studied on this thesis. Also, performance studies are presented for various choices of the jet-clustering algorithm. Therefore, these concepts are introduced to some detail in this section.

Hadrons, groups of quarks held together by the strong force, are copiously produced in proton-proton interactions through parton showers.

The parton shower is a phenomenological approach to describe the emission of quarks and gluons in QCD (Quantum ChromoDynamics) bremsstrahlung radiation from incoming or outgoing quarks or gluons. In this approach, a $2 \to N$ process with a complex final state is modelled starting from a simple $2 \to 2$ process that approximately defines the directions and energies of the hardest partons. A succession of simple parton branchings are then added to build up the full event structure. This branching continues until the partons undergo hadronisation. The probability that a branching occurs is determined by Sudakov form factors and splitting functions [40] derived from the DGLAP equation [41–43].

Jets, collimated sprays of particles produced through the interaction of hadrons with matter, are the objects to which quarks and gluons (partons) are associated to in particle detectors. The momentum carried by a parton is then spread in a cone around its incoming direction.

Sequential jet clustering algorithms use a distance measure between particles[1], that for a particle i is given by

$$d_{ij} = \min(p_{\mathrm{T}i}^{2p}, p_{\mathrm{T}j}^{2p}) \frac{\Delta R_{ij}^2}{R^2} \tag{1.31}$$

where the exponential factor p differentiates between the k_t [44–46] ($p = 1$), Cambridge-Aachen (C/A) [47, 48] ($p = 0$) and anti-k_t [49, 50] ($p = -1$) algorithms. Here, ΔR_{ij}^2 is given by

$$\Delta R_{ij}^2 = (y_i - y_j)^2 + (\phi_i - \phi_j)^2 \tag{1.32}$$

where the rapidity is given by

$$y = \frac{1}{2} \ln \left(\frac{E + p_z}{E - p_z} \right) \tag{1.33}$$

and ϕ is the azimuthal angle. R corresponds to the jet radius parameter and $p_{\mathrm{T}i}$ to the transverse momentum of particle i.

A given particle i is merged with any particle j if d_{ij} is smaller than the distance of the i-particle to the beam (B), $d_{i\mathrm{B}} = p_{\mathrm{T}i}^{2P}$. Otherwise i is called a jet, and excluded from the list of particles. These infra-red (IR) and collinear safe algorithms are used by experiments, in particular the anti-k_t has become the default choice, partly due to the circular shape of its area.

IR and collinear safety are requirements made on jet algorithms such that measurements can be compared to theoretical predictions. In order to achieve this, an algorithm must be insensitive to the emission of soft or collinear gluons [51].

A jet can be divided in subjets by repeating the steps of the jet clustering. For this only the constituents of the jet are used and some R_{subjet} such that $R_{\mathrm{subjet}} < R_{\mathrm{jet}}$ is chosen. An illustrative case results from setting $R_{\mathrm{subjet}} = R_{\mathrm{jet}}$ and using the same jet clustering algorithm. Here, a single subjet identical to the original jet is obtained.

[1]Particles are not observed in detectors, hence the clustering uses calorimeter clusters. This is discussed in Section 2.3

1.4 Monte Carlo modelling of high energy interactions

Monte Carlo (MC) event generators are used in this thesis to model the production and kinematics of SM and Beyond Standard Model (BSM) processes. Starting from an energetic few-body interaction, produced in proton-proton collisions, these generators produce a stochastic simulation of the parton evolution and decay processes that particles undergo, resulting in multihadronic final states, together with leptons and photons.

In this thesis, different MC generators are used to model particular processes. This is discussed in detail in Section 2.4. In this section, the principles underlying these generators are outlined below, focusing on the hard component of high-energy collisions. Detailed summaries are available in their respective manuals and other sources [52, 53].

General purpose MC generators such as Pythia [54, 55], Herwig [56] and Sherpa [57] simulate the hadronisation and fragmentation processes through parton shower models. The Pythia 6 [54] and Pythia 8 [55] MC generators use the Lund String Fragmentation Model [58]. In this model, each final-state hadron corresponds to a small piece of a string connecting a parton-pair. As the partons move apart, potential energy is released by the breaking of this string. Here, the string fragmentation continues until only on-shell hadrons remain. Herwig uses the Cluster Hadronisation Model [59]. In this model, non-perturbative splitting of gluons into quark-antiquark pairs is enforced at the shower cutoff scale, which is related to the hadronisation scale. Then, contiguous colour lines can form massive clusters. These clusters decay into pairs of hadrons, where the kind is regulated according to the available space phase. Sherpa uses a modified cluster model [60]. The string and clusters models are illustrated in Figure 1.9.

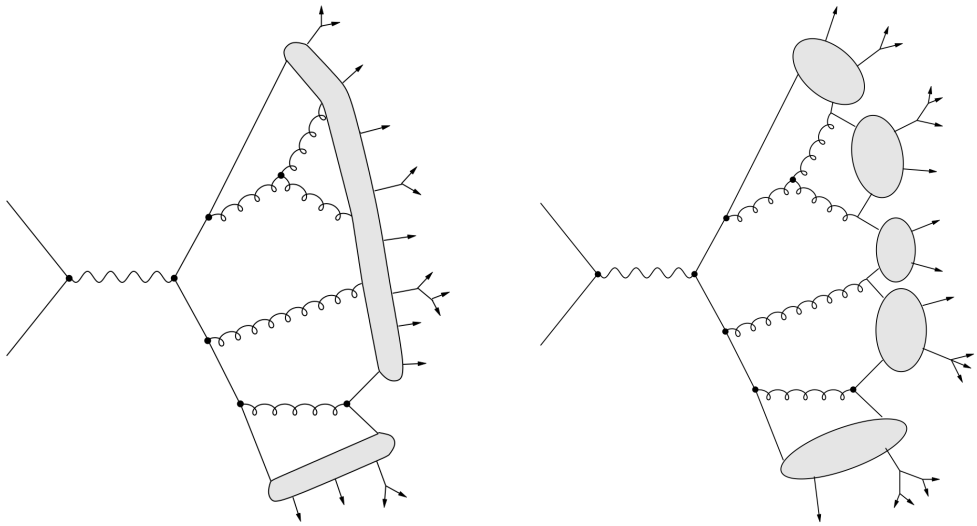

Figure 1.9: Schematic representation of the string (left) and cluster (left) hadronisation models. Taken from Ref. [61].

Shower algorithms concentrate on small angle and energy emissions and are therefore imprecise for hard (large-angle) emissions. Next-to-Leading Order (NLO) MC generators combine parton shower generators, such as Pythia and Herwig with NLO QCD computations (NLO+PS). These include the radiation of an extra parton as a NLO correction to the basic process. In this thesis the Powheg-BOX framework [62] and the MC@NLO [63, 64] generator are used.

Processes with several well-separated jets are important backgrounds for some of the studies presented in this thesis, see Chapter 4 and Chapter 5. The Matrix Element and Parton Shower matching (ME+PS) method allows for the use of tree-level matrix elements for hard (wide-angle) emissions up to some scale, after which parton showers are added. This is illustrated in Figure 1.10. Sherpa uses the CKKW method [65], however other implementations exist, such as Alpgen [66] and Madgraph [67].

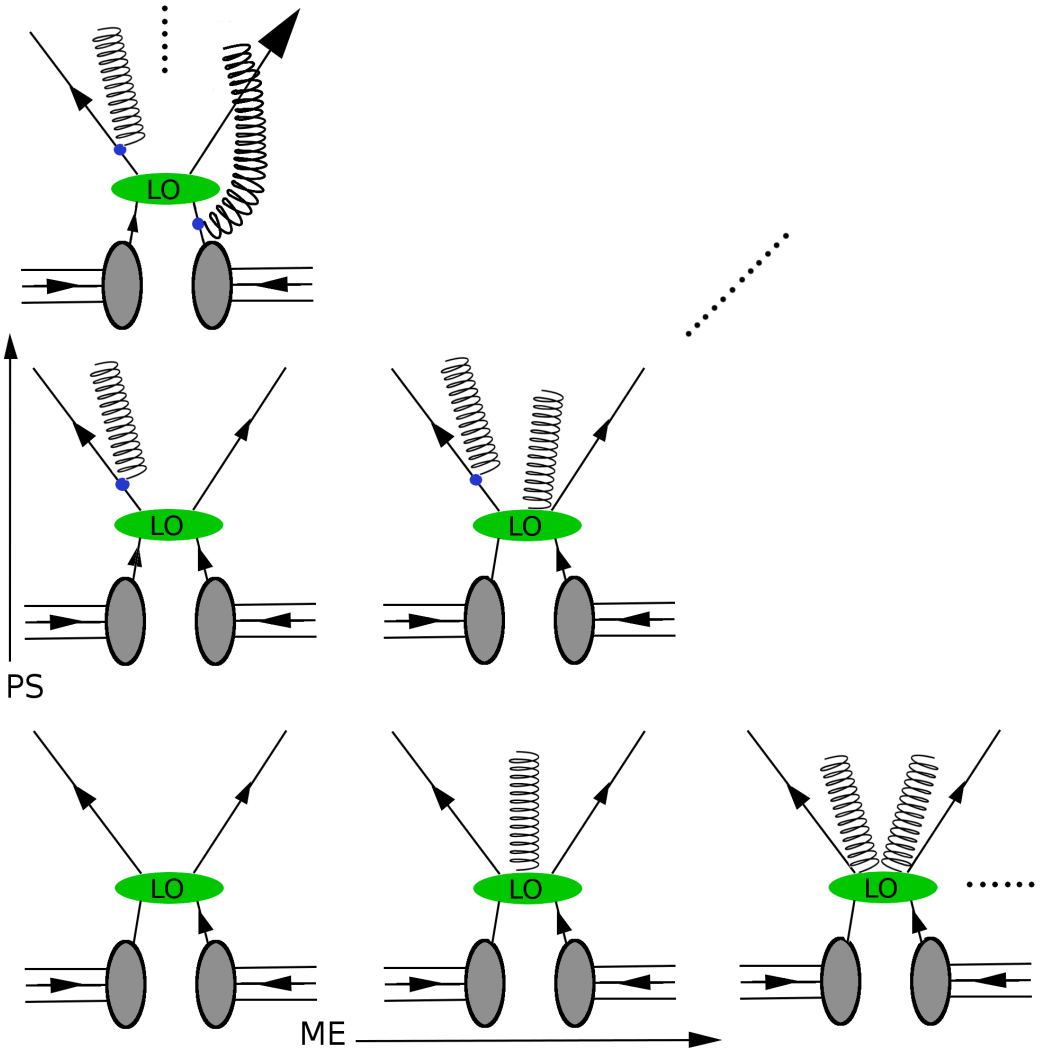

Figure 1.10: Diagrammatic description of the ME+PS method. Here, a n-parton final state can be produced by combining LO matrix element with parton showers.

Chapter 2

Experimental setup

2.1 Introduction

This chapter documents the instruments and techniques used in the data collection, processing and analysis, and is organised as follows: the essential features of the ATLAS detector are introduced in Section 2.3 and the samples used in Section 2.4; the software used to analyse the data is discussed in Section 2.5; Section 2.6 reviews the physics objects definition and reconstruction and finally Section 2.7 examines the strategies for the evaluation of systematic uncertainties.

2.2 The Large Hadron Collider

With a 27-kilometre ring of superconducting magnets, the Large Hadron Collider (LHC) is the largest and most powerful particle accelerator ever built. In the LHC, two beams of protons travel in opposite directions along two separate beam pipes, as illustrated in Figure 2.1. Dipole and quadrupole magnets alternate throughout the ring. The former keeps the beam on its circular trajectory, while the latter focus it. These magnets operate at a very low temperature, approximately 2 K. Liquid helium is used to cool the magnets. Protons are accelerated through radiofrequency cavities, transferring energy through an electromagnetic field, and pushing protons forward along the LHC ring. At the collision point, beams cross at an angle of between 150 and 200 μrad, avoiding additional undesired bunch crossings. Following this, the path of each beam is tuned to re-direct them into their original trajectories along the ring, effectively recycling the beams.

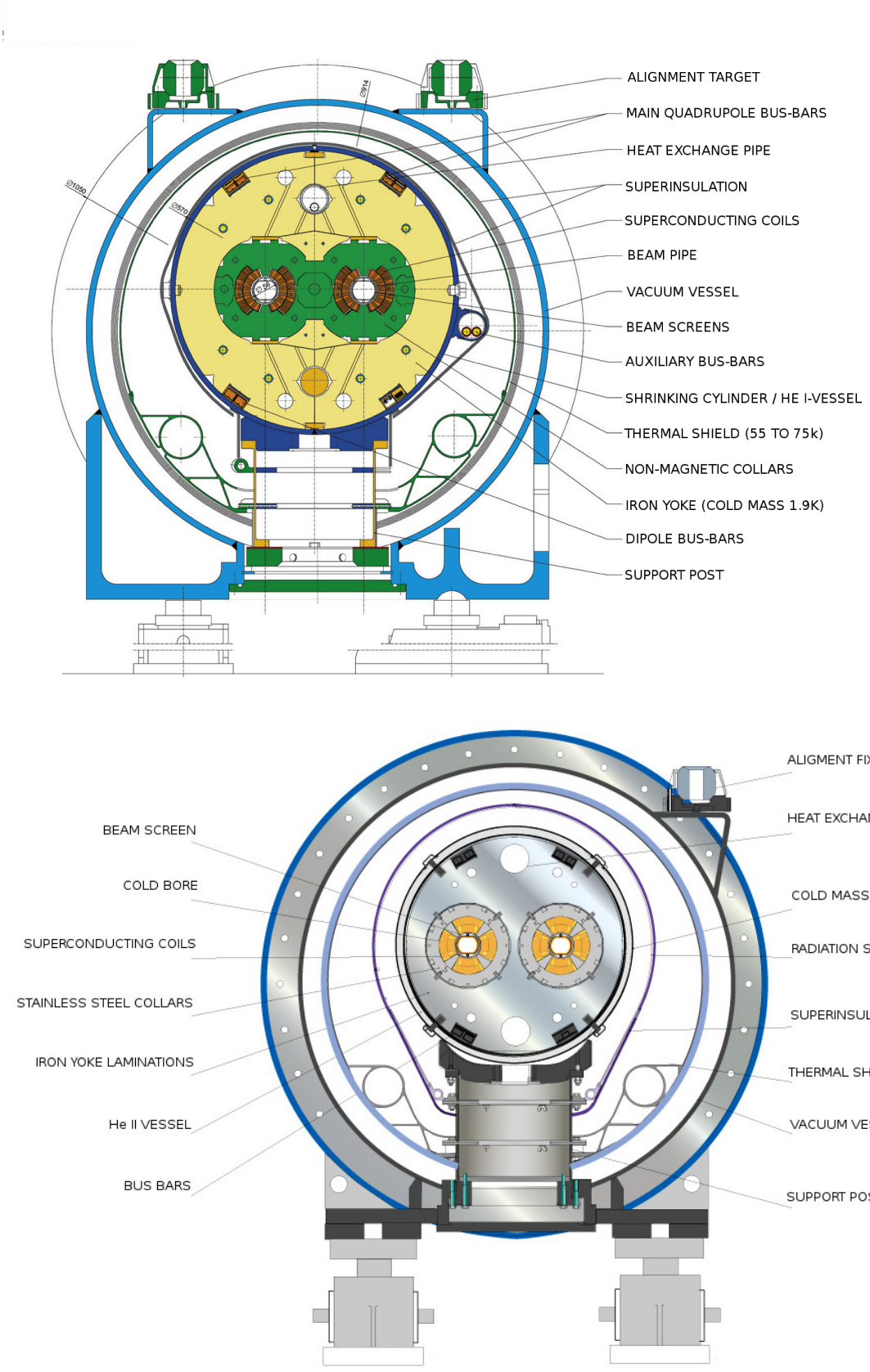

Figure 2.1: Top: diagram showing the cross-section of an LHC dipole magnet with cold mass and vacuum chamber. Bottom: LHC quadrupole cross section. Figures taken from Ref. [68]

The LHC is the culmination of a series of accelerators, as illustrated in Figure 2.2. The chain starts with hydrogen gas. Here, protons are obtained by stripping hydrogen atoms of their electrons using an electric field. The energy of these protons is then increased to 50 MeV by a linear accelerator (LINAC2) These are then pushed to 25 GeV by a series of synchrotron rings: first the Proton Synchrotron Booster (PSB) and then the Proton Synchrotron (PS). In a final step, before being injected into the LHC ring, the proton beam is accelerated to 450 GeV by the Super Proton Synchrotron (SPS).

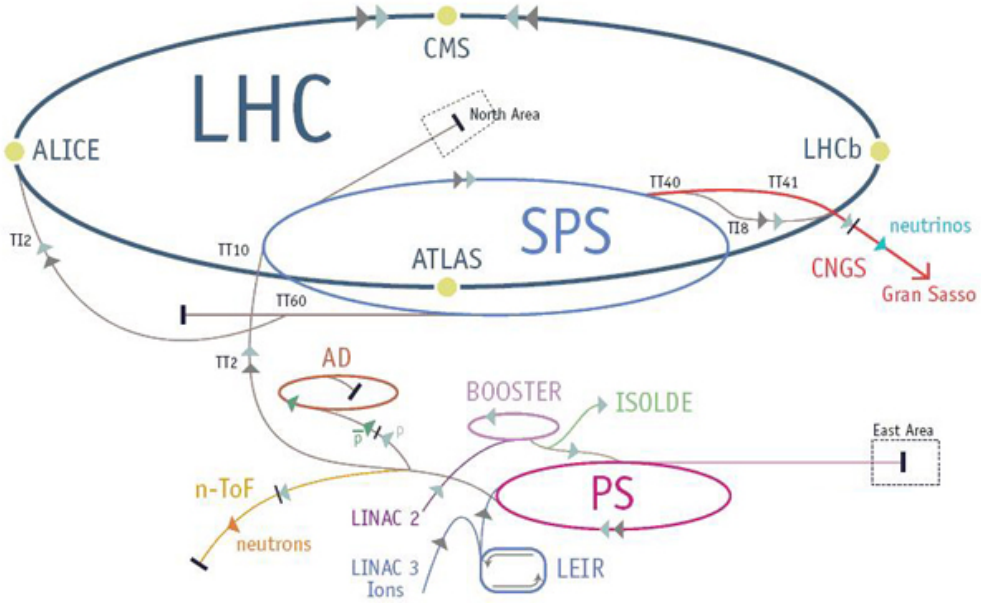

Figure 2.2: CERN accelerator complex. Figure from Ref. [69].

During the 2011 (2012) LHC operation period, the beam operated at an energy of 7 TeV (8 TeV), with approximately 1.5×10^{11} protons per bunch, 1380 bunches per beam, and with a bunch crossing frequency of 16 MHz and spacing of down to 50 ns. During 2012, the average number of events per crossing (in-time pileup) ranged from 5 to 40, with a mean of approximately 20. Additionally, out-of-time pileup, resulting from multiple bunch crossings within a single detector-response cycle, must also be taken into account. High-precision charged-particle tracking is used to distinguish between different interaction points and corrections are applied to mitigate the effects of pileup, this is discussed in Section 2.3.2 and Section 2.6 respectively. The instantaneous luminosity is given by

$$L = \frac{N_{\mathrm{b}}^2 n_{\mathrm{b}} f \gamma}{4\pi \epsilon_{\mathrm{n}} \beta^*} F \tag{2.1}$$

where N_b denotes the number of particles per bunch, n_b the number of bunches per beam, f the revolution frequency and γ the relativistic factor. ϵ and $\beta*$ express the beam size, and correspond to the normalised transverse emittance and to the amplitude function at the interaction point respectively. Emittance is a measure of the parallelism of a beam, and a low β^* correspond to a narrower beam. The factor F accounts for the beam crossing angle. The integrated luminosity $\mathcal{L}$ corresponds to the total luminosity collected over a period of time.

2.3 The ATLAS detector

2.3.1 General description

ATLAS (A Toroidal LHC ApparatuS) is a multi-purpose particle detector for the LHC, located in the Geneva area, near the French-Swiss border. It is approximately 25 metres in diameter, 46 metres in length, and it weights approximately 7,000 tonnes. The ATLAS collaboration involves more than 3000 scientist in 38 countries. ATLAS is divided in specialised subsystems built in layers around the LHC beam collision point. It has a forward-backward symmetry and it provides almost full coverage around the beam pipe.

2.3.2 Inner detector

The ATLAS Inner Detector (ID) is designed to measure the momentum of particles, and to reconstruct their trajectory in order to determine their production vertex. Vertices can correspond to the main (*primary*) vertex, to additional beam interactions in the same proton-bunch crossing and to displaced (*secondary*) vertices produced in the decay of particles with a long lifetime. The momentum measurement is possible due to the bending of the trajectory of particles, resulting from a 2 T superconducting solenoid magnet surrounding the ID.

Figure 2.3 illustrates the arrangement of the various layers of the ID around the LHC beam pipe. This figure also shows the ATLAS coordinate system. The z-axis runs along the beam pipe, and therefore the transverse, (x, y), plane is orthogonal to the incoming beams. The azimuthal angle (ϕ) describes the position in the transverse plane, while the pseudorapidity[1] (η) describes the

[1]The pseudorapidiy is defined as $\eta = -\ln \tan(\theta/2)$

angle with respect to the z (beam) axis. The distance between particles is defined by $\Delta R = \sqrt{\Delta\eta^2 + \Delta\phi^2}$.

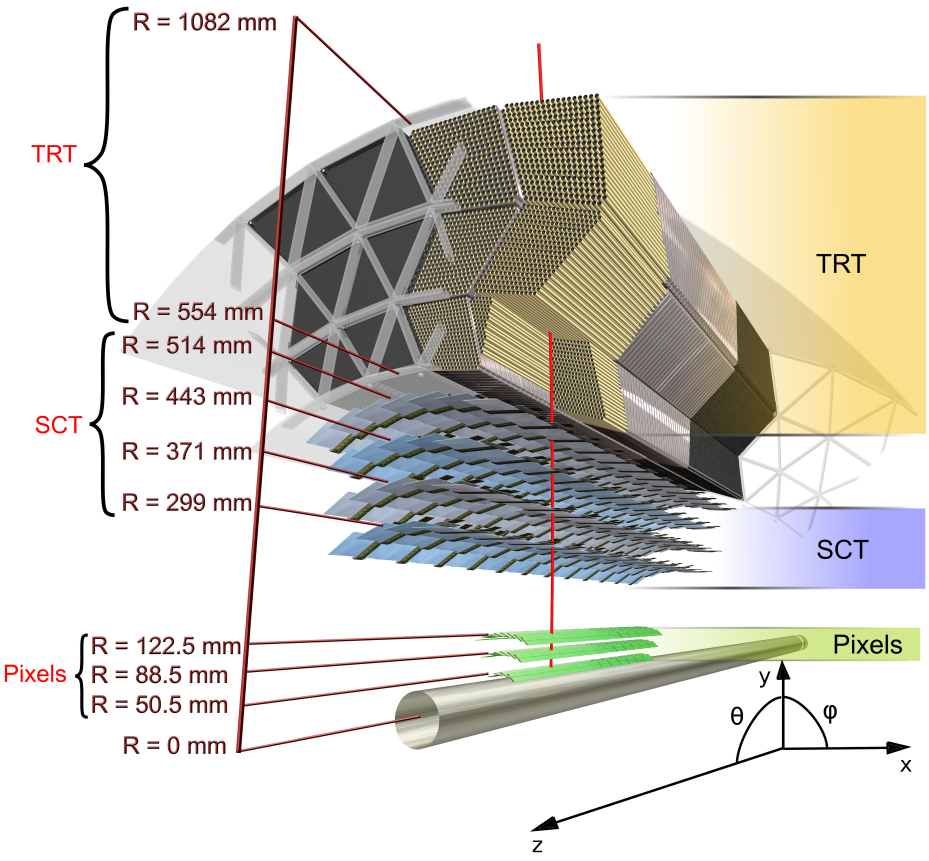

Figure 2.3: A schematic view of the ATLAS inner detector. Here the pixel, Semi-Conductor Tracker (SCT) and Transition Radiation Tracker (TRT) subsystems are shown. Figure from Ref. [70].

The pixel detector composing the first three layers, only a few centimetres apart from the beam pipe, is designed for tracking close to the interaction point, hence radiation hard material is used. The tracking resolution for $|\eta| < 2.5$ and $z < 400$ mm is 10 (150) μm in the radial-ϕ plane (z) and for $z > 500$ mm and $2.0 < |\eta| < 2.5$ is 10 (150) μm in the radial-ϕ plane (radial). The pixel detector has approximately 80.4 million readout channels. The SCT (Semi-Conductor Tracker) has a high position measurement precision. The resolution for $|\eta| < 1.5$ and $z < 700$ mm is 17 (580) μm in the radial-ϕ plane (z) and for $z > 750$ mm and $1.0 < |\eta| < 2.5$ is 17 (580) μm in the radial-ϕ plane (radial). The approximate total number of readout channels in the SCT is 6.3 million. The SCT is surrounded by the TRT (Transition Radiation Tracker),

designed to detect the radiation emitted by ultra-relativistic particles when travelling through inhomogeneous media. The amount of emitted radiation is proportional to the relativistic γ-factor, and is therefore used to discriminate between heavy and light particles with the same momentum. The TRT has an resolution of 130 μm (radial-ϕ) for $|\eta| < 2$. The approximately total number of TRT readout channels is 351,000.

The combined ID tracking system reaches a transverse momentum resolution of about 75 MeV for a track of around 5 GeV and between 3.3 GeV and 11 GeV for a track around 100 GeV [71, 72]. Furthermore, for a track of around 5 GeV, it reaches an angular resolution of about 11 (7) mrad in the polar direction (ϕ). For a track of around 100 GeV, the corresponding resolution is 9 (2) mrad in η (ϕ). In the transverse plane the impact parameter (IP) resolution is better than 15 μm.

2.3.3 Electromagnetic and hadronic calorimeters

The ATLAS electromagnetic (hadronic) calorimeter is designed to measure the energy of electrons and photons (jets). Figure 2.4 illustrates the arrangement of the various subsystems around the beam pipe, providing full coverage on η, excluding the inactive areas in the transition regions These are sampling calorimeters, alternating series of dense shower-triggering absorbing materials and energy-measuring active materials. The electromagnetic (EM) calorimeter is made by layers of lead and stainless steel, and Liquid Argon (LAr). The hadronic calorimeter is made of layers of steel and scintillating tiles, with the forward section made of layers of copper and tungsten, and LAr. The volume of the calorimeter systems should provide good shower containment and should prevent contaminating the systems around it, and also ensures a good measurement of the missing transverse momentum.

The LAr barrel (end-cap) calorimeter covers $|\eta| < 1.457$ ($1.375 < |\eta| < 3.2$). An end-cap component is located at each end of the detector. The tile hadronic calorimeter surrounds the EM calorimeter, and it has an inner radius of 2.28 m and an outer radius of 4.25 m. Its barrel (extended barrel) covers $|\eta| < 1.0$ ($0.8 < |\eta| < 1.7$). An extended barrel is located at each end. A LAr Hadronic End-cap Calorimeter (HEC) is located behind each end-cap EM calorimeter. The LAr forward calorimeter is made of three modules: one made of copper, aiming at EM showers; and two made of tungsten, aiming at hadronic showers.

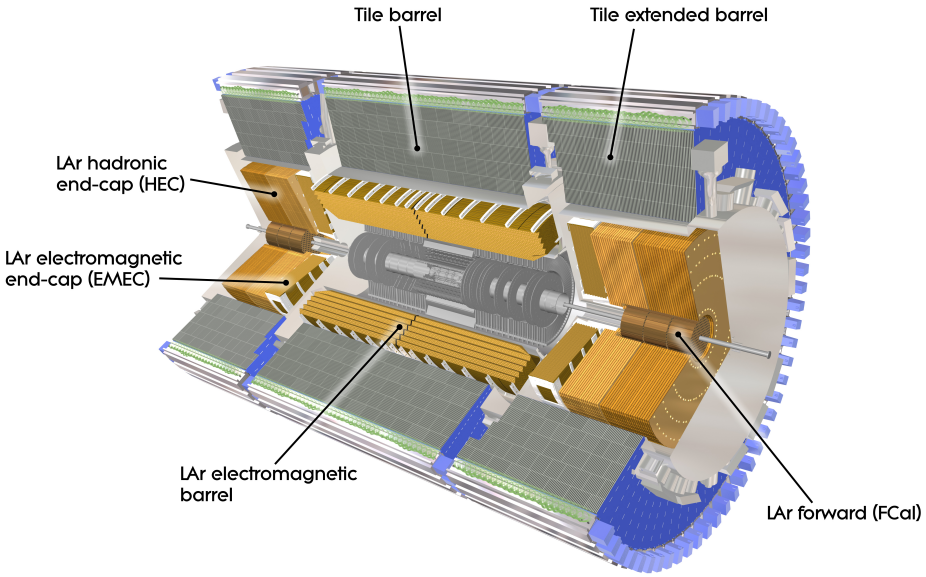

Figure 2.4: Computer generated image of the ATLAS calorimeter. Figure from Ref. [70].

The calorimeters are divided in cells, narrowly segmented for the EM calorimeter, allowing for a precise (∼0.025 radians) measurement of the position where the energy is deposited, and more coarse (∼0.1 radians) for the hadronic calorimeter. Clusters of cells are arranged by seeding on large energy depositions, adding neighbouring cells within certain thresholds of the core energy, rejecting cells with energies under noise thresholds. These thresholds are different for EM and hadronic clusters. EM and hadronic clusters are combined into Locally Calibrated (LCW) topological clusters. The LCW procedure aims at correcting for the difference in response of more EM-like and hadronic-like interactions [73, 74].

The jet energy resolution of the ATLAS calorimeter varies between subsystems, and depends on η. The calorimeter performance expectation metrics are approximately represented by three independent contributions, the effective noise (N), stochastic (S) and constant (C) terms

$$\frac{\sigma_{p_{\mathrm{T}}}}{p_{\mathrm{T}}} = \frac{N}{p_{\mathrm{T}}} \oplus \frac{S}{\sqrt{p_{\mathrm{T}}}} \oplus C \tag{2.2}$$

however, because of the high degree of correlation between these terms, early jet energy resolution measurements [75] could not unequivocally disentangle their contributions. For the EM calorimeter, the energy resolution is within 2% for electrons of around 50 GeV. The measurement of the energy of jets within

$3.1 < |\eta| < 4.9$ relies on the forward hadronic calorimeter, which achieves energy resolutions of 20% and 10% for pions of around 20 GeV and 200 GeV [76]. For the tile hadronic calorimeter, the intrinsic energy resolution is about 15% for a jet of around 100 GeV and about 3% for a jet of around 1 TeV.

2.3.4 Muon spectrometer

The ATLAS Muon Spectrometer (MS) is designed to measure the momentum of muons, travelling through the calorimeters without being absorbed. Due to the muon mass, which is over 200 times larger than the electron, the energy loss of a muon in the EM calorimeter is small compared to an electron. As muons do not interact through the strong interaction, their interaction with the materials in the hadronic calorimeter is small compared to that of hadrons. Muon momentum is measured by reconstructing its trajectory, bent by 8 central radially-arranged and two end-cap superconducting toroidal magnets, located around the calorimeters and inside the MS. These magnets have a field in the central (end-cap) region of approximately 0.5 (1) T. The configuration of the MS and toroidal magnets systems is illustrated in Figure 2.5.

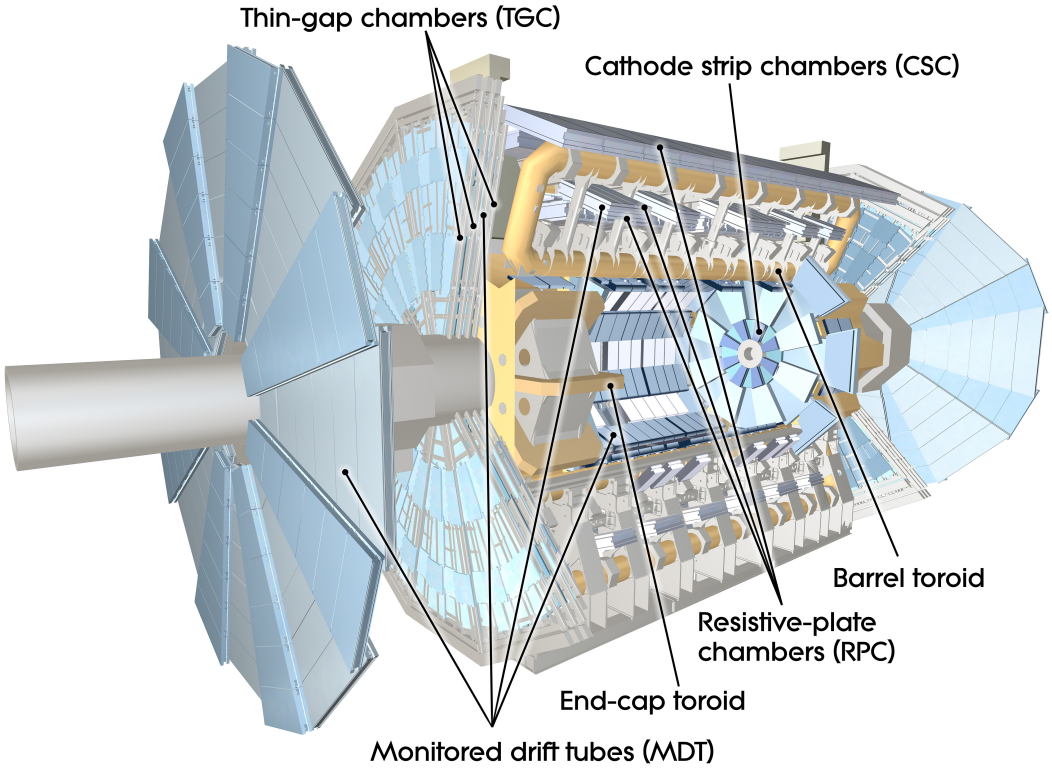

Figure 2.5: Schematic view of the muon spectrometer. Figure from Ref.1 [70].

Precision muon tracking is achieved through Monitored Drift Tubes (MTD) and Cathode Strip Chambers (CSC). The outer layers of the MDT system cover $|\eta| < 2.7$ and have 1,088 chambers and 339,000 channels, while the innermost layer covers $|\eta| < 2$ and has 1,150 chambers and 354,000 channels. The CSC covers $2.0 < |\eta| < 2.7$ and has 32 chambers and 31,000 channels. Chambers are arranged in two sets of three layers each: on the barrel region a set of cylindrical layers around the beam axis, and on the transition and end-cap rations a set of layers perpendicular to the beam. For triggering, a set of Resistive Plate Chambers (RPC) covering $|\eta| < 1.05$, and a set of Thin Gap Chambers (TGC) covering $1.05 < |\eta| < 2.4$ are used.

The standalone momentum resolution of the MS tracking system is about 4% for a muon of around 100 GeV and between 8% and 11% for a muon of around 1 TeV, depending on the η of the muon.

2.3.5 Jet trigger

Chapter 3 presents a jet trigger study, therefore this topic is outlined here. The ATLAS experiment jet-triggering scheme [77] starts by looking at transverse energy, E_{T}, depositions in calorimeter towers, looking for energy depositions above certain thresholds and for selected multiplicities of well-separated energy depositions. This first, hardware-based, stage of the scheme is known as Level 1 (L1), and it is designed to quickly ($\sim 20\mu s$) decide whether or not to record an event. Furthermore, L1 triggers must decrease the output from a bunch-crossing rate of 40 MHz down to 75 kHz.

The High Level Trigger (HLT) stages following the L1 event selection are the Level 2 (L2) and Event Filter (EF). At L2, Regions-of-Interest (RoI) identified at L1 are used to seed algorithms that by means of a more finely grained calorimeter data and improved calibrations, allow for more accurate selection of events using the E_{T} and other quantities associated with the RoI. This stage is designed to further decrease the output rate from $\sim$70 kHz down to 2 kHz.

The last stage of the HLT event selection uses jet-finding algorithms very similar to those used by physics analysis (offline). Here, rather than seeding on RoI, a full scan of the detector takes place allowing signals such as combinations of multi-jet, missing transverse momentum and tracking information, and various jet radii to have an associated trigger object. At this stage, the energy thresholds are very close to what will be used offline, so that particular physics analysis can request custom triggers targeting selected final state topologies and energy thresholds.

The ATLAS data recording is divided into streams which are labelled according to whether an electron, muon or jet was found at L1. Trigger prescales change between streams. Prescaling is a method for keeping only a fraction of events passing certain trigger. The larger the prescale, the smaller this fraction is. The delayed stream, inactive during 2012 at the beginning of high intensity runs, contained unprescaled jet triggers with low-p_{T} thresholds. This stream can be combined with the electron or muon streams, due to its orthogonality to them, in order to recover acceptance loss from lepton trigger coverage.

2.4 Data and Monte Carlo samples

2.4.1 Proton-proton collision data

The studies in this document are done using data collected during 2011 and 2012, at two centre-of-mass energies, corresponding to 5.25 fb^{-1} of 7 TeV data and 20.3 fb^{-1} of 8 TeV data. The jet trigger performance study in Chapter 3 uses a fraction of the 8 TeV dataset, corresponding to 14 fb^{-1} collected up to September 2012, and the entire 7 TeV dataset. The jet-tagging performance study in Chapter 4 and the search for new physics in Chapter 5 use only the 8 TeV dataset.

2.4.2 Monte Carlo simulation

Samples of simulated SM and BSM processes are generated in order to compare observation with expectation. This comparison is used to test the modelling of various observables, and to quantify deviations from the SM, in search for new physics. Also, comparisons between simulated samples are used to examine the robustness of the expectation to changes in the environment.

MC simulations are generated according to the scope of a particular study. In this thesis, these correspond to studies of: jet trigger efficiency; performance of shower deconstruction; and a search for VLQs. These methods are outlined below.

Trigger efficiency:

7 TeV and 8 TeV light- and heavy-quark (top) samples are generated in order to study the performance of jet triggers in an inclusive, dijet dominated, selection of events, and in a $t\bar{t}$ environment with one lepton in the final state. Multijet production is modelled using Pythia 8. SM $t\bar{t}$

production is modelled using the MC@NLO generator, with HERWIG for parton showering and hadronisation and JIMMY [78] for multiple-parton scattering. A sample of simulated high p_{T} top quarks are obtained from a sample of Z' with a mass, $m_{Z'}$, of 1.75 TeV decaying to $t\bar{t}$, modelled using PYTHIA 8.

The study of the jet trigger efficiency does not require information on the normalisation, however, it is necessary in the combination of the PYTHIA dijet p_{T} *slices*. These samples are generated in slices of transverse momentum, each aiming at populating a particular region of the space phase. In order to obtain a smooth distribution, their relative cross-section needs to be accounted for. Here, the predictions from PYTHIA are used.

Performance of shower deconstruction and search for VLQs:

8 TeV samples of all SM processes with a substantial contribution to the lepton plus jets final state are generated. The dominant processes are $t\bar{t}$, W+jets, single top, and multijets where a jet is misidentified as an lepton. Other smaller processes are Z+jets and diboson production.

The shapes of all SM processes, excluding the multijet background, are obtained from theoretical predictions. W+jets and Z+jets samples are generated using ALPGEN, with up to five extra final-state partons at leading order without virtual corrections, and are showered by PYTHIA 6. Top quark pair and single top-quark processes are produced using POWHEG interfaced with PYTHIA 6 for parton showering. Diboson samples are produced using HERWIG.

The multijet background includes all background sources from processes with non-prompt leptons or jets misreconstructed as lepton. It is derived from data using the matrix method [79, 80]. In this method two samples with different lepton selections are obtained: a *tight* selection, corresponding to what is used in this analysis, and a *loose* selection where some of the lepton identification requirements are relaxed. The loose selection contains a larger fraction of fake or non-prompt leptons than the tight selection.

For the study of systematic uncertainties due to the modelling of W+jets, the nominal sample is compared to SHERPA. Also, for the top-quark pair process, samples generated with ACERMC [81] interfaced with PYTHIA 6, MC@NLO interfaced to HERWIG for parton showering and JIMMY

for the underlying event, and with the nominal POWHEG but changing the showering and underlying event interface to HERWIG and JIMMY respectively are used. Similarly, for the t-channel single top-quark process, the nominal sample is compared to aMC@NLO [82] interfaced with HERWIG.

The $t\bar{t}$ and W+jets normalisation are obtained from data. This will be discussed further in Section 5.6.2. The Z+jets, single-top and diboson normalisation are obtained from theoretical predictions. The inclusive Z+jets cross-section is calculated to NNLO using FEWZ [83]. The single-top production cross section prediction is calculated at NLO+NNLL precision in QCD. The uncertainty for the t-channel single top-quark cross-section is +3.9% -2.2% [84].

Single production of VLQs:

Samples of heavy VLQs produced through the electroweak interaction are generated using MADGRAPH following Ref. [85]. Here, only events where the VLQ decays into Wb are produced. Events are filtered applying a cut of 20 GeV on the minimum p_{T} of the leading muon or electron in the event. These samples are generated for various VLQ masses between 400 and 1200 GeV in steps of 100 GeV. Table 2.1 presents the signal process cross sections for various masses.

Table 2.1: NLO single production cross sections for the Wb fusion for a unit EW coupling. Numbers from Ref [37].

Mass [GeV]	$\sigma_{W^+\bar{b}} + \sigma_{W^-b}$ [fb]
600	2100
700	1230
800	746
900	470
1000	298
1100	194
1200	127

2.5 Analysis software

2.5.1 The TopRootCore package

The `TopRootCore` [86] (TRC) event processing software is designed to apply the object calibrations and selections necessary to account for data to MC differences on the metrics of these objects, and to correct for the impact of the inactive regions of the ATLAS detector. This is further discussed in following sections. The TRC package is based in the `RootCore` [87] package.

Figure 2.6 shows a diagram of the event-by-event flow of the TRC package. Here, n-tuples, `C++` class objects based on `TTree` [88] objects, containing the entire data and MC datasets, are taken as input. The information in these n-tuples is organised in class objects, associated to final state observables. For every object a calibration tool exists. This is discussed in Section 2.6 and Section 2.7. Once the calibration loop ends, event-wide observables, based in these objects, are calculated. These are all then taken by the event filtering software, which selects only those events which might be potentially interesting for a particular analysis, for instance, final states looking for exactly one lepton and a given number of jets can safely discard multi-lepton or fully-hadronic events. The various tools are aware of the systematic variations which can be including during the event processing. Therefore, the whole process is repeated as many times as there are variations which affect the object calibration. This ultimately produces clones of the mini n-tuples, allowing for thorough studies of how systematic uncertainties affect the physics objects.

2.5.2 The BoostedSLUtils package

The `BoostedSLUtils` package is an extension of TRC, which includes tools and class objects necessary for the inclusion of the physics objects, missing in TRC, that are essential for the high-p_{T} (boosted) studies on following chapters. This package is based in the concept of inheritance. Here, only the necessary third-party packages are added, and the remaining class objects are minimal extensions of already existing class objects, therefore cloning their functionality. This preserves the normal flow of TRC, allowing either package to be updated easily.

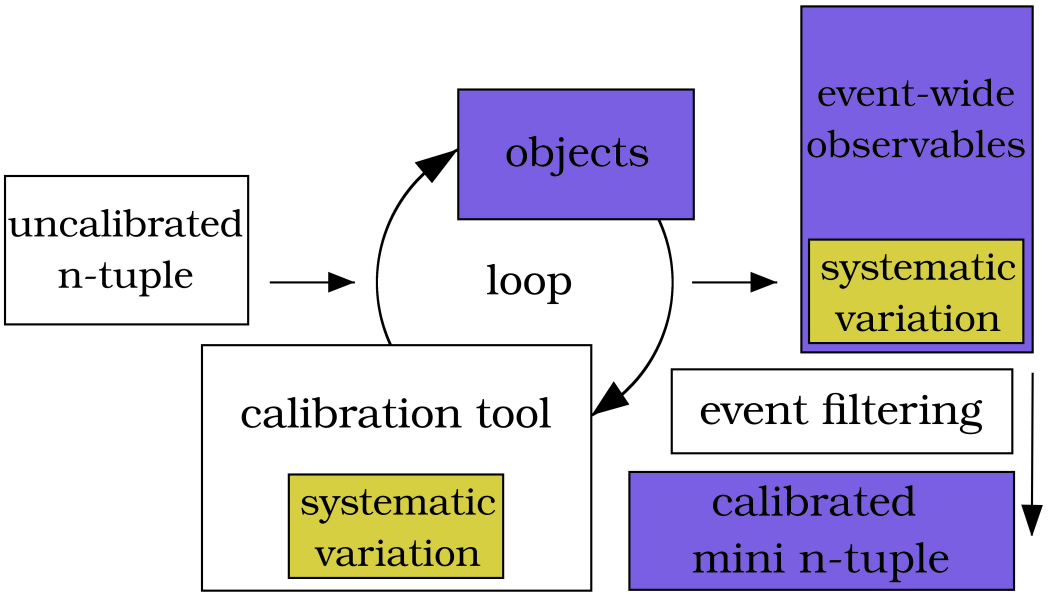

Figure 2.6: Internal flow of the TRC package. Input n-tuples (trees) are processed into object classes which are calibrated, selected and exported into a small selection (mini-ntuple) of events.

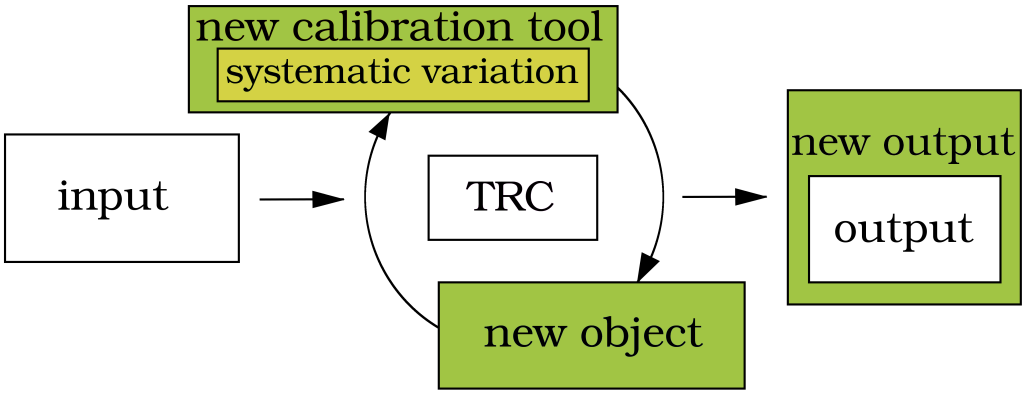

Figure 2.7: Internal flow of the BoostedSLUtils package. The normal flow of the TRC is extended to include the minimum necessary new tools and objects. The output is also an extension of the basic setup.

2.6 Object reconstruction and identification

2.6.1 Electrons

Electrons are reconstructed using energy depositions in the ElectroMagnetic calorimeter (EM clusters) associated with tracks in the ID. The associated tracks are used to set the direction of the electron, while the clusters are used to measure its energy.

The electron trigger combines information from the three different stages of the ATLAS triggering scheme. First L1 rapidly decides whether a group of EM clusters, isolated from activity in the hadronic calorimeter, is above certain threshold. Then at L2 and EF algorithms are used to select the set of clusters that will form the electron, and corrections are applied to account for detector inefficiencies and dead material. In following chapters, the L1→EF chain used is `L1_EM18VH`→`L2_vh_medium1`→`EF_e24vhi_medium1`, where V (v) in L1 (L2 and EF) stands for varied threshold, which corresponds to a dead material correction, and H (h) in L1 (L2 and EF) denotes hadronic isolation. To mitigate the inefficiency at high transverse energy, E_{T}, resulting from the hadronic isolation, this trigger is combined with `EF_e60_medium1`, using a logical OR.

Electrons are required to be within the EM calorimeter acceptance, $|\eta| < 2.47$, excluding the barrel-endcap transition region, $1.37 < |\eta| < 1.52$. The minimum E_{T} is 25 GeV. To ensure good separation between isolated electrons and jets(faking electrons), electrons are required to satisfy the `Tight++` [89] identification criteria. This includes stringent requirements on the matching between the track and the EM cluster, and on the ratio of the cluster energy to the track momentum, Additional isolation cuts are applied to mitigate the multijet background. Using a cone with $\Delta R = 0.2$, a maximum is set to the energy depositions around the electron, relative to its energy. Similarly, using a cone with $\Delta R = 0.3$, a maximum is set to the total p_{T} of tracks around the electron, relative to its p_{T}. As both electrons and jets are reconstructed using energy depositions in the calorimeter, the closest jet within $\Delta R < 0.2$ around an electron corresponds to the same object and is therefore removed. Then, if the electron is within a cone of $\Delta R < 0.4$ around a jet, the electron is discarded. In TRC, these selections are applied using the `egammaAnalysisUtils` [90] package, and are expected to have an isolation efficiency of 90%.

For the determination of the multijet contribution to final states with at least one electron, a relaxed identification criteria, `Medium++` [89], without isolation cuts, is used to select electrons. `Medium++` electrons are selected without requiring a tight ($\Delta\eta$,$\Delta\phi$) matching between the track and the EM cluster, and without cutting on the E/p ratio.

MC to data scale factors on the electron trigger, identification, isolation and reconstructions are determined by the ATLAS egamma Combined Performance (CP) working group [91] using $Z \rightarrow e^+e^-$ events, and the tag and probe method. These correction factors are determined as a function of the electron E_{T} and η [92], and are applied in TRC using the `TopElectronSFUtils` [93] package.

2.6.2 Muons

Muons are reconstructed using track segments from the ID and the muon spectrometer.

In following chapters two muon trigger chains are used, `L1_MU15` $\rightarrow$ `L2_mu24_tight` $\rightarrow$ `EF_mu24i_tight` and `L1_MU15` $\rightarrow$ `L2_mu36_tight` $\rightarrow$ `EF_mu36_tight`. These differ in the isolation requirement applied to the one with the lowest p_{T} threshold, `EF_mu24i_tight`. Here, a maximum of 12% is set to the p_{T} sum of the tracks within a cone with $\Delta R = 0.2$ around the muon, relative to its p_{T}.

Muons are selected following the `muid` algorithm [94]. Here, muons are required to be within the detector acceptance, $|\eta| < 2.5$, and are required to have a p_{T} larger than 25 GeV, given by the plateau (99 % efficiency) region of the trigger. Also, muons must satisfy a tight set of track quality requirements, given by a minimum number of hits on the subdetectors of the ID. To reject cosmic rays, the longitudinal distance of the muon relative to the primary vertex must be less than 2 mm. Finally, to remove the background of muons from semi-leptonic decays of heavy-flavour quarks, muons are required to satisfy the mini isolation requirement described in Ref. [95]. Here, the p_{T} sum of tracks with $p_{\mathrm{T}} > 1$ GeV within a cone with a muon p_{T}-dependent radii, $\Delta R = 10$ GeV $/p_{\mathrm{T}}$, must be smaller than 0.05, relative to the p_{T} of the muon. Any muon within $\Delta R < 0.4$ to a jet is removed.

Muons selected without the mini isolation requirement are also used. In particular, for the determination of the contribution of multijet processes to the l+jets final state.

MC to data scale factors on the muon reconstruction and isolation efficiency are determined by the ATLAS muon CP working group using $Z \to \mu^+\mu^-$ events, and simulated samples of $b\bar{b}$ and $c\bar{c}$ where one of the heavy-quarks decays into a muon, and the tag and probe method [96]. These correction factors are determined as a function of the muon p_{T} and η, and are applied in TRC using the `TopMuonSFUtils` [97] package.

2.6.3 Jets

Jets are reconstructed using the anti-k_t algorithm with $R = 0.4$ for small-radii (small-R) and $R = 1.0$ for large-radius (large-R) jets. This algorithm uses sequential recombination to merge LCW topological clusters into jets. The LCW procedure aims at correcting for the difference in response of more electromagnetic-like and hadronic-like interactions [73, 74].

2.6.3.1 Small-R jets

Small-R jets are calibrated to the hadronic scale using p_{T}-η dependent corrections derived from simulation [73]. Also in-situ calibrations from Z+jet , γ+jet, dijet and multijet samples are used to bring the MC expectation closer to the data. In particular, the η intercalibration method [98], uses dijet balance to extend the coverage of the jet energy scale calibration and its uncertainties to the forward region. To reduce the flavour dependence of the jet energy scale, a sequential jet calibration [99] using tracking information and the energy deposition in different layers of the ATLAS calorimeters, is also used. Jets are corrected for the effects of pileup using jet areas [100].

In TRC, the `ApplyJetCalibration` [101] package is used to calibrate small-R jets. Jets are required to be within $|\eta| < 4.5$, and to have $p_{\mathrm{T}} \geq 25$ GeV. In addition, for jets with $p_{\mathrm{T}} < 50$ GeV and $|\eta| < 2.4$, the Jet Vertex Fraction (JVF), a track-based method, is used to suppress pileup jets. In this method, tracks are associated to jets, then, the p_{T} fraction of tracks which originated from the primary vertex is required to be greater than 50%. For jets outside the ID acceptance, a $p_{\mathrm{T}} \geq 35$ GeV requirement is made to mitigate the effects of pileup. Jets are also required to be labelled as *good*, removing jets produced by various sources different from energy depositions originated from the hard scatter, such as a calorimeter malfunction and cosmic rays among others.

2.6.3.2 b-tagging

The identification of small-R jets produced in the decay of b-quarks is mainly based on the long lifetime of b-hadrons. Their significant flight path results on displaced secondary vertices and measurable longitudinal impact parameters. In ATLAS, the output of a neural network, which takes as input the output from three taggers [102] (IP3D, JetFitter and SV1), the MV1 algorithm, is used for the b-tagging of jets. In this analysis, the working point corresponding to a 70% b-tagging efficiency, given by a MV1 output larger than 0.7892, is used. As the key object for b-tagging are the tracks associated to a jet, only jets falling within the acceptance of the ID ($|\eta| < 2.5$) are considered as b-tagged jet candidates.

Scale factors to correct for b-tagging efficiency differences between the data and the simulation are used here. These are derived using a calibration based on a combination of dijet and $t\bar{t}$ (dilepton) calibrations [103] The $t\bar{t}$ part dominates the systematic uncertainties. In TRC, these scale factors are applied using the `calibration data interface` [104].

2.6.3.3 Large-R jets

Large-R jets are calibrated to the hadronic scale using p_{T}-η dependent correction factors derived from simulation [105]. To mitigate the effects of pileup, the *trimming* [106] algorithm is used. In trimming, subjets are formed by applying the k_t jet algorithm with smaller radius parameter, R_{sub}, and then soft subjets with less than a certain fraction, f_{cut}, of the original jet p_{T} are removed. In this study, the trimming parameters used are $f_{\mathrm{cut}} = 0.05$ and $R_{\mathrm{sub}} = 0.3$.

2.6.3.4 Top-tagging with shower deconstruction

Boosted heavy objects, such as vector bosons or top quarks with very high transverse momentum, p_{T}, are found in many new physics signals at the LHC. The decay products of a heavy particle produced with p_{T} much greater than its mass are contained within a large-R jet. Many algorithms [107, 108] have been proposed to identify and reconstruct boosted heavy particles by using the substructure of large-R jets. Shower Deconstruction [109] (SD) is one such algorithm, combining information from the hard-scattering process, initial-state and final-state radiation, and colour flow.

In this document, the focus is on using SD as a top-tagger [110]. The input to SD is a collection of subjets clustered from the constituents of the large-R jet. These are used to calculate a likelihood ratio for the observed subjets to be produced by a hadronically decaying top quark compared to a multijet background process.

The SD algorithm constructs a discriminant, χ_{SD}, optimised to distinguish jets produced in decays of signal particles (S) from jets produced by background processes (B). In this thesis, the signal process used in the SD calculation is a hadronic top quark decay, and the background process is a jet originating from a single gluon. This background hypothesis could be improved by including also quark-initiated jets, but these are not implemented in the current version of the algorithm. The discriminant χ_{SD} is derived considering the probabilities for parton showers from the signal and background process to produce the observed jet substructure.

A specific configuration containing N subjets with four-momenta $\{p\}_N = \{p_1, p_2, \ldots, p_N\}$ can be generated in many different ways in the parton shower approach, and each of these constitutes a possible *shower history*. For a given shower history $\{p, c^j\}_N$, where j is the index of the shower history, each subjet with four momentum p_i is assigned to one of several categories c_i^j. For signal, the categories are: the decay products of the top quark and their parton emissions; top parton radiation emission and parton showers starting from initial-state radiation. Although it is usually considered negligible due to the short top-quark lifetime, parton radiation from the top quark itself may become significant for very highly boosted top quarks. It should be noted that here no additional information, such as b-tagging, is considered in the classification. For background, the categories are: final-state radiation; and initial-state radiation.

After assigning the subjets to categories, SD calculates the probability that a given shower history was realised in a given event. A splitting probability is assigned to each branching, taking colour flow into account. These probabilities are approximately the splitting probabilities that are used in parton-shower event generators. Each propagator in the shower history corresponds to a Sudakov factor. By combining all of these propagators, shower histories are constructed [109, 110].

The shower histories are used to construct a likelihood ratio $\chi_{\mathrm{SD}}(\{p\}_N)$ using the subjet four-vectors as inputs

$$\chi_{\mathrm{SD}}(\{p\}_N) = \frac{P(\{p\}_N|\mathrm{S})}{P(\{p\}_N|\mathrm{B})} = \frac{\sum_{\mathrm{histories}} P(\{p, c^j\}_N|\mathrm{S})}{\sum_{\mathrm{histories}} P(\{p, c^j\}_N|\mathrm{B})} \tag{2.3}$$

where $P(\{p\}_N|\mathrm{S})$ is the probability of obtaining $\{p\}_N$ given the signal hypothesis, and $P(\{p\}_N|\mathrm{B})$ is the probability for obtaining $\{p\}_N$ from background jets arising from background processes. $P(\{p\}_N|\mathrm{B})$ and $P(\{p\}_N|\mathrm{S})$ are calculated as the sum of the probabilities for each shower history. The total probability depends on the number of shower histories considered, which is usually larger for the background hypothesis than for the signal hypothesis.

The signal and background have different colour structures and subjet kinematics because the signal contains a massive electroweak-scale resonance decay with associated radiation, and the background comes only from splittings of energetic partons. These differences are reflected in the decay matrix element, splitting functions and the Sudakov factors, resulting in different values for $P(\{p\}_N|\mathrm{S})$ and $P(\{p\}_N|\mathrm{B})$ when testing the same input. Thus, based on the kinematics of the subjets, the large-R jet looks either more like a top jet or more like a QCD jet.

It is only possible to define χ_{SD} when the subjets are kinematically compatible with a hadronic top quark decay. This leads to the following requirements: the jet has at least three subjets; two or more subjets must have a mass close to the W boson mass; and at least one more subjet can be added to obtain a total mass close to the top mass. Events failing these requirements have undefined χ_{SD} and are labelled as χ_{SD}(fail) in the subsequent sections and plots. Events satisfying these requirements are labelled as χ_{SD}(pass). The mass windows and other parameters used in this study are listed in Table 2.2. The computation time needed for the calculation of χ_{SD} grows exponentially with the subjet multiplicity, thus the input is restricted to the nine leading subjets of the leading large-R jet.

Figure 2.8 illustrates the SD algorithm for a simulated anti-k_t [50] large-R jet from $Z' \to t\bar{t}$ decay for $m_{Z'} = 1.75$ TeV. It has six C/A subjets, selected and reconstructed as described in Section 4.4.1, from which more than 1500 (35000) possible shower histories for the signal (background) hypothesis can be created. The three shower histories with the largest signal probabilities are shown. Two features of SD are shown here. First, multiple interpretations of the substructure of a jet are used. Here, two different combinations of subjets

Table 2.2: List of shower deconstruction input parameters with their nominal values. For the initial shower scale, the p_{T} and m are those of the large-R jet.

Parameter	Nominal value
Subjet R parameter	0.2
Number of leading subjets to consider	9
Large-R jet R parameter	1
Minimum subjet p_{T}	20 GeV
W mass	80.4 GeV
W mass window	$\pm$ 12 GeV
Initial shower scale	$Q^2 = p_{\mathrm{T}}^2 + m^2$
Top quark mass	172.3 GeV
Top quark mass window	$\pm$ 40 GeV

can be built with masses close to the W boson mass. Second, all the input subjets are used by the algorithm; they are assigned to the top decay and parton emissions from its decay products, to parton emission from the top or to initial-state radiation.

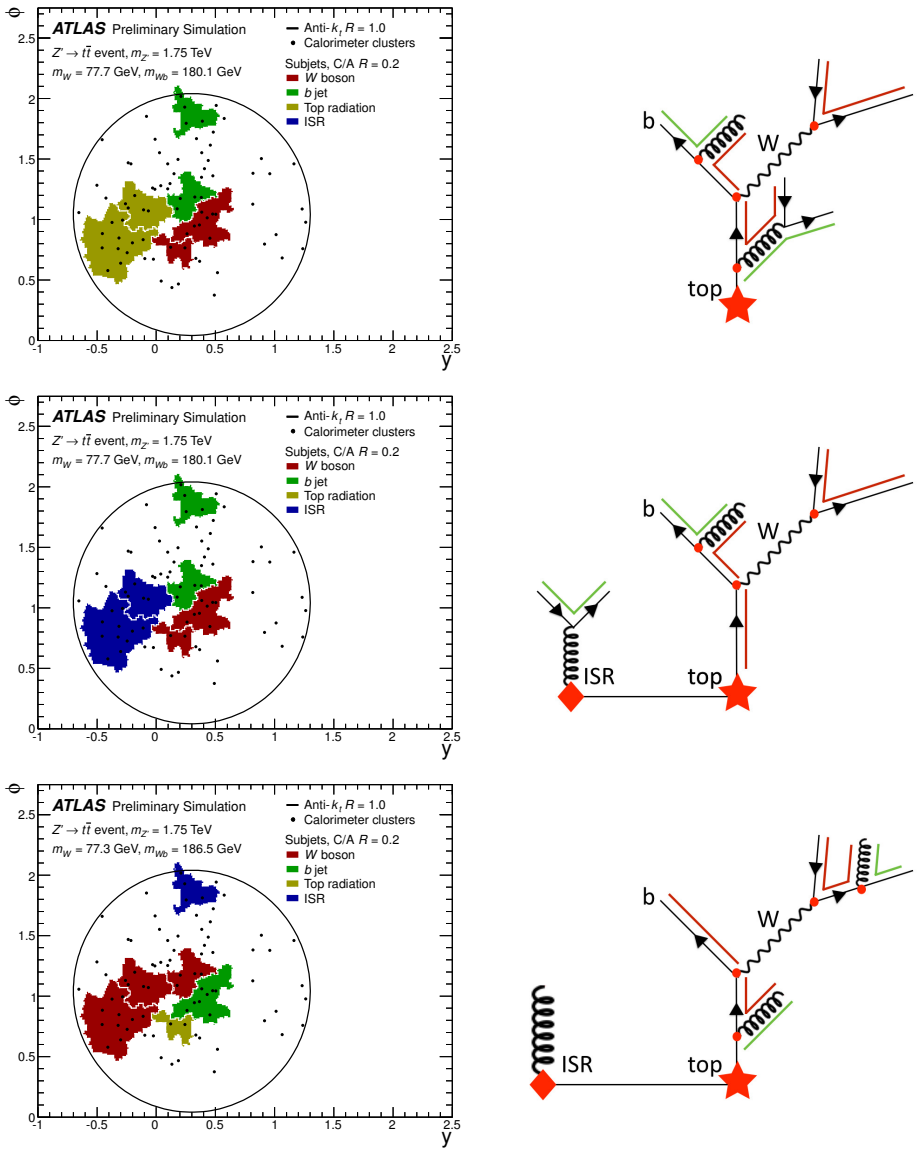

Figure 2.8: Illustration of the three (out of more than 1500) shower histories with the largest signal probabilities for a simulated large-R jet from a top quark produced in a $Z' \to t\bar{t}$ decay with $m_{Z'} = 1.75$ TeV. On the left panels are event displays showing the subjets used by the algorithm. Subjets of a particular category have the same fill colour and their extent represents the subjet active catchment area [111]. Jet constituents are shown as black dots. On the right panels are the corresponding shower histories. The hard scatter is indicated as the (red) star. Initial-state emissions are indicated by diamonds. Parton emissions are indicated by filled circles. Coloured straight lines represent the colour flow. Figure from Ref. [2].

2.6.4 Missing transverse momentum

The transverse components of E^{miss} are calculated from the sum of various terms

$$E_{x,y}^{\text{miss}} = E_{x,y}^{\text{RefEle}} + E_{x,y}^{\text{RefJet}} + E_{x,y}^{\text{SoftJets}} + E_{x,y}^{\text{CellOut}} \tag{2.4}$$

where $E_{x,y}^{\text{RefEle}}$ and $E_{x,y}^{\text{RefJet}}$ are the energy depositions associated with the electrons and small-R jets, reconstructed, selected and calibrated as described in this chapter. Here $E_{x,y}^{\text{SoftJets}}$ corresponds to the term due to small-R jets with $10 \leq p_{\text{T}} < 20$ GeV. The $E_{x,y}^{\text{CellOut}}$ term uses the eflow algorithm, that uses tracking information to exploit the better track resolution and calibration at low-p_{T}, and corresponds to the energy depositions that are not associated with any reconstructed object. The $E_{\text{T}}^{\text{miss}}$ is corrected for the muon momentum, reconstructed as in the `muid` algorithm. Also, an additional pileup offset correction is applied.

The $E_{\text{T}}^{\text{miss}}$ reconstruction calibration scheme[2] uses correction weights corresponding to the calibrations from specific objects [112]. In TRC, this is done using the `MissingETUtility` [113] package.

The longitudinal component of the neutrino momentum is calculated using the $t\bar{t}$ resonances `NeutrinoBuilder` [114] package. Here, an on-shell W mass constraint is imposed on the lepton+$E_{\text{T}}^{\text{miss}}$ system. This yields a quadratic equation, where from the two solutions, the one real with the smallest $|p_z|$ is taken. Further details can be found in Ref. [115].

2.7 Systematic uncertainties

2.7.1 General strategy

In this section, an overview of the general strategy for the evaluation of systematic uncertainties is presented. Those that are only relevant for a particular study within this thesis are discussed in their respective chapters. The evaluation of systematic uncertainties follows, whenever possible, the standard ATLAS top working group recommendations documented in Ref. [116], which follows the strategies established by the respective ATLAS CP groups.

Recommendations and packages exist for electrons [117], muons [118], and $E_{\text{T}}^{\text{miss}}$ [119]. Also for the small-R jet energy scale [120], reconstruction effi-

[2] `http://atlas.web.cern.ch/Atlas/GROUPS/PHYSICS/JETS/EMISREC/MET_schema_2.pdf`

ciency [121] and energy resolution [122], and b-tagging and large-R jet energy and mass scale uncertainties. In addition, recommendations also exist for the evaluation of $t\bar{t}$ MC modelling uncertainties [123].

2.7.2 Luminosity

The luminosity uncertainty from the respective group is 2.8%, estimated using the methodology detailed in Ref. [124] for beam-separation scans performed in November 2012.

2.7.3 Electrons and muons

The `TElectronEfficiencyCorrectionTool` [125] (`TrigMuonEfficiency` [126]) package is used to apply electron (muon) trigger scale factor uncertainties, as $\pm 1\sigma$, with σ being the error on the scale factor.

The `TElectronEfficiencyCorrectionTool` package is used to evaluate uncertainties on the electron reconstruction efficiency, identification and isolation scale factors. An additional uncertainty is provided by the TWG to account for differences between the Z+jets and $t\bar{t}$ environments. For the evaluation of uncertainties on the electron energy scale and resolution, the `EnergyRescalerUpgrade` [127] package is used. Here, the electron energy is rescaled using a correction provided in $|\eta|$ bins with a E_{T} validity range of 10 GeV to 1 TeV. Also, the electron energy is smeared using the uncertainty on the measurement of its energy resolution. The smearing factor is provided as a function of the electron energy and η.

Uncertainties on the muon reconstruction efficiency, identification and isolation scale factors are applied using the `MuonEfficiencyCorrections` [128] package. Uncertainties on the muon momentum scale and resolution are applied using the `MuonMomentumCorrections` [129] package. Here, the variance on the charge-over-momentum, extracted from the covariance matrix of the fitted muon-track parameters, is used to rescale the momentum of the muon. Also, the muon momentum is smeared using the uncertainty on the measurement of its momentum resolution.

2.7.4 Jets

The `JetUncertainties` [130] package is used to evaluate uncertainties on the small-R jet energy scale. Here, 20 nuisance parameters from the in-situ analysis, Z+jet, γ+jet and multijet balance, 2 from η intercalibration, which in-

cludes statistical on MC modelling uncertainties, 1 from MC non-closure on the small-R jet calibration, and 4 on the modelling of the pileup conditions and metrics used in the areas correction.

For the evaluation of the small-R jet reconstruction efficiency, jets within the ID acceptance are randomly thrown away. The reconstruction efficiency for small-R jets with $p_{\mathrm{T}} \geq 30$ GeV is assumed to be equal to 1. The reconstruction inefficiency is 2.7% (0.23%) for small-R jets with $15 \leq p_{\mathrm{T}} < 20$ ($20 \leq p_{\mathrm{T}} < 30$).

Uncertainties on the small-R jet energy resolution are applied using the `ApplyJetResolutionSmearing` [131] package. As for the 2012 data the measured and expected small-R jet resolution agree within uncertainty, the recommendation is to smear the MC by $+1\sigma$ of the uncertainty.

The `JVFUncertaintyTool` [132] package is used to evaluate the uncertainty associated with a JVF cut on an analysis, for small-R jets with $p_{\mathrm{T}} < 50$ GeV and $|\eta| < 2.4$. Here, small-R jets are sorted according to whether or not they can be geometrically matched to a particle small-R jet. Then, the package calculates a new JVF cut for each jet. The analysis is run for the nominal and new JVF cuts, and the difference is taken as the uncertainty.

The evaluation of the b-tagging calibration scale factor uncertainties uses the eigenvector variation method [133]. Here, the number of variations corresponds to the number of bins used for the calibration. The effect of the $\pm 1\sigma$ variation of each source of uncertainty on the scale factor calibration produce a covariance matrix. Eigenvalues can be derived from the sum of these covariance matrices, resulting in set of independent variations.

The `UJUncertaintyProvider` [134] package is used for the evaluation of large-R p_{T} and mass scale uncertainties. These uncertainties are derived combining track-jet double ratios [135] with γ+jet balance [136] for the large-R jet p_{T}, depending on the p_{T} and η of the large-R jet, and include an uncertainty due to the transition between these two methods. The γ+jet uncertainty is broken into components given by the various sources of uncertainties on the data-to-MC ratio of the photon response. Also, a MC-based topology uncertainty is included to account for differences on the response for various mixtures of gluon and light/heavy-quark initiated jets. An uncertainty is also assigned to account for changes in the large-R jet response for different pileup conditions. For the large-R jet mass, only track-jet double ratio uncertainties are available.

The large-R jet energy (mass) resolution uncertainties are evaluated by smearing the resolution, as estimated in MC using the FitCR, such that it is

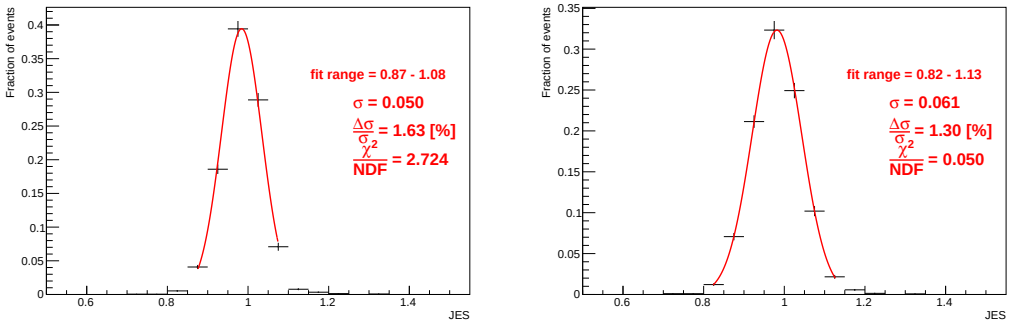

(a) nominal (b) smeared

Figure 2.9: Distribution of the large-R jet energy response both before (left) and after (right) smearing.

increased by 20% [137]. Here, the energy (mass) resolution is obtained in three mass bins: 0-70 GeV, 70-120 GeVand above 120 GeV. Each bin is subsequently divided in four large-R p_{T} bins. This results in 12 large-R jet mass-p_{T} bins, where for each the energy (mass) resolution is obtained by fitting the energy response distribution to a gaussian form. Then, for every mass bin, the energy (mass) resolution is parametrised in terms of the large-R jet p_{T}. The number of bins is limited due to the available statistics.

Figure 2.9 shows an example of the large-R jet energy response, fitted to a gaussian form, before and after smearing, for a particular large-R jet mass-p_{T} bin. The fitted σ corresponds to the resolution estimation. Here the energy resolution has increased by about 23%, as expected from the smearing.

Figure 2.10 shows an example of the large-R jet mass response, fitted to a gaussian form, before and after smearing, for a particular large-R jet mass-p_{T} bin. The fitted σ corresponds to the resolution estimation. Here the mass resolution has increased by about 27%.

2.7.5 Missing transverse momentum

The uncertainties on the $E_{\mathrm{T}}^{\mathrm{miss}}$ calculation correspond to the energy scale and resolution of the SoftJets and CellOut terms. These uncertainties are evaluated using the `MissingETUtility` package, and correspond to a $\pm 1\sigma$ variation on the $E_{\mathrm{T}}^{\mathrm{miss}}$ soft terms scale and resolution errors.

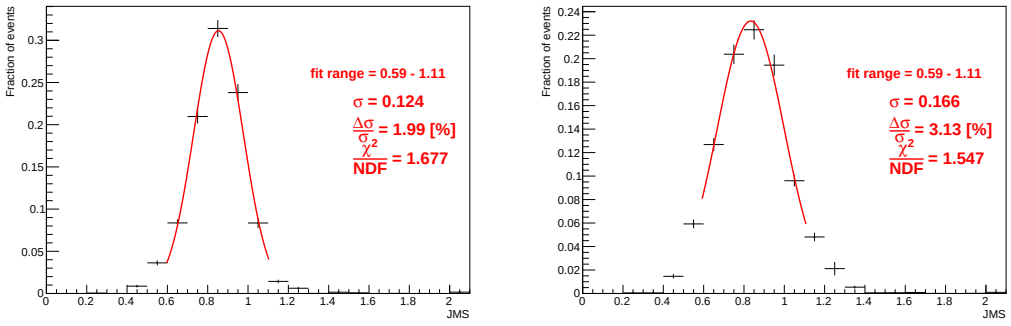

(a) nominal (b) smeared

Figure 2.10: Distribution of the large-R jet mass response both before (left) and after (right) smearing.

2.7.6 $t\bar{t}$ modelling

The $t\bar{t}$ modelling uncertainties correspond to comparisons between MC event generators and showering: Powheg +Pythia 6 vs Powheg +Herwig; Powheg +Pythia 6 vs MC@NLO and Powheg +Pythia 6 vs Alpgen +Herwig. The Uncertainty due to the modelling of QCD Initial- and Final-State Radiation (ISR/FSR) is estimated by varying the Pythia ISR and FSR parameters within ranges allowed by a previous ATLAS measurement of $t\bar{t}$ production with a veto on additional central jet activity [138].

2.7.7 Single top t-channel modelling

The nominal Powheg + Pythia 6 is compared to aMC@NLO +Herwig for the estimation of a shape uncertainty on the single top t-channel modelling uncertainty.

2.7.8 Multijets estimation

The `FakesMacros` [139] package provides an estimation of the multijet background. Also, recommendations on how to estimate the uncertainties for this estimation are provided [140]. These correspond to 5 variations, given by: a 10% variation of the MC prediction in the multijet CR; the use of a different multijet CR for the efficiency of tagging a jet as a lepton; the difference between the tag-and-probe and high $E_{\mathrm{T}}^{\mathrm{miss}}$ and high m_{T} methods to estimate the lepton tagging efficiency and a change on the parametrisation of the weights.

2.8 Summary

In this section, the parameters of the experimental setup have been presented. The LHC beam and pileup conditions, as well as the ATLAS ID track-momentum resolution, the jet-energy resolution of its calorimeters, and the ATLAS jet-triggering and MS performance metrics have been discussed.

The data and MC samples used in this thesis have been listed. Also, the sample processing and analysis scheme has been illustrated.

The reconstruction and calibration of the physics objects used in all following chapters has been examined. Also, the corresponding strategy for the evaluation of systematic uncertainties on the metrics of these objects and on the modelling of the SM expectation have been presented.

Chapter 3

Large-R jet trigger

3.1 Introduction

One of the kinematic regions for which jet triggers are available is the high E_{T}, large-R jet physics of hadronic final states. Known as the boosted regime, it is widely accepted that at this scale hard and heavy objects often decay in such a way that all of its decay products will be collimated within a single large-R jet. Here, the substructure of multi-prong large-R jets from the decay of heavy particles will be different from QCD backgrounds, therefore allowing to better differentiate between signal and background events.

For the 2011 ATLAS detector data collection of LHC beam collisions, a set of EF triggers were included aiming at those boosted searches and physics analysis. In particular the `EF_j240_a10tc_EFFS` trigger is of interest from the performance evaluation point of view, as it corresponds to the unprescaled trigger chain with the lowest E_{T} threshold available, namely `L1_J75` $\rightarrow$ `L2_j95` $\rightarrow$ `EF_j240_a10tc_EFFS`, illustrated in Figure 3.1. Due to the large volume of data that survives the ATLAS trigger event selection, scaling factors are, in some cases, applied to triggers to further decrease the data output rate. Then, in most cases, a unprescaled trigger chain will select larger samples of events than its corresponding prescaled version.

The jet trigger naming scheme at the EF level follows a convention where four fields are separated by underscores. The first field denotes the trigger level, the second corresponds to the E_{T} threshold, and the third to the jet-clustering algorithm, radius parameter and input. For instance, `a10tc` means that topological-clusters [141, 142] were clustered with the anti-k_t [50] algorithm using a jet radius parameter equal to 1. The last field, `EFFS`, indicates that a full scan of the detector took place during the clustering of the jet.

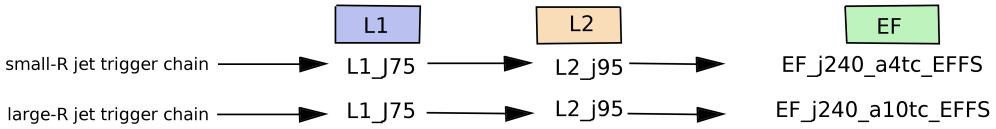

Figure 3.1: Small- and large-R jet trigger chains used to study the performance of large-R jet triggers.

Another interesting feature of that unprescaled large-R jet trigger chain is that a similar one does exist, also unprescaled, with the only difference being the use of small-R jets, namely `L1_J75` $\rightarrow$ `L2_j95` $\rightarrow$ `EF_j240_a4tc_EFFS`, illustrated in Figure 3.1. Due to the wide use of small-R jet triggers in ATLAS [73, 75, 77, 108, 143–164], they are used as a reference to which the large-R jet triggers are compared.

In this chapter, the performance of large-R jet triggers during the 7 TeV 2011 data taken period is presented, and an application to a physics analysis using 8 TeV data is discussed.

3.2 Event selection

For this study only a minimum set of requirements is applied to obtain an inclusive sample of jets events :

- to have at least one primary vertex with at least five tracks with $p_{\mathrm{T}} \geq 0.4$ GeV,
- to contain at least one large-R jet with $E_{\mathrm{T}} > 50$ GeV and $|\eta| < 2.8$.

In addition, a prescaled trigger chain is used as a reference trigger. This chain is observed to have the lowest prescale of any chain reaching plateau before the activation of the trigger chains studied in this chapter. The EF E_{T} threshold of this reference chain is 100 GeV.

3.3 Large-R jet trigger performance

The jet trigger efficiency is the main performance metric. The efficiency is given by the probability that an offline jet will also be reconstructed online. This can be presented in terms of some offline event property, such as the leading jet E_{T}.

In order to measure this efficiency either random or reference triggers are

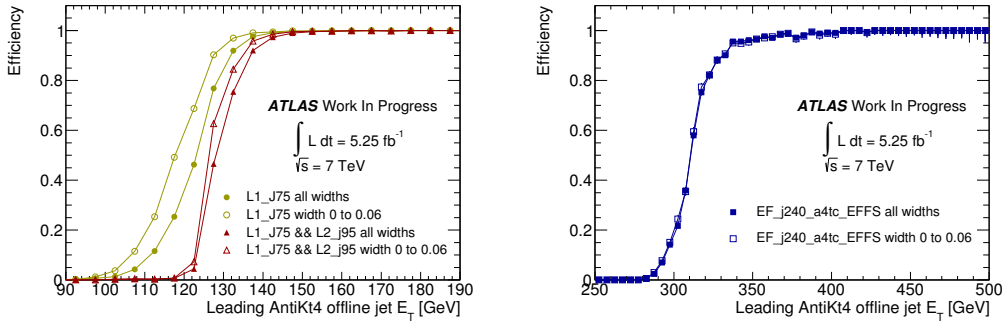

Figure 3.2: The efficiency of the L1 and L2 (left) and EF triggers (right) as a function of the leading offline jet E_{T}, inclusively (filled markers) and for narrow jets (open markers).

used. Random triggers are usually prescaled, resulting in a low event rate. Due to the steeply falling E_{T} spectrum of most SM processes, the low event rate makes them desirable only to evaluate the performance of jet triggers in the low E_{T} region. Reference triggers are required to be fully efficient in the E_{T} region where the performance of a trigger is being evaluated. Hence, a measurement of their efficiency is needed.

The use of EF, instead of L1 or L2 triggers results in an improvement of the trigger performance. This is due to the good energy resolution resulting from the similarity between the jets used online and offline. Figure 3.2, shows the trigger efficiency versus the leading offline small-R jet E_{T} for `L1_J75` and a logical AND of `L1_J75` and `L2_j95`, compared to `EF_j240_a4tc_EFFS`. Also here, the efficiency is presented in two bins of the jet width [165], inclusively and for narrow jets, with widths in the range of 0 to 0.06. The physics bias given by the difference between these two bins for `L1_J75` is gradually reduced when advancing through the trigger chain, becoming minimum for `EF_j240_a4tc_EFFS`.

The curves shown in Figure 3.2 are referred to as the trigger *turn-on* curve, and its relevance comes from the requirement made by physics analysis that the E_{T} for selected offline jets lie in the region where the trigger efficiency is at the plateau region. This is done to minimise systematic uncertainties associated with the trigger. A steeper curve indicates good performance of the trigger.

A key motivation for the introduction of large-R jet triggers is that the energy deposition of a boosted multi-prong final state may not be contained within a single small-R jet. This could result in the deterioration of the trigger performance with respect to offline large-R jets. Figure 3.3 shows the turn-on

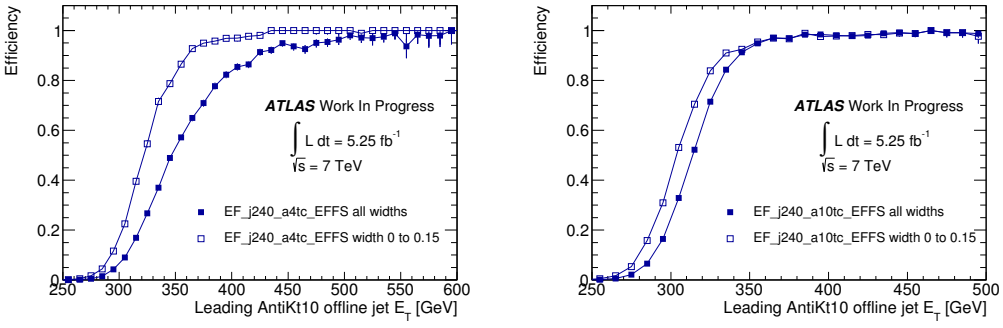

Figure 3.3: The efficiency of the standard `a4tc` (left) and large-R jet `a10tc` (right) triggers as a function of the leading offline large-R jet E_{T}, inclusively (filled markers) and for narrow jets (open markers).

curve for `EF_j240_a4tc_EFFS` with respect to the leading large-R jet E_{T}, compared to a large-R jet trigger, `EF_j240_a10tc_EFFS`. Here, for the inclusive jet-width bin, the large-R jet trigger reaches plateau at around 380 GeV, while the small-R jet trigger only reaches this region at around 550 GeV. Also here, the considerable difference in performance between the narrow and inclusive bins for the small-R jet trigger demonstrates the physics bias that using this trigger causes when selecting events with large-R jets.

Figure 3.4 shows the turn-on curve for `L1_J75` and `L2_j95` in bins of the offline large-R jet mass and mass/p_{T}, compared to `EF_j240_a10tc_EFFS`. Here, the differences between bins are larger for `L1_J75` and `L2_j95`, than for `EF_j240_a10tc_EFFS`. This further demonstrates the robustness of large-R jet triggers when selecting jets for a wide jet-kinematics range.

The data to MC comparison of the large-R jet performance is necessary in order to determine the level of agreement between the expectation and the observation. A correction factor or systematic uncertainty would be necessary to account for any observed difference. Figure 3.5 shows this comparison both for `a4tc` and `a10tc`. Here, the difference between the Z' and data samples is larger for `a4tc` than for `a10tc`. The Z' is dominated by multi-prong large-R jets while the data is mainly composed of multijet processes. This clearly indicates a physics bias in selecting events with large-R jets through a small-R jet trigger. Also here, due to their wide area, large-R jet triggers have a steeper turn on curve.

Figure 3.6 shows that comparison, both for `a4tc` and `a10tc`, in bins of the large-R jet width. Here, the physics bias favouring narrow jets is smaller for `a4tc` than for `a10tc`.

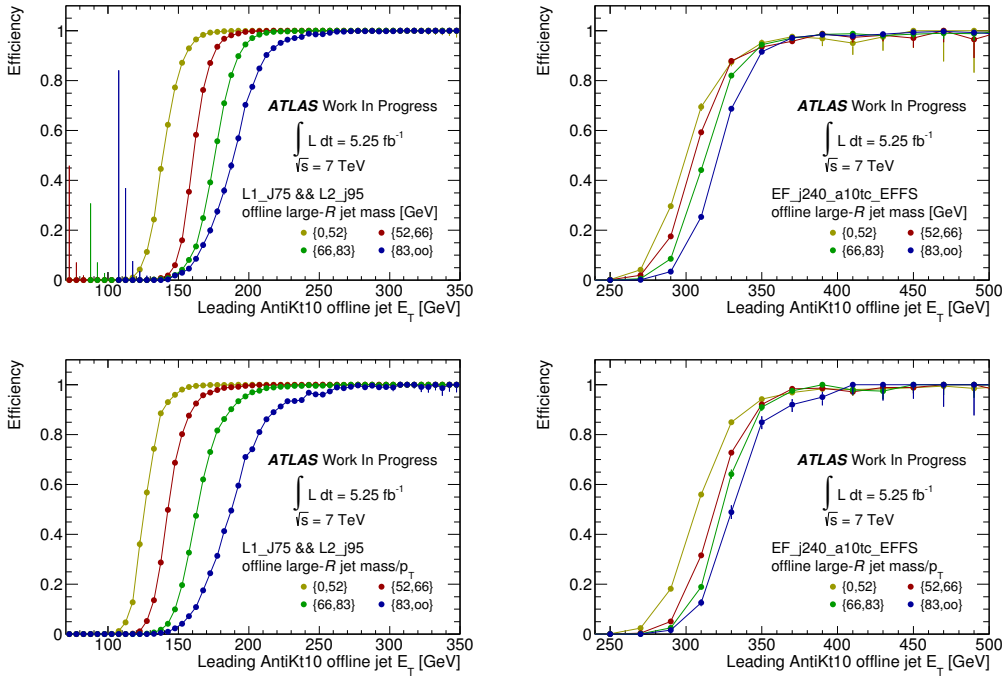

Figure 3.4: The efficiency of the L1 and L2 (left) and EF triggers (right) as a function of the leading offline large-R jet E_{T}, in bins of the large-R jet mass (top) and mass/p_{T} (bottom).

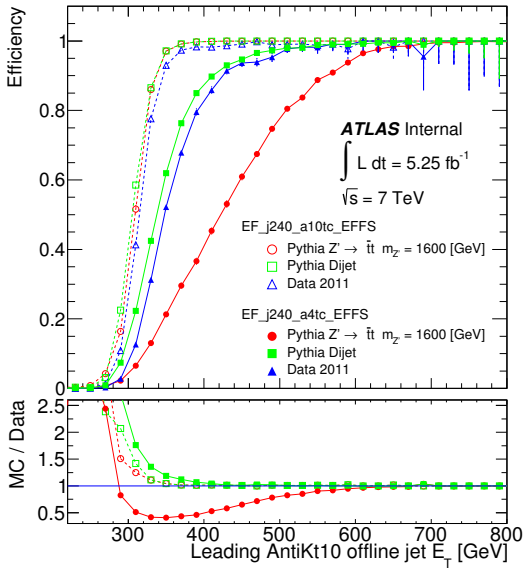

Figure 3.5: The efficiency of standard `a4tc` (filled markers) and large-R `a10tc` (open markers) jet triggers as a function of the leading offline large-R jet E_{T} for data and MC.

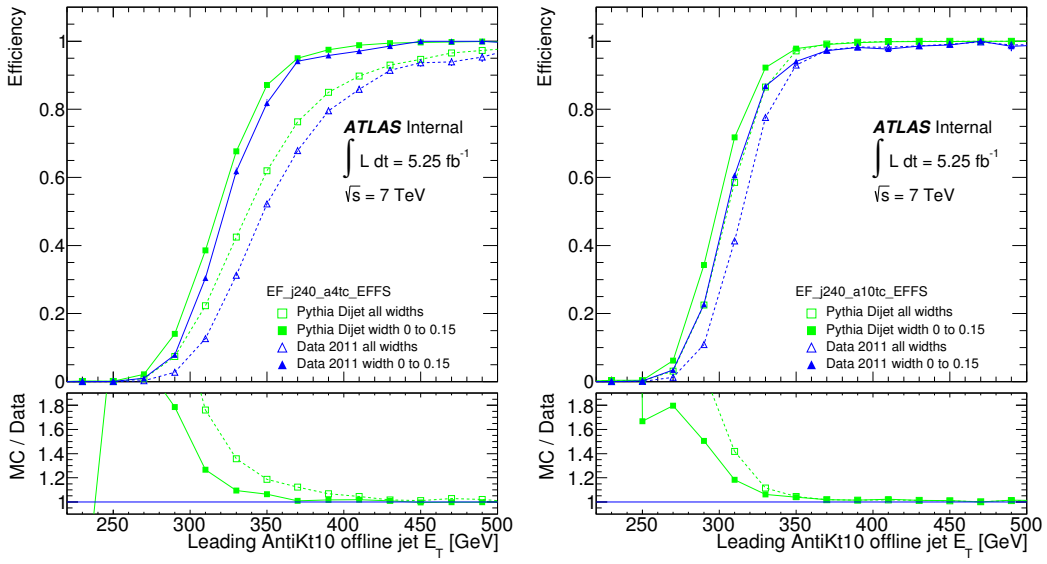

Figure 3.6: The efficiency of standard `a4tc` (left) and large-R jet `a10tc` (right) jet triggers as a function of the leading offline large-R jet E_{T} for data and MC, inclusively (open markers) and for narrow (filled markers) jets.

3.4 Large-R jet trigger emulation for the $t\bar{t}$ resonances search

The $t\bar{t}$ resonances search [156, 166] use lepton triggers targeting events with a semi-leptonic $t\bar{t}$ decay. This analysis approaches the reconstruction of the final state in two ways, boosted and resolved, depending on whether or not the decay products of the hadronically decaying top are collimated inside a large-R jet. The latter case accepts events with a large-R of $p_{\mathrm{T}} \geq 300$ GeV. The addition of the delayed stream could significantly increase the analysis acceptance. With the delayed stream, ATLAS makes the most of its capability to write out data, without worrying about reconstructing it. The reconstruction comes afterwards, whenever resources are available again. The result from including this stream is shown in Figure 3.7. Here, the boosted muon channel acceptance increased by about 20%.

This study is performed using a stream where `EF_j220_a10tcem_delayed` is not available. Hence the trigger decision is emulated. This is done by looking for an online jet with E_{T} above the threshold of the trigger within the detector acceptance. Figure 3.8 demonstrates the trigger emulation for two triggers for which the actual trigger decision is available.

Figure 3.9 shows the turn-on curve for the emulated `EF_j220_a10tcem_delayed` large-R jet trigger for a sample of high p_T tops, multijets and data.

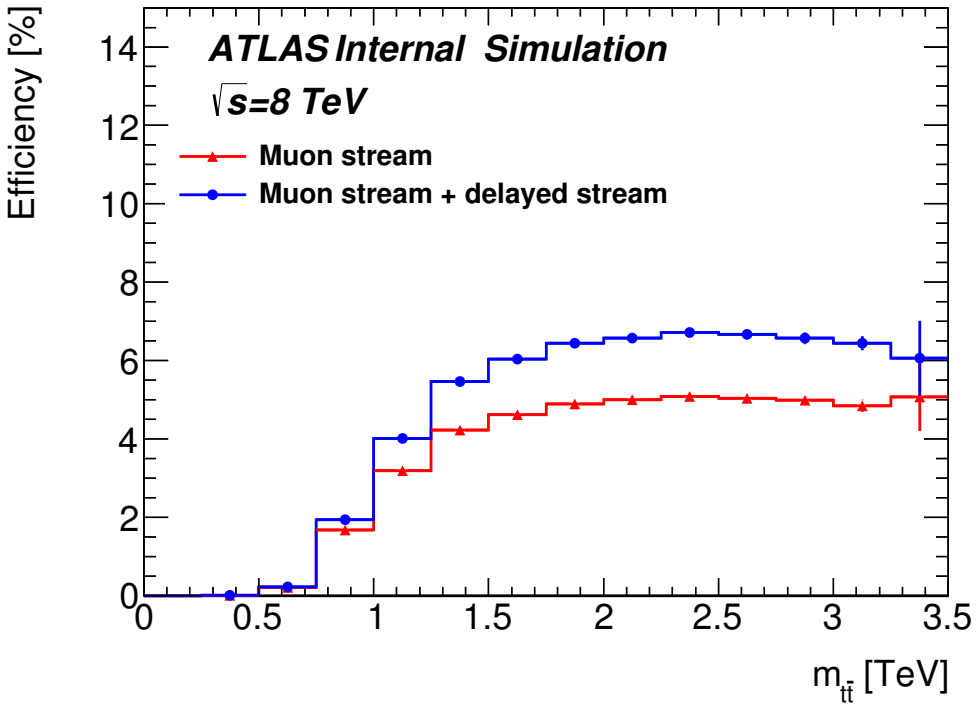

Figure 3.7: Boosted muon channel selection efficiency as function of the true $m_{t\bar{t}}$ for the Z' resonance, with and without the delayed stream. Figure taken from Ref. [1].

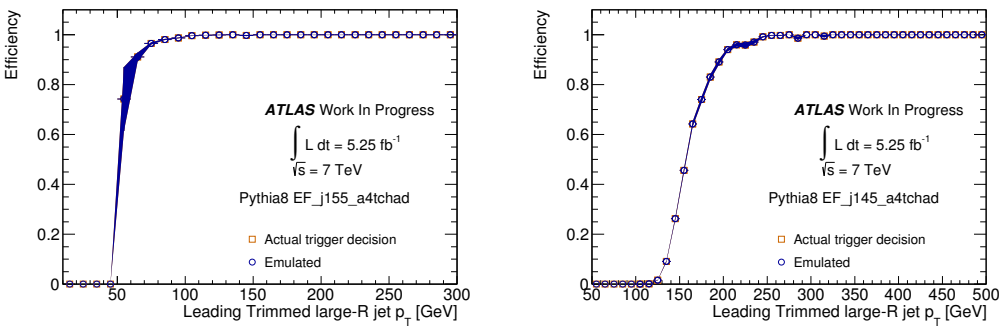

Figure 3.8: The efficiency of the `EF_j55_a4tchad` (left) and `EF_j145_a4tchad` (right) jet triggers for the actual (open markers) and emulated (filled markers) trigger decision as a function of the leading offline trimmed large-R jet E_{T}.

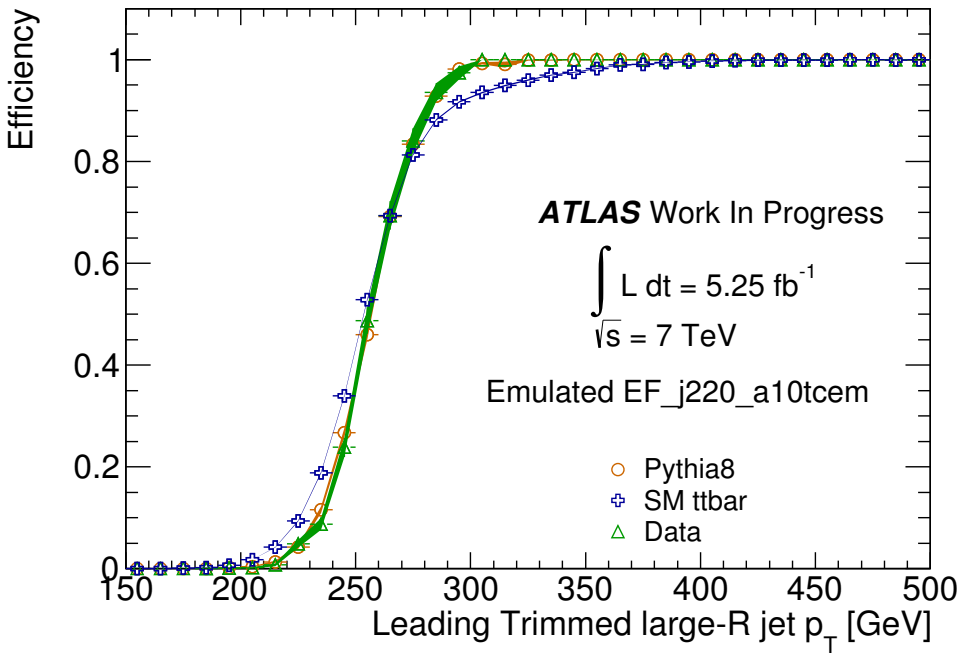

Figure 3.9: The efficiency of the `EF_j220_a10tcem_delayed` emulated large-R jet trigger as a function of the leading offline trimmed large-R jet E_{T} for data and MC.

Here, for trimmed large-R jets with $p_{\mathrm{T}} \geq 380$ GeV this trigger is fully efficient.

3.5 Summary

The performance of large-R jet triggers is presented for the 2011 and 2012 ATLAS data. These triggers have been compared to standard small-R jet triggers in terms of their capability to identify events selecting offline large-R jets. They have been shown to have a better performance and robustness in a wide range of jet properties, such as the width, mass and mass/p_{T}. Also, the performance of these triggers in data has been shown to be well modelled by the simulation.

Using an emulation technique, large-R jet triggers have been applied to a physics analysis in ATLAS using 2012 data. These triggers offer an alternative to lepton triggers in the selection of boosted $t\bar{t}$ events. The addition of large-R jet triggers in the $t\bar{t}$ resonance analysis [1] has increased its efficiency by 20%.

Chapter 4

Shower deconstruction

4.1 Introduction

This chapter examines the modelling of the SD χ_{SD} observable, introduced in Section 2.6.3.4. Data to MC comparisons are performed, and its sensitivity to systematic variations is discussed. Due to the use that the SD algorithm makes of the soft radiation information, the dependence of this observable to pileup is also examined. In addition, its performance is tested against changes on the subjet-clustering algorithm. Furthermore, its performance as a top-tagging algorithm is demonstrated by comparing to various other jet-substructure algorithms.

4.2 Event selection

In the following sections the performance of shower deconstruction is examined in two samples, a signal ($t\bar{t}$) sample where the aim is to identify a hadronically decaying top-quark, and a background (W+jets) sample. In the latter case, the jets produced in association with the leptonically decaying W are potentially faking the signal. The selection used for both samples is outlined below.

Events must have a reconstructed primary vertex with at least five tracks. Also, extra requirements on $E_{\mathrm{T}}^{\mathrm{miss}}$, the transverse mass[1], m_{T}, and the lepton kinematics are used to suppress multijet backgrounds:

- Electron (muon)-triggered events are required to have exactly one trigger-associated reconstructed electron (muon) with $E_{\mathrm{T}} > 25$ ($p_{\mathrm{T}} > 25$) GeV;
- $E_{\mathrm{T}}^{\mathrm{miss}} > 20$ GeV;

[1]The transverse mass is defined as $m_{\mathrm{T}} = \sqrt{2p_{\mathrm{T}}E_{\mathrm{T}}^{\mathrm{miss}}(1-\cos\Delta\phi)}$, where p_{T} is the p_{T} of the charged lepton and $\Delta\phi$ is the azimuthal angle between the charged lepton and $E_{\mathrm{T}}^{\mathrm{miss}}$.

- $E_{\mathrm{T}}^{\mathrm{miss}} + m_{\mathrm{T}} > 60$ GeV.

In addition, events must contain at least two small jets with $p_{\mathrm{T}} \geq 25$ GeV for $|\eta| \leq 2.4$, and $p_{\mathrm{T}} \geq 35$ GeV for $2.4 < |\eta| < 4.5$. The two-jet selection helps reducing the number of selected events and is compatible with the semi-leptonic $t\bar{t}$ topology, where both jets could be required to be b-tagged. To suppress jets produced by any vertex other than the hard scatter, jets are required to have a JVF> 0.5. This requirement is only applied to jets with a p_{T} of less than 50 GeV and within the inner tracker acceptance ($|\eta| \leq 2.4$). The large-R jet and b-tagging selection changes according to the scope of the two regions that are examined in this study. These are outlined below.

$t\bar{t}$-dominated sample: a large-R jet with $p_{\mathrm{T}} \geq 350$ GeV with a minimum $\Delta\phi$ to the lepton of 1.5, ensuring the hadronic nature of the large-R jet. Also, events are required to have at least one b-tagged jet.

W+jets-dominated sample: a large-R jet with $p_{\mathrm{T}} \geq 250$ GeV with a minimum $\Delta\phi$ to the lepton of 1.5. This lower p_{T} threshold is used to maximise the number of selected events. Also, events are required to have exactly zero b-tagged jets.

4.3 Subjet reconstruction and selection

Various jet-reconstruction algorithms are used to cluster the subjets that are the input for SD. Subjets are clustered using either the anti-k_t, k_t or C/A jet-reconstruction algorithms.

In this study, subjets are used both before and after calibrating to the hadronic scale using p_{T}-η dependent calibration constants. Figure 4.1 shows an example of the typical differences between calibrated and uncalibrated energy responses. A crucial step of SD is to test whether a combination of the input subjets, given by the addition of their four-vectors, lies within the mass windows around the W-boson or top-quark masses (see Table 2.2). When using uncalibrated subjets as input, the result of this test is expected to depend on p_{T} and η, affecting the overall performance of the algorithm. This is discussed in detail in Section 4.4.2.

Figure 4.2 shows the mean subjet multiplicity for different pileup conditions and different subjet-p_T thresholds. This is shown for subjets reconstructed using the C/A algorithm, after applying the calibration factors. For a minimum subjet p_{T} of 20 GeV the mean subjet multiplicity shows no strong dependence

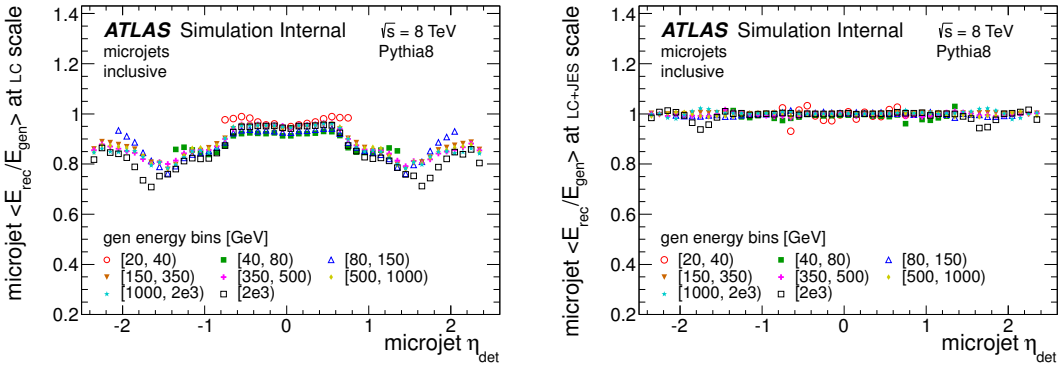

Figure 4.1: Energy response of reconstructed subjets (microjets), both before (left) and after (right) correcting to the hadronic scale. This is shown versus the subjet $|\eta|$ in various bins of the subjet energy.

on pileup. In this study, subjets are required to have $p_{\mathrm{T}} \geq 20$ GeV, regardless of whether they are calibrated or not, and of the subjet reconstruction algorithm that is used.

4.4 Performance in a $t\bar{t}$-dominated sample

4.4.1 Input for SD

This section presents various distributions of the input for SD. These are shown for various jet-reconstruction algorithms.

Figure 4.3 shows the distribution of the subjet multiplicity. This is shown for C/A and anti-k_t subjets. In all cases the data and the MC are in very good agreement. According to what is expected from partially contained top-quark three-body hadronic decays, these distributions peak at between two and three subjets per large-R jet. The fraction of jets that arise from non-$t\bar{t}$ sources is higher at low subjet multiplicities.

Figure 4.4 shows the mean number of subjets for different pileup conditions. The observed mean number of subjets is well predicted by the MC simulation and is not strongly dependent on pileup.

Figures 4.5 and 4.6 shows the leading-subjet and subleading-subjet p_{T} distributions. The peak in the leading-subjet p_{T} distribution close to the large-R jet threshold of 350 GeV arises from jets with a single subjet. Figures 4.7 and 4.8 shows the leading-subjet and subleading-subjet η distributions. In all cases, a good agreement between data and MC predictions is observed.

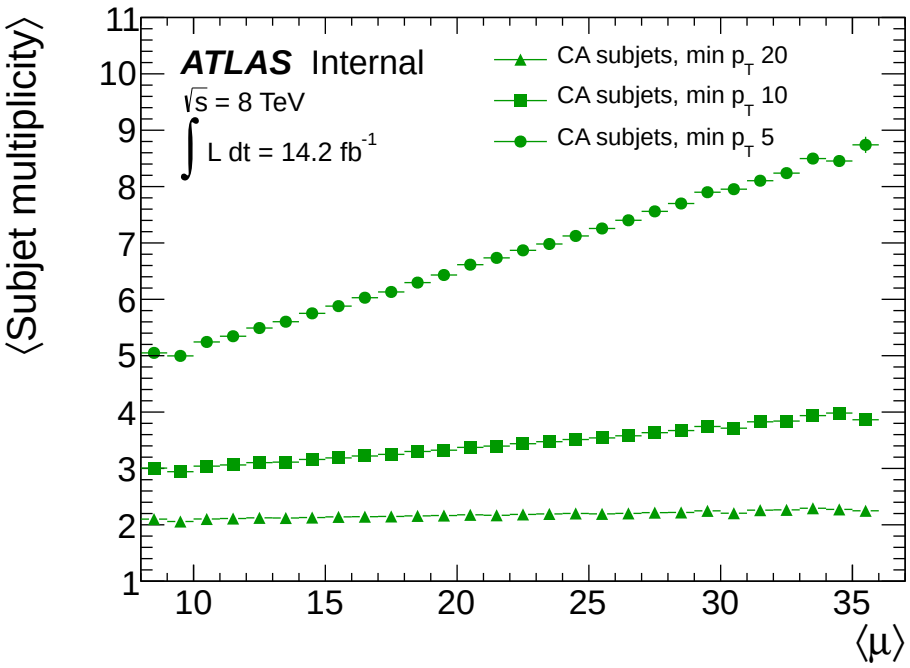

Figure 4.2: Mean C/A $R = 0.2$ subjet multiplicity for various values of the minimum subjet p_{T} as a function of the mean number of collisions per bunch crossing. Figure from Ref. [167].

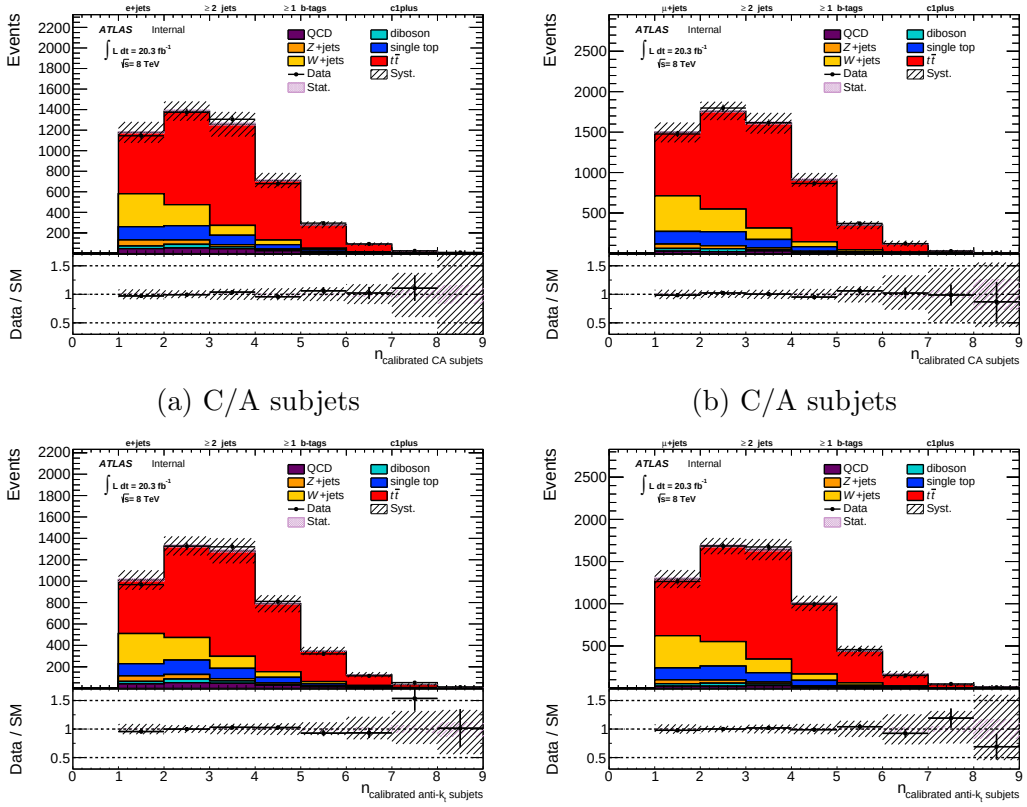

(a) C/A subjets

(b) C/A subjets

(c) anti-k_t subjets

(d) anti-k_t subjets

Figure 4.3: Data to MC comparison of the subjet multiplicity for C/A (top) and anti-k_t (bottom) subjets. This is shown for the electron (left) and muon channels (right). No calibration factors are applied.

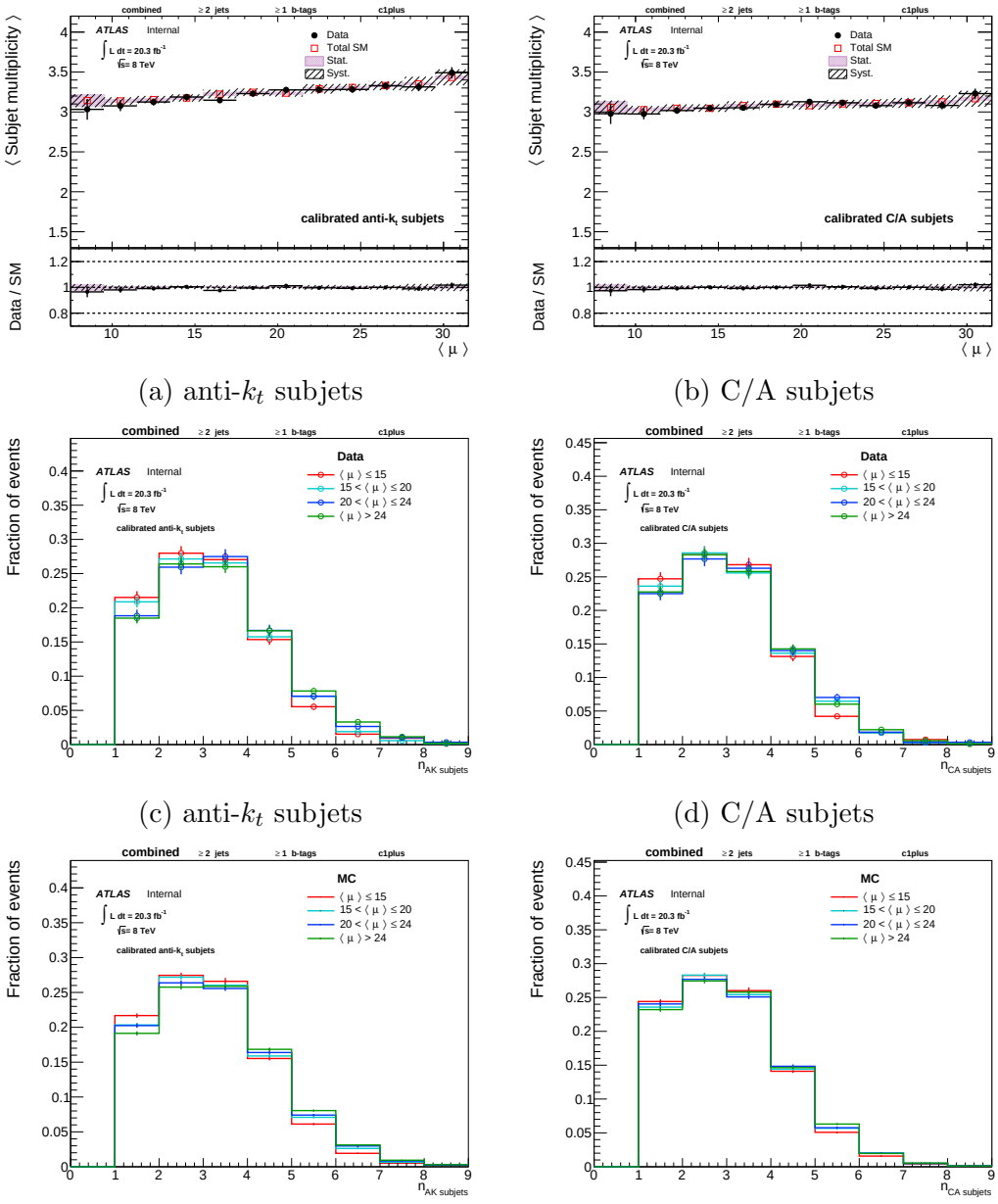

(a) anti-k_t subjets

(b) C/A subjets

(c) anti-k_t subjets

(d) C/A subjets

(e) anti-k_t subjets

(f) C/A subjets

Figure 4.4: Mean subjet multiplicity versus mean number of collisions per bunch crossing $\langle\mu\rangle$ (top). Subjet multiplicity in various μ bins for data (middle) and MC (bottom). This is shown for calibrated anti-k_t (left) and C/A (right) subjets.

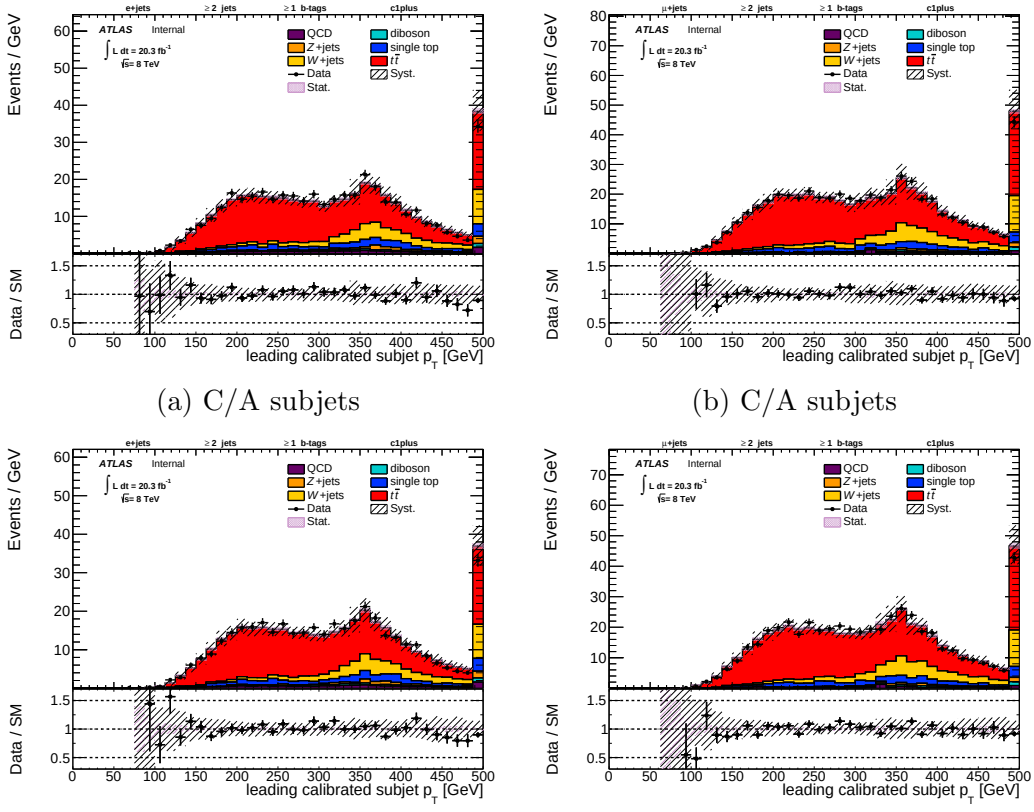

(a) C/A subjets

(b) C/A subjets

(c) anti-k_t subjets

(d) anti-k_t subjets

Figure 4.5: Data to MC comparison of the leading subjet p_{T} for C/A (top) and anti-k_t (bottom) subjets. This is shown for the electron (left) and muon channels (right). No calibration factors are applied.

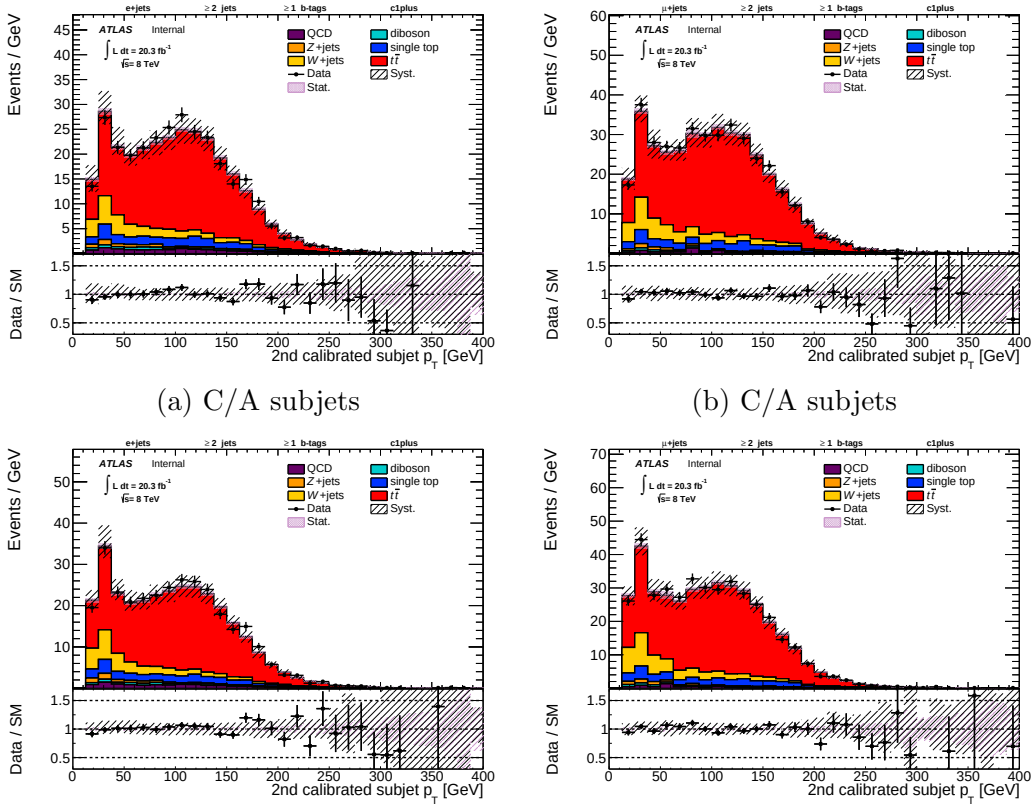

(a) C/A subjets (b) C/A subjets

(c) anti-k_t subjets (d) anti-k_t subjets

Figure 4.6: Data to MC comparison of the subleading subjet p_{T} for C/A (top) and anti-k_t (bottom) subjets. This is shown for the electron (left) and muon channels (right). No calibration factors are applied.

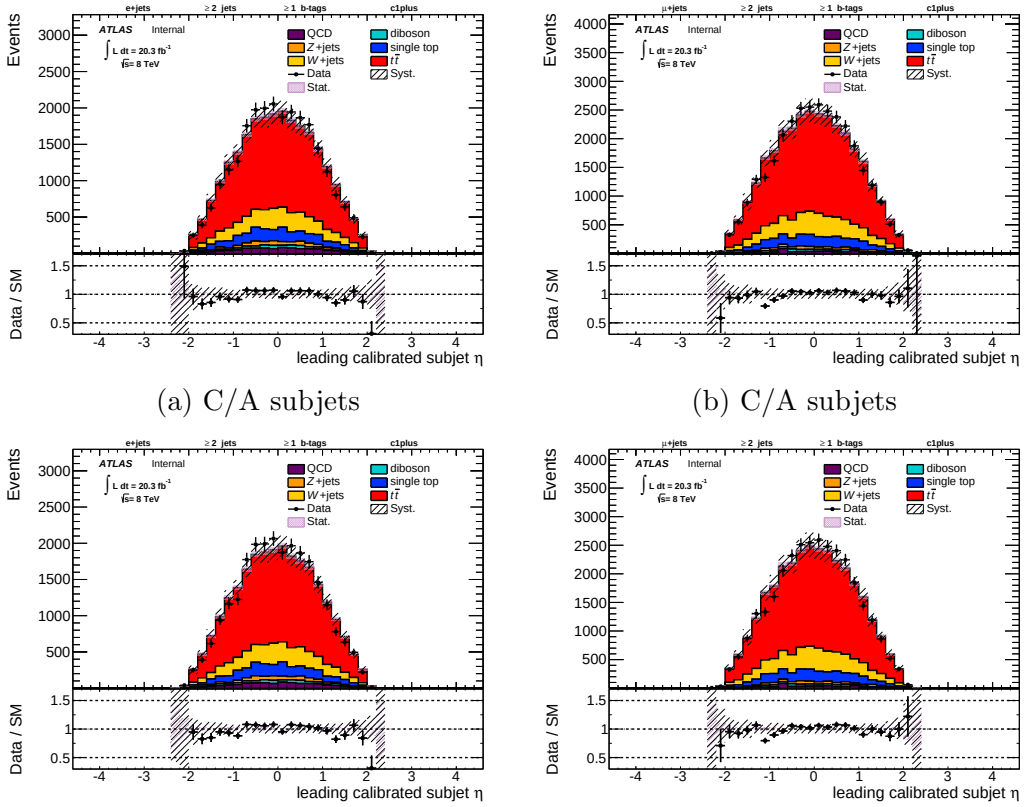

(a) C/A subjets

(b) C/A subjets

(c) anti-k_t subjets

(d) anti-k_t subjets

Figure 4.7: Data to MC comparison of the leading subjet η for C/A (top) and anti-k_t (bottom) subjets. This is shown for the electron (left) and muon channels (right). No calibration factors are applied.

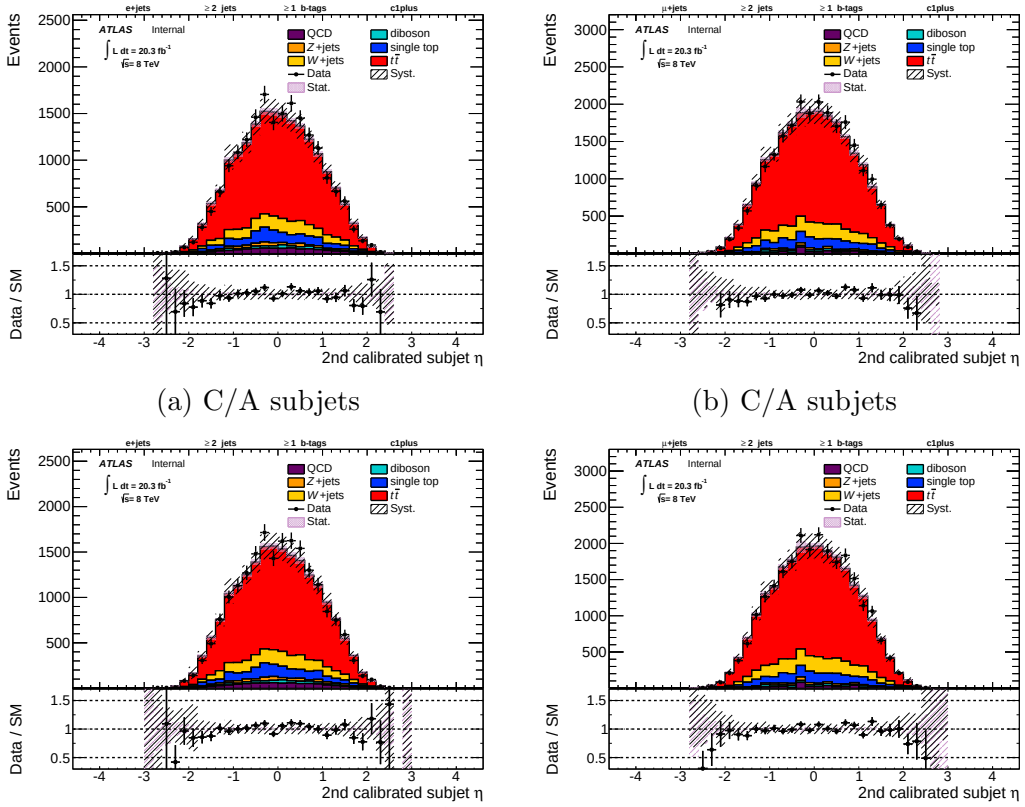

(a) C/A subjets

(b) C/A subjets

(c) anti-k_t subjets

(d) anti-k_t subjets

Figure 4.8: Data to MC comparison of the subleading subjet η for C/A (top) and anti-k_t (bottom) subjets. This is shown for the electron (left) and muon channels (right). No calibration factors are applied.

4.4.2 Shower deconstruction χ_{SD} observable

The C/A and k_t subjet-reconstruction algorithms are *apriori* the best choice for the input to the SD algorithm because they have a modelling of the parton shower compatible with the underlying physics of the SD algorithm. However, the subjet area for these algorithms suffers from large fluctuations and irregular shapes (see Fig 2.8 in Ref. [167]), which would largely depend on the environment. This complicates the application of the full ATLAS jet-calibration scheme, where the contribution from pileup is subtracted based on the median p_{T} event density multiplied by the subjet area. In this section, this *apriori* choice is tested by comparing the efficiency of the minimum requirements of the SD algorithm and the performance of the $\log(\chi_{\mathrm{SD}})$ discriminant, for various subjet-reconstruction algorithms.

Figure 4.9 shows the flow of the minimum requirements of the SD algorithm for anti-k_t subjets. After applying the event selection, large-R jets are required to have no less than three subjets. Then, all possible combinations of subjets, are tested against mass windows about the top and W-boson masses. At least one combination should exist with a mass within each of these mass windows. Only for large-R jets passing these criteria a value of χ_{SD} exists.

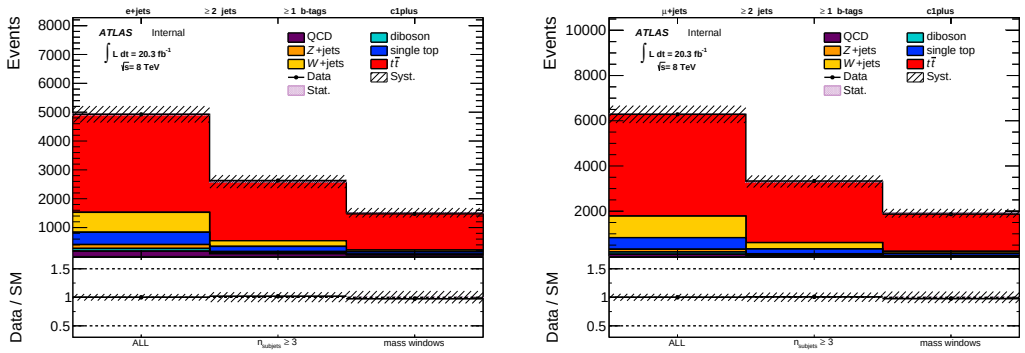

(a) e+jets (b) μ+jets

Figure 4.9: Data to MC comparison of the flow of the minimum requirements of the SD algorithm, for anti-k_t subjets. This is shown for the electron (left) and muon channels (right).

Table 4.1 shows the efficiency of the SD minimum requirements for the selected sample of events. The efficiency is given by the ratio between the number of events passing these criteria and the total number of selected events. Here, data and MC are showing good agreement. Also, the agreement between subjet-reconstruction algorithms is reasonably good.

Table 4.1: Comparison between the observed and expected efficiency of the SD minimum requirements, for various subjet-reconstruction algorithms. For MC, the uncertainty is given by the statistical and systematic uncertainties added in quadrature. For data, the statistical uncertainty is only shown if it is greater than 1%.

	C/A	anti-k_t	k_t
uncalibrated input subjets			
	e+jets		
ϵ^{MC}	0.23 ± 15%	0.23 ± 15%	0.24 ± 14%
ϵ^{data}	0.22 ± 4%	0.22 ± 3%	0.23 ± 3%
	μ+jets		
ϵ^{MC}	0.23 ± 13%	0.23 ± 13%	0.24 ± 13%
ϵ^{data}	0.22 ± 3%	0.22 ± 3%	0.23 ± 3%
calibrated input subjets			
	e+jets		
ϵ^{MC}	0.29 ± 13%	0.31 ± 13%	–
ϵ^{data}	0.28 ± 3%	0.30 ± 3%	–
	μ+jets		
ϵ^{MC}	0.29 ± 12%	0.30 ± 12%	–
ϵ^{data}	0.28 ± 3%	0.30 ± 3%	–

Figure 4.10 shows $\log(\chi_{\mathrm{SD}})$ for various subjet-reconstruction algorithms. Here, no jet-calibration has been applied to the input subjets. Figure 4.11 shows $\log(\chi_{\mathrm{SD}})$ for calibrated C/A and anti-k_t subjets. In all cases the data and the MC are in reasonably good agreement.

Figure 4.12 shows a comparison between subjet-reconstruction algorithms for the $\log(\chi_{\mathrm{SD}})$ discriminant. Here, both for data and MC, the various subjet-reconstruction algorithms agree within uncertainties.

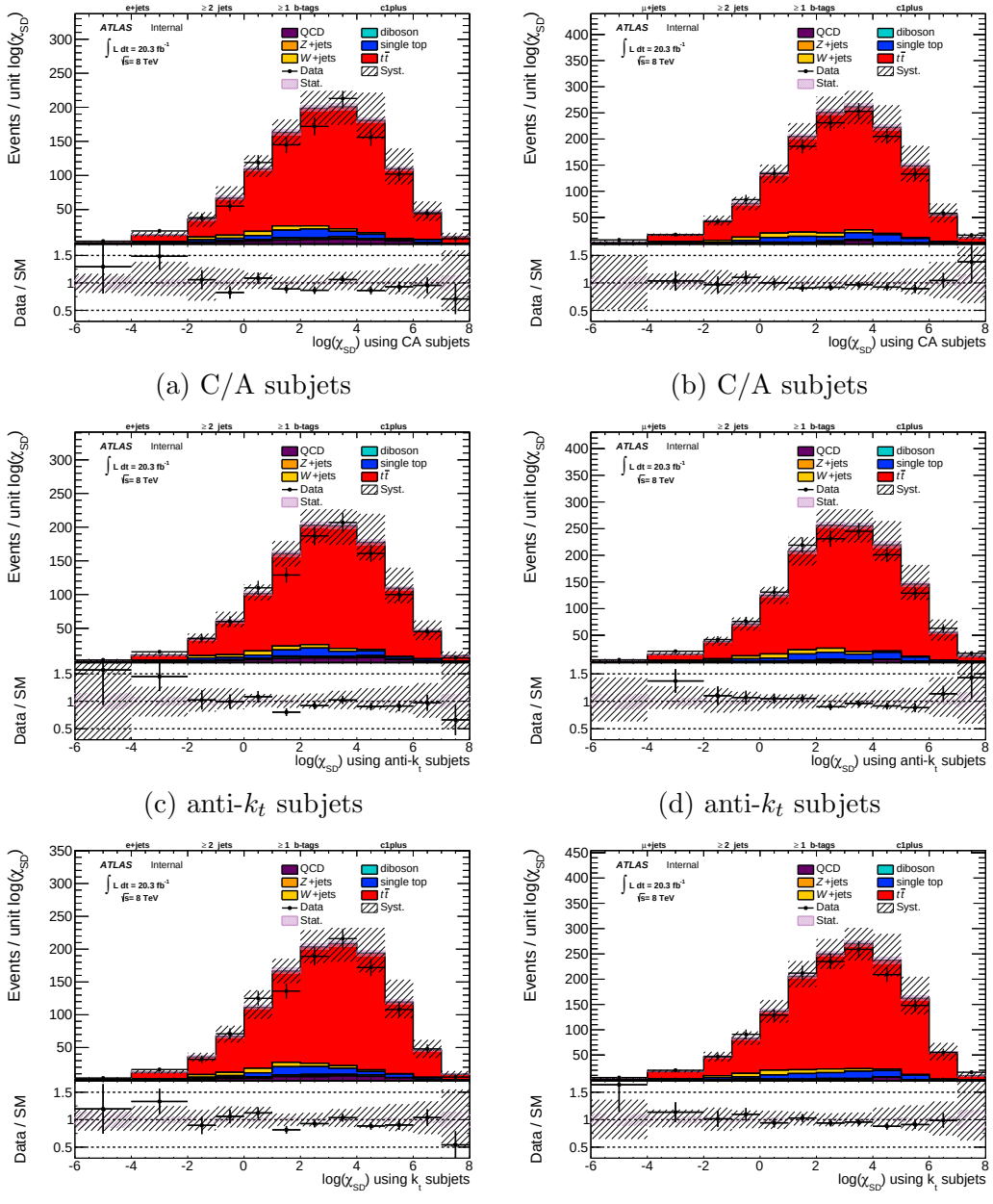

(a) C/A subjets

(b) C/A subjets

(c) anti-k_t subjets

(d) anti-k_t subjets

(e) k_t subjets

(f) k_t subjets

Figure 4.10: Data to MC comparison of the $\log(\chi_{\mathrm{SD}})$ discriminant for C/A (top), anti-k_t (middle), and k_t (bottom) subjets. This is shown for the electron (left) and muon channels (right). No jet-calibration factors are applied.

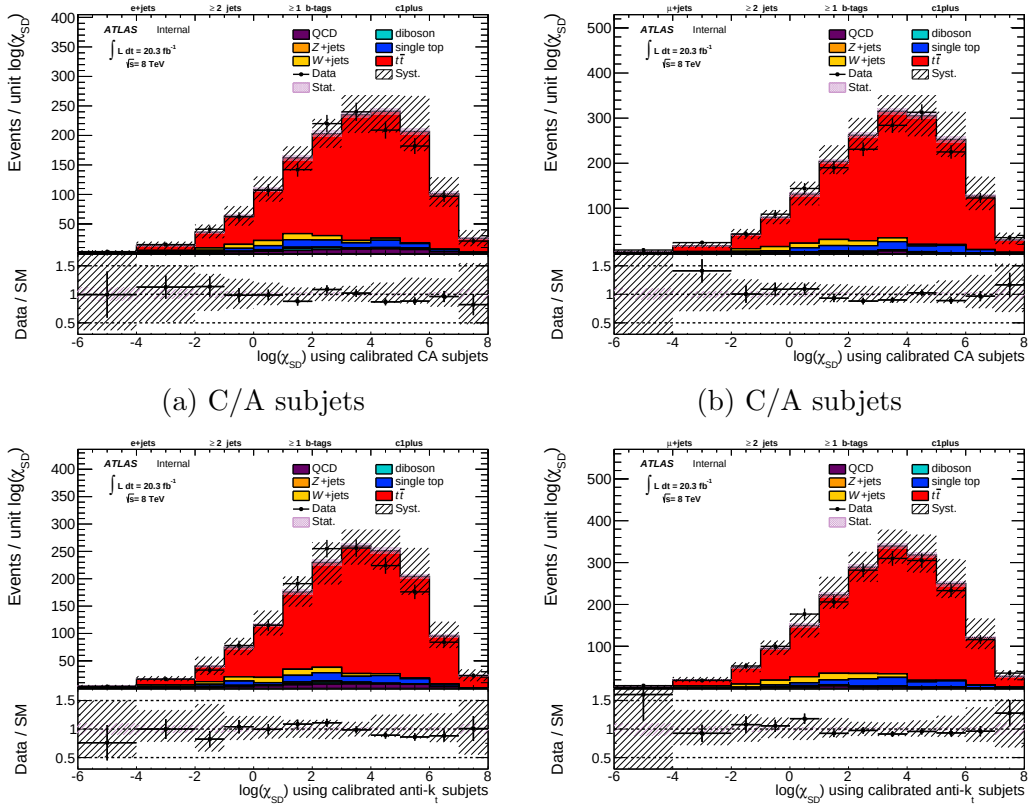

(a) C/A subjets

(b) C/A subjets

(c) anti-k_t subjets

(d) anti-k_t subjets

Figure 4.11: Data to MC comparison of the $\log(\chi_{\mathrm{SD}})$ discriminant for calibrated C/A (top) and anti-k_t (bottom) subjets. This is shown for the electron (left) and muon channels (right).

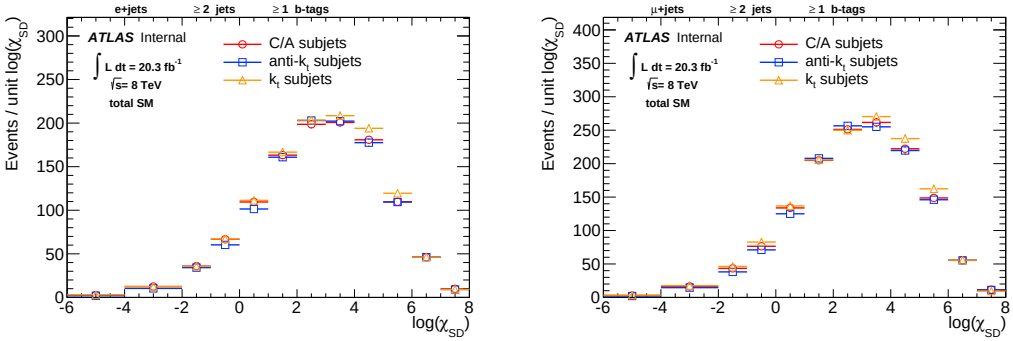

(a) e+jets

(b) μ+jets

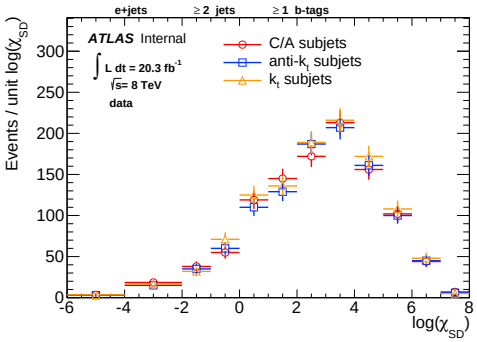

(c) e+jets

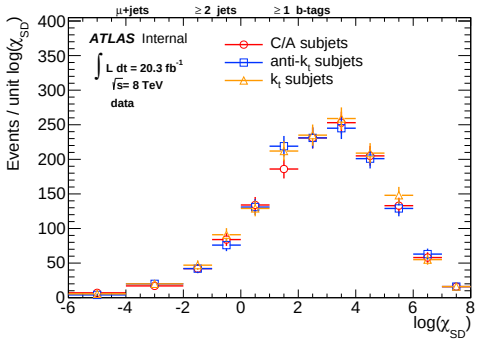

(d) μ+jets

Figure 4.12: Comparison between subjet-reconstruction algorithms of the $\log(\chi_{\mathrm{SD}})$ discriminant for MC (top) and data (bottom). This is shown for the electron (left) and muon channels (right). No calibration factors are applied.

Figure 4.13 shows a comparison between calibrated and uncalibrated input for the SD algorithm. Here, the fraction of large-R jets passing the minimum requirements of the SD algorithm increases when using calibrated input. This is understood in terms of non-central large-R jets from $t\bar{t}$ events for which the subjet energy calibration brings their combinations closer to the W-boson and top-quark masses, increasing the likelihood of this calibrated input to satisfy the mass windows requirements. Also here, for calibrated input, the mean $\log(\chi_{\mathrm{SD}})$ increases, and is therefore more signal-like, which could potentially increase the discriminating strength of this observable.

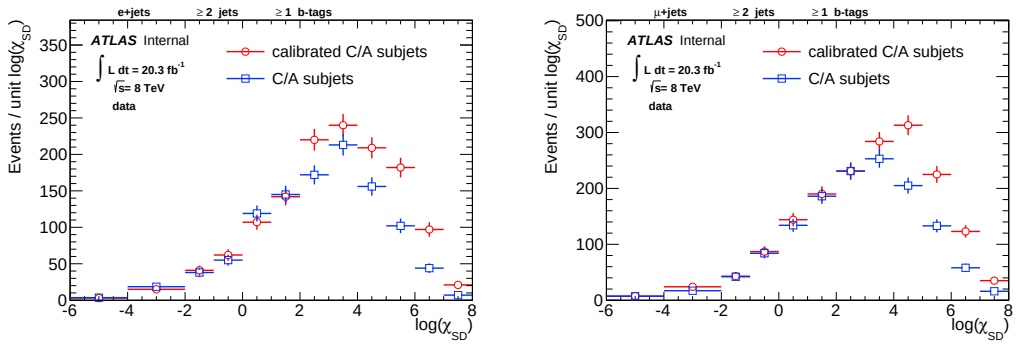

(a) e+jets

(b) μ+jets

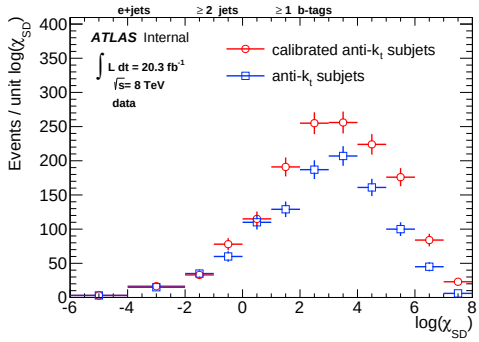

(c) e+jets

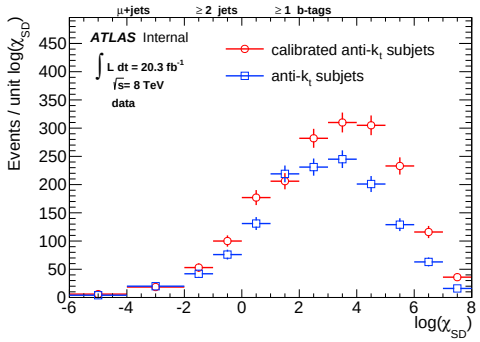

(d) μ+jets

Figure 4.13: Comparison of the measured $\log(\chi_{\mathrm{SD}})$ for calibrated and uncalibrated input, for C/A (top) and anti-k_t (bottom) subjets. This is shown for the electron (left) and muon channels (right). No calibration factors are applied.

Figure 4.14 shows the mean $\log(\chi_{\mathrm{SD}})$ for different pileup conditions. The observed mean number of subjets is well predicted by the MC simulation and is not strongly dependent on pileup. Also here, the distribution of $\log(\chi_{\mathrm{SD}})$ is shown in pileup bins, where in all cases the distributions agree within statistical uncertainty.

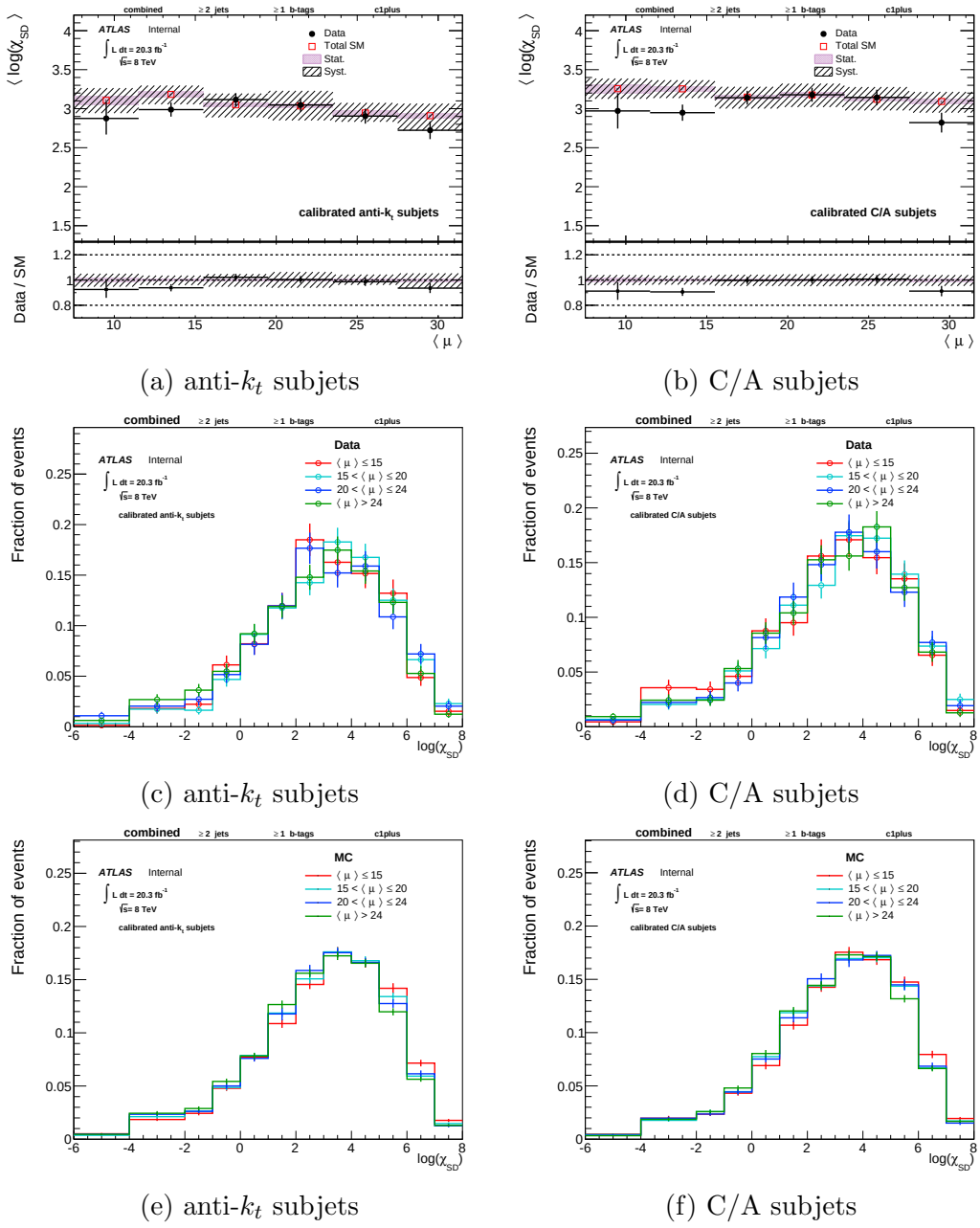

(a) anti-k_t subjets (b) C/A subjets

(c) anti-k_t subjets (d) C/A subjets

(e) anti-k_t subjets (f) C/A subjets

Figure 4.14: Mean $\log(\chi_{\mathrm{SD}})$ versus mean number of collisions per bunch crossing $\langle\mu\rangle$ (top). $\log(\chi_{\mathrm{SD}})$ in various μ bins for data (middle) and MC (bottom). This is shown for calibrated anti-k_t (left) and C/A (right) subjets.

4.4.3 χ_{SD} observable sensitivity to systematic variations

The systematic variations with the largest impact on the χ_{SD} observable, are the large-R jet p_T and $t\bar{t}$ modelling variations. This is understood in terms of the dependence of the subjet multiplicity and kinematics on the large-R jet p_T, and on the attempt this algorithm makes to exploit information on the showering and initial and final state radiation patterns. In this section, the sensitivity of the χ_{SD} observable to these variations is examined by comparing to the sensitivity of another 3-prong substructure observable, N-subjettiness [168].

Figure 4.15 shows the distribution of τ_{32} [168]. This 3-prong observable is given by the ratio of τ_3 and τ_2, where each quantifies the compatibility of the energy spread of a large-R jet with a three or a two body decay respectively. Here, the fraction of non-$t\bar{t}$ events is about 30%. This fraction is considerably larger than in the log χ_{SD} distribution (see Figures 4.10 and 4.11), where non-$t\bar{t}$ events are less than 10% of the total.

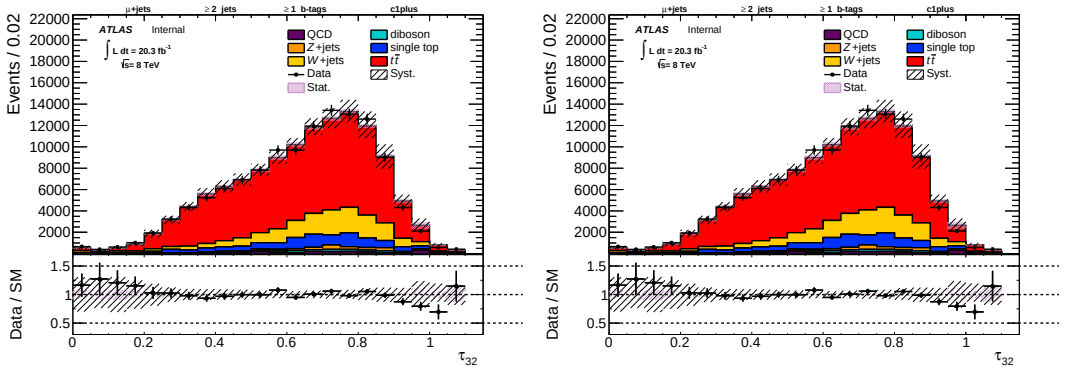

(a) e+jets (b) μ+jets

Figure 4.15: Data to MC comparison of the τ_{32} observable. This is shown for the electron (left) and muon (right) channels.

Figure 4.16 shows a comparison of the total SM model prediction of log χ_{SD} and τ_{32}, to systematic variations on the $t\bar{t}$ modelling. Here, log χ_{SD} is shown for calibrated anti-k_t subjets. For most of the spectrum the impact of this variation on log χ_{SD} is within 20%, which is larger than for τ_{32} by a factor compatible with the drop on the $t\bar{t}$ purity on the τ_{32} distribution. Hence, in most cases, both observables are shown to have relatively the same sensitivity to $t\bar{t}$ modelling uncertainties. For very large values of log χ_{SD}, the difference between POWHEG and ALPGEN grows beyond 20%.

Figure 4.17 shows a comparison of the total SM model prediction of log χ_{SD} and τ_{32}, to the systematic variation on the amount of radiation associated with

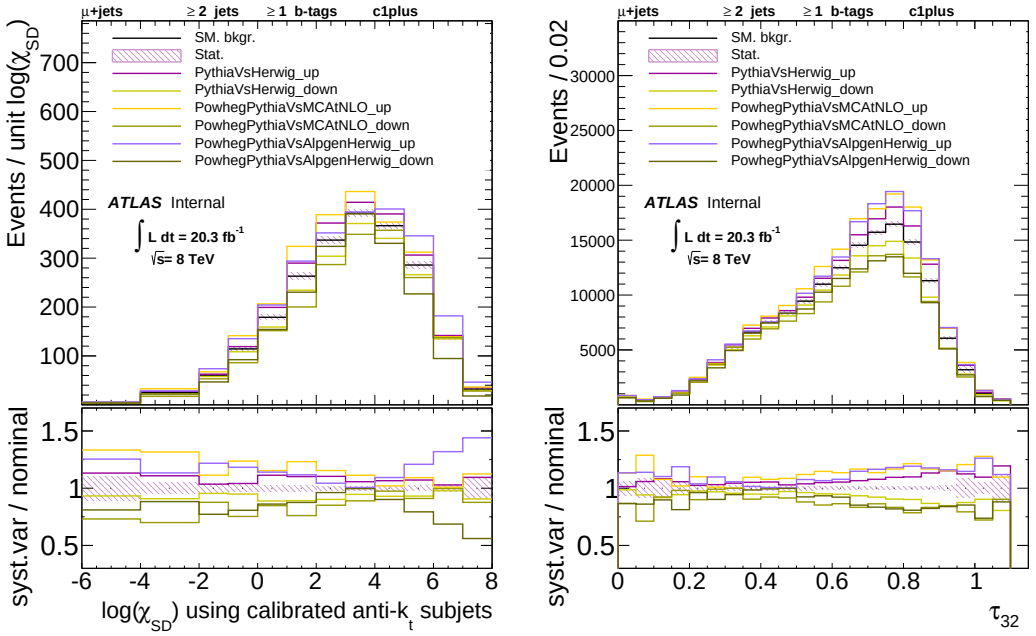

(a) $\log \chi_{\mathrm{SD}}$ (b) τ_{32}

Figure 4.16: Comparison between the nominal SM prediction and systematic variations on the $t\bar{t}$ modelling. This is shown for $\log \chi_{\mathrm{SD}}$ (left) and τ_{32} (right) in the muon channel.

$t\bar{t}$ production. Here, the sensitivity of both observables is in agreement when taking into account the change in the fraction of non-$t\bar{t}$ events.

Figure 4.18 shows a comparison of the total SM model prediction of $\log \chi_{\mathrm{SD}}$ and τ_{32}, to the systematic variation on the large-R jet energy scale with the largest impact on these observables. This topology uncertainty, described in 2.7.4 and labelled `FatJPtS_Topo`, accounts for different quark/gluon makeup and for differences in jet energy response between QCD jets and jets from boosted W-boson and Top-quark decays. Here, the sensitivity of both observables is in agreement when taking into account the change in the fraction of non-$t\bar{t}$ events.

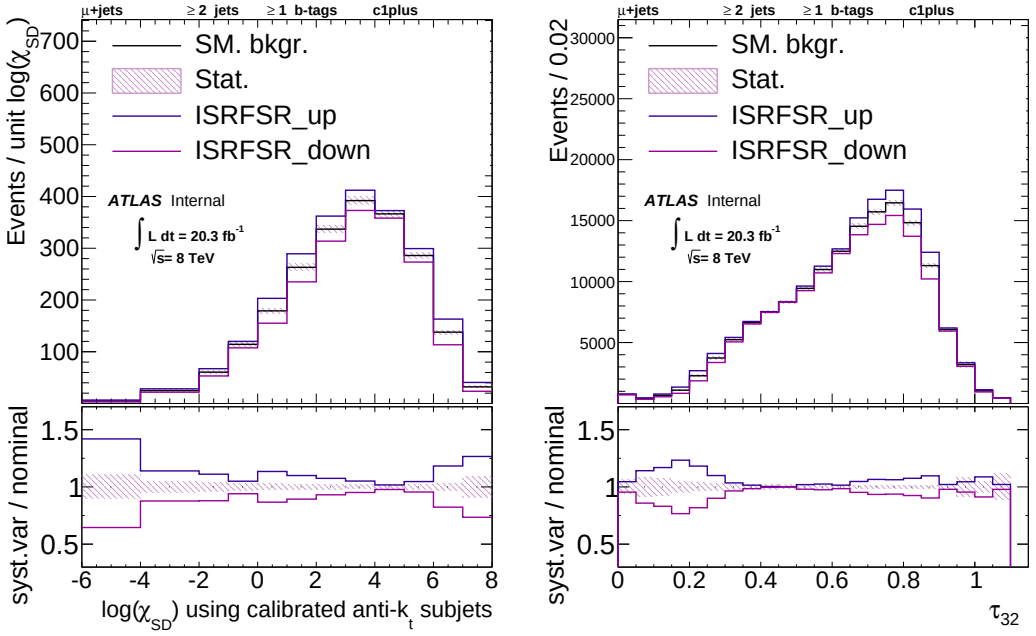

(a) $\log \chi_{\mathrm{SD}}$ (b) τ_{32}

Figure 4.17: Comparison between the nominal SM prediction and systematic variations on the amount of radiation associated with $t\bar{t}$ production. This is shown for $\log \chi_{\mathrm{SD}}$ (left) and τ_{32} (right) in the muon channel.

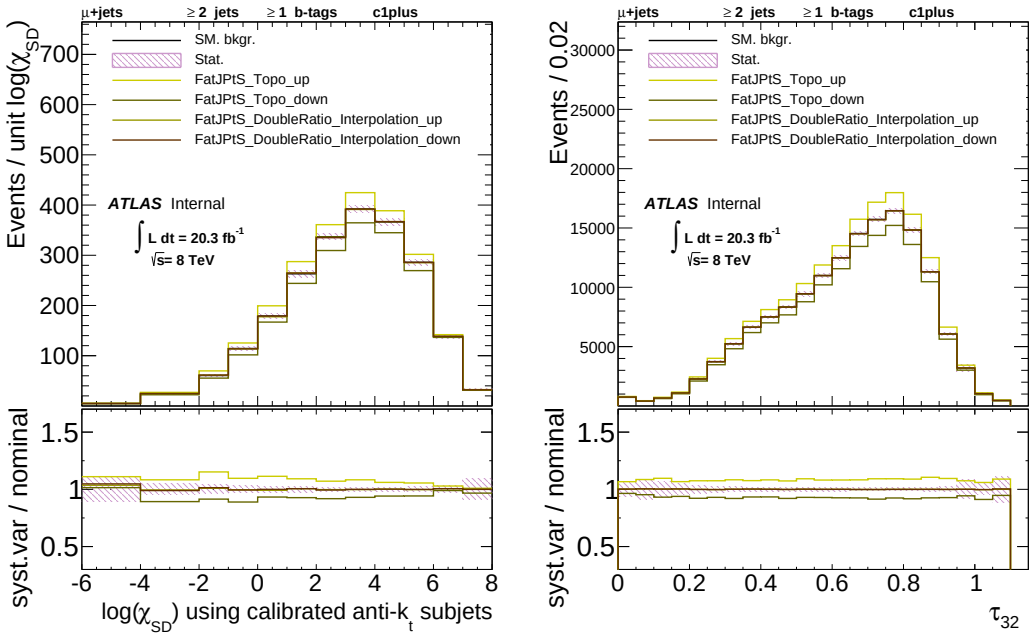

(a) e+jets (b) μ+jets

Figure 4.18: Comparison between the nominal SM prediction and systematic variations on the large-R jet p_{T} jet energy scale. This is shown for $\log \chi_{\mathrm{SD}}$ (left) and τ_{32} (right) in the muon channel.

4.5 Performance in a W+jets-dominated sample

The large-R jet from the W+jets-dominated sample results from the showering of light-quarks and gluons with high-p_{T}. Therefore, its study is complementary to that of top-initiated jets.

Figure 4.19 shows $\log(\chi_{\mathrm{SD}})$ for various subjet-reconstruction algorithms. Here, no jet-calibration has been applied to the input subjets. For all the various input the data is well modelled by the MC. The slight differences between the systematic error bands is understood in terms of the sensitivity of the subjet multiplicity and kinematics to variations on the large-R jet energy scale.

Figure 4.20 shows $\log(\chi_{\mathrm{SD}})$ for calibrated C/A and anti-k_t subjets. The data and MC are in reasonably good agreement. Similar results are observed for both subjet-clustering algorithms. Compared to the performance observed for non-calibrated subjets (see Figure 4.19), a slight mismodelling of the high-$\log(\chi_{\mathrm{SD}})$ region is observed for the electron channel. Changes between calibrated and non-calibrated input are understood in terms of the modelling of soft-subjets. In average, the subjet energy is increased after calibration. Then, softer subjets which would not be selected at the uncalibrated scale are moved above the selection threshold, and are therefore added to the input for SD.

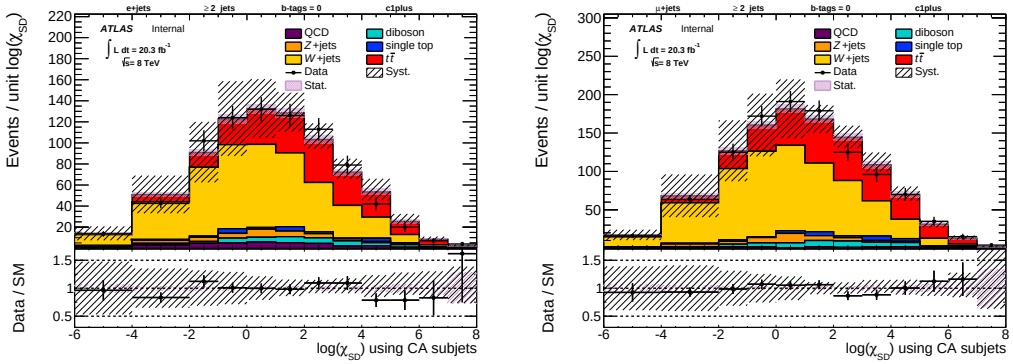

(a) C/A subjets

(b) C/A subjets

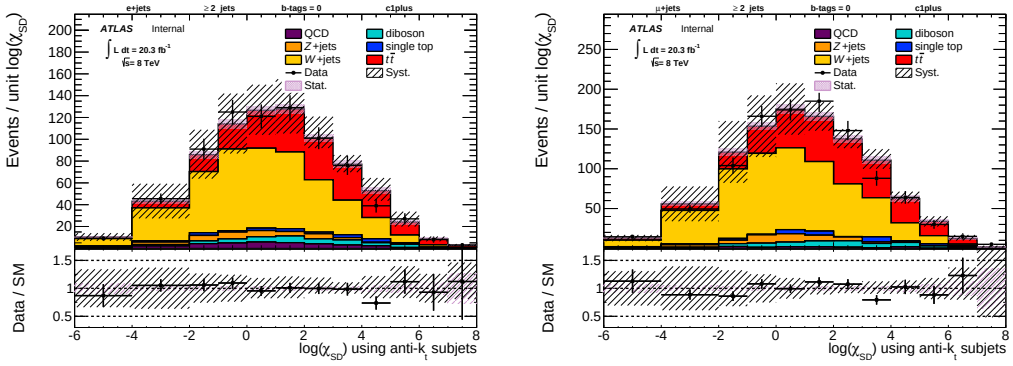

(c) anti-k_t subjets

(d) anti-k_t subjets

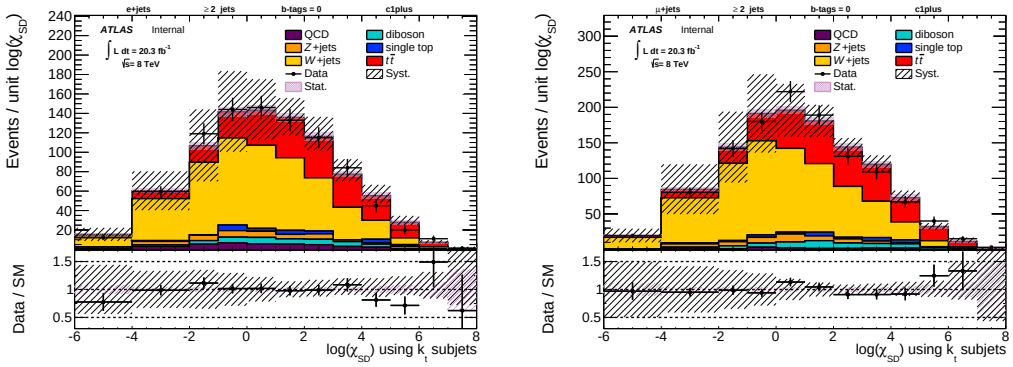

(e) k_t subjets

(f) k_t subjets

Figure 4.19: Data to MC comparison of the $\log(\chi_{\mathrm{SD}})$ discriminant for C/A (top), anti-k_t (middle), and k_t (bottom) subjets. This is shown for the electron (left) and muon channels (right). No jet-calibration factors are applied.

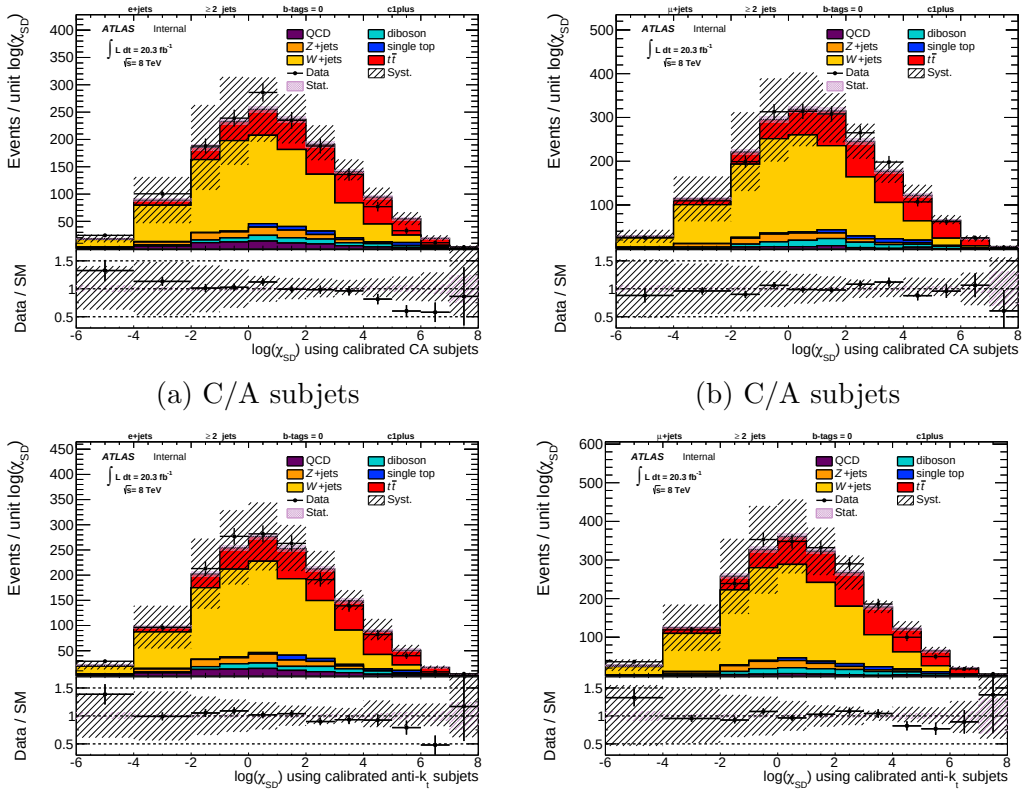

(a) C/A subjets

(b) C/A subjets

(c) anti-k_t subjets

(d) anti-k_t subjets

Figure 4.20: Data to MC comparison of the $\log(\chi_{\mathrm{SD}})$ discriminant for calibrated C/A (top) and anti-k_t (bottom) subjets. This is shown for the electron (left) and muon channels (right).

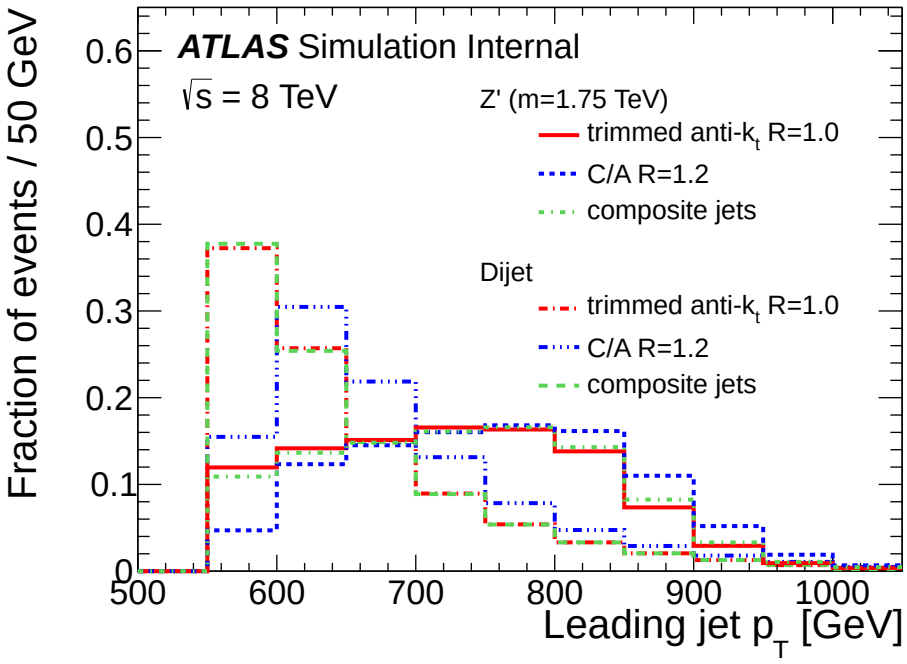

Figure 4.21: Jet p_{T} spectra for signal $Z' \rightarrow t\bar{t}$ and background multijet simulated samples.

4.6 Boosted top tagging

In this section, a study of top-tagging efficiency and background rejection with SD is performed using MC samples. As noted in Section 2.4, signal high p_{T} top quarks are obtained using a Z' sample with $m_{Z'} = 1.75$ TeV and background light quark and gluon jets are obtained using a dijet sample. The input samples and selection criteria used are identical to those used in Ref. [85] to facilitate a direct comparison between different algorithms. Here, reconstruction-level large-R jets are required to be matched within $\Delta R < 0.75 \times R$ to truth-level large-R jets. For signal samples, truth-level large-R jets are required to be within $\Delta R < 0.75 \times R$ of parton-level hadronically-decaying top quarks. The reconstruction-level large-R jet with $p_{\mathrm{T}} \geq 550$ GeV and $|\eta| < 1.2$ closest to a truth-level large-R jet is probed as a top-jet.

Figure 4.21 shows the shape of the leading jet p_{T} for signal and background. The composite jet p_{T} is compared with that used in Ref. [85] by other tagging techniques. As in Section 4.4.1 this composite jet is made from all the subjets considered by the SD algorithm. The trimmed anti-k_t $R = 1.0$ jet p_{T} is seen to be similar to that of the composite jet, while the C/A $R = 1.2$ jet p_{T} is slightly larger.

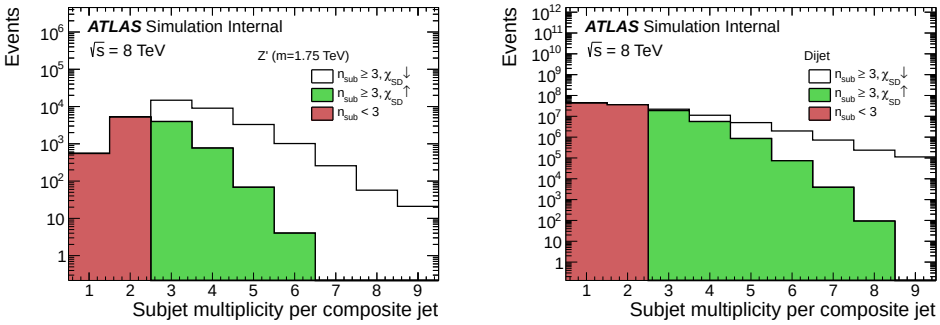

(a) (b)

Figure 4.22: Number of C/A $R = 0.2$ subjets with $p_{\mathrm{T}} \geq 20$ GeV for the leading composite jet for signal $Z' \rightarrow t\bar{t}$ (a) and background multijet (b) simulated samples.

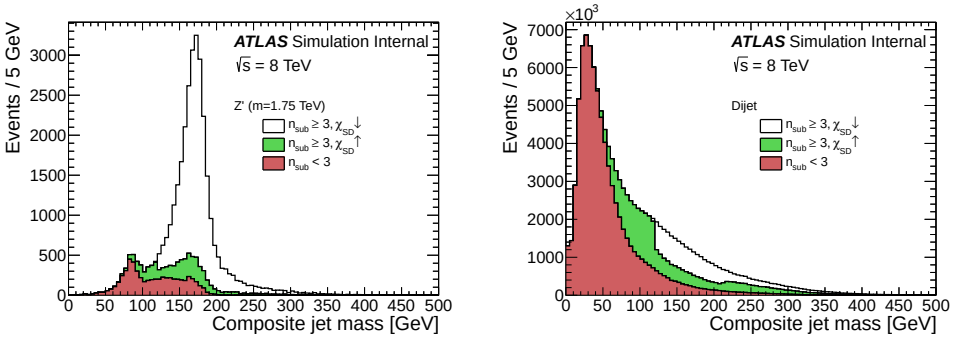

(a) (b)

Figure 4.23: Jet mass for leading composite jet for signal $Z' \rightarrow t\bar{t}$ (a) and background multijet (b) simulated samples.

Figure 4.22 shows the distribution of the subjet multiplicity for signal and background. Here, samples are divided in categories of the subjet multiplicity and status of the SD algorithm (see Section 2.6.3.4), where events with a defined (undefined) χ_{SD} are labelled as $\chi_{\mathrm{SD}} \downarrow$ ($\chi_{\mathrm{SD}} \uparrow$). A large fraction of background jets are rejected by the SD algorithm because of low subjet multiplicity.

Figure 4.23 shows the mass distribution for composite jets for signal and background. A large fraction of jets with low masses are rejected by the SD algorithm. The fraction of jets passing these criteria is about 70% for signal and 15% for background.

Figure 4.24 shows the shape of $\log(\chi_{\mathrm{SD}})$ for signal and background. For the selected jets, $\log(\chi_{\mathrm{SD}})$ has an average value of approximately five for top-jets and two for multijets. This figure illustrates how a cut on $\log(\chi_{\mathrm{SD}})$ could help to discriminate between signal and background.

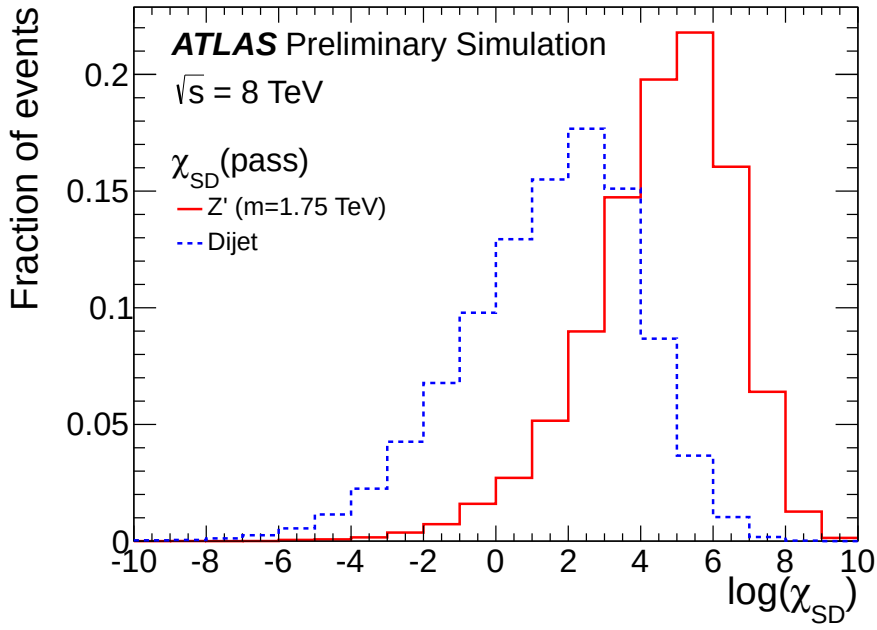

Figure 4.24: Logarithm of the χ_{SD} observable for signal $Z' \rightarrow t\bar{t}$ and background multijet simulated samples for events satisfying the minimum requirements of the SD algorithm.

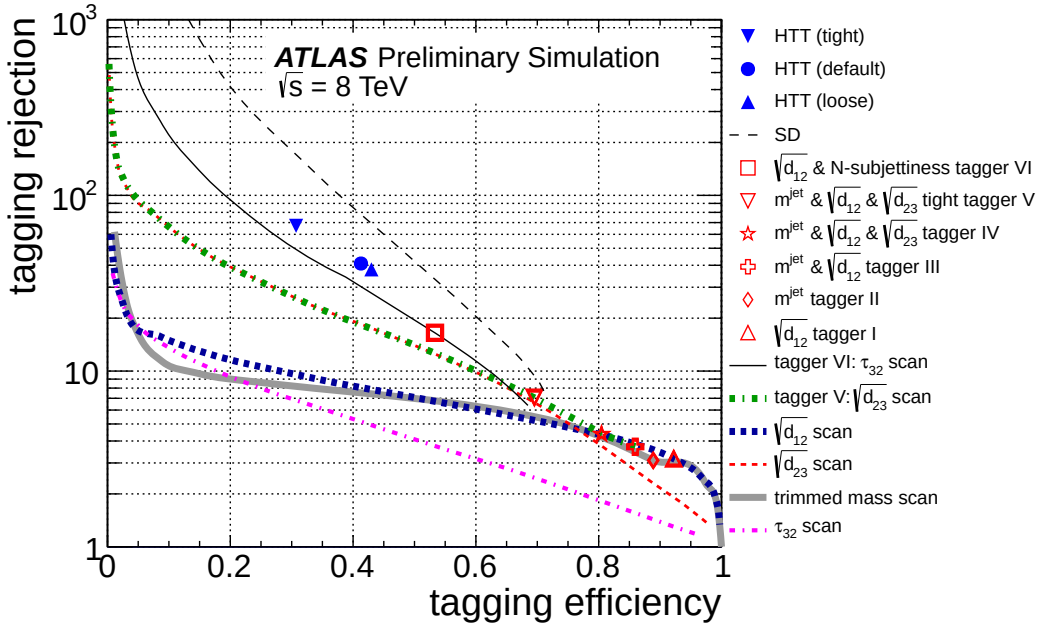

Figure 4.25: Comparison of expected top jet tagging efficiency and light quark/gluon jet rejection. All substructure taggers and scans use trimmed anti-k_t $R = 1.0$ jets, except the HEPTopTagger (HTT) that uses C/A $R = 1.2$. The same $Z' \rightarrow t\bar{t}$, $m_{Z'} = 1.75$ TeV signal samples and multijet background samples and selection are used for all taggers. Systematic uncertainties are not considered for any of the algorithms.

Figure 4.25 shows the background rejection versus signal efficiency curve for SD, compared to that of other tagging techniques from Ref. [85]. The rejection is defined as the reciprocal of the efficiency. The best background rejection over a wide range of signal efficiency is obtained with SD. The maximum signal efficiency and minimum background rejection are given by the fraction of events satisfying the minimum requirements of the SD algorithm. For signal this fraction is about 70% and for background about 12%. These values are consistent with those of the tight tagger V. This tagger uses a lower cut on the trimmed large-R jet mass of 100 GeV, and lower cuts of 40 and 10 GeV on the large-R jet first and second k_t splitting scales respectively.

4.7 Summary

An application of the shower deconstruction algorithm as a top-quark-tagger is implemented using the ATLAS detector. The performance of this algorithm has been examined in detail for data and MC samples of events predominantly arising from top-quark pair production observed in the lepton plus jets final state. The data were compared to simulation for three key observables, the subjet multiplicity, the subjet p_{T} and η and the $\log(\chi_{\mathrm{SD}})$ observable. Satisfactory agreement was found between data and simulation as well as stable performance as a function of the pileup conditions.

The dependence of the performance of the SD algorithm on the choice of the subjet jet-reconstruction algorithm is studied in detail. Both the efficiency of the minimum requirements of the SD algorithm and the modelling of the $\log(\chi_{\mathrm{SD}})$ observable have been shown to be robust against the choice of the jet-reconstruction algorithm.

The sensitivity of the SD algorithm to the modelling of the $t\bar{t}$ process and to the modelling of the large-R jet kinematics has been explored by comparing it to a similar 3-prong jet substructure algorithm. SD has been shown not to be more sensitive to these uncertainties than other comparable observables.

The expected performance of the SD algorithm and of other top-tagging and substructure techniques has been estimated using samples of simulated high-p_{T} top quarks from $Z' \to t\bar{t}$ decays with $m_{Z'} = 1.75$ TeV as the signal and dijets as the background. For this scenario, the SD algorithm shows the best light quark and gluon jet background rejection over a wide range of top-jet signal efficiency, when systematic uncertainties are not considered.

Chapter 5

Single production of vector-like quarks

5.1 Introduction

In this chapter, a search for single production of heavy VLQs decaying into Wb is presented. The search targets the process $pp \to qQb$ with subsequent $Q \to Wb \to lvb$, where the lepton can be either an electron or a muon, and where Q can be either a T quark, with charge $+2/3$, or a Y quark, with charge $-4/3$. The light quark typically produces a jet in the forward region of the detector and the extra b-jet may be observed either in the forward or central region.

5.2 Analysis strategy

This analysis uses the search strategy and event selection presented in Ref. [3]. This strategy is illustrated in Figure 5.1. Here, the mass of a large-R jet, geometrically matched to the leading b-tagged jet in the event, is used as a proxy to its expected isolation. By cutting on the large-R jet p_{T} and mass a significant fraction of $t\bar{t}$ background is rejected. Also, to further exploit the low multiplicity of hard jets in the signal process, a cut on the number of jets outside the large-R with p_{T} above a given threshold is applied. Furthermore, similar to t-channel single-top production, the single production of VLQs is characterised by a forward jet. This analysis strategy is used to increase the relative strength of the signal with respect to the background.

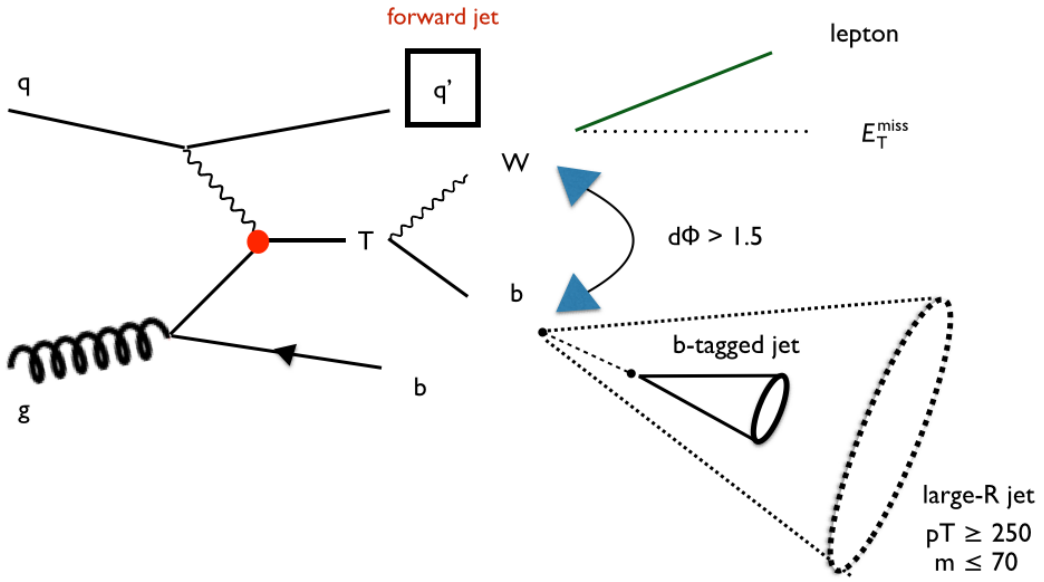

Figure 5.1: Diagrammatic description of the $T \to Wb$ final state in the single production mode. The event selection requires at least one lepton and large missing transverse momentum, corresponding to the leptonic decay of the W-boson. Also, a b-tagged jet, geometrically matched to a light large-R jet is required. The reconstructed W-boson and the b-tagged jet are used to reconstruct the VLQ. These are required to have a large azimuthal separation, which results from the large VLQ masses considered in this search. Finally, a forward jet requirement is applied to select events compatible with the topology of single production of VLQs.

The analysis strategy used here is compared to various other approaches. Large-R jet uncertainties are relatively large, hence strategies without using them are particularly interesting. In all cases, the strategy based on large-R jets shows the best expected performance. This is further discussed in Appendix A.

5.3 Event selection

preselection: The event preselection follows Section 4.2, as also here a boosted l+jets final state is used. The same primary vertex, $E_{\mathrm{T}}^{\mathrm{miss}}$, m_{T} and electron and muon requirements are used. At least two small-R jets, with the same p_{T} and $|\eta|$ cuts, are required. Finally, events must contain either a b-tagged with $p_{\mathrm{T}} \geq 150$ GeV or a $p_{\mathrm{T}} \geq 200$ GeV trimmed large-R jet.

C1, large-R jet transverse momentum: Figure 5.2 shows a signal to SM background comparison of the shape of the leading large-R jet p_{T}, for events passing the event preselection. Here, the background shows a steeply falling distribution while the signal distribution peaks at around half the mass of the VLQ. Therefore, the leading large-R jet can be used as a measure of the boost in the event, and setting a cut on the minimum large-R jet p_{T} rejects a large fraction of the SM background, mainly partially merged hadronic top jets from $t\bar{t}$. In this analysis, this cut is set to 250 GeV.

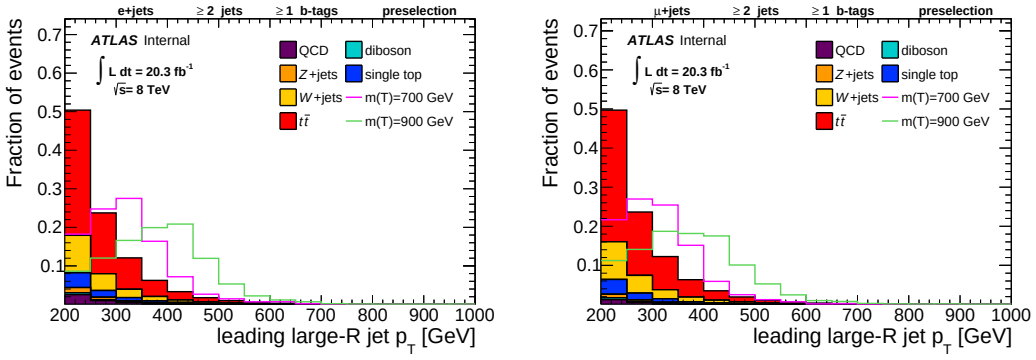

(a) e+jets channel (b) μ+jets channel

Figure 5.2: Signal to SM background shape-only comparison of the leading large-R jet p_{T}, both for the electron (left) and muon (right) channels. This is shown for events passing the event preselection.

C2, boosted $t\bar{t}$ veto using large-R jet mass: Figure 5.3 shows a signal to SM background comparison of the leading large-R jet mass, for events passing the event preselection and C1. Here a considerable fraction of events have a large-R jet with more than one of the top decay products, while the signal shows a steeply falling distribution. This feature of the signal large-R jet mass is expected, as it corresponds to the b-hadron and it gains mass from additional nearby jet activity in the event. Figure 5.4 illustrates how the difference in the nearby jet activity between boosted $t\bar{t}$ and signal events would result in a difference in the large-R jet mass. In this analysis, a cut on the maximum large-R jet mass of 70 GeV is used.

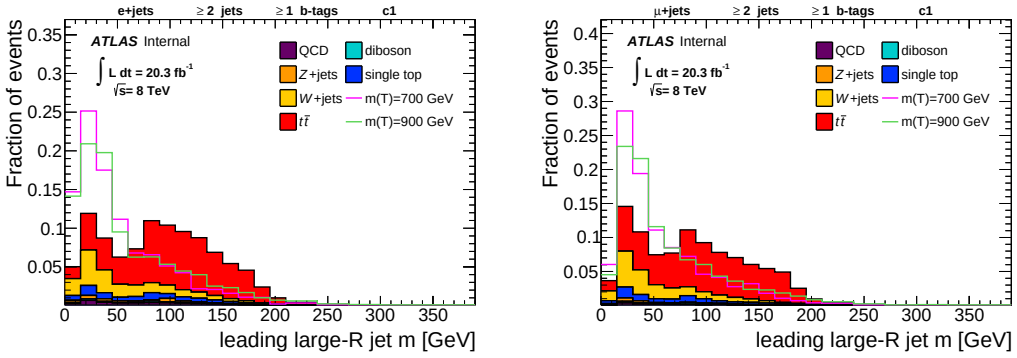

(a) e+jets channel (b) μ+jets channel

Figure 5.3: Signal to SM background shape-only comparison of the leading large-R jet mass, both for the electron (left) and muon (right) channels. This is shown for events passing the event preselection and with a minimum large-R jet p_{T} of 250 GeV.

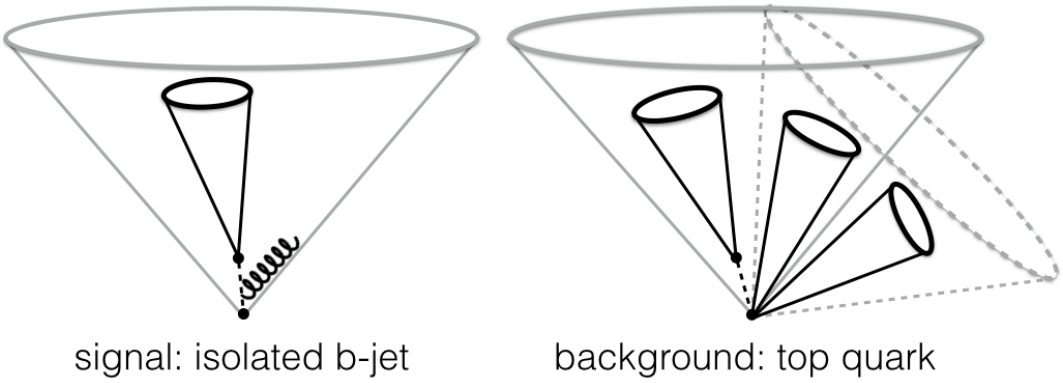

Figure 5.4: Illustration of the usage of large-radius jet mass to veto $t\bar{t}$ background. For the signal $T \to Wb$ (left) the b-quark recoils against the W-boson. Thus the hardest large-R jet in the event typically contains a b-hadron plus additional soft and collinear radiation, and tends to have a low mass. For the semileptonic $t\bar{t}$ background (right) a mildly boosted hadronically decaying top quark produces large-R jets containing a significant fraction of the top decay products. The fraction of top decay products contained, and therefore the jet mass, increases with jet p_{T}. Hence, a cut based on the large-R jet p_{T} and mass can be optimised to distinguish between signal and $t\bar{t}$ background, whilst still retaining good signal efficiency. Figure from Ref [3].

Figure 5.5 demonstrates the impact this cut has on the nearby jet activity. Here, the number of jets nearby the b-tagged jet ($\Delta R < 0.8$) is shown before and after applying C2. The fraction of surviving background events with no nearby jets is 85%, and therefore an additional cut on the nearbyjet multiplicity would not improve the significance of the signal. This is achieved without applying a direct cut on the jet multiplicity. A direct comparison between cutting on the number of nearby jets and on the large-R jet mass is performed, yielding 15% more background events passing the former, while both have a nearly identical signal acceptance of about 70%.

The efficiency of C1 and C2 are highly correlated. Hence, their optimisation is performed by scanning the two dimensional plane of the large-R jet p_{T} vs its mass. This is discussed in Subsection 5.5.

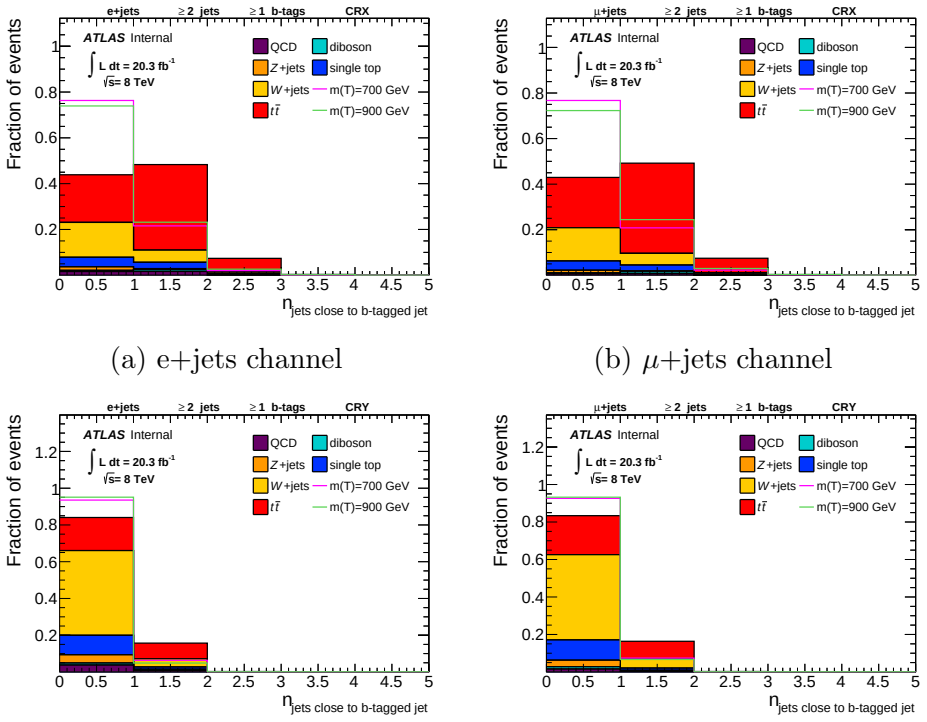

(a) e+jets channel

(b) μ+jets channel

(c) e+jets channel

(d) μ+jets channel

Figure 5.5: Signal to SM background shape-only comparison of the number of jets within $\Delta R < 0.8$ of the b-tagged jet, both for the electron (left) and muon (right) channels, before (top) and after (bottom) applying a cut on the maximum large-R jet mass of 70 GeV. This is shown for events passing the event preselection, with a minimum large-R jet p_{T} of 250 GeV and a b-tagged jet inside the large-R jet. Also, a minimum $\Delta\phi$ between the lepton and the large-R jet of 1.5 is required.

C3, b-tagged jet in large-R jet: Figure 5.6 shows a signal to SM background comparison of the number of b-tagged jets geometrically matched to the large-R jet, for events passing the event preselection and cuts C1 and C2. The matching is done using $\Delta R = \sqrt{\Delta\eta^2 + \Delta\phi^2}$, and by requiring $\Delta R < 0.8$. Here, about 80% of signal events have a b-tagged jet inside the large-R jet, while for the total SM background this fraction is only 30%. In this analysis at least one b-tagged jet inside the large-R jet is required.

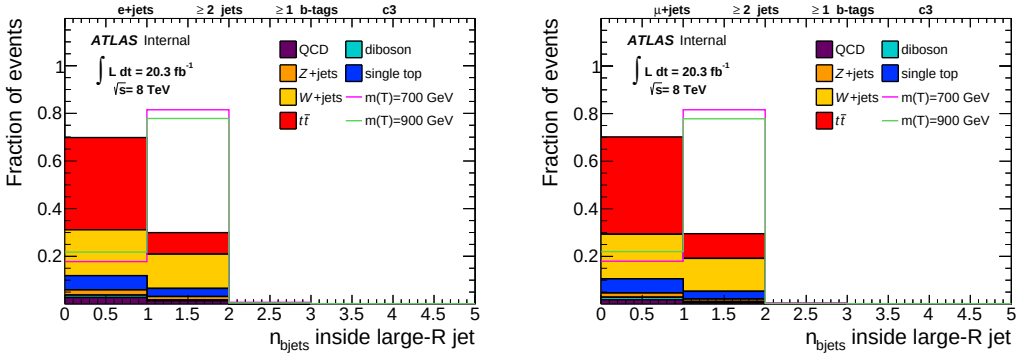

(a) e+jets channel (b) μ+jets channel

Figure 5.6: Signal to SM background shape-only comparison of the number of b-tagged jets geometrically matched to the leading large-R jet, both for the electron (left) and muon (right) channels. This is shown for events passing the event preselection, with a minimum large-R jet p_{T} of 250 GeV and a maximum large-R jet mass of 70 GeV.

C4, minimum lepton to large-R jet $\Delta\phi$ separation: Figure 5.7 shows a signal to SM background comparison of the $\Delta\phi$ between the lepton and the large-R jet, for events passing the event preselection and cuts C1 to C3. For signal events, a large $\Delta\phi$ separation is expected between the lepton and the large-R jet due to the large mass of the VLQ. In this analysis a minimum $\Delta\phi$ of 1.5 is required. This cut is 99% efficient for signal events.

C5, central jet veto: Figure 5.8 shows a signal to SM background comparison of the number of jets outside the large-R jet ($\Delta R > 1.4$) for events passing the event preselection and cuts C1 to C4. Here, only jets with $p_{\mathrm{T}} \geq 75$ GeV and $|\eta| \leq 2.4$ are counted. The optimisation of this criteria is discussed in Subsection 5.5. Apart from soft and collinear radiation

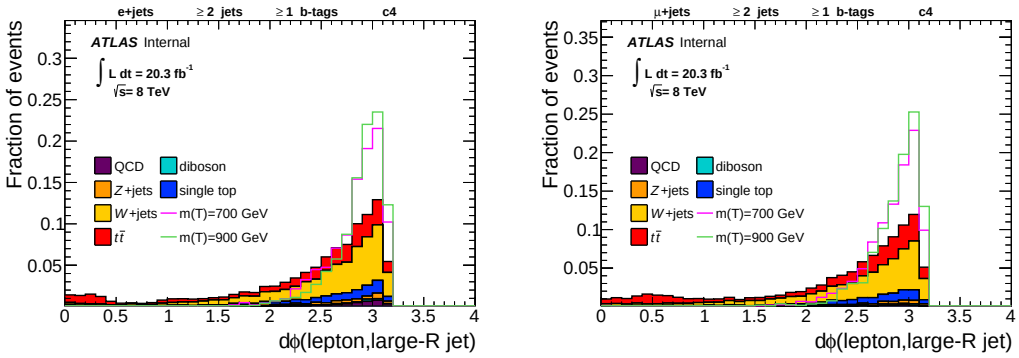

(a) e+jets channel (b) μ+jets channel

Figure 5.7: Signal to SM background shape-only comparison of the $\Delta\phi$ between the lepton and the large-R jet, both for the electron (left) and muon (right) channels. This is shown for events passing the event preselection, with a minimum large-R jet p_{T} of 250 GeV and a maximum large-R jet mass of 70 GeV. Also, the large-R jet is required to be geometrically matched to a b-tagged jet.

around the b-tagged jet, already contained within the large-R jet, signal events are expected to have little additional hard jet activity. This is clearly shown in this figure, where approximately 60% of signal events have zero extra jets above 75 GeV, while for the total SM background about 50% of events have at least one such jet. In this analysis, events with one or more of these jets are vetoed.

C6, forward jet tag: Figure 5.9 shows a signal to SM background comparison of the number of forward, $2.4 < |\eta| < 4.5$, jets, for events passing the event preselection and cuts C1 to C5. Here, about 80% of the background events have no such jet, while for signal about 50% of events have at least one. The presence of a forward jet is a characteristic feature of single production of VLQs (see Figure 5.1). In this analysis, events are required to have at least one forward jet.

Figure 5.10 shows a data to SM background comparison of the event yield at each step of the event selection used in this analysis. Also, two signal samples, with masses of 700 and 900 GeV are included to illustrate the relative signal strength. The data and the SM background prediction are in reasonable agreement throughout the cut flow. This figure also shows how after applying the full event selection the signal to background ratio rises by more than 40 (50) times for the 700 (900) GeV mass point, with respect to the values after the event preselection.

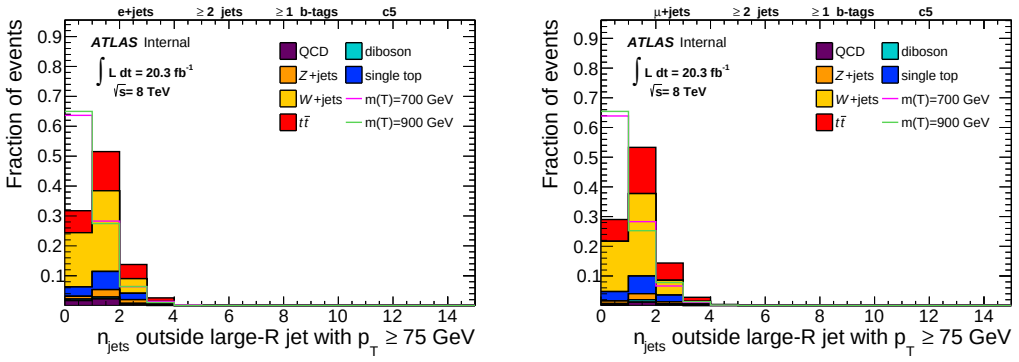

(a) e+jets channel (b) μ+jets channel

Figure 5.8: Signal to SM background shape-only comparison of the number of jets outside the large-R jet with $p_{\mathrm{T}} \geq 75$ GeVand $|\eta| \leq 2.4$, both for the electron (left) and muon (right) channels. This is shown for events passing the event preselection, with a minimum large-R jet p_{T} of 250 GeV and a maximum large-R jet mass of 70 GeV. Also, the large-R jet is required to be geometrically matched to a b-tagged jet, and a minimum $\Delta\phi$ between the lepton and the large-R jet of 1.5 is required.

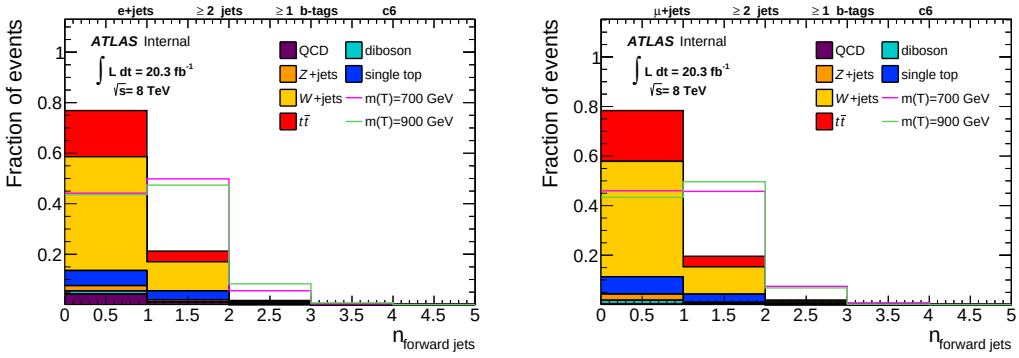

(a) e+jets channel (b) μ+jets channel

Figure 5.9: Signal to SM background shape-only comparison of the number of forward jets, both for the electron (left) and muon (right) channels. This is shown for events passing the event preselection, with a minimum large-R jet p_{T} of 250 GeV and a maximum large-R jet mass of 70 GeV. Also, the large-R jet is required to be geometrically matched to a b-tagged jet, and a minimum $\Delta\phi$ between the lepton and the large-R jet of 1.5 is required. In addition, events should not contain any jet outside the large-R jet with $p_{\mathrm{T}} \geq 75$ GeV and $|\eta| \leq 2.4$.

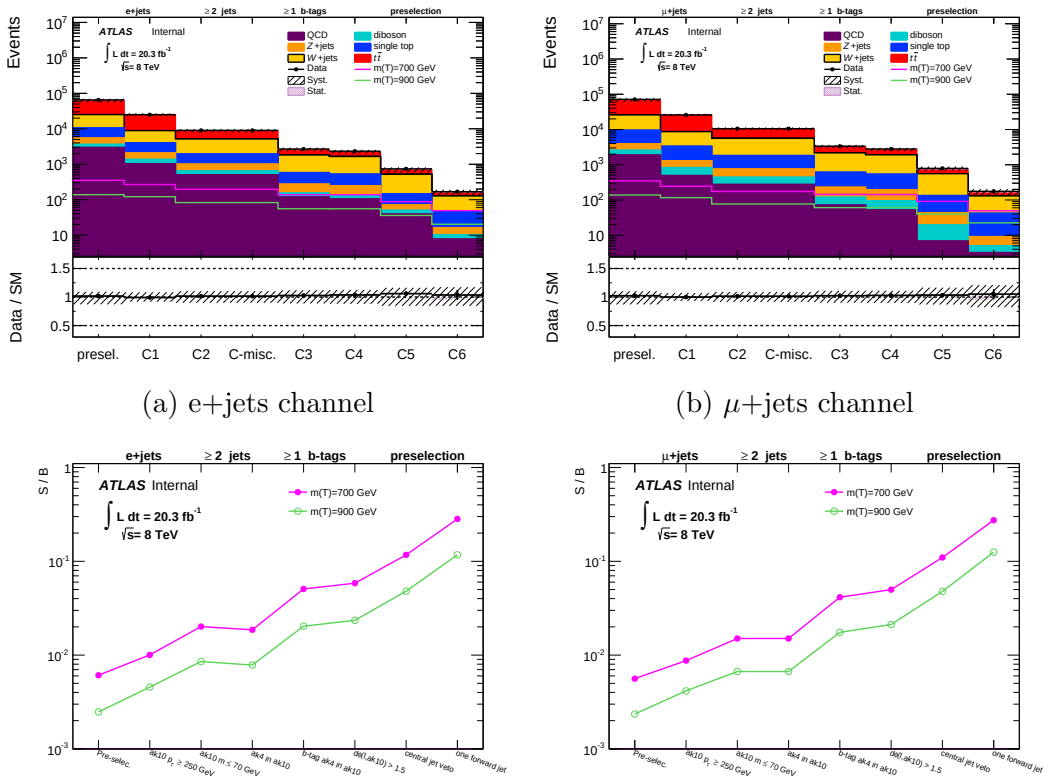

(a) e+jets channel

(b) μ+jets channel

(c) e+jets channel

(d) μ+jets channel

Figure 5.10: Signal to SM background comparison of the event yield (top) and event yield ratio (bottom) at each step of the event selection, both for the electron (left) and muon (right) channels. The signal cross sections are for a unit EW coupling and for BR($T \to Wb$)=0.5.

5.4 Final discriminant

The mass of the VLQ candidate is used as the final signal to background discriminant. This candidate is reconstructed using the sum of the momentum of the lepton, the b-tagged jet and the reconstructed neutrino candidate.

Figure 5.11 shows a signal to SM background comparison of the mass of the reconstructed VLQ candidate mass after applying the full event selection. Here, the background shape, peaking at between 500 and 600 GeV, falls by about 50% for masses above 700 GeV. The aim of this analysis is to search for VLQs with masses above this point, as limits already exist [169–172] for masses under 700 GeV.

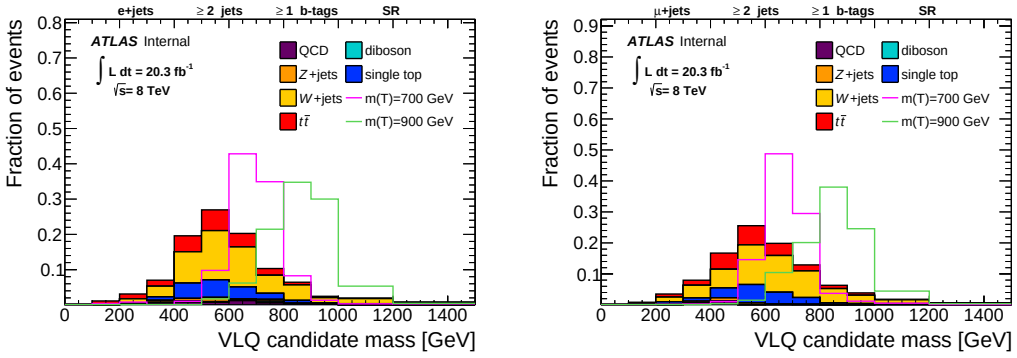

(a) e+jets channel (b) μ+jets channel

Figure 5.11: Signal to SM background shape-only comparison of the mass of the reconstructed VLQ candidate for events passing the full event selection.

Figures 5.12 and 5.13 show a signal to SM background comparison, for the electron and muon channels respectively, of the mass of the reconstructed VLQ candidate mass for the preselection and cuts C1 to C5 applied in sequence. In the steps before the matching between the large-R jet and the b-tagged jet (C3), the leading b-tagged jet in the whole event is used in the reconstruction of the VLQ candidate. Here, the background shape gradually changes from a steeply falling distribution into a shape that peaks at between 500 and 600 GeV. Also here, the signal shape is shown only to gradually become slightly narrower, with about 85% (65%) of events within the two largest bins at C5, compared with about 60% (40%) at the preselection stage, for the 700 (900) GeV mass point. In this figure the signal to background shape separation decreases as the steps of the event selection are applied, however, this selection reduces the background yield considerably (see Figure 5.10), resulting in an overall increase on the signal to background significance.

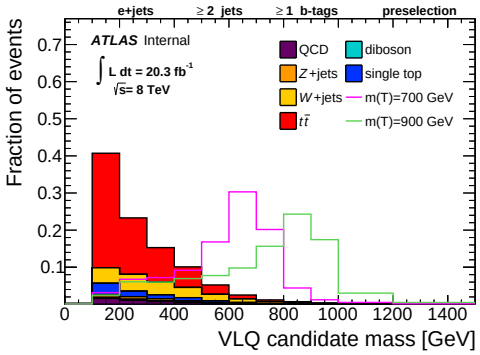

(a) preselection

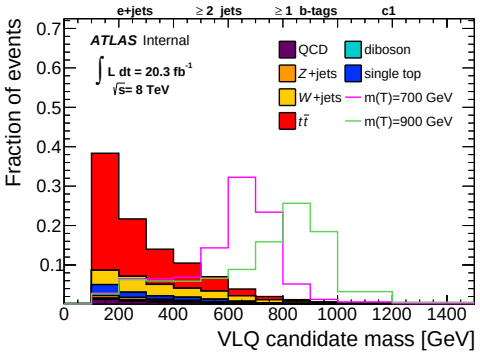

(b) C1, large-R jet p_{T}

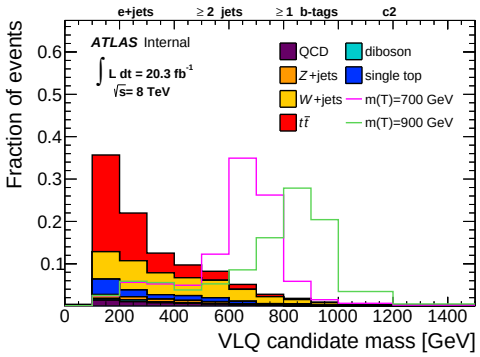

(c) C2, boosted $t\bar{t}$ veto

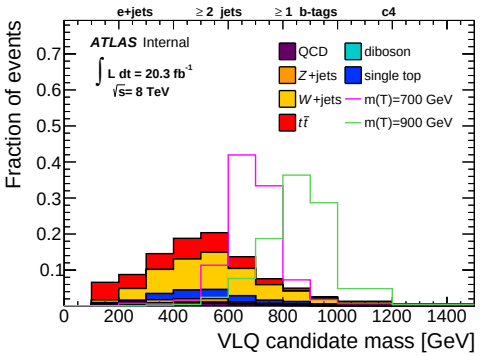

(d) C3, b-tagged jet in large-R jet:

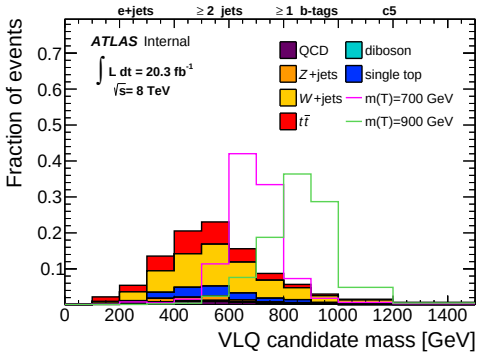

(e) C4, minimum lepton to large-R jet $\Delta\phi$ separation

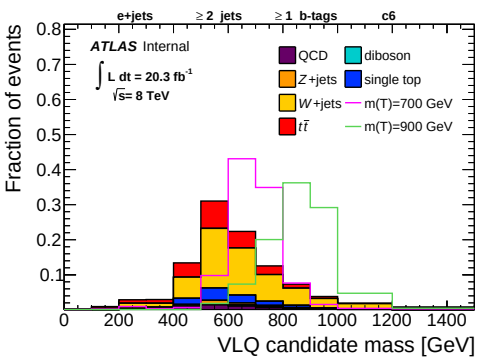

(f) C5, central jet veto

Figure 5.12: Signal to SM background shape-only comparison of the mass of the reconstructed VLQ candidate for the electron channel, after applying in sequence each one of the event selection criteria up to the central jet veto.

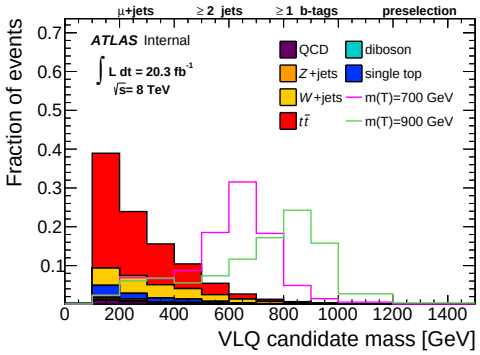

(a) preselection

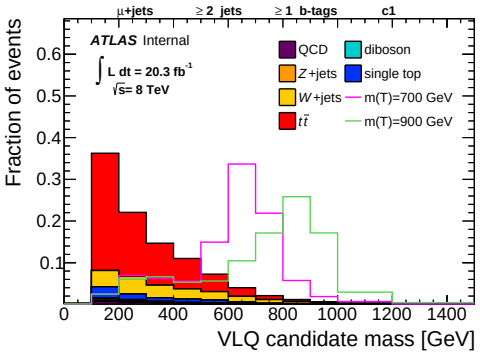

(b) C1, large-R jet p_{T}

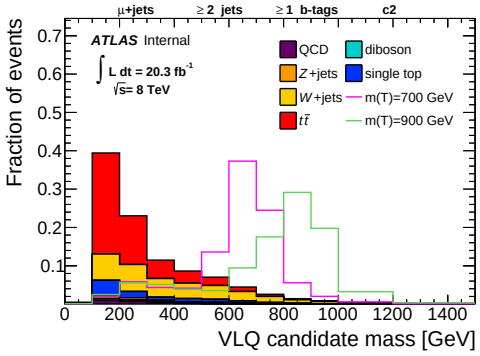

(c) C2, boosted $t\bar{t}$ veto

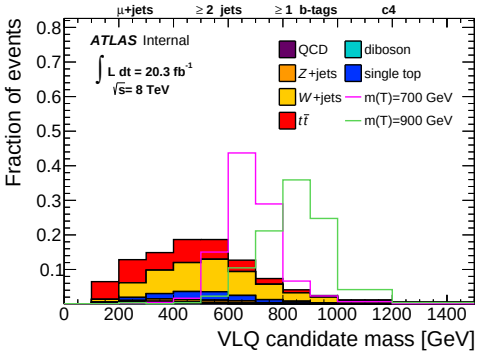

(d) C3, b-tagged jet in large-R jet:

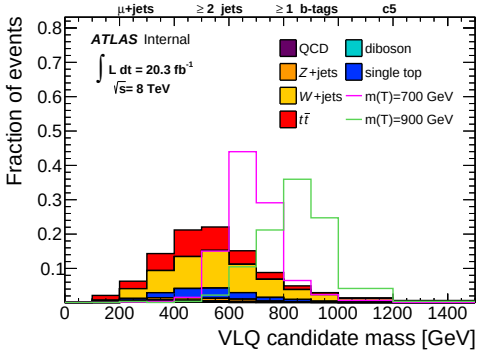

(e) C4, minimum lepton to large-R jet $\Delta\phi$ separation

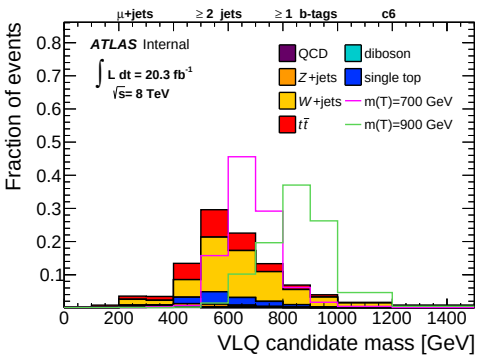

(f) C5, central jet veto

Figure 5.13: Signal to SM background shape-only comparison of the mass of the reconstructed VLQ candidate for the muon channel, after applying in sequence each one of the event selection criteria up to the central jet veto.

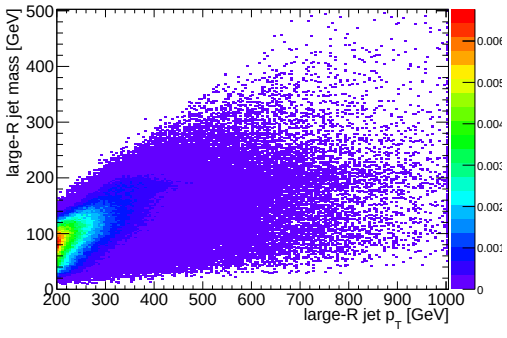

Figure 5.14: large-R jet p_{T} versus mass for a sample of $t\bar{t}$ events.

5.5 Event selection optimisation

The search strategy optimisation is presented in in Ref. [3]. In this section, this optimisation procedure is outlined using the pure MC information contained in the nominal signal and background ATLAS samples. Here, only the three main backgrounds, W+jets, $t\bar{t}$ and single top are taken into account. Their cross sections are taken from theoretical predictions. Here, a signal sample with a mass of 700 GeV is used.

The event selection optimisation is based on truth level events. The truth-level lepton, jet and missing transverse momentum identification and reconstruction is identical to that described in Ref. [3].

The event selection is optimised by looking for cuts that maximise the gain in the signal to background significance ($\mathrm{S}/\sqrt{\mathrm{B}}$). This is done by comparing $\mathrm{S}/\sqrt{\mathrm{B}}$ before and after applying certain cut. A cut increases the expected significance if

$$\mathrm{S_f}/\sqrt{\mathrm{B_f}} > \mathrm{S_i}/\sqrt{\mathrm{B_i}} \tag{5.1}$$

where the index i (f) denotes before (after) selection, which can be written in terms of efficiency as

$$\mathrm{eff_S}/\sqrt{\mathrm{eff_B}} > 1 \tag{5.2}$$

and where $\mathrm{eff_S}/\sqrt{\mathrm{eff_B}}$ is referred to as the significance gain.

Figure 5.14 shows the correlation between the large-R jet p_{T} and mass, for a sample of $t\bar{t}$ events. Due to the observed correlation, the optimisation of the cuts applied on these variables is performed by simultaneously scanning over both variables.

Figure 5.15 shows the significance gain for three values of the minimum large-R jet p_{T}, each combined with five values of the maximum large-R jet

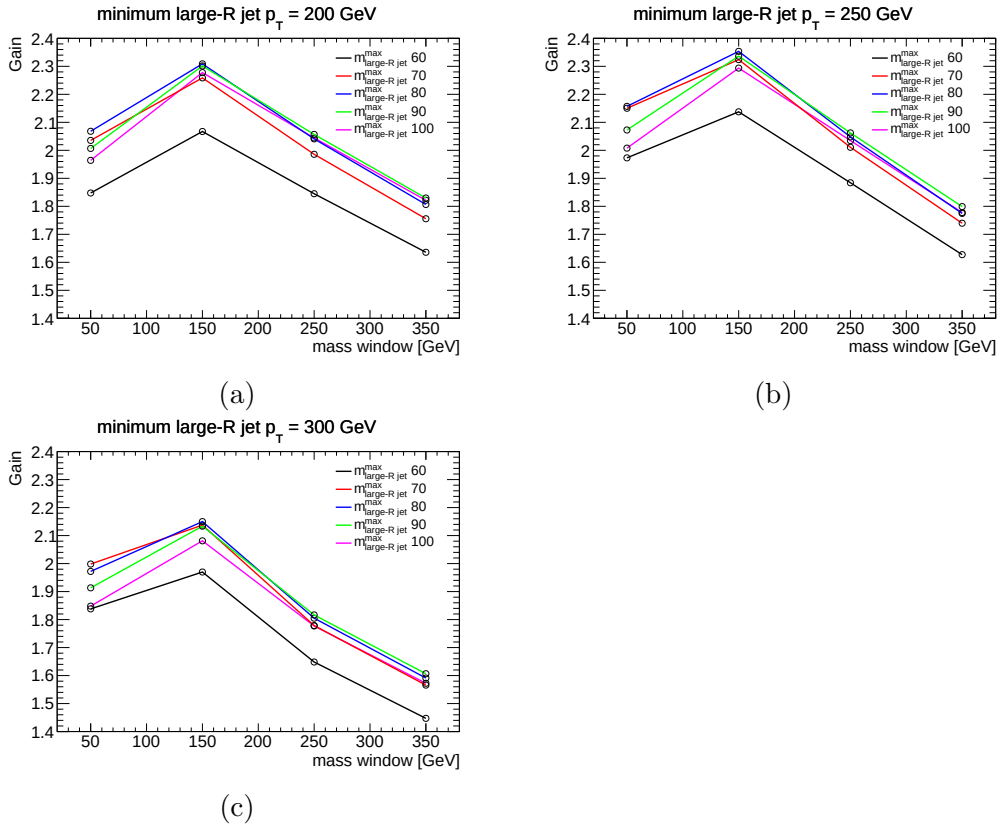

Figure 5.15: Signal to background significance gain after applying the boosted $t\bar{t}$ veto, for a scan of the cuts on the large-R jet p_{T} and mass. This is shown for events within a given mass window about 700 GeV, corresponding to the mass of the signal sample.

mass. Any selection cut would affect the shape of the VLQ candidate mass, both for signal and background events, altering its strength as the final discriminant of this analysis. This is accounted for by presenting the significance gain versus various values of a mass window about the mass of the signal sample used. For instance, for $m(T) = 700$ GeV and a mass window of 100 GeV, events are selected if the reconstructed VLQ mass is within 600 and 800 GeV. In this figure, the largest gains are observed when requiring a minimum large-R jet p_{T} of 250 GeV and a maximum mass of between 70 to 100 GeV. This is in agreement with what is presented in Ref. [3]. The change of the maximum gain versus the large-R jet p_{T} and mass is understood in terms of the $t\bar{t}$ background rejection, and of the signal efficiency. The higher the large-R jet p_{T} is, the more likely is for it to contain all of the top decay products, increasing the large-R jet mass for $t\bar{t}$ background events. This would help to further increase the fraction of vetoed boosted $t\bar{t}$ events using the large-R jet mass, but would also decrease the signal acceptance.

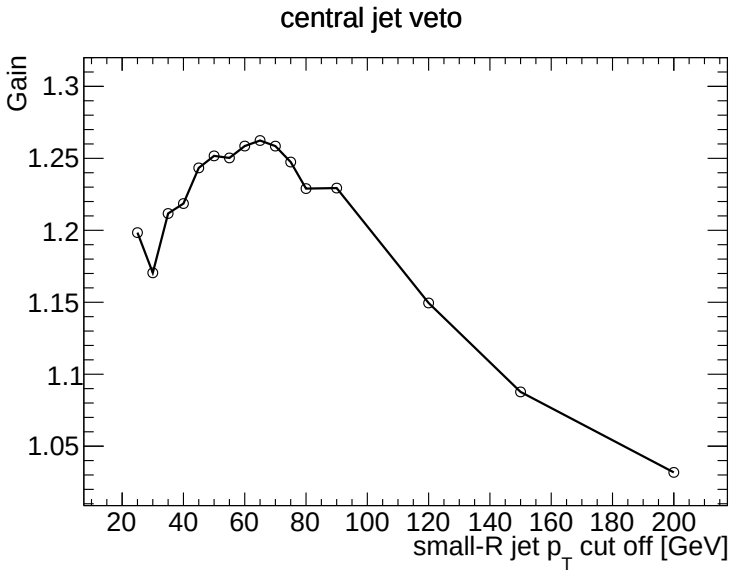

Figure 5.16: Signal to background significance gain after applying the central jet veto criteria versus the small-R jet p_{T} cut-off, where only jets above this threshold are counted. This is shown for events passing the large-R jet p_{T}, boosted $t\bar{t}$ veto, and b-tagged jet in large-R jet selection criteria.

Figure 5.16 shows the significance gain after applying a veto on the number of central jets outside the large-R jet versus the jet p_{T} cut-off, where only jets above this threshold are counted. This is shown for events passing the large-R jet p_{T}, the boosted $t\bar{t}$ veto, and b-tagged jet in large-R jet selection criteria. Here, the largest gain is obtained by vetoing events with any such jet with p_{T} above 60 to 80 GeV. This is in agreement with what is presented in Ref. [3]. To test the dependence of this conclusion on the large-R jet p_{T} and boosted $t\bar{t}$ veto cuts, this optimisation is performed for various cases, failing to observe any considerable change.

Figure 5.17 shows the significance gain after requiring at least one forward jet. This is shown versus the minimum p_{T} of the forward jet. Here, a considerable gain is observed as a result of this requirement. This gain decreases as the minimum jet p_{T} increases, and hence the lowest value (35 GeV) is chosen, which is in agreement with what is presented in Ref. [3]. The optimal jet p_{T} threshold is not expected to be correlated with any of the previous selection criteria. This is tested by varying those cuts, and no change is found.

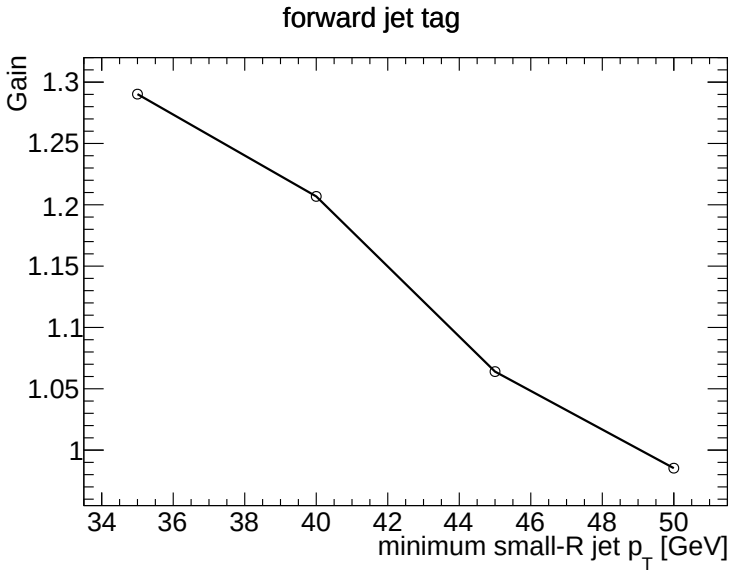

Figure 5.17: Signal to background significance gain after applying the forward jet tag criteria versus the minimum jet p_{T}. This is shown for events passing the boosted $t\bar{t}$ veto and central jet veto criteria.

5.6 Control plots and background normalisation

5.6.1 Control regions

To validate the modelling of the kinematic variables used to reconstruct the VLQ candidate, a Control Region (CR) with the same W+jets heavy-flavour fraction, and similar large-R jet kinematics is used. This control region is given by the events failing the central jet veto, resulting in a sample orthogonal to the Signal Region (SR). Also here, no cut on the large-R jet mass or requirement on a forward jet are used. This control region is labelled as FitCR.

Two additional control regions, W1CR and W2CR, are used to validate the modelling of the main background, W+jets. Here, similarly to FitCR, the central jet veto requirement is inverted, and no requirement is made on the forward jets. Unlike FitCR, the large-R jet mass cut is used for W1CR and W2CR. The latter selects a larger sample of events. This is achieved by removing the b-tagged jet inside large-R jet requirement. To reduce the $t\bar{t}$ contamination in W2CR, a cut of at least 175 GeV is placed in the mass of the lepton plus b-tagged jet system. Table 5.1 shows a comparison between the selections applied in the signal and control regions.

Table 5.1: Comparison between the event selections applied in the SR and the CRs.

Cut	SR	FitCR	W1CR	W2CR
preselection	✓	✓	✓	✓
large-R jet $p_{\mathrm{T}} \geq 250$ GeV	✓	✓	✓	✓
boosted $t\bar{t}$ veto	✓	✗	✓	✓
b-tagged jet inside large-R jet	✓	✓	✓	✗
mass(lepton+b-tagged jet) > 175 GeV	✗	✗	✗	✓
$\Delta\phi$(lepton,large-R jet) > 1.5	✓	✓	✓	✓
central small-R jet veto	✓	inverted	inverted	inverted
at least one forward small-R jet	✓	✗	✗	✗

Tables 5.2, 5.3 and 5.4 show the expected and observed event yields in the three control regions. Here, data and MC agree within uncertainties for all the control regions.

Table 5.2: Comparison between the expected and observed number of events in the W1CR, after applying the W+jets and $t\bar{t}$ normalisation correction factors, described in Section 5.6.2, and the Wp_{T} reweighting, described in Section 5.6.3. Uncertainties are presented as ± stat. for each individual background process and for data, and as ± stat.$^{+\text{syst.}}_{-\text{syst.}}$ for the total SM background prediction, allowing for asymmetric systematic variations. The systematic uncertainties correspond to those described in Section 5.7. The signal cross sections are for a unit EW coupling and for BR($T \to Wb$)=0.5.

	e+jets	μ+jets
$T \to Wb$ $m(T) = 700$ GeV	50 ± 2	51 ± 2
$T \to Wb$, $m(T) = 900$ GeV	19 ± 1	21 ± 1
W+jets	758 ± 11	955 ± 13
$t\bar{t}$	418 ± 6	599 ± 7
single top	203 ± 9	251 ± 9
Z+jets	88 ± 7	75 ± 6
diboson	21 ± 2	31 ± 3
multijets	65 ± 2	45 ± 4
total SM bkgr.	$1553 \pm 1^{+260}_{-248}$	$1956 \pm 19^{+304}_{-291}$
data	1595 ± 40	2007 ± 45

Table 5.3: Comparison between the expected and observed number of events in the W2CR, after applying the W+jets and $t\bar{t}$ normalisation correction factors, described in Section 5.6.2, and the Wp_{T} reweighting, described in Section 5.6.3. Uncertainties are presented as ± stat. for each individual background process and for data, and as ± stat.$^{+\text{syst.}}_{-\text{syst.}}$ for the total SM background prediction, allowing for asymmetric systematic variations. The systematic uncertainties correspond to those described in Section 5.7. The signal cross sections are for a unit EW coupling and for BR($T \to Wb$)=0.5.

	e+jets	μ+jets
$T \to Wb$ $m(T) = 700$ GeV	62 ± 3	65 ± 3
$T \to Wb$, $m(T) = 900$ GeV	25 ± 1	28 ± 1
W+jets	1263 ± 14	1558 ± 16
$t\bar{t}$	685 ± 7	939 ± 9
single top	244 ± 10	315 ± 11
Z+jets	146 ± 8	128 ± 8
diboson	46 ± 3	57 ± 4
multijets	108 ± 3	68 ± 9
total SM bkgr.	$2492 \pm 21^{+373}_{-357}$	$3065 \pm 24^{+445}_{-416}$
data	2494 ± 50	3197 ± 57

Table 5.4: Comparison between the expected and observed number of events in the FitCR, after applying the W+jets and $t\bar{t}$ normalisation correction factors, described in Section 5.6.2, and the Wp_{T} reweighting, described in Section 5.6.3. Uncertainties are presented as ± stat. for each individual background process and for data, and as ± stat.$^{+\text{syst.}}_{-\text{syst.}}$ for the total SM background prediction, allowing for asymmetric systematic variations. The systematic uncertainties correspond to those described in Section 5.7. The signal cross sections are for a unit EW coupling and for BR($T \to Wb$)=0.5.

	e+jets	μ+jets
$T \to Wb$ $m(T) = 700$ GeV	71 ± 3	75 ± 3
$T \to Wb$, $m(T) = 900$ GeV	30 ± 1	32 ± 1
W+jets	1152 ± 14	1465 ± 15
$t\bar{t}$	3821 ± 17	5263 ± 21
single top	409 ± 14	504 ± 15
Z+jets	143 ± 8	124 ± 8
diboson	59 ± 4	79 ± 4
multijets	187 ± 3	128 ± 15
total SM bkgr.	$5772 \pm 28^{+586}_{-577}$	$7563 \pm 35^{+747}_{-755}$
data	5808 ± 76	7601 ± 87

5.6.2 Background normalisation

Figure 5.18 shows the large-R jet mass in the FitCR. The difference in the shape between W+jets and $t\bar{t}$ can be exploited to determine their normalisation with respect to the data.

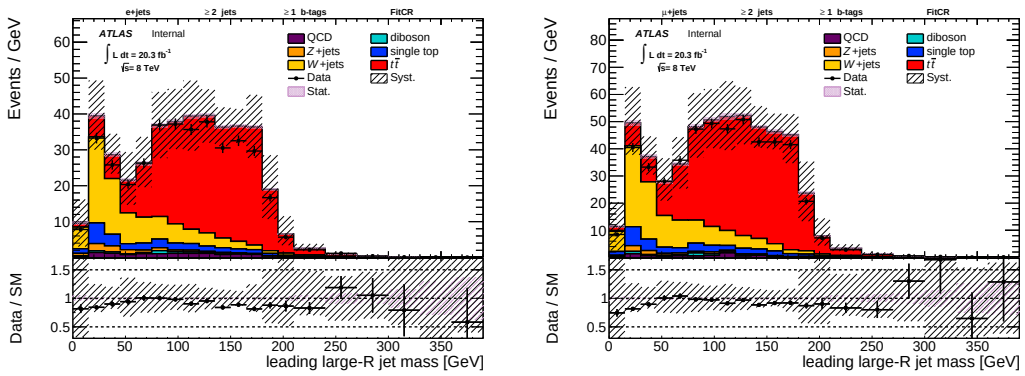

(a) e+jets channel (b) μ+jets channel

Figure 5.18: Data to MC comparison in the FitCR of the large-R jet mass for the electron (a) and muon (b) channels.

Using the W+jets and $t\bar{t}$ background shapes from MC as templates, the fraction of W+jets and $t\bar{t}$ is fitted to the data, after subtracting the contribution of smaller backgrounds. This fitting is performed using TFractionFitter[1] [173]. The obtained correction factors with respect to the theoretical predictions (NNLO for inclusive W+jets and NNLO+NNLL for $t\bar{t}$) for the muon (electron) channels are 0.815 (0.938) and 0.965 (0.906) for W+jets and $t\bar{t}$ respectively, with a statistical uncertainty of 23% (30%) and 9% (12%). These uncertainties and their correlation are used to derive the systematic uncertainty due to this normalisation procedure.

The results from TFractionFitter are crosschecked with a manual computation of the correction factors using the χ^2 method. Here, χ^2 is given by

$$\chi^2 = \sum_{\text{bins}} \frac{1}{\sigma^2_{\text{stat.}}} \left(N_i^{\text{data}-\text{other bkgr.}} - \left(\text{corr}_{\,W+\text{jets}} \cdot N_i^{W+\text{jets}} + \text{corr}_{\,t\bar{t}} \cdot N_i^{t\bar{t}} \right) \right)^2 \tag{5.3}$$

where $\text{corr}_{\,W+\text{jets}}$ ($\text{corr}_{\,t\bar{t}}$) corresponds to the W+jets ($t\bar{t}$) correction factors. After expanding this expression, the values of the correction factors that minimise χ^2 can be obtained from the two equation system resulting from the partial derivatives: $\delta\chi^2/\delta\text{corr}_{\,W+\text{jets}} = 0$ and $\delta\chi^2/\delta\text{corr}_{\,t\bar{t}} = 0$. The obtained

[1] `http://root.cern.ch/root/htmldoc/TFractionFitter.html`

results are in very good agreement with that obtained though TFractionFitter. However, TFractionFitter is preferred as it allows to rapidly repeat this calculations many times, and a proper estimation of the uncertainties on the correction factors.

The systematic uncertainty due to the W+jets and $t\bar{t}$ normalisation correction factors are derived using error propagation. TFractionFitter allows for the retrieval the covariance matrix of the estimated parameters. In a given bin, the uncertainty on the total W+jets plus $t\bar{t}$ background prediction

$$\sigma_{\text{total}} = \pm\sqrt{N^2_{W+\text{jets}} \cdot \sigma^2_{W+\text{jets}} + N^2_{t\bar{t}} \cdot \sigma^2_{t\bar{t}} + 2 \cdot N_{W+\text{jets}} \cdot N_{t\bar{t}} \cdot \text{cov}_{W+\text{jets},\ t\bar{t}}} \quad (5.4)$$

where $N_{W+\text{jets}}$ is the number of W+jets entries in this bin, and $\sigma_{W+\text{jets}}$ the uncertainty on the W+jets correction factor, similarly for $t\bar{t}$, and $\text{cov}_{W+\text{jets},\ t\bar{t}}$ is the covariance term of the W+jets and $t\bar{t}$ correction factor uncertainties.

Figure 5.19 shows the large-R jet mass in FitCR after applying the W+jets and $t\bar{t}$ correction factors. Here, the overall data to MC agreement shows an improvement. These corrections are derived for every systematic variation accounted for in these analysis. This reduces the scaling component of these uncertainties, to an extent that is visible when comparing this Figure with Figure 5.18. The residual data to MC differences, after applying the W+jets and $t\bar{t}$ correction factors, are within systematic uncertainties.

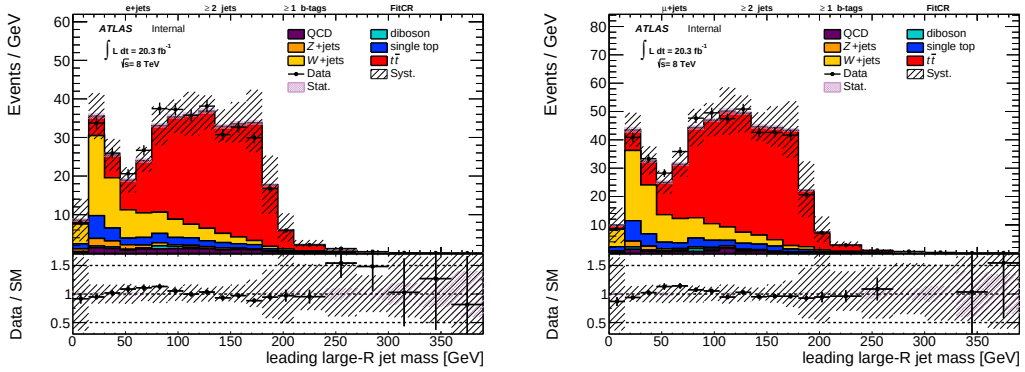

(a) e+jets channel (b) μ+jets channel

Figure 5.19: Data to MC comparison in the FitCR of the large-R jet mass for the electron (a) and muon (b) channels, after applying the W+jets and $t\bar{t}$ normalisation correction factors.

5.6.3 W+jets event reweighting

The W+jets mismodelling at high-p_{T}, affecting the lepton, jets and $E_{\mathrm{T}}^{\mathrm{miss}}$, is a feature observed by various analysis [174, 175]. Figure 5.20 shows the reconstructed W-boson p_{T} (Wp_{T}), given by the sum of the lepton an $E_{\mathrm{T}}^{\mathrm{miss}}$ four-vectors, for W2CR and FitCR. Here, $t\bar{t}$ and W+jets correction factors are derived as a function of Wp_{T} from the observed data to MC differences, using a two-equation system where the two unknowns correspond to the correction factors for each sample. For $t\bar{t}$, these are statistically compatible with unity, and hence no correction is applied. For W+jets, correction factors are derived and a systematic uncertainty is assigned. This is discussed in Section 5.7.4. For the derivation of these weights, backgrounds other that W+jets and $t\bar{t}$ are subtracted from data and from the total SM background prediction. Their statistical uncertainty is propagated in this subtraction, and is therefore taken into account in the resulting weights, and in their statistical uncertainty.

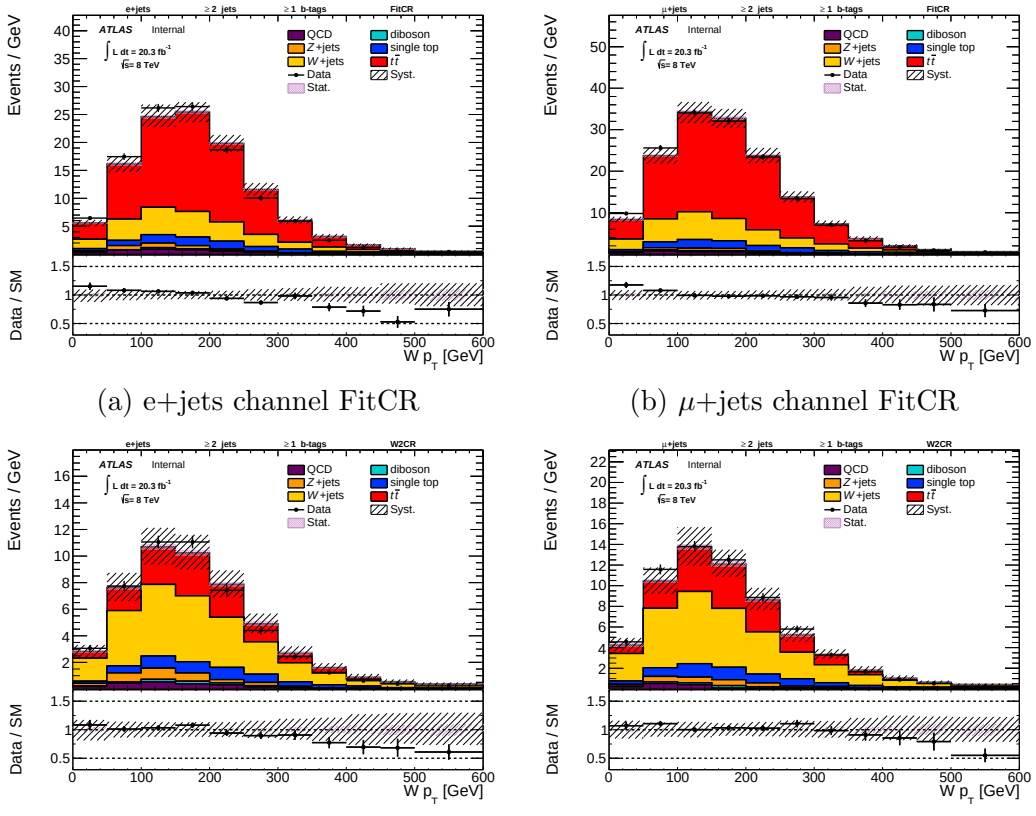

(a) e+jets channel FitCR

(b) μ+jets channel FitCR

(c) e+jets channel W2CR

(d) μ+jets channel W2CR

Figure 5.20: Data to MC comparison of the reconstructed W-boson p_{T} in the FitCR (top) and the W2CR (bottom), both for the electron (left) and muon (right) channels, after applying the W+jets and $t\bar{t}$ normalisation correction factors.

Figure 5.21 shows the W-boson p_{T} before and after applying the correction factors. This is shown for W1CR (closest to SR), which is not used in the derivation of these correction factors.

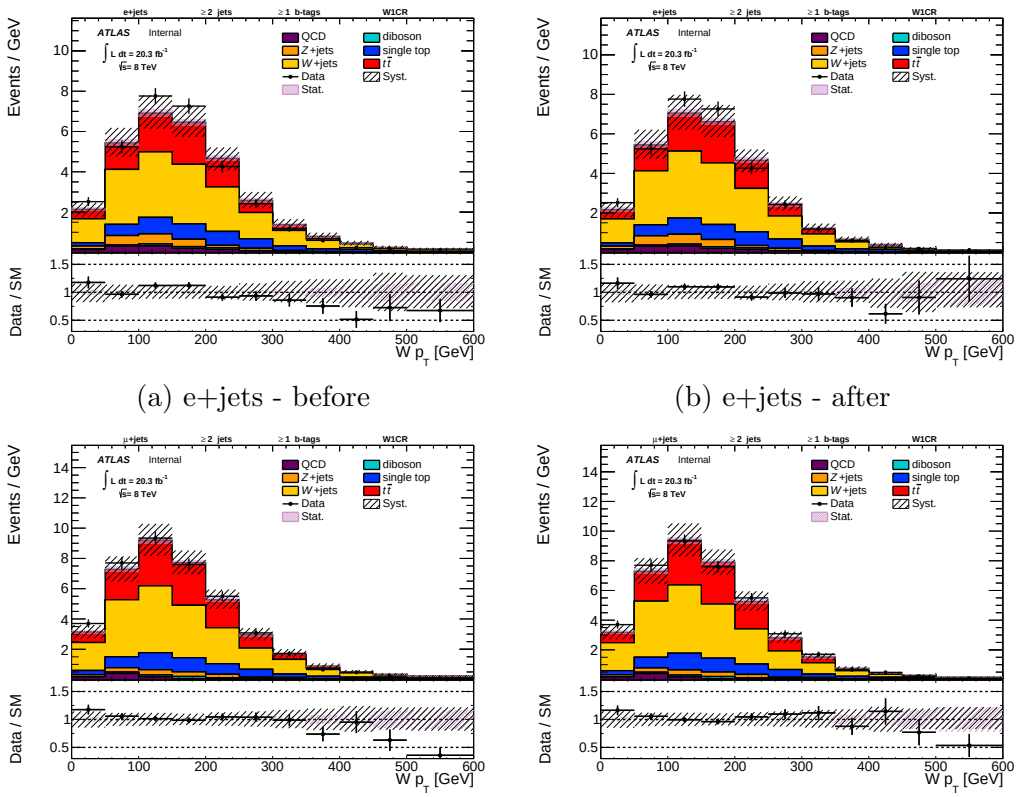

(a) e+jets - before

(b) e+jets - after

(c) μ+jets - before

(d) μ+jets - after

Figure 5.21: Data to MC comparison of the reconstructed W-boson p_{T} in the W1CR both for the electron (top) and muon (bottom) channels, before (left) and after (right) applying the W+jets Wp_{T} reweighting. This is shown after applying the W+jets and $t\bar{t}$ normalisation correction factors.

5.6.4 Control plots

Figure 5.22 shows the reconstructed VLQ mass in the three control regions, after applying the W+jets Wp_{T} reweighting and the W+jets and $t\bar{t}$ normalisation correction factors. The observed distributions are very well described by the simulation.

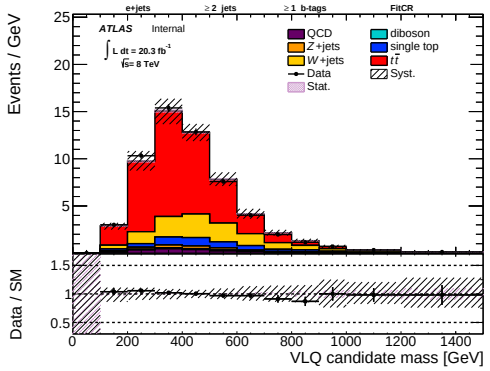

(a) e+jets channel FitCR

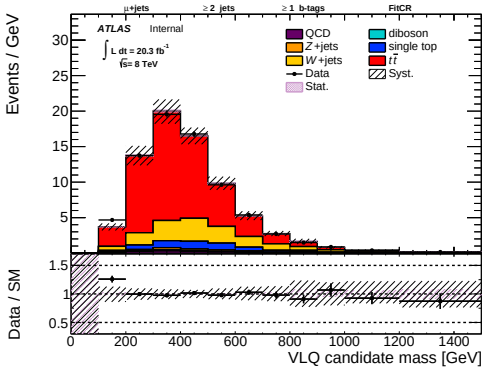

(b) μ+jets channel FitCR

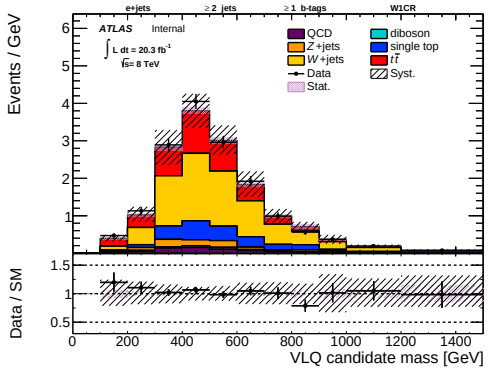

(c) e+jets channel W1CR

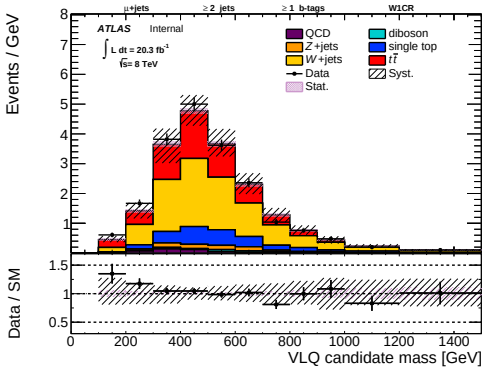

(d) μ+jets channel W1CR

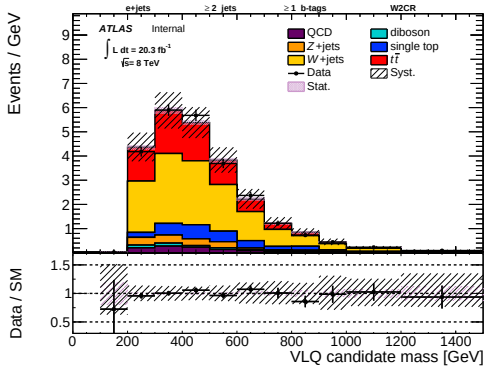

(e) e+jets channel W2CR

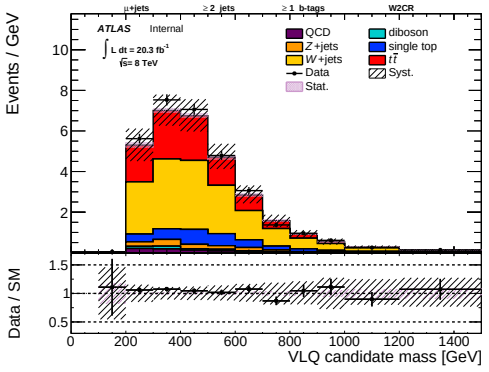

(f) μ+jets channel W2CR

Figure 5.22: Data to MC comparison of the reconstructed VLQ mass in the control regions, both for the electron (left) and muon (right) channels, after applying the W+jets and $t\bar{t}$ normalisation correction factors.

5.7 Impact of systematic uncertainties

In this analysis uncertainties on the object reconstruction and identification, and background modelling are taken into account. These are described in Section 2.7. Tables 5.5 and 5.6 show the impact of systematic uncertainties on the predicted yield of SM background events for the electron and muon channel respectively. Other additional sources of systematic uncertainties, unique to the analysis presented in this chapter, are outlined in this section. Also, uncertainties with the largest impact on the expected yields are examined in detail. To alleviate the statistical fluctuations in the systematic uncertainties estimation, a smoothing procedure is applied. This is further discussed in Appendix B.

Table 5.5: Average impact of systematic uncertainties on the total prediction of SM background in the electron channel. Whenever available, $\pm 1\sigma$ variations are shown as 1σ (-1σ)

Source of systematic uncertainty	Raw relative yield uncertainties [%]
W+jets and $t\bar{t}$ normalisation	15 (15)
large-R jet energy scale	8 (9)
multijet estimation	5 (1)
large-R jet mass scale and resolution	4 (4)
t-channel single top modelling	5
$t\bar{t}$ modelling	4
luminosity	3 (3)
W+jets modelling	2 (2)
small-R jet energy scale	4 (2)
b-tagging	1 (1)
small-R jet energy resolution	< 1
small-R jet reconstruction efficiency	< 1
small-R jet vertex fraction	< 1
lepton identification and reconstruction	< 1
$E_{\mathrm{T}}^{\mathrm{miss}}$	< 1

The dominant uncertainties are those due to the W+jets and $t\bar{t}$ normalisation, and to the large-R jet energy scale. The combined impact on this analysis of the lepton uncertainties is below 1%. The combined impact of the small-R jet reconstruction efficiency, energy scale and resolution, and JVF are below the 5%, with the largest contribution coming from the η intercalibration MC modelling component. The combined impact of the b-tagging uncertainties, including the light-quark jet and c-jet mistagging is below 5%. The combined impact of the uncertainties on the $E_{\mathrm{T}}^{\mathrm{miss}}$ calculation is smaller than 1%.

Table 5.6: Average impact of systematic uncertainties on the total prediction of SM background in the muon channel. Whenever available, $\pm 1\sigma$ variations are shown as 1σ (-1σ)

Source of systematic uncertainty	Raw relative yield uncertainties [%]
W+jets and $t\bar{t}$ normalisation	14
large-R jet energy scale	11 (5)
multijet estimation	< 1
large-R jet mass scale and resolution	6 (4)
t-channel single top modelling	9
$t\bar{t}$ modelling	5
luminosity	3 (3)
W+jets modelling	2 (2)
small-R jet energy scale	4 (2)
b-tagging	1 (1)
small-R jet energy resolution	< 1
small-R jet reconstruction efficiency	< 1
small-R jet vertex fraction	< 1
lepton identification and reconstruction	< 1
$E_{\mathrm{T}}^{\mathrm{miss}}$	< 1

5.7.1 Large-R jet p_{T} uncertainties

Figure 5.23 shows the effect of the largest large-R jet p_{T} scale uncertainty on the final discriminant for the SM background prediction. This topology uncertainty, labelled `FatJPtS_Topo`, accounts for different quark/gluon makeup and for differences in jet energy response between QCD jets and jets from boosted W-boson and top-quark decays. Also in this figure, the double ratio component is shown, which only affects the large-R jet high p_{T} region and has therefore a negligible impact on this analysis. Bin by bin, the topology uncertainty is within 50%, with the largest variations being observed in both ends of the mass range, which coincides with the bins where the largest MC statistical uncertainties are also observed. For masses between 500 and 1000 GeV this uncertainty is within 15%. Tables 5.7 and 5.8 show the average impact of this uncertainty on the expected yield of SM background events.

Table 5.7: Average impact of the dominant large-R jet JES systematic uncertainty on the total prediction of SM background in the electron channel. Whenever available, $\pm 1\sigma$ variations are shown as 1σ (-1σ)

Source of systematic uncertainty	Relative yield uncertainties [%]
topology dependence	8 (8)

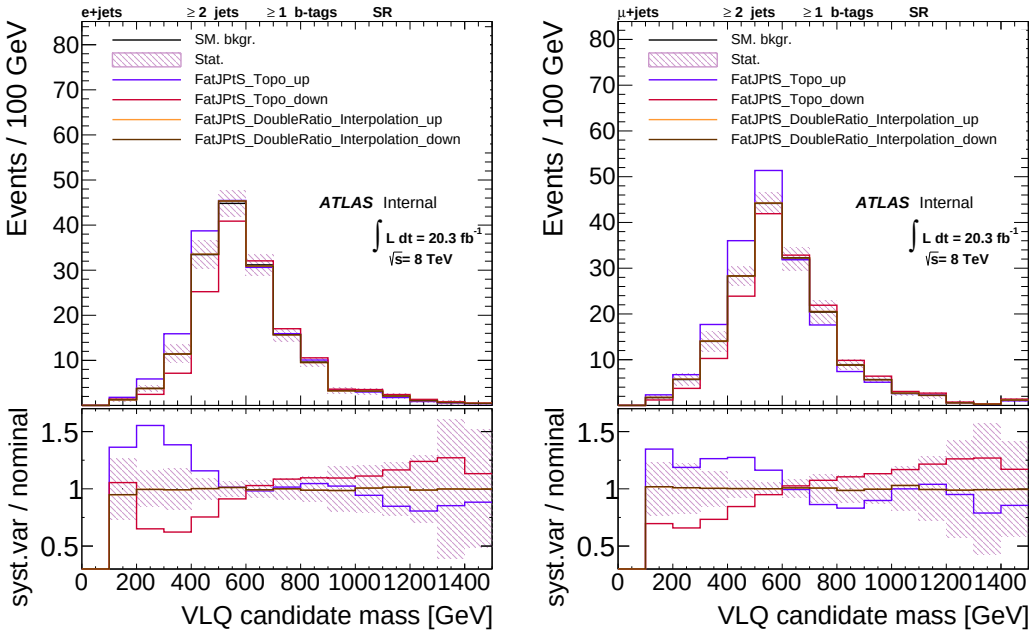

(a) e+jets channels (b) μ+jets channel

Figure 5.23: Comparison between the nominal SM background prediction and systematic variations on the large-R jet p_{T}, after applying the W+jets and $t\bar{t}$ normalisation correction factors. This is shown for the electron (left) and muon (right) channels.

Table 5.8: Average impact of the dominant large-R jet JES systematic uncertainties on the total prediction of SM background in the muon channel. Whenever available, $\pm 1\sigma$ variations are shown as 1σ (-1σ)

Source of systematic uncertainty	Relative yield uncertainties [%]
topology dependence	10 (5)

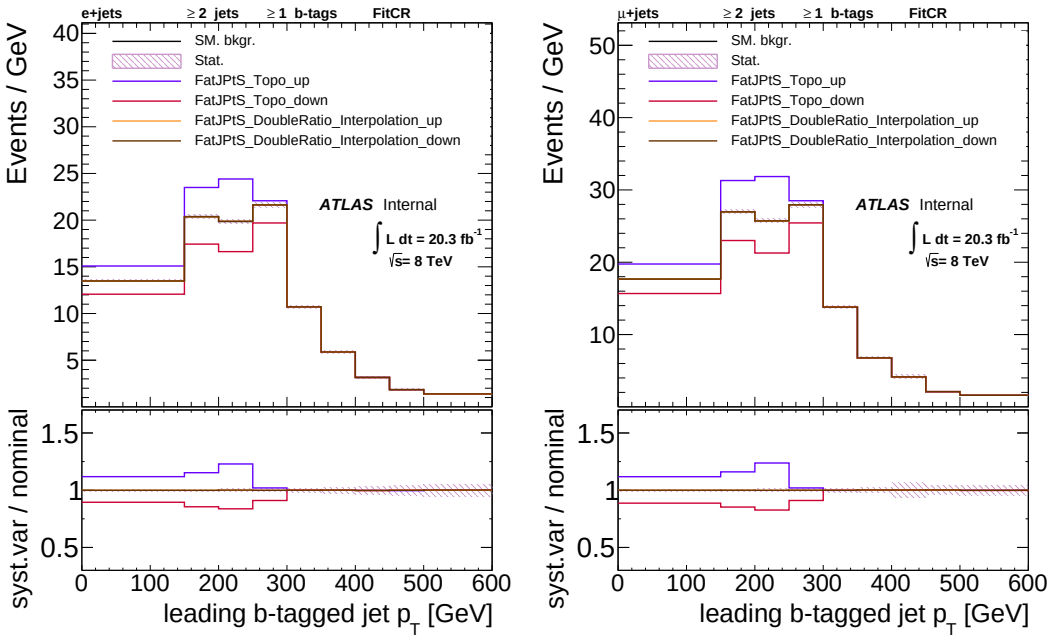

(a) e+jets channels (b) μ+jets channel

Figure 5.24: Comparison between the nominal SM background prediction and systematic variations on the large-R jet p_{T}, before applying the W+jets and $t\bar{t}$ normalisation correction factors. This is shown for the electron (left) and muon (right) channels.

Figure 5.24 shows the impact of the large-R jet p_{T} scale topology uncertainty on the p_{T} of the b-tagged geometrically matched to the large-R jet. This is shown for FitCR in an attempt to minimise the statistical component of the observed variation, and before constraining this uncertainty by fitting the W+jets and $t\bar{t}$ fractions to data. Here, this uncertainty is shown to affect only the first bins of the p_{T} spectrum. This behaviour suggest a strong correlation between the large-R jet p_{T} and migration of events between these first p_{T} bins. Events with a high-p_{T} b-tagged jet, as those produced in decays of heavy VLQs, would contain in nearly all cases a large-R jet with p_{T} above 250 GeV. Hence, variations on the large-R jet p_{T} spectrum would have no effect in this regime. On the other hand, whether an event with a low-p_{T} b-tagged jet would pass the large-R jet p_{T} cut would largely depend on the topology and therefore variations on the large-R jet p_{T} spectrum would yield the observed large changes on the event rate on this regime.

Figure 5.25 shows the various components of the large-R p_{T} scale uncertainty derived from the γ+jet balance method. Bin by bin, these uncertainties are within 5% and 10%, with the exception of the mass range under 500 GeV where these uncertainties reach the 25 %. Tables 5.9 and 5.10 show the average

impact of these uncertainties on the expected yield of SM background events.

Table 5.9: Average impact of large-R jet JES from γ+jet systematic uncertainties on the total prediction of SM background in the electron channel. Whenever available, $\pm 1\sigma$ variations are shown as 1σ (-1σ)

Source of systematic uncertainty	Relative yield uncertainties [%]
data to MC photon response ratio	3 (3)
cut on the leading small-R jet outside large-R jet	< 1
variation of the $\Delta\phi(\gamma$,large-R jet) cut	1 (2)
photon purity	< 1
photon energy scale	2 (2)
generator uncertainty, Pythia 6 vs Herwig	< 1
data to MC difference on the k-term	< 1
smearing of the large-R jet energy scale by 20%	< 1
variation of small-R jet inside/outside the large-R jet definition	< 1
variation on the subleading small-R jet p_{T} in the event	< 1
statistical uncertainty	< 1
$\mathrm{M}/p_{\mathrm{T}}$ < 0.15 vs > 0.15	< 1

Table 5.10: Average impact of large-R jet JES from γ+jet systematic uncertainties on the total prediction of SM background in the muon channel. Whenever available, $\pm 1\sigma$ variations are shown as 1σ (-1σ)

Source of systematic uncertainty	Relative yield uncertainties [%]
data to MC photon response ratio	4 (2)
cut on the leading small-R jet outside large-R jet	< 1
variation of the $\Delta\phi(\gamma$,large-R jet) cut	1 (1)
photon purity	< 1
photon energy scale	1 (1)
generator uncertainty, Pythia 6 vs Herwig	1 (1)
data to MC difference on the k-term	< 1
smearing of the large-R jet energy scale by 20%	< 1
variation of small-R jet inside/outside the large-R jet definition	< 1
variation on the subleading small-R jet p_{T} in the event	< 1
statistical uncertainty	< 1
$\mathrm{M}/p_{\mathrm{T}}$ < 0.15 vs > 0.15	1 (1)

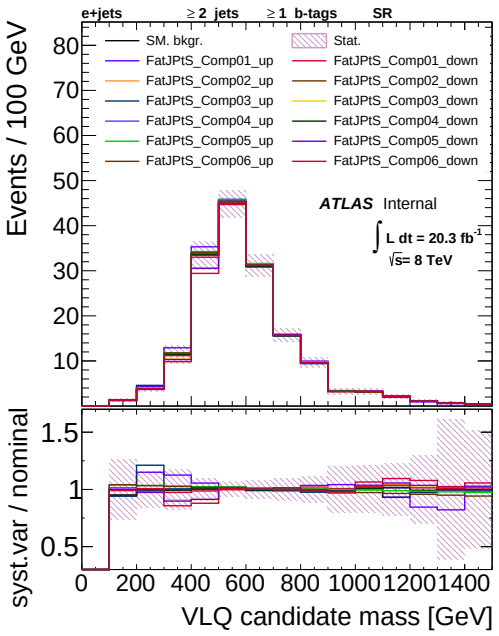

(a) e+jets channel

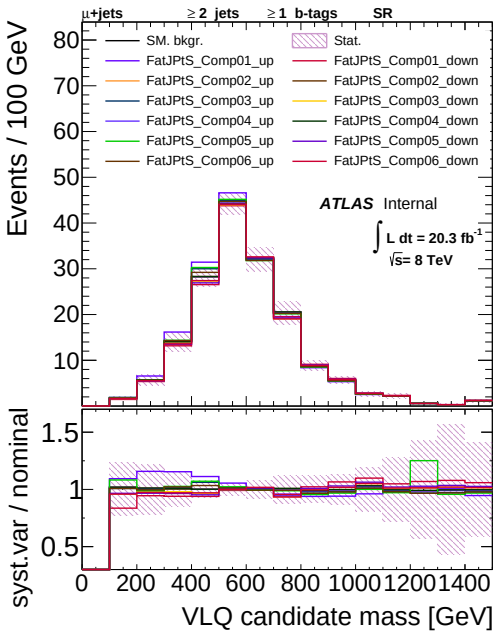

(b) μ+jets channel

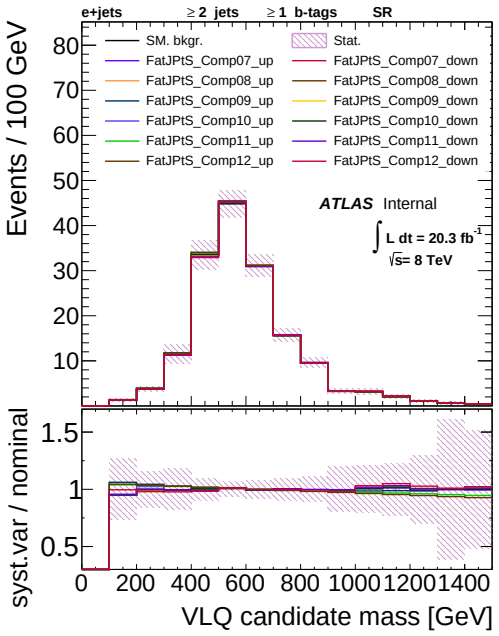

(c) e+jets channel

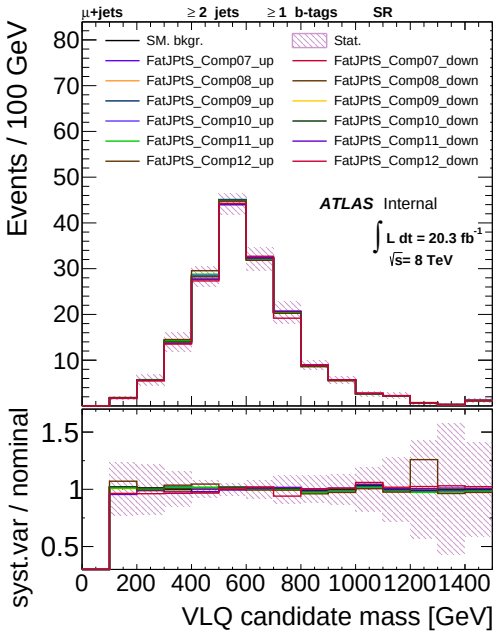

(d) μ+jets channel

Figure 5.25: Comparison between the nominal SM background prediction and systematic variations on the large-R jet p_{T}, after applying the W+jets and $t\bar{t}$ normalisation correction factors. This is shown for the electron (left) and muon (right) channels.

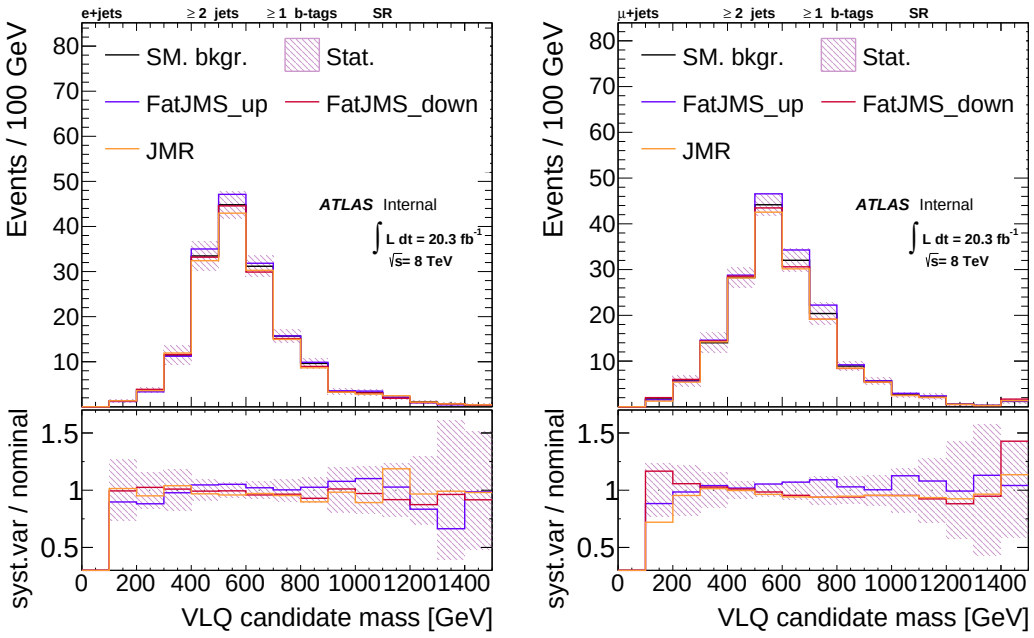

(a) e+jets channel (b) μ+jets channel

Figure 5.26: Comparison between the nominal SM background prediction and systematic variations on the large-R jet mass, after applying the W+jets and $t\bar{t}$ normalisation correction factors. This is shown for the electron (left) and muon (right) channels.

5.7.2 Large-R jet mass uncertainties

Figure 5.26 shows the effect of the large-R jet mass scale and resolution uncertainties on the final discriminant for the SM background prediction. Bin by bin, these uncertainties are within 25%, with the largest variations being observed in both ends of the mass range, which coincides with the bins where the largest MC statistical uncertainties are also observed. For masses between 400 and 1000 GeV these uncertainties are within 10%. Tables 5.11 and 5.12 show the average impact of these uncertainties on the expected yield of SM background events.

Table 5.11: Average impact of large-R jet JMS and JMR systematic uncertainties on the total prediction of SM background in the electron channel. Whenever available, $\pm 1\sigma$ variations are shown as 1σ (-1σ)

Source of systematic uncertainty	Relative yield uncertainties [%]
track to calo-jet uncertainty	3 (2)
20% mass resolution smearing	3

Table 5.12: Average impact of large-R jet JMS and JMR systematic uncertainties on the total prediction of SM background in the muon channel. Whenever available, $\pm 1\sigma$ variations are shown as 1σ (-1σ)

Source of systematic uncertainty	Relative yield uncertainties [%]
track to calo-jet uncertainty	5 (1)
20% mass resolution smearing	3

5.7.3 $t\bar{t}$ and W-boson+jets normalisation uncertainties

Figure 5.27 show the impact of the systematic uncertainties due to the W+jets and $t\bar{t}$ normalisation. Bin by bin, this symmetric uncertainty is within 10% and 15%. This is a flat uncertainty on the W+jets and $t\bar{t}$ yield predictions. Hence fluctuations are due only to changes in the relative W+jets and $t\bar{t}$ predictions. The W+jets theoretical uncertainty estimated from Berends-Giele scaling [176, 177] for a similar topology [178] yields 34%. Hence, the estimation from data used in this analysis results in a reduction of this uncertainty. On the other hand, the $t\bar{t}$ normalisation from data yields a conservative uncertainty estimation, compared with the 5.9% quoted in Ref. [178]. This, as current measurements do not explore the residual $t\bar{t}$ background produced by the large jet p_{T} and central jet veto requirements. The extrapolation uncertainty, from the CRs to the SR, is evaluated by examining the effect that changes on event selection have on the measured correction factors. No significant change is observed, therefore, no extra uncertainty is added.

5.7.4 W+jets modelling

Polynomial functions of several orders are fitted. In an event by event basis the weight is therefore calculated as $e^{\mathrm{pol}_i(Wp_{\mathrm{T}})}$, hence is positively defined for any value of Wp_{T}. Here, pol_i denotes a polynomial function of order i. Figure 5.28 shows the various fittings. Here, the nominal weight, given by the mean of the various fittings, is shown in red. For any value of Wp_{T} a systematic up (down) variation is given by the nominal weight plus the largest positive (negative) difference between any of the fitted functional forms and the nominal. These differences are shown in the bottom panel of this figure. The extrapolation uncertainty, from the CRs to the SR, is evaluated by examining the effect that changes on event selection have on the measured weights. No significant change is observed, therefore, no extra uncertainty is added.

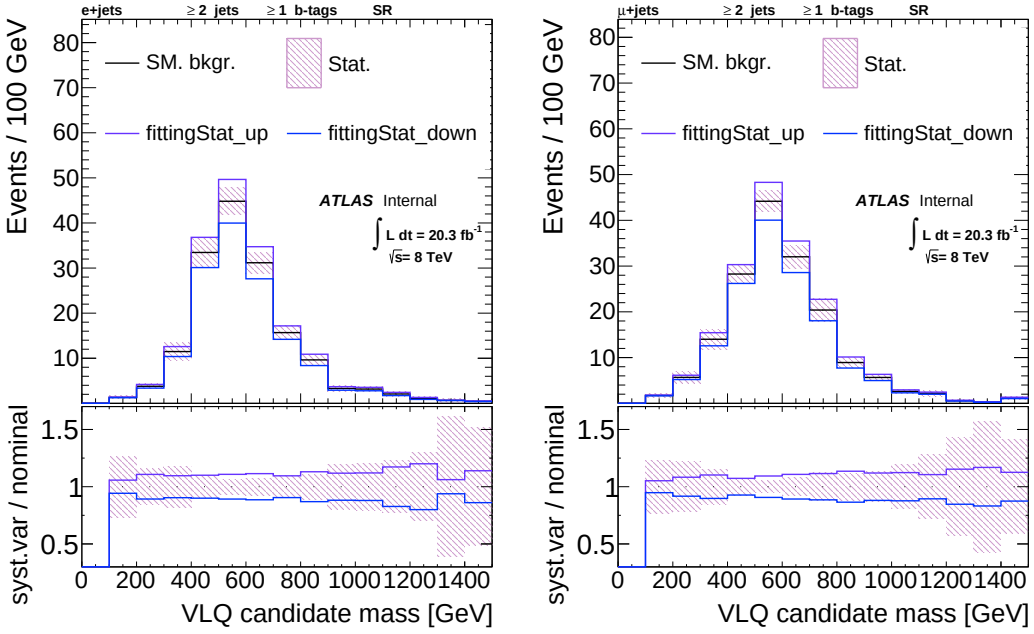

(a) (b)

Figure 5.27: Comparison between the nominal SM background prediction and systematic variations due to the W+jets and $t\bar{t}$ normalisation. This is shown for the electron (left) and muon (right) channels.

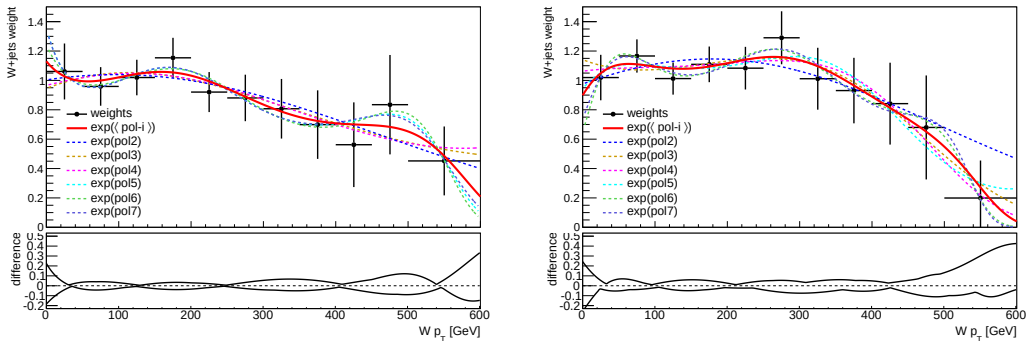

(a) e+jets channel (b) μ+jets channel

Figure 5.28: Nominal (red) Wp_{T} reweighting factors and their up/down systematic variations (bottom panel).

5.7.5 Signal acceptance uncertainties

Tables 5.13 and 5.14 show the impact of the systematic uncertainties on the signal acceptance for a VLQ mass of 700 GeV, and tables 5.15 and 5.16 for a mass of 900 GeV. Here, there largest uncertainty results from the b-tagging scale factors, which is dominated by the high-p_{T} scale factor extrapolation component.

Table 5.13: Average impact of systematic uncertainties on the signal acceptance in the electron channel. for a VLQ mass of 700 GeV. Whenever available, $\pm 1\sigma$ variations are shown as 1σ (-1σ)

Source of systematic uncertainty	Raw relative yield uncertainties [%]
b-tagging	8 (8)
large-R jet energy scale	7 (8)
large-R jet mass scale and resolution	4 (4)
small-R jet energy scale	2 (1)
luminosity	3 (3)
lepton identification and reconstruction	3 (3)
small-R jet energy resolution	4
small-R jet reconstruction efficiency	< 1
small-R jet vertex fraction	< 1
$E_{\mathrm{T}}^{\mathrm{miss}}$	< 1

Table 5.14: Average impact of systematic uncertainties on the signal acceptance in the muon channel, for a VLQ mass of 700 GeV. Whenever available, $\pm 1\sigma$ variations are shown as 1σ (-1σ)

Source of systematic uncertainty	Raw relative yield uncertainties [%]
b-tagging	8 (8)
large-R jet energy scale	6 (9)
large-R jet mass scale and resolution	5 (5)
small-R jet energy scale	4 (3)
luminosity	3 (3)
lepton identification and reconstruction	2 (2)
small-R jet energy resolution	< 1
small-R jet reconstruction efficiency	< 1
small-R jet vertex fraction	< 1
$E_{\mathrm{T}}^{\mathrm{miss}}$	< 1

Figure 5.29 shows the kinematics of the 2$^{\mathrm{nd}}$ b-jet (see Figure 5.1) for a signal sample with a mass of 700 GeV. Here, truth-level particle jets are geometrically matched ($\Delta R < 0.3$) to b-hadrons in order to find the particle jet associated to the b-hadron from gluon splitting. The p_{T} of the 2$^{\mathrm{nd}}$ b-jet is shown for events

Table 5.15: Average impact of systematic uncertainties on the signal acceptance in the electron channel. for a VLQ mass of 900 GeV. Whenever available, $\pm 1\sigma$ variations are shown as 1σ (-1σ)

Source of systematic uncertainty	Raw relative yield uncertainties [%]
b-tagging	10 (10)
large-R jet energy scale	2 (4)
large-R jet mass scale and resolution	3 (3)
small-R jet energy scale	4 (3)
luminosity	3 (3)
lepton identification and reconstruction	3 (3)
small-R jet energy resolution	< 1
small-R jet reconstruction efficiency	< 1
small-R jet vertex fraction	< 1
$E_{\mathrm{T}}^{\mathrm{miss}}$	< 1

Table 5.16: Average impact of systematic uncertainties on the signal acceptance in the muon channel, for a VLQ mass of 900 GeV. Whenever available, $\pm 1\sigma$ variations are shown as 1σ (-1σ)

Source of systematic uncertainty	Raw relative yield uncertainties [%]
b-tagging	9 (9)
large-R jet energy scale	4 (4)
large-R jet mass scale and resolution	3 (3)
small-R jet energy scale	1 (2)
luminosity	3 (3)
lepton identification and reconstruction	2 (2)
small-R jet energy resolution	< 1
small-R jet reconstruction efficiency	< 1
small-R jet vertex fraction	< 1
$E_{\mathrm{T}}^{\mathrm{miss}}$	< 1

passing the event selection, but before applying the central jet veto. The $|\eta|$ of this jet is shown for events before applying the forward jet tag. The impact that the modelling of this jet has on the signal acceptance is examined by checking how often would it change the decision of these cuts. This is found to be a negligible effect. Its impact on other aspects of this analysis is negligible as an inclusive 1 b-tag requirement is used, and the reconstructed VLQ mass uses the leading b-tag jet, which for nearly all selected events comes from the $T \to Wb$ decay.

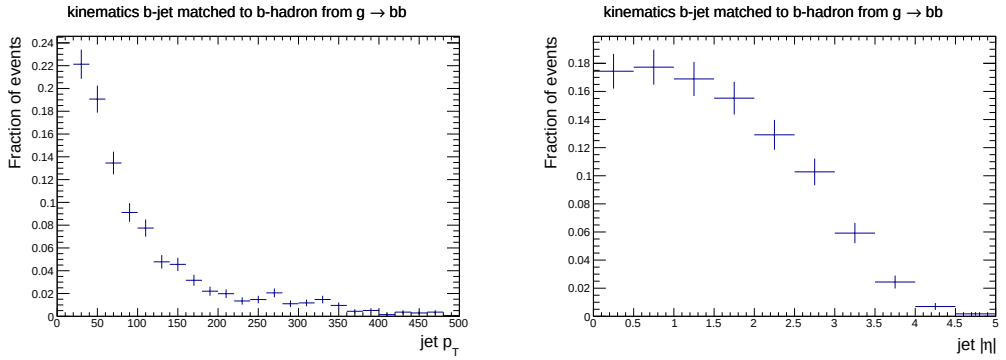

(a) 2nd b-jet p_{T} (b) 2nd b-jet $|\eta|$

Figure 5.29: Kinematics of the 2nd b-jet, showing the p_{T} for events passing the event selection up to C4 (left) and $|\eta|$ for events passing the event selection up to C5 (right).

5.8 Results

Figures 5.30 and 5.31 show the mass of the reconstructed VLQ mass for events passing the event selection, for the electron and muon channels respectively. These distributions are the input for the statistical analysis that is described in this section. Here, the SM background expectation and the observation agree within uncertainties. The ratio panels of this figure show the $(\mathrm{S}+\mathrm{B})/\mathrm{B}$ ratio for two signal samples, with masses of 700 and 900 GeV. Table 5.17 shows the expected and observed event yields in the SR. Here, the total number of SM background expected events agree with the data within uncertainties. Given that no significant deviation from the SM is observed, limits on the production of VLQs and on their coupling are presented in this section.

The statistical analysis is performed using the `HistFitter` [179, 180] package. This package uses the `HistFactory` tool [181] to build parametrised probability density functions (pdfs) in the `RooFit` [182]/`RooStats` [183] framework. These pdfs are used to construct a binned likelihood function $\mathcal{L}(\mu, \theta)$, where μ represents the signal strength on the signal plus background hypothesis $\mu\mathrm{S}+\mathrm{B}$, and θ corresponds to a set of parameters where each systematic variation i is described by a nuisance parameter θ_i. Here, the $\mu = 0$ case is referred to as the background only hypothesis.

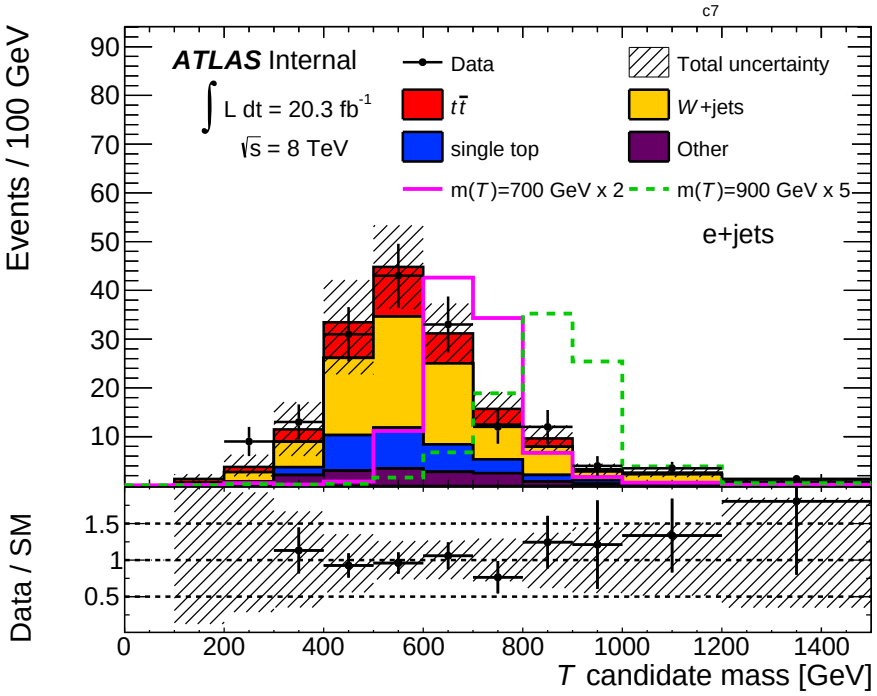

Figure 5.30: Distribution of the reconstructed VLQ candidate mass for the electron channel. The signal cross sections are for a unit coupling and for BR($T \to Wb$)=0.5. The systematic uncertainty band includes all the uncertainties listed in Section 5.7.

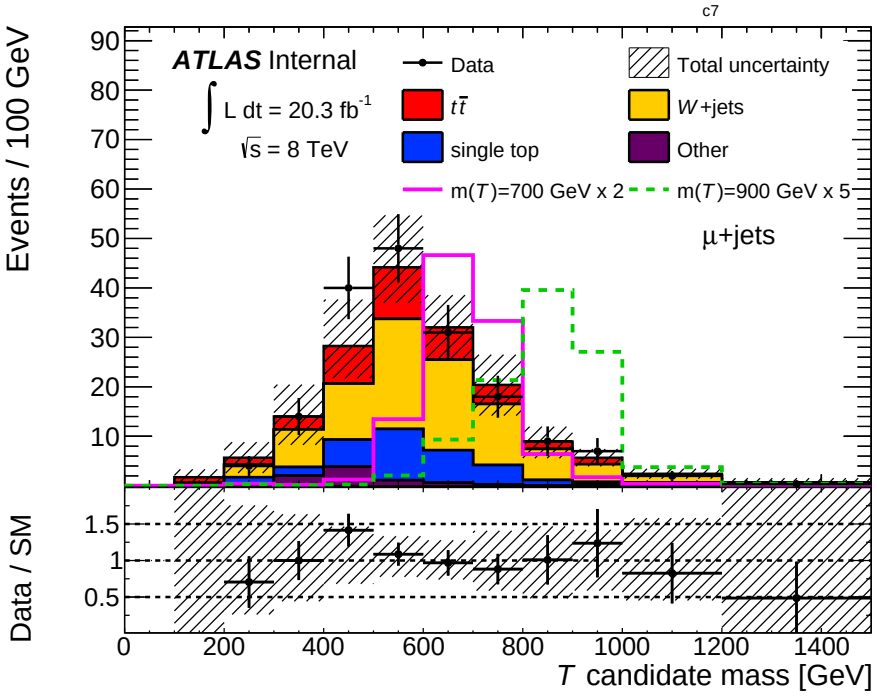

Figure 5.31: Distribution of the reconstructed VLQ candidate mass for the muon channel. The signal cross sections are for a unit coupling and for BR($T \to Wb$)=0.5. The systematic uncertainty band includes all the uncertainties listed in Section 5.7.

Table 5.17: Comparison between the expected and observed number of events in the SR, after applying the W+jets and $t\bar{t}$ normalisation correction factors, described in Section 5.6.2, and the Wp_{T} reweighting, described in Section 5.6.3. Uncertainties are presented as ± stat. for each individual background process and for data, and as ± stat.$^{+\text{syst.}}_{-\text{syst.}}$ for the total SM background prediction, allowing for asymmetric systematic variations. The systematic uncertainties correspond to those described in Section 5.7. The signal cross sections are for a unit EW coupling and for BR($T \to Wb$)=0.5.

	e+jets	μ+jets
$T \to Wb$, $m(T) = 700$ GeV	49 ± 2	49 ± 2
$T \to Wb$, $m(T) = 900$ GeV	20 ± 1	22 ± 1
W+jets	82 ± 5	89 ± 4
$t\bar{t}$	34 ± 2	37 ± 2
single top	29 ± 3	33 ± 3
Z+jets	6 ± 2	4 ± 1
diboson	3 ± 1	2 ± 1
multijets	8 ± 1	3 ± 1
total SM bkgr.	$162 \pm 6^{+40}_{-41}$	$168 \pm 6^{+59}_{-50}$
S/B, $m(T) = 700$ GeV	0.303	0.292
S/$\sqrt{\text{B}}$, $m(T) = 700$ GeV	3.850	3.780
data	168 ± 13	176 ± 13

5.8.1 Limits on VLQ production and coupling

Figure 5.32 shows the expected upper limit (95% CL) on the single VLQ production cross section times branching ratio versus the VLQ mass, for the combination of the electron and muon channels. See Table 5.18 for a list of the corresponding numerical values. Starting from masses above 900 GeV, the observed limit is weaker than the expected. This is understood in terms of the large statistical uncertainty on the data in that range.

The cross section for the single production of VLQs depends on the TWb coupling. Hence the results are also interpreted on the coupling versus mass plane. Following Ref. [37], the limit on the coupling $|\mathrm{c}_{\mathrm{L}}^{Wb}|$, in the context of CHMs, is simply extracted from the limit on the cross section using

$$|\mathrm{c}_{\mathrm{L}}^{Wb}| = \sqrt{\frac{\sigma_{\text{limit}}}{\sigma_{\text{theory}}}} \tag{5.5}$$

where the values of the theoretical cross sections are those from Table 2.1. Figure 5.33 shows the observed limit and excluded region, for BR($T \to Wb$) = 0.5. Here, for masses between 600 and 900 GeV, couplings above 0.6 to 0.8 are excluded, and for masses of up to 1 TeV, couplings above 1 are excluded.

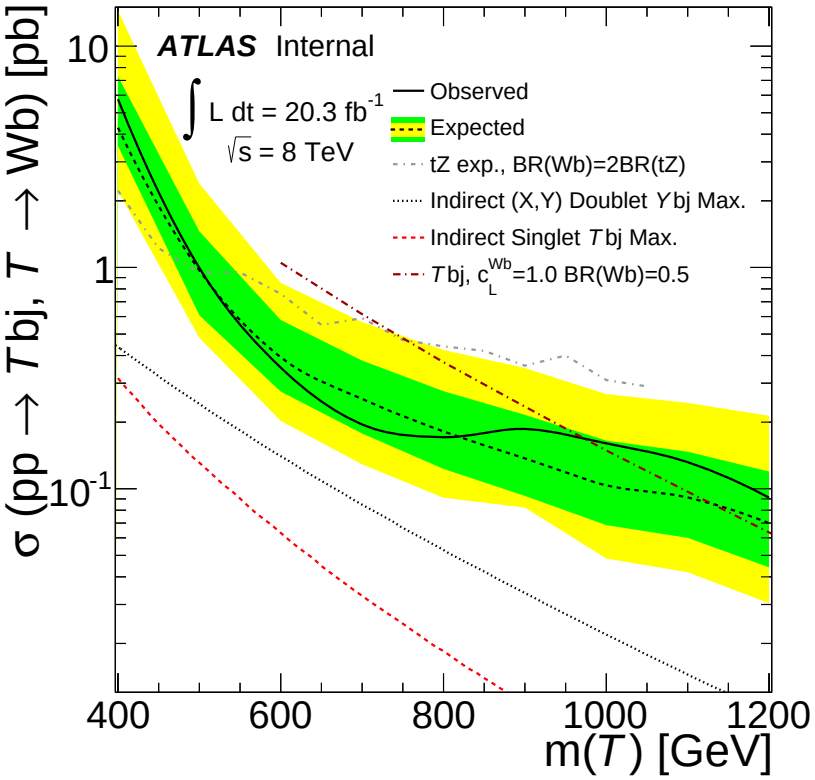

Figure 5.32: Observed and expected 95% CL upper limits on the single production cross section times branching ratio versus the VLQ mass. In addition, the observed limit from Ref. [172], and the theoretical expectations from Refs. [34, 37], are also shown.

Table 5.18: Cross section times branching ratio in pb for various VLQ masses. These values correspond to the observed and expected 95% CL upper limits.

Mass [GeV]	Observed	Expected				
		-2σ	-1σ	nominal	$+1\sigma$	$+2\sigma$
400	3.9	2.5	3.6	5.9	$1.1{\cdot}10^{1}$	$2.4{\cdot}10^{1}$
500	$9.9{\cdot}10^{-1}$	$5.4{\cdot}10^{-1}$	$7.8{\cdot}10^{-1}$	1.2	2.2	4.1
600	$4.7{\cdot}10^{-1}$	$2.2{\cdot}10^{-1}$	$3.0{\cdot}10^{-1}$	$4.4{\cdot}10^{-1}$	$6.7{\cdot}10^{-1}$	1.0
700	$2.4{\cdot}10^{-1}$	$1.5{\cdot}10^{-1}$	$2.1{\cdot}10^{-1}$	$3.0{\cdot}10^{-1}$	$4.6{\cdot}10^{-1}$	$7.0{\cdot}10^{-1}$
800	$2.0{\cdot}10^{-1}$	$1.0{\cdot}10^{-1}$	$1.5{\cdot}10^{-1}$	$2.1{\cdot}10^{-1}$	$3.3{\cdot}10^{-1}$	$5.2{\cdot}10^{-1}$
900	$1.9{\cdot}10^{-1}$	$6.9{\cdot}10^{-2}$	$9.7{\cdot}10^{-2}$	$1.4{\cdot}10^{-1}$	$2.3{\cdot}10^{-1}$	$3.6{\cdot}10^{-1}$
1000	$1.7{\cdot}10^{-1}$	$5.4{\cdot}10^{-2}$	$7.7{\cdot}10^{-2}$	$1.2{\cdot}10^{-1}$	$1.9{\cdot}10^{-1}$	$3.1{\cdot}10^{-1}$
1100	$1.9{\cdot}10^{-1}$	$5.0{\cdot}10^{-2}$	$7.0{\cdot}10^{-2}$	$1.1{\cdot}10^{-1}$	$1.7{\cdot}10^{-1}$	$2.9{\cdot}10^{-1}$
1200	$2.3{\cdot}10^{-1}$	$4.4{\cdot}10^{-2}$	$6.4{\cdot}10^{-2}$	$9.9{\cdot}10^{-2}$	$1.7{\cdot}10^{-1}$	$2.9{\cdot}10^{-1}$

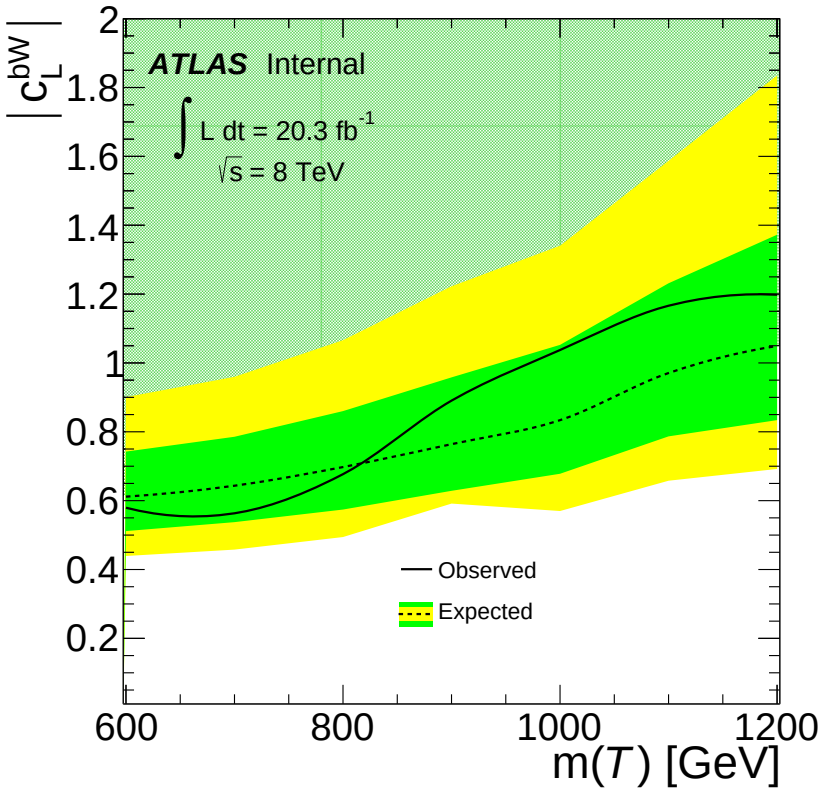

Figure 5.33: Observed and expected 95% CL upper limits on the coupling of the VLQ to SM W-boson and b-quark. The excluded region is given by the filled area.

Following Ref. [34], limits can be set on the strength of the mixing of the VLQ with the SM, denoted as $\sin\theta_{\mathrm{L}}$, in the context of a minimum renormalisable extension of the SM, including VLQs. Figure 5.34 shows the parametrisation of the mixing and the branching ratio in terms of the VLQ mass, for a singlet vector-like T. Here, the branching ratios are shown for $\sin\theta_{\mathrm{L}} = 0.1$, but in general they are given as a function of the mass and the mixing, following formulae that are thoroughly described in Ref. [34].

The limit on the cross section is interpreted as a limit on the mixing using

$$2 \times \sigma_{\mathrm{theory}} \times \sin^2\theta_{\mathrm{L}} \times BR(m(T), \sin\theta_{\mathrm{L}}) \tag{5.6}$$

here, all $\sin\theta_{\mathrm{L}}$ where this value is larger than the limit on the cross section times branching ratio are excluded. Figure 5.35 shows the expected limit and excluded region on the mixing versus mass plane. Here, for masses between 600 and 900 GeV, mixing in the range above 0.4 and 0.5 are excluded, and for masses of up to 1 TeV, mixing above 0.65 are excluded.

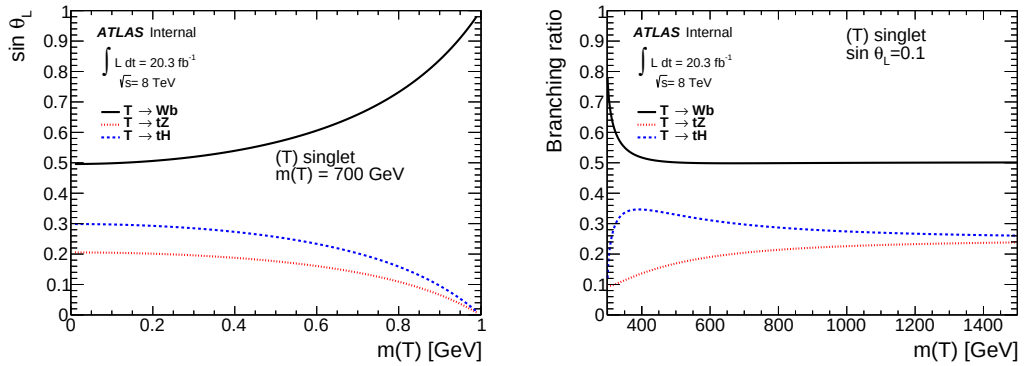

(a) (b)

Figure 5.34: Singlet vector-like T quark mixing (a) and branching ratios (b) as a function of its mass. Here, for $\sin\theta_{\mathrm{L}} = 0.1$ the branching ratio to Wb is mainly constant at a value of 0.5.

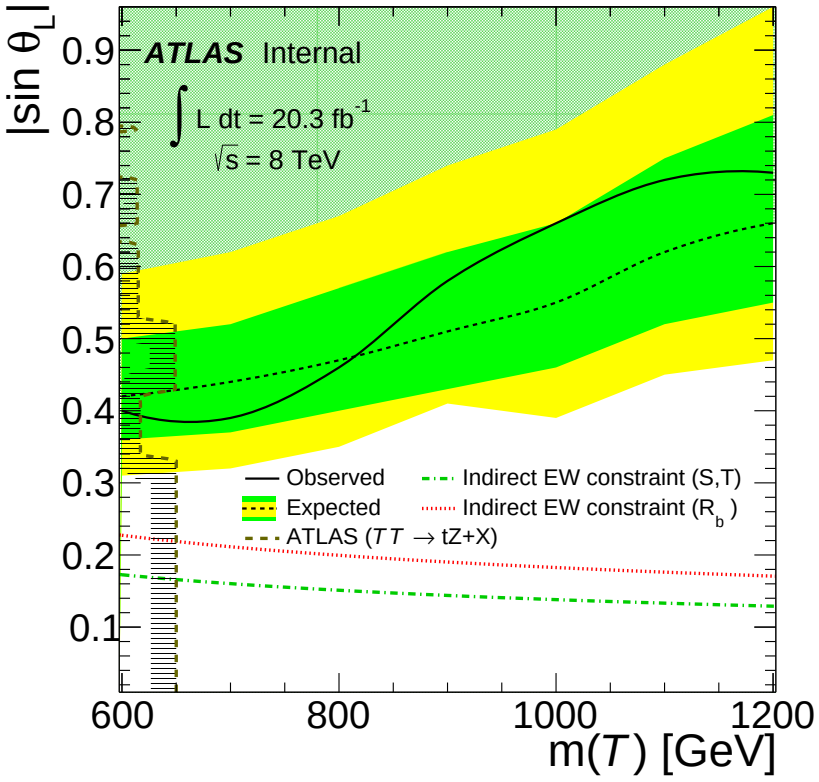

Figure 5.35: Observed and expected 95% CL upper limits on the mixing of a singlet vector-like T quark to the SM sector. The excluded region is given by the filled area. Here, in addition to the expected limits from the $T \to Wb$ channel, there observed limits from Ref. [172] are interpreted in this plane, and the indirect EW constraints from Ref. [34] are also shown.

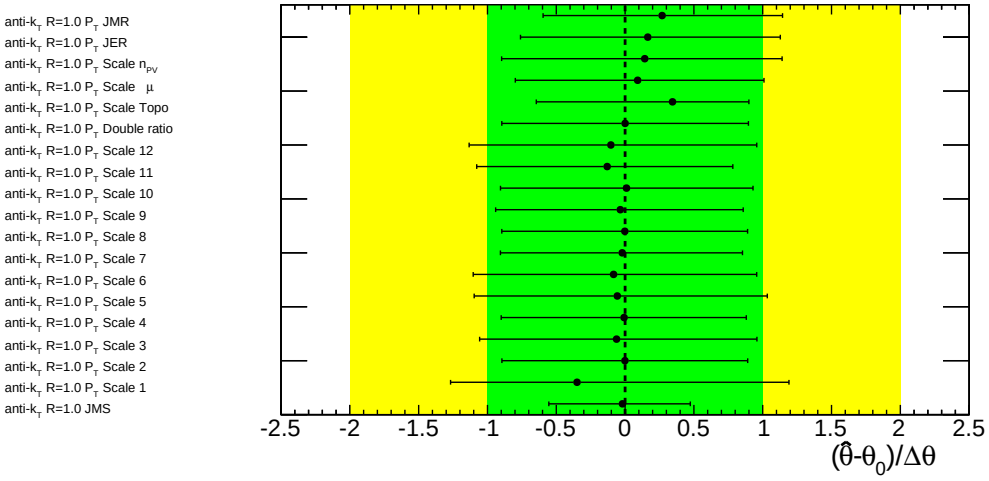

Figure 5.36: large-R jet uncertainties

5.8.2 Fit diagnostics

The sensitivity of the observed limits to the nuisance parameter fit is examined in two ways, namely, for each parameter:

- Constraint resulting from the fitting.
- Pre- and post-fit impact on the fitted signal strength.

Here, parameters being constrained beyond a reasonable expectation, based on the knowledge about the derivation of their corresponding systematic variations, and/or showing a dramatic change on their pre- post-fit relevance are understood as an indication that such parameters are driving the observed results.

Figure 5.36 shows the pulls and constraints for all nuisance parameters associated to large-R jet uncertainties. Figure 5.37 shows this for small-R jet uncertainties (a) and all the remaining ones (b). The post-fit constraint on a nuisance parameter is given by the change with respect to the default ± 1, corresponding to one standard deviation. The parameters with the largest pulls are those from the W+jets and $t\bar{t}$ shape uncertainties, labelled `W+jets shape` and $t\bar{t}$ `ALPGEN` respectively. This means that the data to SM background agreement improves if the latter is pulled towards these uncertainty variations. Overall, the nuisance parameter constraining is small. The largest constraints are observed for large-R jet mass scale and single top modelling uncertainties, labelled `anti-`k_t `R=1.0 JMS` and `single-top aMC@NLO` respectively. These uncertainties are, before fit, quite large, and understood as a conservative estimation. Therefore, the observed small constraints are a reasonable expectation.

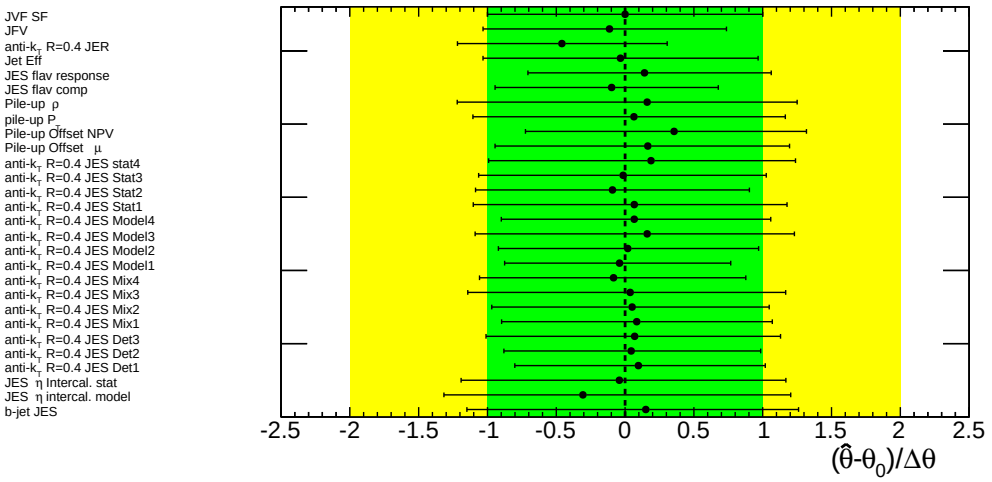

(a) small-R jet uncertainties

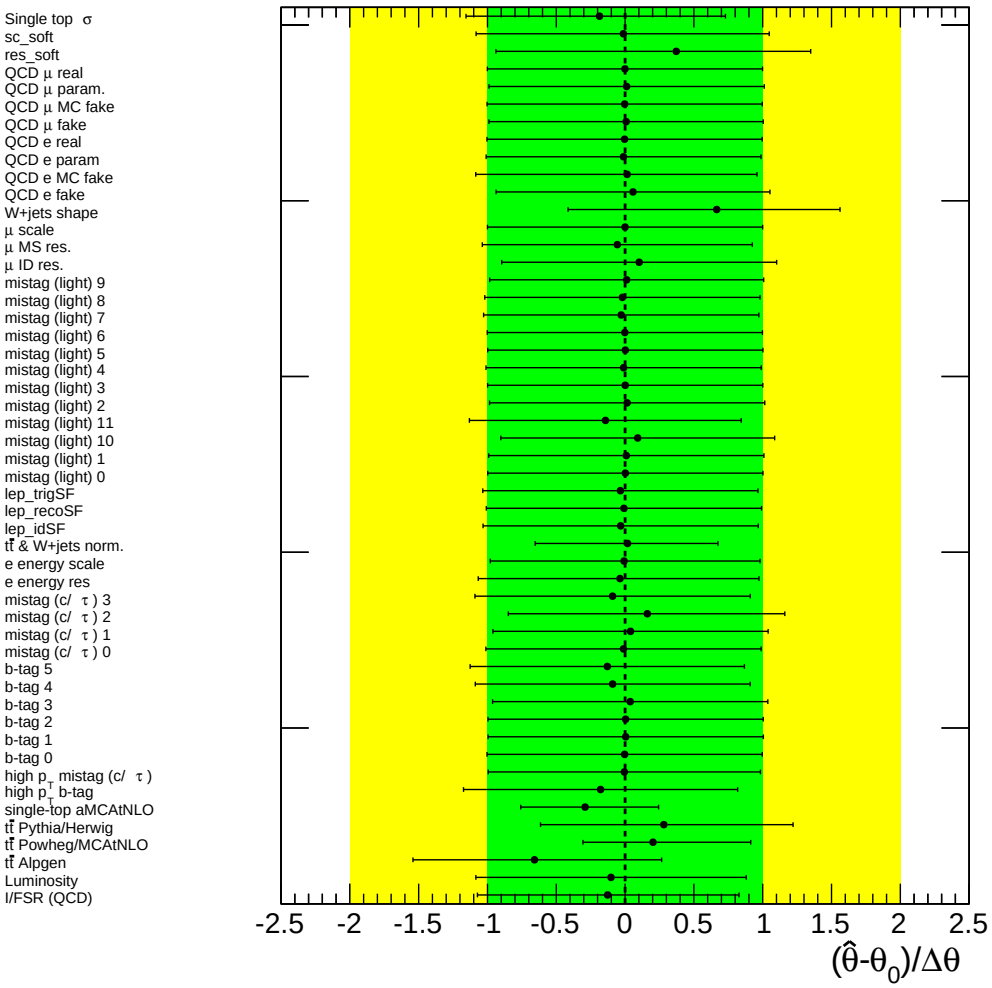

(b) others

Figure 5.37: Fitted nuisance parameters in the background-only hypothesis. The constraint is given as the difference to the pre-fit ±1 values.

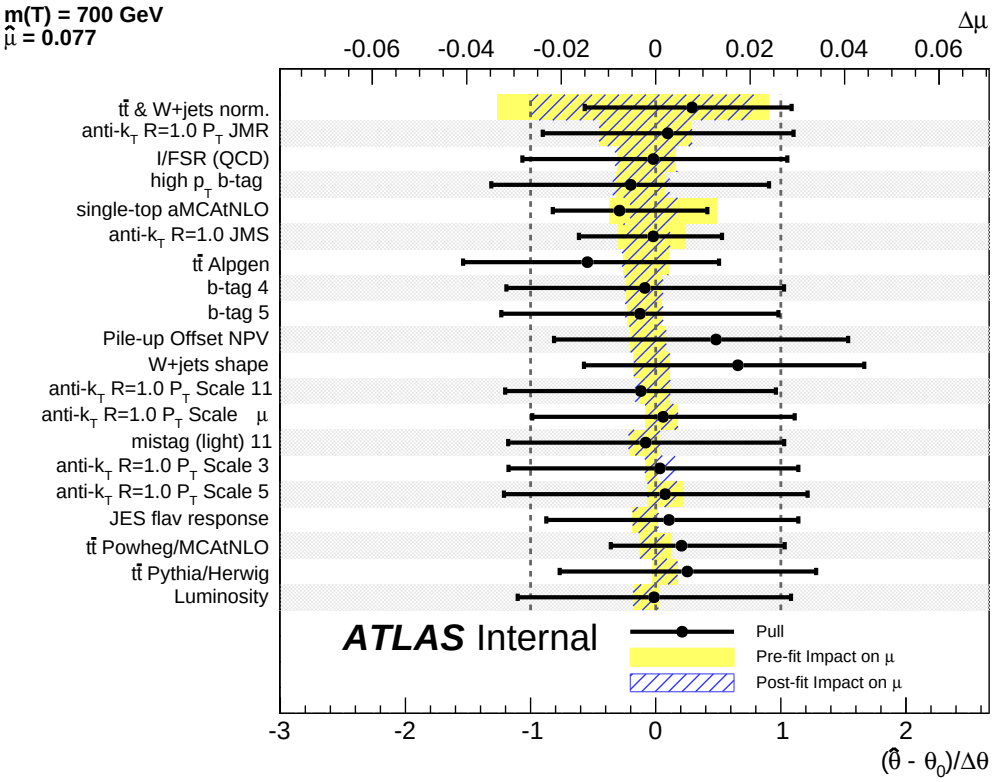

Figure 5.38: Top 20 of the nuisance parameters ordered from top to bottom according to their impact on the median signal strength. Pre-fit (post-fit) impact is shown as the yellow (dashed-blue).

Figures 5.38, 5.39 and 5.40 show a ranking of the nuisance parameters according to their absolute post-fit effect on the median signal strength $\hat{\mu}$, for the 700 GeV, 900 GeV and 1 TeV mass points. This is the most interesting range, as masses under it are already excluded by previous studies, and the observed limits weakens above it. This ranking is performed by re-running the fitting and fixing each nuisance parameter to the fitted $+1\sigma$ and -1σ values, and taking the maximum difference of the fitted signal strength[2]. No dramatic change on the pre- post-fit impact is observed. For $m(T) = 700$ GeV, the top ranked nuisance parameters are those corresponding to the $t\bar{t}$ and W+jets normalisation and the large-R jet mass resolution uncertainties, with an impact of about 30% and 10% respectively. For $m(T) = 900$ GeV, the large-R jet energy scale topology uncertainty is ranked highest, with an impact of about 15%. For $m(T) = 1$ TeV, at the top of the rank are the $t\bar{t}$ and W+jets normalisation and the large-R jet energy scale topology uncertainties, with an impact below 10%.

[2]Code was provided by the W,Z+$t\bar{t}$ measurement analysis team. See `https://cds.cern.ch/record/1698058` for further details.

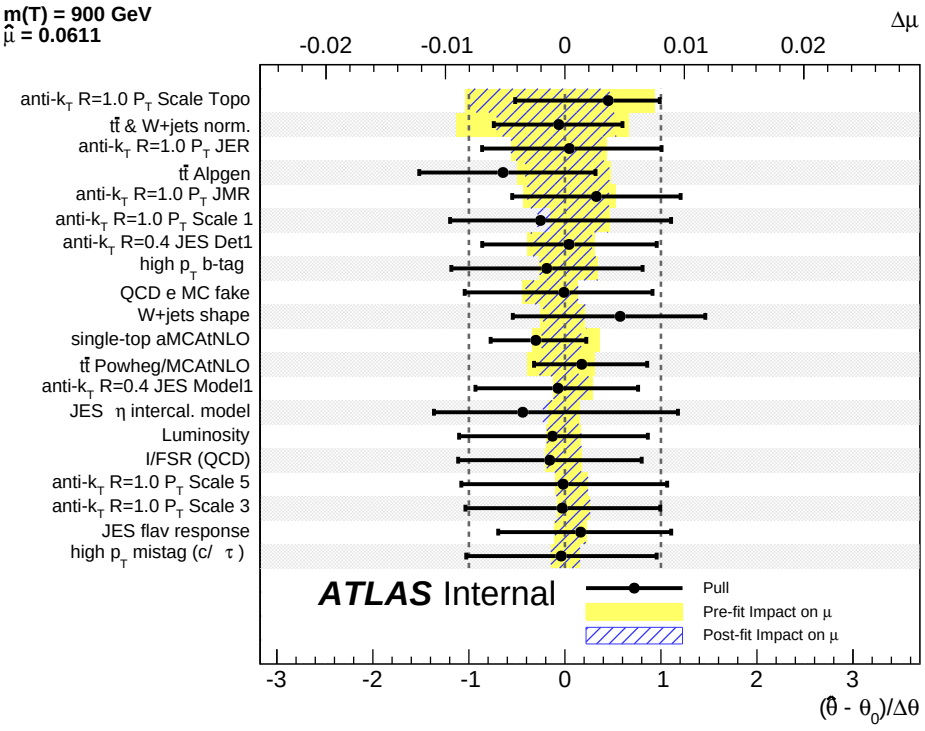

Figure 5.39: Top 20 of the nuisance parameters ordered from top to bottom according to their impact on the median signal strength. Pre-fit (post-fit) impact is shown as the yellow (dashed-blue).

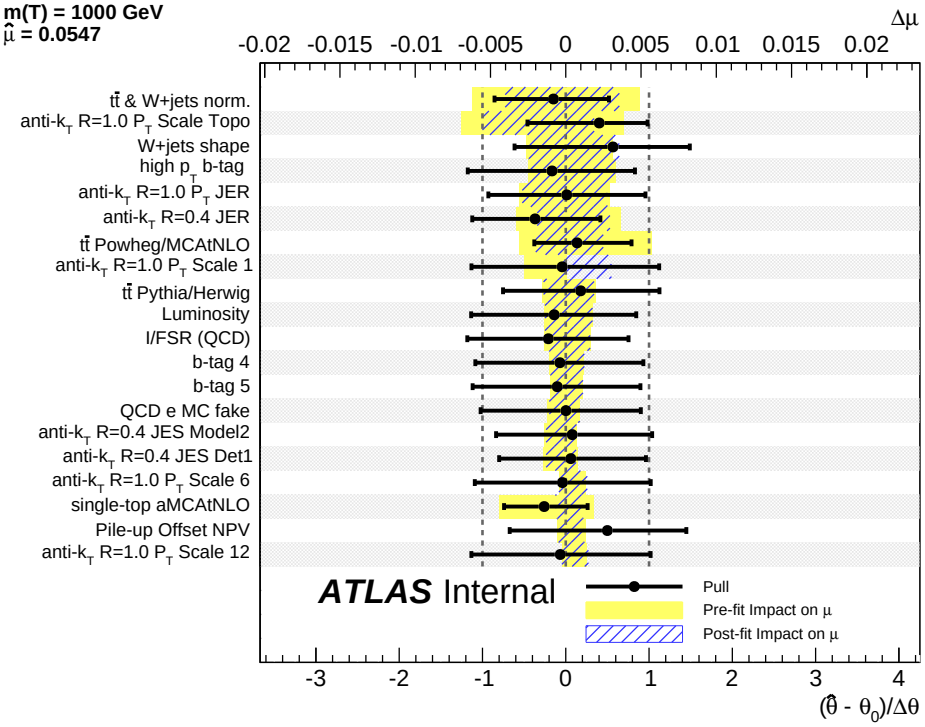

Figure 5.40: Top 20 of the nuisance parameters ordered from top to bottom according to their impact on the median signal strength. Pre-fit (post-fit) impact is shown as the yellow (dashed-blue).

5.9 Summary

A dedicated search for single production of heavy vector-like T quarks decaying to Wb, with a subsequent W-boson semileptonic decay, has been presented using 8 TeV data collected with the ATLAS detector.

Events with exactly one lepton, electron or muon, large $E_{\mathrm{T}}^{\mathrm{miss}}$ and one isolated b-tagged jet are selected. The lepton and jet are required to be back-to-back in ϕ. A vector-like T candidate decaying into Wb is reconstructed from the sum of the four-vectors of these objects.

The distribution of the reconstructed VLQ candidate mass was analysed in a nuisance parameter fit. No significant deviation from the SM expectation was observed and limits were set on the $T \to Wb$ cross-section times branching ratio and on the coupling of the VLQ to Wb.

The limits obtained in this search excluded vector-like quark masses beyond the reach of pair production searches, for suitably large VLQ weak couplings. The interpretation of the observed limits on the coupling (mixing) vs VLQ mass plane constitute the strongest limits on single production of vector-like T quarks decaying to Wb.

Chapter 6

Summary and outlook

Studies of a broad range of LHC Run1 large-R jets and jet-substructure physics applications have been presented, using data collected with the ATLAS detector. These studies contribute to the understanding of these tools, and to the consolidation of jet-substructure as a necessary item of the high energy physics toolkit. This work expands the frontiers of jet-substructure by developing new applications of basic observables and by examining the potential of new algorithms. In this thesis, large-R jet triggers are shown to perform better than standard jet triggers in the identification of events where the decay products of a heavy particle are collimated in a small region of the detector. Shower deconstruction, a novel jet-substructure algorithm, has been shown to surpass the top-tagging capabilities of the various techniques used during Run 1. Also, its observable, $\log(\chi_{\mathrm{SD}})$, is proven to be well modelled by the simulation, and to be robust against the choice of the jet-reconstruction algorithm. In addition, the reach of searches for VLQs has been extended by using the large-R jet mass, a simple observable, as a proxy for jet-isolation.

The single production of VLQs in the Wb final state has been presented for the first time in a dedicated search. The larger cross-sections, compared to pair production, have allowed for the extension of the current limits from 700 to 950 GeV, for a unit EW coupling, in the context of composite-Higgs models. The model-dependence of searches on this channel has been addressed by presenting the results in the coupling versus mass space, for two representative VLQ scenarios. This result contributes to the Run1 BSM searches as part of a SM that holds its current form all the way to the TeV scale.

For the LHC Run2, with higher centre-of-mass energy and larger cross-sections, the strategy established here for the search for single production of VLQs is expected to help in the search for new physics beyond the TeV scale. A

comprehensive future programme should extend this work by exploring other heavy-boson plus heavy-quark final states: Hb, Ht, Zt, Zb, Wt. This will allow for the exploration of BSM models with higher VLQ multiplicities. Due to the high-p_{T} injected by large VLQ masses on the decay products of these final states, and to their large BRs to hadrons, jet-substructure techniques will play a predominant role in such a physics programme. Its success will depend on a proper design and optimisation of strategies, for a maximal use of their potential, within the limitations of the ATLAS detector. Shower deconstruction as a top-quark-tagger, and potentially also as a heavy boson-tagger, shows the most promising performance for searches using hadronic final sates, where QCD processes are the main background.

Appendix A

Alternative analysis strategies

The analysis in Chapter 5 uses large-R jets in various ways: to separate signal from background, and to estimate the $t\bar{t}$ and W+jets normalisation. There are caveats associated with this, namely the large uncertainties associated with the modelling of the kinematics of these objects. In order to motivate their usage, the results from this analysis are compared to those of various scenarios that do not involve large-R jets. This appendix presents various distributions and tables with event yields for all the various cases studied.

A.1 Analysis strategies without large-R jets

Figure A.1 shows a signal to SM background shape comparison of the p_{T} of the leading b-tagged jet after event preselection. Here, the SM background peaks at 150 GeV, resulting from the b-tagged jet threshold. Additional softer b-jets are within the acceptance of the large-R criteria.

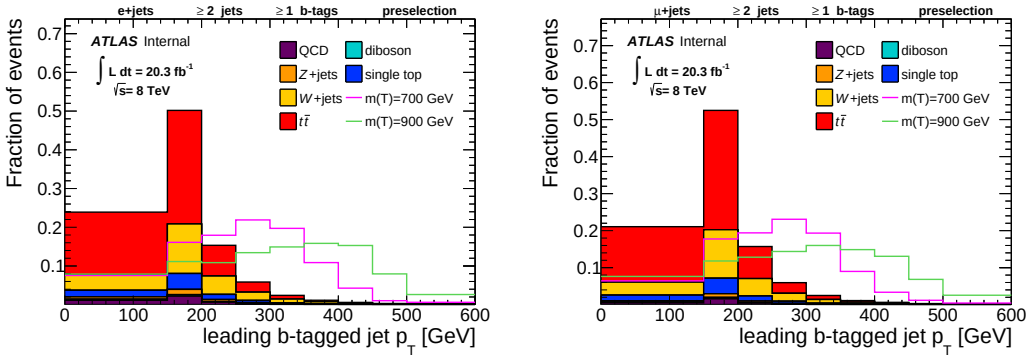

(a) e+jets channel

(b) μ+jets channel

Figure A.1: Signal to SM background shape comparison of the p_{T} of the leading b-tagged jet. This is shown for events passing the event preselection.

Case A:

This case follows the event selection described in Section 5.2. In order to avoid using large-R jets, C1, the cut on the large-R jet p_{T} is removed. Instead, the leading b-tagged jet p_{T} is required to be at least 150 GeV. C2, the cut on the large-R jet mass is also removed. C4, the central jet veto is modified, by counting the numbers of jets with $\Delta R > 1.4$ to the leading b-tagged jet, instead of to the large-R jet. C5 and C6 are used.

Figure A.2 shows the mass of the reconstructed VLQ for events passing the Case A event selection. The ratio panels of this figure show the $(\mathrm{S}+\mathrm{B})/\mathrm{B}$ ratio for two signal samples, with masses of 700 and 900 GeV. Table A.1 shows the expected and observed event yields.

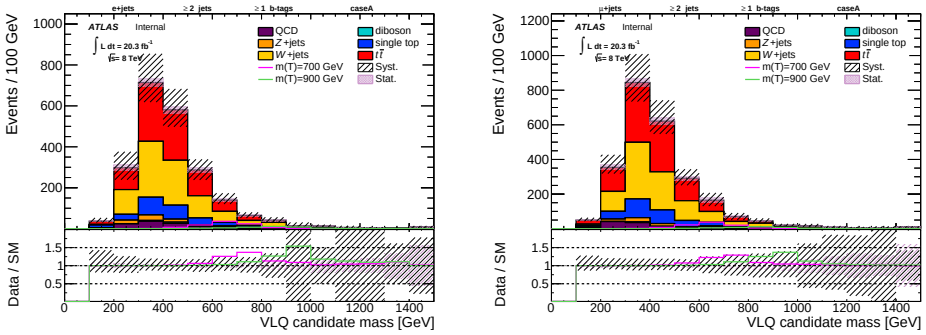

(a) Case A: e+jets channel (b) Case A: μ+jets channel

Figure A.2: Distribution of the reconstructed VLQ candidate mass. The signal cross sections are for a unit EW coupling and for BR($T \to Wb$)=0.5.

Table A.1: Expected event yield for Case A. Uncertainties are presented as ± stat. for each individual background process, and as ± stat.$^{+\mathrm{syst.}}_{-\mathrm{syst.}}$ for the total SM background prediction, allowing for asymmetric systematic variations. The signal cross sections are for a unit EW coupling and for BR($T \to Wb$)=0.5.

	e+jets	μ+jets
$T \to Wb$, $m(T) = 700$ GeV	94 ± 3	95 ± 3
$T \to Wb$, $m(T) = 900$ GeV	37 ± 1	38 ± 1
W+jets	850 ± 31	943 ± 33
$t\bar{t}$	885 ± 9	1053 ± 10
single top	264 ± 9	318 ± 9
Z+jets	79 ± 7	66 ± 6
diboson	16 ± 2	14 ± 2
multijets	115 ± 3	112 ± 14
total SM bkgr.	$2210 \pm 34^{+381}_{-494}$	$2505 \pm 39^{+376}_{-546}$
S/B, $m(T) = 700$ GeV	0.04	0.04
$\mathrm{S}/\sqrt{\mathrm{B}}$, $m(T) = 700$ GeV	2.00	1.90

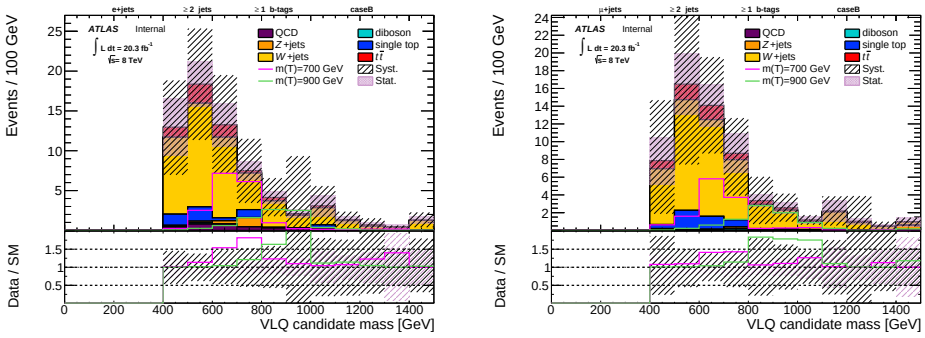

(a) Case B: e+jets channel (b) Case B: μ+jets channel

Figure A.3: Distribution of the reconstructed VLQ candidate mass. The signal cross sections are for a unit EW coupling and for BR($T \to Wb$)=0.5.

Case B:

This case is an implementation of the strategy presented in Ref. [184]. Here, instead of large-R jets, the expected high p_{T} of the b-tagged jet is used, in addition to a forward jet tag and a large cut in H_{T}, given by the sum of the lepton, b-tagged jet, and forward jet transverse momentum. Also, this reference considers cuts on the mass of the b-tagged jet plus lepton, and the b-tagged jet plus forward jet systems. Additional cuts also include a maximum number of small-R jets (three).

Figure A.3 shows the mass of the reconstructed VLQ for events passing the Case B event selection. Table A.2 shows the expected and observed event yields in the signal region.

Table A.2: Expected event yield for Case B. Uncertainties are presented as ± stat. for each individual background process, and as ± stat.$^{+\text{syst.}}_{-\text{syst.}}$ for the total SM background prediction, allowing for asymmetric systematic variations. The signal cross sections are for a unit EW coupling and for BR($T \to Wb$)=0.5.

	e+jets	μ+jets
$T \to Wb$, $m(T) = 700$ GeV	18 ± 2	13 ± 1
$T \to Wb$, $m(T) = 900$ GeV	8 ± 1	8 ± 1
W+jets	47 ± 5	46 ± 6
$t\bar{t}$	7 ± 1	6 ± 1
single top	5 ± 1	6 ± 1
Z+jets	2 ± 1	1 ± 1
diboson	0 ± 0	0 ± 0
multijets	3 ± 0	0 ± 0
total SM bkgr.	$65 \pm 6^{+38}_{-38}$	$59 \pm 6^{+35}_{-35}$
S/B, $m(T) = 700$ GeV	0.27	0.22
S/$\sqrt{\mathrm{B}}$, $m(T) = 700$ GeV	2.20	1.65

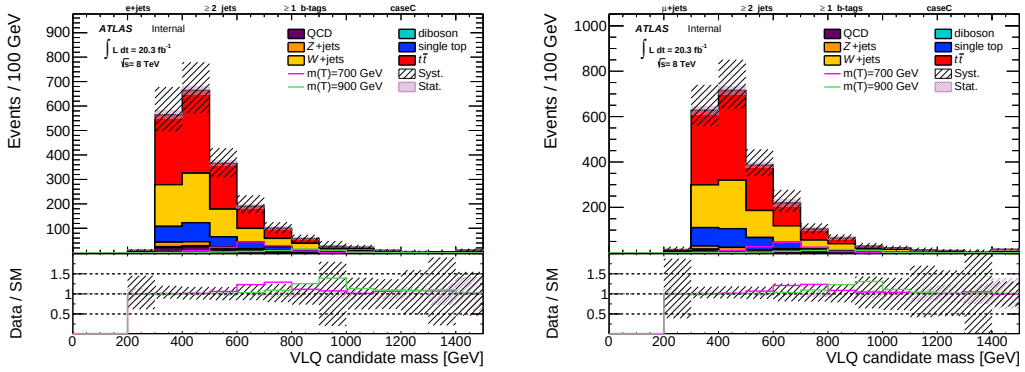

(a) Case C: e+jets channel (b) Case C: μ+jets channel

Figure A.4: Distribution of the reconstructed VLQ candidate mass. The signal cross sections are for a unit EW coupling and for BR($T \to Wb$)=0.5.

Case C:

This case uses a minimum set of cuts inspired on the differences observed between the signal and background event kinematics. Here, the leading b-tagged jet p_{T} is required to be at least 150 GeV. Also, the p_{T} of the reconstructed W-boson is required to be greater than 120 GeV. Finally, the azimuthal separation between the lepton and the b-tagged jet is required to be greater than 2.4.

Figure A.4 shows the mass of the reconstructed VLQ for events passing the Case C event selection. Table A.3 shows the expected and observed event yields in the signal region.

Table A.3: Expected event yield for Case C. Uncertainties are presented as ± stat. for each individual background process, and as ± stat.$^{+\text{syst.}}_{-\text{syst.}}$ for the total SM background prediction, allowing for asymmetric systematic variations. The signal cross sections are for a unit EW coupling and for BR($T \to Wb$)=0.5.

	e+jets	μ+jets
$T \to Wb$, $m(T) = 700$ GeV	116 ± 4	118 ± 4
$T \to Wb$, $m(T) = 900$ GeV	50 ± 2	49 ± 2
W+jets	640 ± 25	718 ± 27
$t\bar{t}$	995 ± 9	1138 ± 10
single top	244 ± 9	280 ± 10
Z+jets	59 ± 6	45 ± 5
diboson	17 ± 2	16 ± 2
multijets	78 ± 2	36 ± 13
total SM bkgr.	$2033 \pm 29^{+333}_{-427}$	$2231 \pm 33^{+330}_{-478}$
S/B, $m(T) = 700$ GeV	0.06	0.05
S/$\sqrt{\mathrm{B}}$, $m(T) = 700$ GeV	2.56	2.50

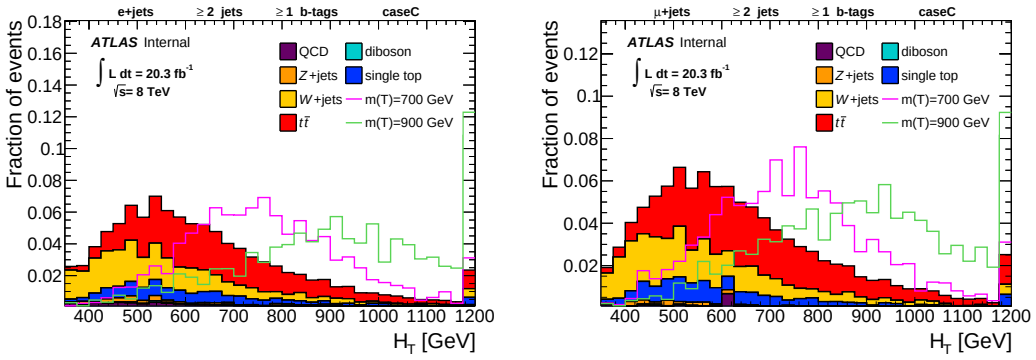

(a) Case C: e+jets channel (b) Case C: μ+jets channel

Figure A.5: Signal to SM background shape comparison of H_{T}. This is shown for events passing the Case C event selection.

Case D:

This case is an extension of Case C. Here, the most promising variables between the following list are used: H_{T}, given by the sum of the p_{T} of the selected jets, $E_{\mathrm{T}}^{\mathrm{miss}}$ and the p_{T} of the lepton; the mass of the b-tagged jet plus lepton system; the mass of the b-tagged jet plus forward jet system; the ΔR between the b-tagged jet and the jet closest to it; the number of nearby jets (within $\Delta R < 1$); the sum of the p_{T} of nearby jets; and the ratio between the leading b-tagged jet p_{T} and the leading b-tagged jet p_{T} plus the sum of the p_{T} of nearby jets.

The following figures show a signal to SM shape comparison for the most promising variables: Figure A.5 shows H_{T}, here a minimum of 650 GeV is required; Figure A.6 shows the mass of the b-tagged jet plus lepton system, here a minimum of 400 GeV is required; Figure A.7 shows the number of nearby jets, here events with one or more nearby jets are rejected; Figure A.8 shows the ratio between the leading b-tagged jet p_{T} and the leading b-tagged jet p_{T} plus the sum of the p_{T} of nearby jets, here only events where this value is greater than 0.8 are accepted.

Figure A.9 shows the mass of the reconstructed VLQ for events passing the Case D event selection. Table A.4 shows the expected and observed event yields in the signal region.

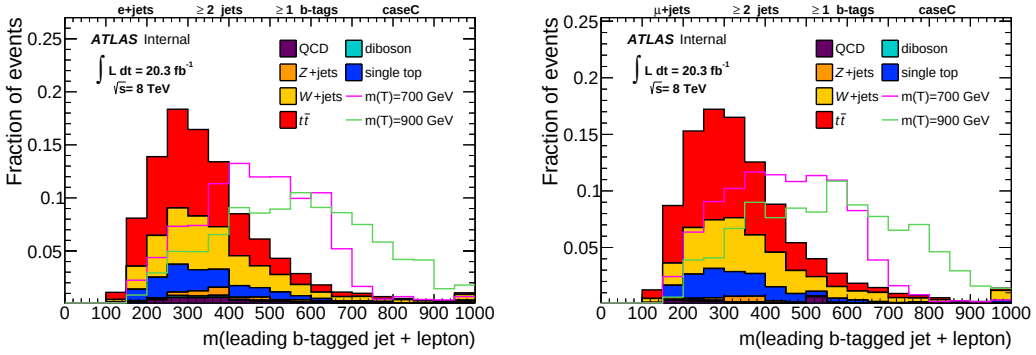

(a) Case C: e+jets channel (b) Case C: μ+jets channel

Figure A.6: Signal to SM background shape comparison of the mass of the b-tagged jet plus lepton system. This is shown for events passing the Case C event selection.

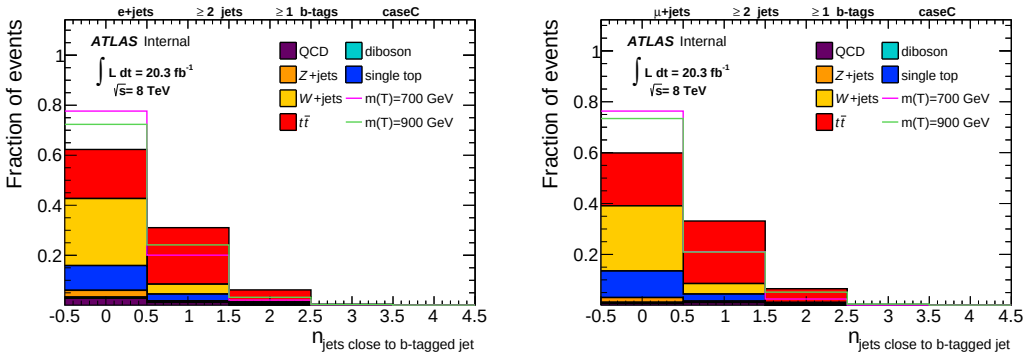

(a) Case C: e+jets channel (b) Case C: μ+jets channel

Figure A.7: Signal to SM background shape comparison of the number of nearby jets. This is shown for events passing the Case C event selection.

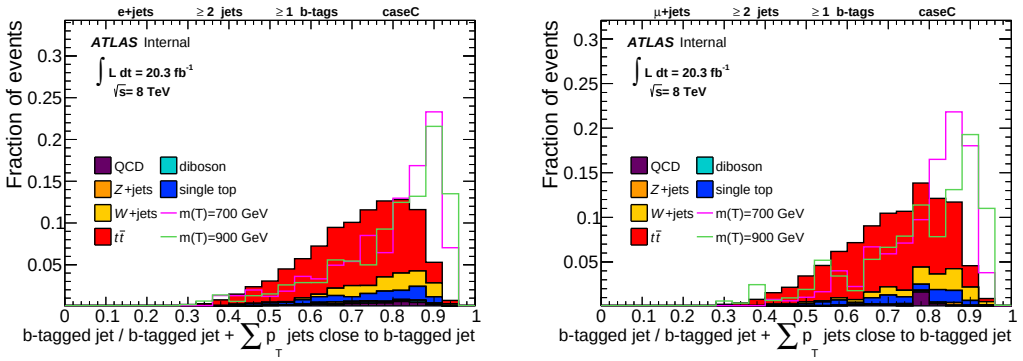

(a) Case C: e+jets channel (b) Case C: μ+jets channel

Figure A.8: Signal to SM background shape comparison of the ratio between the leading b-tagged jet p_{T} and the leading b-tagged jet p_{T} plus the sum of the p_{T} of nearby jets. This is shown for events passing the Case C event selection.

Table A.4: Expected event yield for Case D. Uncertainties are presented as ± stat. for each individual background process, and as ± stat.$^{+\text{syst.}}_{-\text{syst.}}$ for the total SM background prediction, allowing for asymmetric systematic variations. The signal cross sections are for a unit EW coupling and for BR($T \to Wb$)=0.5.

	e+jets	μ+jets
$T \to Wb$, $m(T) = 700$ GeV	48 ± 2	39 ± 2
$T \to Wb$, $m(T) = 900$ GeV	26 ± 1	25 ± 1
W+jets	74 ± 4	89 ± 6
$t\bar{t}$	51 ± 2	58 ± 2
single top	29 ± 3	32 ± 3
Z+jets	11 ± 2	4 ± 1
diboson	1 ± 1	3 ± 1
multijets	8 ± 1	0 ± 0
total SM bkgr.	$174 \pm 6^{+56}_{-63}$	$185 \pm 7^{+56}_{-68}$
S/B, $m(T) = 700$ GeV	0.28	0.21
S/$\sqrt{\text{B}}$, $m(T) = 700$ GeV	3.64	2.85

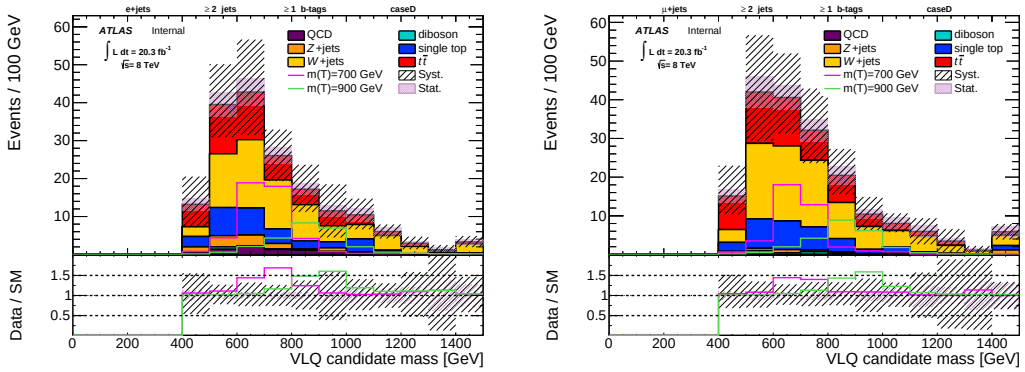

(a) Case D: e+jets channel (b) Case D: μ+jets channel

Figure A.9: Distribution of the reconstructed VLQ candidate mass. The signal cross sections are for a unit EW coupling and for BR($T \to Wb$)=0.5.

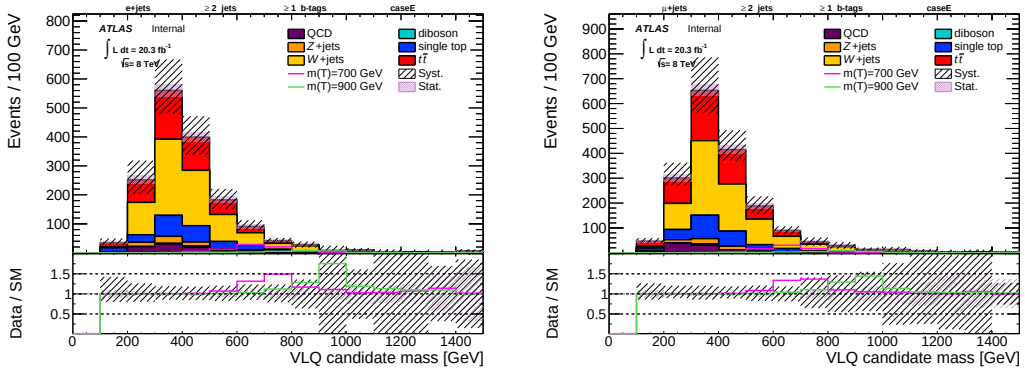

(a) Case E: e+jets channel (b) Case E: μ+jets channel

Figure A.10: Distribution of the reconstructed VLQ candidate mass. The signal cross sections are for a unit EW coupling and for BR($T \to Wb$)=0.5.

Case E:

This case is an extension of Case A, with the addition that isolated b-tagged jets are obtained by cutting on two of the variables from case D. Namely the number of nearby jets, by requiring exactly zero nearby jets, and the ratio between the leading b-tagged jet p_{T} and the leading b-tagged jet p_{T} plus the sum of the p_{T} of nearby jets, by cutting on 0.8.

Figure A.10 shows the mass of the reconstructed VLQ for events passing the Case E event selection. Table A.5 shows the expected and observed event yields in the signal region.

Table A.5: Expected event yield for Case E. Uncertainties are presented as ± stat. for each individual background process, and as ± stat.$^{+\text{syst.}}_{-\text{syst.}}$ for the total SM background prediction, allowing for asymmetric systematic variations. The signal cross sections are for a unit EW coupling and for BR($T \to Wb$)=0.5.

	e+jets	μ+jets
$T \to Wb$, $m(T) = 700$ GeV	75 ± 3	74 ± 3
$T \to Wb$, $m(T) = 900$ GeV	27 ± 1	28 ± 1
W+jets	764 ± 30	832 ± 31
$t\bar{t}$	467 ± 7	562 ± 7
single top	221 ± 8	259 ± 8
Z+jets	70 ± 6	60 ± 6
diboson	9 ± 2	10 ± 2
multijets	92 ± 3	89 ± 7
total SM bkgr.	$1623 \pm 32^{+304}_{-380}$	$1811 \pm 34^{+291}_{-411}$
S/B, $m(T) = 700$ GeV	0.05	0.04
S/$\sqrt{\text{B}}$, $m(T) = 700$ GeV	1.86	1.74

A.2 Summary

Table A.6 shows the expected limit for the various cases described, and the percent variation with respect to the nominal event selection. Here, in all cases, the expected limit deteriorates. The most promising results are observed for cases E+ and E++. In both cases, the expected result degrades by less than 10% for the 700 GeV mass point, but by more than 20% for 900 GeV. Therefore, none of the alternative strategies studied here can improve on the results obtained through the strategy used in Chapter 5.

Table A.6: Expected limit on the cross section times branching ratio in pb for VLQ masses of 700 and 900 GeV for various alternative event selections that do not involve using large-R jets. The percent variations shown are with respect to the nominal event selection, that yields an expected limit of 0.0897 (0.0465) for a VLQ mass of 700 (900) GeV. The + (++) symbol indicates that the minimum leading b-tagged jet p_{T} has been raised from 150 to 200 (250) GeV. All systematic uncertainties are included.

Case	$m(T) = 700$ GeV	$m(T) = 900$ GeV
A	0.1150 (+28.2%)	0.0618 (+32.9%)
A+	0.0975 (+ 8.8%)	0.0544 (+16.9%)
A++	0.0972 (+ 8.3%)	0.0514 (+10.5%)
B	0.2075 (+131.4%)	0.0856 (+84.1%)
C	0.1198 (+33.6%)	0.0620 (+33.3%)
C+	0.1038 (+15.7%)	0.0555 (+19.3%)
C++	0.1045 (+16.5%)	0.0552 (+18.7%)
D	0.1339 (+49.3%)	0.0648 (+39.3%)
D+	0.1312 (+46.3%)	0.0614 (+32.1%)
D++	0.1240 (+38.2%)	0.0615 (+32.2%)
E	0.1002 (+11.7%)	0.0662 (+42.4%)
E+	0.0930 (+ 3.7%)	0.0571 (+22.8%)
E++	0.0931 (+ 3.8%)	0.0495 (+ 26.4%)

Appendix B

Smoothing of systematic variations

Systematic variations involving a change in the selection or in the MC generator can suffer of large statistical fluctuations. This is the case for some of the uncertainties used in Chapter 5. To address this issue uncertainties that are not significant can be removed to prevent adding noise to the statistical analysis. Alternatively, smoothing algorithms can be used to mitigate statistical fluctuations. In this appendix, the fitting-based smoothing approach that is used in Chapter 5 is documented.

B.1 Fitting-based approach

For a given systematic variation on the SM background prediction, various polynomial functions are fitted to its ratio to the nominal. The polynomial functions with the smallest χ^2 per number of degrees of freedom is chosen. This procedure tends to select lower-order polynomials, as a degree of freedom is lost for every fitted parameter. The smoothed value of the systematic variation is given by the fitted polynomial form evaluated at each bin centre. In this approach the decision on whether or not to apply smoothing is evaluated in a case-by-case basis and for each channel separately. Only variations satisfying the following criteria are considered:

- a 50% increase on the ratio to nominal in any bin compared to its immediate neighbours (spike).
- at least one bin where the ratio to nominal is beyond the statistical uncertainty (apparent significance).

Table B.1 contains, for each channel, the list of the variations passing these criteria.

Table B.1: List of systematic variations for which smoothing is applied.

e+jets	
JER	flavor_response_down
flavor_comp_up	res_soft_up
JesEffectiveDet1_up	JesEffectiveDet1_down
jer	qcd_mm_el_fake_mc_up'
FatJMS_up	FatJPtS_Comp05_up
FatJPtS_Comp01_up	FatJPtS_Comp06_up
FatJPtS_Comp09_up	FatJPtS_Comp11_up
FatJPtS_Comp12_up	FatJPtS_Topo_up
FatJPtS_Topo_down	FatJPtS_mu_down
FatJPtS_nPV_down	Singletop_aMCAtNLO
PowhegPythiaVsMCAtNLO_up	PowhegPythiaVsMCAtNLO_down
PowhegPythiaVsAlpgenHerwig_up	PowhegPythiaVsAlpgenHerwig_down
μ+jets	
JER	JesEffectiveDet1_down
jer	JMR
FatJMS_down	FatJPtS_Comp01_up
FatJPtS_Topo_up	FatJPtS_Topo_down
Singletop_aMCAtNLO	PowhegPythiaVsMCAtNLO_up
PowhegPythiaVsMCAtNLO_down'	–

Figures B.1 to B.4 demonstrate the smoothing procedure, where the chosen polynomial order is shown with a continuous line, and is labelled in red text. In all cases this procedure addresses the spikes. Variations such as Singletop_aMCAtNLO (see Figure B.2 and Figure B.4), where a single bin shows a deviation from nominal beyond the statistical uncertainty, show a noticeable change for those particular bins. In variations such as FatJPtS_Topo_up (see Figure B.1 and Figure B.3) the trend is preserved while fluctuations are minimised.

This fitting-based approach is compared to an alternative based on the systematic to statistical ratio, used in Ref. [185]. Here, bins are merged according to whether the systematic to statistical uncertainty ratio is above certain threshold. Four different values are used. Due to the large MC statistical analysis, a fine tuning of this threshold is necessary to obtain reasonable results. Moreover, the ideal threshold is not necessarily the same among uncertainties or channels.

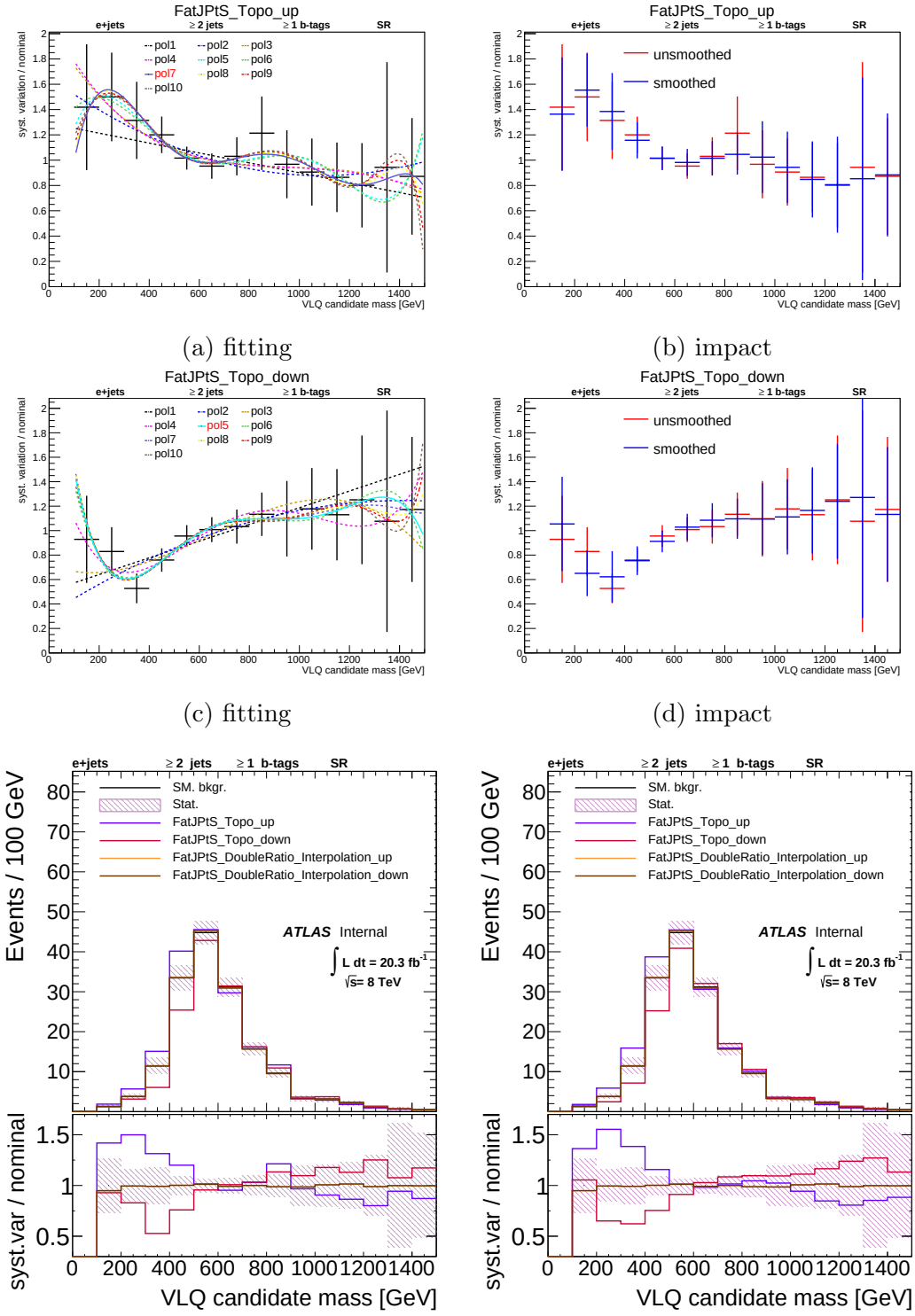

(a) fitting (b) impact

(c) fitting (d) impact

(e) before (f) after

Figure B.1: Demonstration of the smoothing through fitting procedure for the FatJPtS_Topo_up and FatJPtS_Topo_down variations. Top and centre: various fitted functions (left), where the continuous line and red label indicate the chosen polynomial form, and impact on the ratio to nominal (right). Bottom: comparison to nominal before (left) and after (right) smoothing. This is shown for events in the SR, for the electron channel.

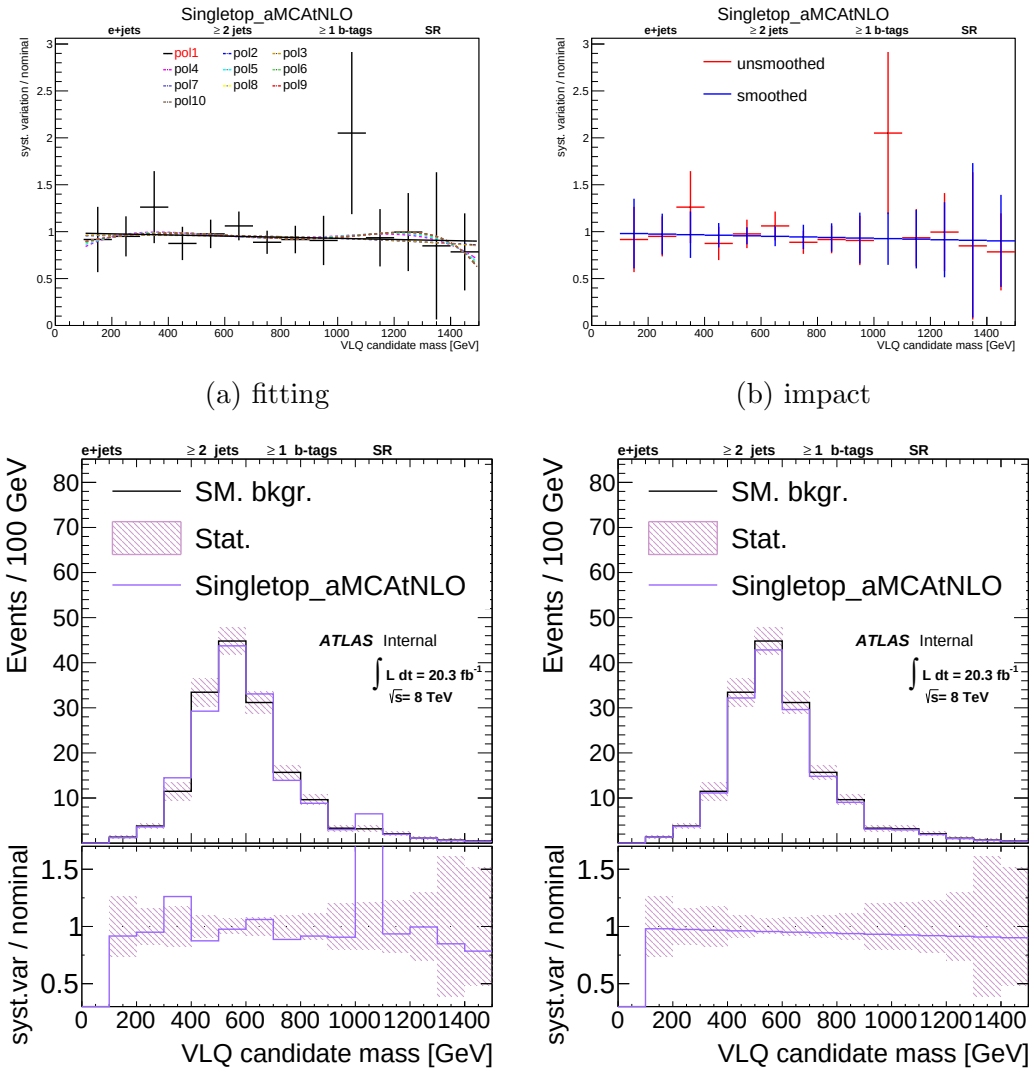

(a) fitting (b) impact

(c) before (d) after

Figure B.2: Demonstration of the smoothing through fitting procedure for the Singletop_aMCAtNLO variation. Top: various fitted functions (left), where the continuous line and red label indicate the chosen polynomial form, and impact on the ratio to nominal (right). Bottom: comparison to nominal before (left) and after (right) smoothing. This is shown for events in the SR, for the electron channel.

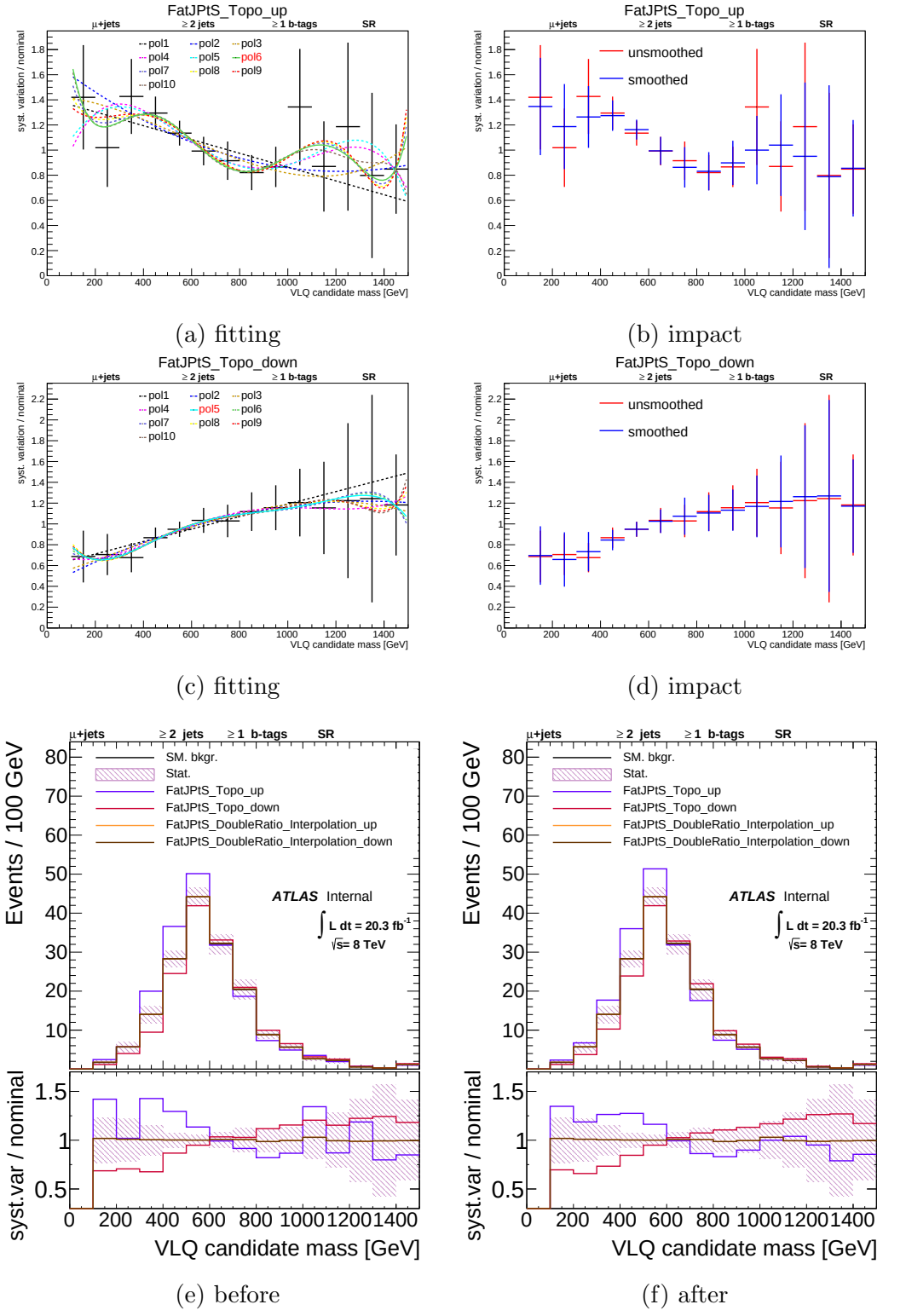

(a) fitting (b) impact

(c) fitting (d) impact

(e) before (f) after

Figure B.3: Demonstration of the smoothing through fitting procedure for the FatJPtS_Topo_up and FatJPtS_Topo_down variations. Top and centre: various fitted functions (left), where the continuous line and red label indicate the chosen polynomial form, and impact on the ratio to nominal (right). Bottom: comparison to nominal before (left) and after (right) smoothing. This is shown for events in the SR, for the muon channel.

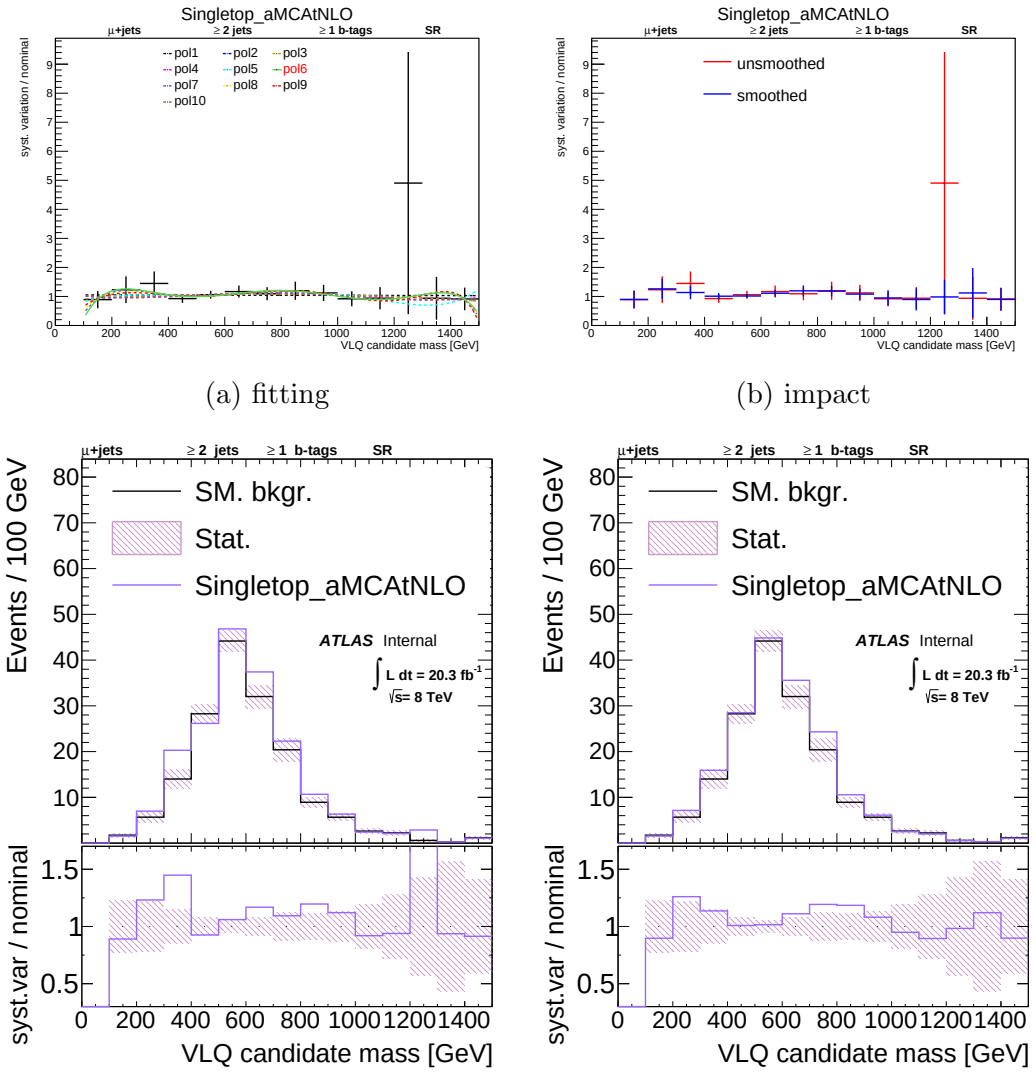

(a) fitting (b) impact

(c) before (d) after

Figure B.4: Demonstration of the smoothing through fitting procedure for the Singletop_aMCAtNLO variation. Top: various fitted functions (left), where the continuous line and red label indicate the chosen polynomial form, and impact on the ratio to nominal (right). Bottom: comparison to nominal before (left) and after (right) smoothing. This is shown for events in the SR, for the muon channel.

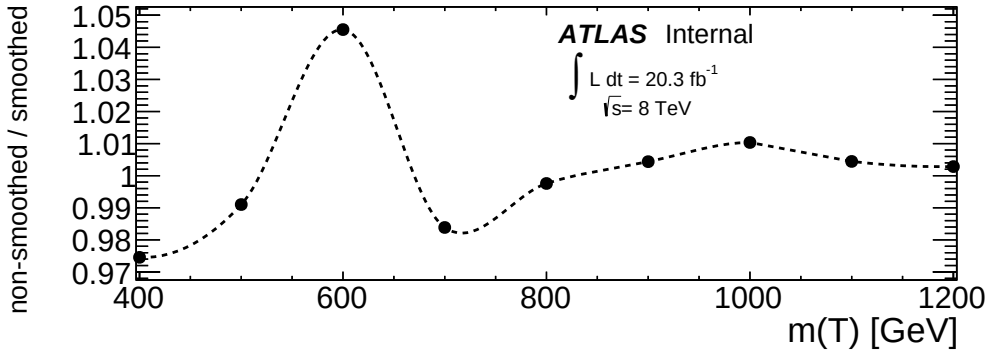

Figure B.5: Non-smoothed to smoothed limit ratio.

B.2 Summary

In this appendix, the fitting-based systematic uncertainty smoothing procedure used in Chapter 5 has been demonstrated. This procedure has been shown to be able to alleviate statistical fluctuations, while preserving trends. Figure B.5 shows that the change on the expected limit, from applying smoothing is within 5%. Figure B.6 shows the impact that smoothing all the relevant systematic variations has on the total systematic uncertainty. Here, while statistical fluctuations are reduced, the overall size of the systematic uncertainty is maintained.

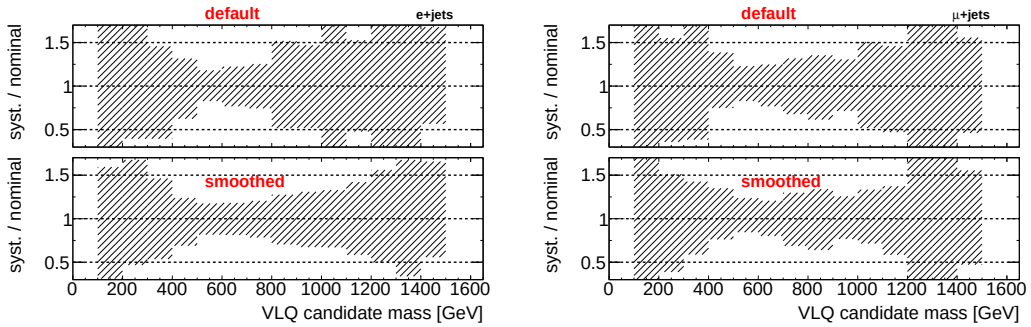

(a) e+jets channel (b) μ+jets channel

Figure B.6: Comparison between the nominal (top) size of the total size of the systematic uncertainty and that after smoothing (bottom). This is shown for events in the SR, both for the electron (left) and muon (right) channels.

Bibliography

[1] ATLAS Collaboration, *A search for $t\bar{t}$ resonances in lepton plus jets events with ATLAS using 20 fb^1 of proton-proton collisions at $\sqrt{s} = 8$ TeV*, Tech. Rep. ATL-COM-PHYS-2014-1451, CERN, Geneva, Nov, 2014.

[2] ATLAS Collaboration, *Performance of shower deconstruction in ATLAS*, ATLAS-CONF-2014-003. `https://cds.cern.ch/record/1648661`.

[3] N. G. Ortiz, J. Ferrando, D. Kar, and M. Spannowsky, *Reconstructing singly produced top partners in decays to* **Wb**, Phys.Rev. **D90** (2014) 075009, `arXiv:1403.7490 [hep-ph]`.

[4] *The Standard Model: The most successful theory ever*, 2015. `http://www.fnal.gov/pub/today/archive/archive_2011/today11-11-18_NutshellStandardModelReadMore.html`.

[5] *Standard Model entry on wikipedia*, 2015. `http://en.wikipedia.org/wiki/Standard_Model`.

[6] A. Zee, *Quantum Field Theory in a Nutshell*. Princeton University Press, 2010.

[7] L. H. Ryder, *Quantum Field Theory*. Cambridge University Press, Cambridge, 1996.

[8] M. Peskin and D. Schroeder, *An Introduction to Quantum Field Theory*. Advanced book classics. Addison-Wesley Publishing Company, 1995.

[9] S. Weinberg, *The Quantum Theory of Fields, Volume 1: Foundations*. Cambridge Univ. Press, Cambridge, 2005.

[10] M. Srednicki, *Quantum Field Theory*. Cambridge Univ. Press, Cambridge, 2007.

[11] K. G. Wilson, *The Renormalization Group: Critical Phenomena and the Kondo Problem*, Rev.Mod.Phys. **47** (1975) 773.

[12] J. Wess and B. Zumino, *Supergauge Transformations in Four-Dimensions*, Nucl.Phys. **B70** (1974) 39–50.

[13] J. Wess and B. Zumino, *A Lagrangian Model Invariant Under Supergauge Transformations*, Phys.Lett. **B49** (1974) 52.

[14] H. P. Nilles, *Supersymmetry, Supergravity and Particle Physics*, Phys.Rept. **110** (1984) 1–162.

[15] S. P. Martin, *A Supersymmetry primer*, Adv.Ser.Direct.High Energy Phys. **21** (2010) 1–153, `arXiv:hep-ph/9709356 [hep-ph]`.

[16] P. Fayet, *Spontaneously Broken Supersymmetric Theories of Weak, Electromagnetic and Strong Interactions*, Phys.Lett. **B69** (1977) 489.

[17] P. Fayet, *Experimental consequences of supersymmetry*, Tech. Rep. LPT-ENS-81-9, Ecole Normale Sup., Paris, May, 1981. https://cds.cern.ch/record/130084.

[18] E. Witten, *Dynamical Breaking of Supersymmetry*, Nucl.Phys. **B188** (1981) 513.

[19] R. K. Kaul, *Gauge Hierarchy in a Supersymmetric Model*, Phys.Lett. **B109** (1982) 19.

[20] L. Susskind, *The Gauge Hierarchy Problem, Technicolor, Supersymmetry, and All That. (talk)*, Phys.Rept. **104** (1984) 181–193.

[21] H. E. Haber and G. L. Kane, *The Search for Supersymmetry: Probing Physics Beyond the Standard Model*, Phys.Rept. **117** (1985) 75–263.

[22] D. B. Kaplan and H. Georgi, *SU(2) x U(1) Breaking by Vacuum Misalignment*, Phys.Lett. **B136** (1984) 183.

[23] D. B. Kaplan, H. Georgi, and S. Dimopoulos, *Composite Higgs Scalars*, Phys.Lett. **B136** (1984) 187.

[24] H. Georgi, D. B. Kaplan, and P. Galison, *Calculation of the Composite Higgs Mass*, Phys.Lett. **B143** (1984) 152.

[25] T. Banks, *Constraints ON SU(2) x U(1) Breaking by Vacuum Misalignment*, Nucl.Phys. **B243** (1984) 125.

[26] H. Georgi and D. B. Kaplan, *Composite Higgs and Custodial SU(2)*, Phys.Lett. **B145** (1984) 216.

[27] M. J. Dugan, H. Georgi, and D. B. Kaplan, *Anatomy of a Composite Higgs Model*, Nucl.Phys. **B254** (1985) 299.

[28] H. Georgi, *A Tool Kit for Builders of Composite Models*, Nucl.Phys. **B266** (1986) 274.

[29] B. Bellazzini, C. Cski, and J. Serra, *Composite Higgses*, Eur.Phys.J. **C74** no. 5, (2014) 2766, arXiv:1401.2457 [hep-ph].

[30] J. Aguilar-Saavedra, *Identifying top partners at LHC*, JHEP **0911** (2009) 030, arXiv:0907.3155 [hep-ph].

[31] A. De Simone, O. Matsedonskyi, R. Rattazzi, and A. Wulzer, *A First Top Partner Hunter's Guide*, JHEP **1304** (2013) 004, arXiv:1211.5663 [hep-ph].

[32] N. Vignaroli, *Early discovery of top partners and test of the Higgs nature*, Phys.Rev. **D86** (2012) 075017, arXiv:1207.0830 [hep-ph].

[33] E. lvarez, L. Da Rold, and J. I. Sanchez Vietto, *Single production of an exotic bottom partner at LHC*, JHEP **1402** (2014) 010, arXiv:1311.2077 [hep-ph].

[34] J. Aguilar-Saavedra, R. Benbrik, S. Heinemeyer, and M. Prez-Victoria, *Handbook of vectorlike quarks: Mixing and single production*, Phys.Rev. **D88** no. 9, (2013) 094010, arXiv:1306.0572 [hep-ph].

[35] CMS Collaboration, *Inclusive search for a vector-like T quark with charge $\frac{2}{3}$ in pp collisions at $\sqrt{s}$ = 8 TeV*, Phys.Lett. **B729** (2014) 149–171, arXiv:1311.7667 [hep-ex].

[36] *Search for production of vector-like quark pairs and of four top quarks in the lepton plus jets final state in pp collisions at $\sqrt{s} = 8$ TeV with the ATLAS detector*, Tech. Rep. ATLAS-CONF-2015-012, CERN, Geneva, Mar, 2015.

[37] O. Matsedonskyi, G. Panico, and A. Wulzer, *On the Interpretation of Top Partners Searches*, `arXiv:1409.0100 [hep-ph]`.

[38] F. del Aguila, M. Perez-Victoria, and J. Santiago, *Effective description of quark mixing*, Phys.Lett. **B492** (2000) 98–106, `arXiv:hep-ph/0007160 [hep-ph]`.

[39] F. del Aguila, M. Perez-Victoria, and J. Santiago, *Observable contributions of new exotic quarks to quark mixing*, JHEP **0009** (2000) 011, `arXiv:hep-ph/0007316 [hep-ph]`.

[40] J. C. Collins, *Sudakov form-factors*, Adv. Ser. Direct. High Energy Phys. **5** (1989) 573–614, `arXiv:hep-ph/0312336 [hep-ph]`.

[41] G. Altarelli and G. Parisi, *Asymptotic Freedom in Parton Language*, Nucl. Phys. **B126** (1977) 298.

[42] V. N. Gribov and L. N. Lipatov, *Deep inelastic e p scattering in perturbation theory*, Sov. J. Nucl. Phys. **15** (1972) 438–450.

[43] Y. L. Dokshitzer, *Calculation of the Structure Functions for Deep Inelastic Scattering and e+ e- Annihilation by Perturbation Theory in Quantum Chromodynamics*, Sov. Phys. JETP **46** (1977) 641–653.

[44] S. Catani, Y. L. Dokshitzer, M. Olsson, G. Turnock, and B. Webber, *New clustering algorithm for multi - jet cross-sections in e+ e- annihilation*, Phys.Lett. **B269** (1991) 432–438.

[45] S. Catani, Y. L. Dokshitzer, M. Seymour, and B. Webber, *Longitudinally invariant K_t clustering algorithms for hadron hadron collisions*, Nucl.Phys. **B406** (1993) 187–224.

[46] S. D. Ellis and D. E. Soper, *Successive combination jet algorithm for hadron collisions*, Phys.Rev. **D48** (1993) 3160–3166, `arXiv:hep-ph/9305266 [hep-ph]`.

[47] Y. L. Dokshitzer, G. Leder, S. Moretti, and B. Webber, *Better jet clustering algorithms*, JHEP **9708** (1997) 001, `arXiv:hep-ph/9707323 [hep-ph]`.

[48] M. Wobisch and T. Wengler, *Hadronization corrections to jet cross-sections in deep inelastic scattering*, `arXiv:hep-ph/9907280 [hep-ph]`.

[49] M. Cacciari and G. P. Salam, *Dispelling the N^3 myth for the k_t jet-finder*, Phys.Lett. **B641** (2006) 57–61, `arXiv:hep-ph/0512210 [hep-ph]`.

[50] M. Cacciari, G. P. Salam, and G. Soyez, *The Anti-k(t) jet clustering algorithm*, JHEP **0804** (2008) 063, `arXiv:0802.1189 [hep-ph]`.

[51] R. K. Ellis, W. J. Stirling, and B. R. Webber, *QCD and Collider Physics*. Cambridge monographs on particle physics, nuclear physics, and cosmology. Cambridge Univ. Press, Cambridge, 2003. Photography by S. Vascotto.

[52] A. Buckley, J. Butterworth, S. Gieseke, D. Grellscheid, S. Hoche, et al., *General-purpose event generators for LHC physics*, Phys.Rept. **504** (2011) 145–233, arXiv:1101.2599 [hep-ph].

[53] Particle Data Group Collaboration, K. Olive et al., *Review of Particle Physics*, Chin.Phys. **C38** (2014) 090001.

[54] T. Sjostrand, S. Mrenna, and P. Skands, *PYTHIA 6.4 physics and manual*, JHEP **05** (2006) 026, hep-ph/0603175.

[55] T. Sjostrand, S. Mrenna, and P. Skands, *A brief introduction to PYTHIA 8.1*, Comput. Phys. Commun. **178** (2008) 852–867, arXiv:0710.3820 [hep-ph].

[56] G. Corcella et al., *HERWIG 6.5 release note*, arXiv:hep-ph/0210213.

[57] T. Gleisberg, S. Hoeche, F. Krauss, M. Schonherr, S. Schumann, et al., *Event generation with SHERPA 1.1*, JHEP **0902** (2009) 007, arXiv:0811.4622 [hep-ph].

[58] B. Andersson, G. Gustafson, and B. Soderberg, *A General Model for Jet Fragmentation*, Z.Phys. **C20** (1983) 317.

[59] G. Marchesini, B. Webber, G. Abbiendi, I. Knowles, M. Seymour, et al., *HERWIG: A Monte Carlo event generator for simulating hadron emission reactions with interfering gluons. Version 5.1 - April 1991*, Comput.Phys.Commun. **67** (1992) 465–508.

[60] J.-C. Winter, F. Krauss, and G. Soff, *A Modified cluster hadronization model*, Eur.Phys.J. **C36** (2004) 381–395, arXiv:hep-ph/0311085 [hep-ph].

[61] B. Isildak, *Measurement of the differential dijet production cross section in proton-proton collisions at $\sqrt{s} = 7$ tev*, arXiv:1308.6064 [hep-ex].

[62] S. Frixione, P. Nason, and C. Oleari, *Matching NLO QCD computations with Parton Shower simulations: the POWHEG method*, JHEP **0711** (2007) 070, arXiv:0709.2092 [hep-ph].

[63] S. Frixione and B. R. Webber, *Matching NLO QCD computations and parton shower simulations*, JHEP **0206** (2002) 029, arXiv:hep-ph/0204244 [hep-ph].

[64] S. Frixione, P. Nason, and B. R. Webber, *Matching NLO QCD and parton showers in heavy flavor production*, JHEP **0308** (2003) 007, arXiv:hep-ph/0305252 [hep-ph].

[65] S. Catani, F. Krauss, R. Kuhn, and B. Webber, *QCD matrix elements + parton showers*, JHEP **0111** (2001) 063, arXiv:hep-ph/0109231 [hep-ph].

[66] M. L. Mangano, M. Moretti, F. Piccinini, R. Pittau, and A. D. Polosa, *ALPGEN, a generator for hard multiparton processes in hadronic collisions*, JHEP **0307** (2003) 001, arXiv:hep-ph/0206293 [hep-ph].

[67] J. Alwall, M. Herquet, F. Maltoni, O. Mattelaer, and T. Stelzer, *MadGraph 5 : Going Beyond*, JHEP **1106** (2011) 128, arXiv:1106.0522 [hep-ph].

[68] *LHC media*, 2015. https://cds.cern.ch/collection/Photos?ln=en.

[69] *CERN accelerator complex*, 2015. http://public.web.cern.ch/public/en/research/AccelComplex-en.html.

[70] *ATLAS photos*, 2015. http://www.atlas.ch/photos/index.html.

[71] ATLAS Collaboration, *The ATLAS Inner Detector commissioning and calibration*, Eur.Phys.J. **C70** (2010) 787–821, arXiv:1004.5293 [physics.ins-det].

[72] *Alignment of the ATLAS Inner Detector and its Performance in 2012*, Tech. Rep. ATLAS-CONF-2014-047, CERN, Geneva, Jul, 2014. https://cds.cern.ch/record/1741021.

[73] ATLAS Collaboration, *Jet energy measurement with the ATLAS detector in proton-proton collisions at* $\sqrt{s} = 7$ *TeV*, Eur.Phys.J. **C73** (2013) 2304, arXiv:1112.6426 [hep-ex].

[74] C. Issever, K. Borras, and D. Wegener, *An Improved weighting algorithm to achieve software compensation in a fine grained LAr calorimeter*, Nucl.Instrum.Meth. **A545** (2005) 803–812, arXiv:physics/0408129 [physics].

[75] ATLAS Collaboration, *Jet energy resolution in proton-proton collisions at* $\sqrt{s} = 7$ *TeV recorded in 2010 with the ATLAS detector*, Eur.Phys.J. **C73** (2013) 2306, arXiv:1210.6210 [hep-ex].

[76] J. Archambault, A. Artamonov, M. Cadabeschi, V. Epshteyn, C. Galt, et al., *Performance of the ATLAS liquid argon forward calorimeter in beam tests*, JINST **8** (2013) P05006.

[77] ATLAS Collaboration, *Performance of the ATLAS Trigger System in 2010*, Eur. Phys. J. C **72** (2012) 1849, arXiv:1110.1530 [hep-ex].

[78] J. M. Butterworth, J. R. Forshaw, and M. H. Seymour, *Multiparton interactions in photoproduction at HERA*, Z. Phys. **C72** (1996) 637–646, arXiv:hep-ph/9601371.

[79] ATLAS Collaboration, *Estimation of non-prompt and fake lepton backgrounds in final states with top quarks produced in proton-proton collisions at* $\sqrt{s} = 8$ *TeV with the ATLAS detector*, ATLAS-CONF-2014-058. http://cds.cern.ch/record/1951336.

[80] ATLAS Collaboration, *Estimation of Fake Lepton Background for Top Analyses Using the* $\sqrt{s} = 8$ *TeV Dataset*, ATL-COM-PHYS-2013-1100. https://cds.cern.ch/record/1571043/.

[81] B. P. Kersevan and E. Richter-Was, *The Monte Carlo event generator AcerMC version 2.0 with interfaces to PYTHIA 6.2 and HERWIG 6.5*, arXiv:hep-ph/0405247 [hep-ph].

[82] J. Alwall, R. Frederix, S. Frixione, V. Hirschi, F. Maltoni, et al., *The automated computation of tree-level and next-to-leading order differential cross sections, and their matching to parton shower simulations*, JHEP **1407** (2014) 079, arXiv:1405.0301 [hep-ph].

[83] C. Anastasiou, L. J. Dixon, K. Melnikov, and F. Petriello, *High precision QCD at hadron colliders: Electroweak gauge boson rapidity distributions at NNLO*, Phys.Rev. **D69** (2004) 094008, arXiv:hep-ph/0312266 [hep-ph].

[84] N. Kidonakis, *Next-to-next-to-leading-order collinear and soft gluon corrections for t-channel single top quark production*, Phys.Rev. **D83** (2011) 091503, arXiv:1103.2792 [hep-ph].

[85] ATLAS Collaboration, *Performance of boosted top quark identification in 2012 ATLAS data*, ATLAS-CONF-2013-084. http://cds.cern.ch/record/1571040.

[86] *TopRootCore package*, 2015. https://twiki.cern.ch/twiki/bin/view/AtlasProtected/TopRootCoreRelease.

[87] *RootCore package*, 2015. https://twiki.cern.ch/twiki/bin/view/AtlasComputing/RootCore?redirectedfrom=Atlas.RootCore.

[88] *TTree class reference*, 2015. https://root.cern.ch/root/html/TTree.html.

[89] ATLAS Collaboration, *Expected electron performance in the ATLAS experiment*, Tech. Rep. ATL-PHYS-INT-2010-126, CERN, Geneva, Nov, 2010.

[90] *egammaAnalysisUtils package*, 2015. https://twiki.cern.ch/twiki/bin/view/AtlasProtected/TopCommonObjects#Electrons.

[91] *Electron scale factors*, 2015. https://twiki.cern.ch/twiki/bin/viewauth/AtlasProtected/EfficiencyMeasurements2012.

[92] *Electron and photon energy calibration with the ATLAS detector using LHC Run 1 data*, Tech. Rep. ATL-COM-PHYS-2013-1652, CERN, Geneva, Dec, 2013.

[93] *TopElectronSFUtils package*, 2015. https://twiki.cern.ch/twiki/bin/view/AtlasProtected/TopCommonScales#Electrons_ElectronTight.

[94] *muid algorithm*, 2015. https://twiki.cern.ch/twiki/bin/view/AtlasProtected/TopCommonObjects#Muons.

[95] K. Rehermann and B. Tweedie, *Efficient Identification of Boosted Semileptonic Top Quarks at the LHC*, JHEP **1103** (2011) 059, arXiv:1007.2221 [hep-ph].

[96] ATLAS Collaboration, *Measurement of the muon reconstruction performance of the ATLAS detector using 2011 and 2012 LHC proton-proton collision data*, arXiv:1407.3935 [hep-ex].

[97] *TopMuonSFUtils package*, 2015. https://twiki.cern.ch/twiki/bin/view/AtlasProtected/TopCommonScales#Muons.

[98] *In situ jet pseudorapidity intercalibration of the ATLAS detector using dijet events in $\sqrt{s} = 7$ TeV proton-proton 2011 data*, Tech. Rep. ATLAS-COM-CONF-2012-079, CERN, Geneva, May, 2012.

[99] *Global Sequential Calibration with the ATLAS Detector in Proton-Proton Collisions at $\sqrt(s) = 8$ TeV with ATLAS 2012 data*, Tech. Rep. ATL-COM-PHYS-2014-753, CERN, Geneva, Jun, 2014.

[100] *Pile-up subtraction and suppression for jets in ATLAS*, Tech. Rep. ATLAS-CONF-2013-083, CERN, Geneva, Aug, 2013.

[101] *ApplyJetCalibration package*, 2015. https://twiki.cern.ch/twiki/bin/view/AtlasProtected/ApplyJetCalibration2012.

[102] ATLAS Collaboration Collaboration, *Commissioning of the ATLAS high-performance b-tagging algorithms in the 7 TeV collision data*, Tech. Rep. ATLAS-CONF-2011-102, CERN, Geneva, Jul, 2011.

[103] M. zur Nedden, G. Piacquadio, J. Jovicevic, F. Filthaut, T. Scanlon, and F. Parodi, *Calibration of b-tagging using dileptonic top pair events in a combinatorial likelihood approach with the ATLAS experiment*, Tech. Rep. ATLAS-COM-CONF-2014-003, CERN, Geneva, Jan, 2014.

[104] *Calibration data interface*, 2015. `https://twiki.cern.ch/twiki/bin/view/AtlasProtected/BTagCalib2014#Information_on_CDI_file_for_8_Te`.

[105] ATLAS Collaboration, *Performance of large-R jets and jet substructure reconstruction with the ATLAS detector*, Tech. Rep. ATLAS-CONF-2012-065, CERN, Geneva, Jul, 2012.

[106] D. Krohn, J. Thaler, and L.-T. Wang, *Jet Trimming*, JHEP **1002** (2010) 084, `arXiv:0912.1342 [hep-ph]`.

[107] A. Altheimer et al., *Jet Substructure at the Tevatron and LHC: New results, new tools, new benchmarks*, J. Phys. **G39** (2012) 063001, `arXiv:1201.0008 [hep-ph]`.

[108] ATLAS Collaboration, *Performance of jet substructure techniques for large-R jets in proton-proton collisions at $\sqrt{s}$ = 7 TeV using the ATLAS detector*, JHEP **1309** (2013) 076, `arXiv:1306.4945 [hep-ex]`.

[109] D. E. Soper and M. Spannowsky, *Finding physics signals with shower deconstruction*, Phys. Rev. **D84** (2011) 074002, `arXiv:1102.3480 [hep-ph]`.

[110] D. E. Soper and M. Spannowsky, *Finding top quarks with shower deconstruction*, Phys. Rev. **D87** (2013) 054012, `arXiv:1211.3140 [hep-ph]`.

[111] M. Cacciari, G. P. Salam, and G. Soyez, *The Catchment Area of Jets*, JHEP **0804** (2008) 005, `arXiv:0802.1188 [hep-ph]`.

[112] ATLAS Collaboration, *Reconstruction and Calibration of Missing Transverse Energy and Performance in Z and W events in ATLAS Proton-Proton Collisions at 7 TeV*, Tech. Rep. ATLAS-CONF-2011-080, CERN, Geneva, Jun, 2011.

[113] *MissingETUtility package*, 2015. `https://twiki.cern.ch/twiki/bin/view/AtlasProtected/MissingETUtility`.

[114] *NeutrinoBuilder package*, 2015. `https://twiki.cern.ch/twiki/bin/viewauth/AtlasProtected/Summer2013TopResonances#NeutrinoBuilder_code`.

[115] ATLAS Collaboration, *A search for $t\bar{t}$ resonances in the lepton plus jets final state using 15 fb^{-1} of pp collisions at $\sqrt{s} = 8$ TeV*, ATL-COM-PHYS-2013-090. `https://cds.cern.ch/record/1509564`.

[116] *Object selection and calibration, background estimations and MC samples for top quark analyses using the full 2012 data set*, Tech. Rep. ATL-COM-PHYS-2013-1016, CERN, Geneva, Jul, 2013.

[117] *Electron systematic uncertainties*, 2015. `https://twiki.cern.ch/twiki/bin/view/AtlasProtected/TopSystematicUncertainties#Electrons`.

[118] *Muon systematic uncertainties*, 2015. `https://twiki.cern.ch/twiki/bin/view/AtlasProtected/TopSystematicUncertainties#Muons`.

[119] *Missing transverse momentum systematic uncertainties*, 2015. https://twiki.cern.ch/twiki/bin/view/AtlasProtected/TopSystematicUncertainties#MET.

[120] *Small-R jet energy scale systematic uncertainties*, 2015. https://twiki.cern.ch/twiki/bin/view/AtlasProtected/JetEtmissRecommendations2012.

[121] *Small-R jet reconstruction efficiency systematic uncertainties*, 2015. https://twiki.cern.ch/twiki/bin/view/AtlasProtected/TopJetReconstructionEfficiency.

[122] *Small-R jet energy resolution systematic uncertainties*, 2015. https://twiki.cern.ch/twiki/bin/viewauth/AtlasProtected/TopJetLiaisonR1727Recommendations#JER_smearing_and_uncertainty.

[123] *$t\bar{t}$ modelling systematic uncertainties*, 2015. https://twiki.cern.ch/twiki/bin/view/AtlasProtected/TopSystematicUncertainties#Systematics_Affecting_Only_TTbar.

[124] ATLAS Collaboration, *Improved luminosity determination in pp collisions at $\sqrt{s} = 7$ TeV using the ATLAS detector at the LHC*, Eur.Phys.J. **C73** no. 8, (2013) 2518, arXiv:1302.4393 [hep-ex].

[125] *TElectronEfficiencyCorrectionTool package*, 2015. https://twiki.cern.ch/twiki/bin/viewauth/AtlasProtected/TElectronEfficiencyCorrectionTool.

[126] *TrigMuonEfficiency package*, 2015. https://twiki.cern.ch/twiki/bin/viewauth/Atlas/TrigMuonEfficiency.

[127] *EnergyRescalerUpgrade package*, 2015. https://twiki.cern.ch/twiki/bin/view/AtlasProtected/TopCommonScales#Electron_momentum_scale_offset_a.

[128] *MuonEfficiencyCorrections package*, 2015. https://twiki.cern.ch/twiki/bin/viewauth/AtlasProtected/MCPAnalysisGuidelinesData2012#Muon_Monte_Carlo_efficiency_scal.

[129] *MuonMomentumCorrections package*, 2015. https://twiki.cern.ch/twiki/bin/viewauth/AtlasProtected/MCPAnalysisGuidelinesData2012#Muon_Momentum_Uncertainty_Correc.

[130] *JetUncertainties package*, 2015. https://twiki.cern.ch/twiki/bin/view/AtlasProtected/JetUncertainties2012.

[131] *ApplyJetResolutionSmearing package*, 2015. https://twiki.cern.ch/twiki/bin/view/AtlasProtected/ApplyJetResolutionSmearing.

[132] *JVFUncertaintyTool package*, 2015. https://twiki.cern.ch/twiki/bin/view/AtlasProtected/JVFUncertaintyTool.

[133] *Eigenvector variation method*, 2015. https://twiki.cern.ch/twiki/bin/view/AtlasProtected/BTaggingCalibrationDataInterface#Eigenvector_variation_method.

[134] *UJUncertaintyProvider package*, 2015. https://twiki.cern.ch/twiki/bin/viewauth/AtlasProtected/UJUncertaintyProvider.

[135] *Track jet double ratio method*, 2015. https://twiki.cern.ch/twiki/bin/viewauth/AtlasProtected/JetMassScaleUncertaintyGuide#Track_jet_double_ratio_studies.

[136] *γ+jet balance method*, 2015. https://twiki.cern.ch/twiki/bin/view/AtlasProtected/GammaLargeRJPTSUncertainties.

[137] *Large-R jet energy resolution smearing*, 2015. https://twiki.cern.ch/twiki/bin/viewauth/AtlasProtected/JetSubstructureRecommendations#Energy_and_Mass_Resolution_Uncer.

[138] ATLAS Collaboration, *Measurement of $t\bar{t}$ production with a veto on additional central jet activity in pp collisions at $\sqrt{s} = 7$ TeV using the ATLAS detector*, Eur.Phys.J. **C72** (2012) 2043, arXiv:1203.5015 [hep-ex].

[139] *Fake lepton estimation package*, 2015. https://twiki.cern.ch/twiki/bin/view/AtlasProtected/TopFakeFull8TeV.

[140] *Fake lepton estimation systematic uncertainties*, 2015. https://twiki.cern.ch/twiki/bin/viewauth/AtlasProtected/FakesWeights#Systematics.

[141] W. Lampl, S. Laplace, D. Lelas, P. Loch, H. Ma, S. Menke, S. Rajagopalan, D. Rousseau, S. Snyder, and G. Unal, *Calorimeter Clustering Algorithms: Description and Performance*, Tech. Rep. ATL-LARG-PUB-2008-002. ATL-COM-LARG-2008-003, CERN, Geneva, Apr, 2008.

[142] C. Cojocaru et al., *Hadronic calibration of the ATLAS liquid argon end-cap calorimeter in the pseudorapidity region in beam tests*, Nucl.Instrum.Meth.A **531** no. 3, (2004) 481 – 514. http://www.sciencedirect.com/science/article/pii/S0168900204012884.

[143] ATLAS Collaboration, *Hunt for new phenomena using large jet multiplicities and missing transverse momentum with ATLAS in 4.7 fb^{-1} of $\sqrt{s} = 7$ TeV proton-proton collisions*, JHEP **1207** (2012) 167, arXiv:1206.1760 [hep-ex].

[144] ATLAS Collaboration, *Search for Massive Colored Scalars in Four-Jet Final States in $\sqrt{s} = 7$ TeV proton-proton collisions with the ATLAS Detector*, Eur.Phys.J. **C71** (2011) 1828, arXiv:1110.2693 [hep-ex].

[145] ATLAS Collaboration, *Measurement of the inclusive and dijet cross-sections of b^- jets in pp collisions at $\sqrt{s} = 7$ TeV with the ATLAS detector*, Eur.Phys.J. **C71** (2011) 1846, arXiv:1109.6833 [hep-ex].

[146] ATLAS Collaboration, *Measurement of dijet production with a veto on additional central jet activity in pp collisions at $\sqrt{s} = 7$ TeV using the ATLAS detector*, JHEP **1109** (2011) 053, arXiv:1107.1641 [hep-ex].

[147] ATLAS Collaboration, *Search for new phenomena in final states with large jet multiplicities and missing transverse momentum using $\sqrt{s} = 7$ TeV pp collisions with the ATLAS detector*, JHEP **1111** (2011) 099, arXiv:1110.2299 [hep-ex].

[148] ATLAS Collaboration, *Search for anomaly-mediated supersymmetry breaking with the ATLAS detector based on a disappearing-track signature in pp collisions at $\sqrt{s} = 7$ TeV*, Eur.Phys.J. **C72** (2012) 1993, arXiv:1202.4847 [hep-ex].

[149] ATLAS Collaboration, *Search for top and bottom squarks from gluino pair production in final states with missing transverse energy and at least three b-jets with the ATLAS detector*, Eur.Phys.J. **C72** (2012) 2174, arXiv:1207.4686 [hep-ex].

[150] ATLAS Collaboration, *Measurement of multi-jet cross sections in proton-proton collisions at a 7 TeV center-of-mass energy*, Eur.Phys.J. **C71** (2011) 1763, arXiv:1107.2092 [hep-ex].

[151] ATLAS Collaboration, *Measurement of the inclusive jet cross section in pp collisions at $\sqrt{s} = 2.76$ TeV and comparison to the inclusive jet cross section at $\sqrt{s} = 7$ TeV using the ATLAS detector*, Eur.Phys.J. **C73** (2013) 2509, arXiv:1304.4739 [hep-ex].

[152] ATLAS Collaboration, *Measurement of the cross section of high transverse momentum $Z \to b\bar{b}$ production in proton–proton collisions at $\sqrt{s}$=8 TeV with the ATLAS Detector*, arXiv:1404.7042 [hep-ex].

[153] ATLAS Collaboration, *Measurement of dijet cross sections in pp collisions at 7 TeV centre-of-mass energy using the ATLAS detector*, arXiv:1312.3524 [hep-ex].

[154] ATLAS Collaboration, *Search for pair-produced massive coloured scalars in four-jet final states with the ATLAS detector in proton-proton collisions at $\sqrt{s} = 7$ TeV*, Eur.Phys.J. **C73** (2013) 2263, arXiv:1210.4826 [hep-ex].

[155] ATLAS Collaboration, *ATLAS search for new phenomena in dijet mass and angular distributions using pp collisions at $\sqrt{s} = 7$ TeV*, JHEP **1301** (2013) 029, arXiv:1210.1718 [hep-ex].

[156] ATLAS Collaboration, *Search for resonances decaying into top-quark pairs using fully hadronic decays in pp collisions with ATLAS at $\sqrt{s} = 7$ TeV*, JHEP **1301** (2013) 116, arXiv:1211.2202 [hep-ex].

[157] ATLAS Collaboration, *Search for new phenomena in final states with large jet multiplicities and missing transverse momentum at $\sqrt{s} = 8$ TeV proton-proton collisions using the ATLAS experiment*, JHEP **1310** (2013) 130, arXiv:1308.1841 [hep-ex].

[158] ATLAS Collaboration, *Search for pair production of massive particles decaying into three quarks with the ATLAS detector in $\sqrt{s} = 7$ TeV pp collisions at the LHC*, JHEP **1212** (2012) 086, arXiv:1210.4813 [hep-ex].

[159] ATLAS Collaboration, *Measurement of event shapes at large momentum transfer with the ATLAS detector in pp collisions at $\sqrt{s} = 7$ TeV*, Eur.Phys.J. **C72** (2012) 2211, arXiv:1206.2135 [hep-ex].

[160] ATLAS Collaboration, *Measurement of the flavour composition of dijet events in pp collisions at $\sqrt{s} = 7$ TeV with the ATLAS detector*, Eur.Phys.J. **C73** (2013) 2301, arXiv:1210.0441 [hep-ex].

[161] ATLAS Collaboration, *Multi-channel search for squarks and gluinos in $\sqrt{s} = 7$ TeV pp collisions with the ATLAS detector*, Eur.Phys.J. **C73** (2013) 2362, arXiv:1212.6149 [hep-ex].

[162] ATLAS Collaboration, *Search for supersymmetry in pp collisions at $\sqrt{s} = 7$ TeV in final states with missing transverse momentum and b^- jets with the ATLAS detector*, Phys.Rev. **D85** (2012) 112006, arXiv:1203.6193 [hep-ex].

[163] ATLAS Collaboration, *Search for squarks and gluinos using final states with jets and missing transverse momentum with the ATLAS detector in $\sqrt{s} = 7$ TeV proton-proton collisions*, Phys.Lett. **B710** (2012) 67–85, arXiv:1109.6572 [hep-ex].

[164] ATLAS Collaboration, *Measurement of the t-channel single top-quark production cross section in pp collisions at $\sqrt{s} = 7$ TeV with the ATLAS detector*, Phys.Lett. **B717** (2012) 330–350, arXiv:1205.3130 [hep-ex].

[165] ATLAS Collaboration, *ATLAS measurements of the properties of jets for boosted particle searches*, Phys.Rev. **D86** (2012) 072006, arXiv:1206.5369 [hep-ex].

[166] ATLAS Collaboration, *A search for $t\bar{t}$ resonances in the lepton plus jets final state with ATLAS using 14 fb^1 of pp collisions at $\sqrt{s} = 8$ TeV*, ATLAS-CONF-2013-052. https://cds.cern.ch/record/1547568.

[167] ATLAS Collaboration, *Performance of shower deconstruction in ATLAS*, ATLAS-COM-CONF-2013-140. https://cds.cern.ch/record/1624075.

[168] J. Thaler and K. Van Tilburg, *Identifying Boosted Objects with N-subjettiness*, JHEP **1103** (2011) 015, arXiv:1011.2268 [hep-ph].

[169] ATLAS Collaboration, *Search for heavy top-like quarks decaying to a Higgs boson and a top quark in the lepton plus jets final state in pp collisions at $\sqrt{s} = 8$ TeV with the ATLAS detector*, Tech. Rep. ATLAS-CONF-2013-018, CERN, Geneva, Mar, 2013.

[170] ATLAS Collaboration, *Search for anomalous production of events with same-sign dileptons and b jets in 14.3 fb^{-1} of pp collisions at $\sqrt{s} = 8$ TeV with the ATLAS detector*, Tech. Rep. ATLAS-CONF-2013-051, CERN, Geneva, May, 2013. Not published in the proceedings.

[171] ATLAS Collaboration, *Search for pair production of heavy top-like quarks decaying to a high-p_{T} W boson and a b quark in the lepton plus jets final state in pp collisions at $\sqrt{s} = 8$ TeV with the ATLAS detector*, Tech. Rep. ATLAS-CONF-2013-060, CERN, Geneva, Jun, 2013.

[172] ATLAS Collaboration, *Search for pair and single production of new heavy quarks that decay to a Z boson and a third generation quark in pp collisions at $\sqrt{s} = 8$ TeV with the ATLAS detector*, Tech. Rep. ATLAS-CONF-2014-036, CERN, Geneva, Jul, 2014.

[173] R. J. Barlow and C. Beeston, *Fitting using finite Monte Carlo samples*, Comput.Phys.Commun. **77** (1993) 219–228.

[174] ATLAS Collaboration, *Search for Pair Produced New Heavy Quarks that Decay into a W Boson and a Light Quark in pp collisions at $\sqrt{s} = 8$ TeV with the ATLAS Detector*, Tech. Rep. ATL-COM-PHYS-2013-1005, CERN, Geneva, Jul, 2013.

[175] ATLAS Collaboration, *Search for single top quark production via strong FCNC in $\sqrt{s}$ = 8 TeV ATLAS data*, Tech. Rep. ATL-COM-PHYS-2014-907, CERN, Geneva, Jul, 2014.

[176] F. A. Berends, H. Kuijf, B. Tausk, and W. Giele, *On the production of a W and jets at hadron colliders*, Nucl.Phys. **B357** (1991) 32–64.

[177] S. Ellis, R. Kleiss, and W. J. Stirling, *W's, Z's and Jets*, Phys.Lett. **B154** (1985) 435.

[178] ATLAS Collaboration, *Measurement of the top quark mass in topologies enhanced with single top-quarks produced in the t-channel in $\sqrt{s} = 8$ TeV ATLAS data*, ATLAS-CONF-2014-055. `http://cds.cern.ch/record/1951323`.

[179] M. Baak, G. Besjes, D. Cote, A. Koutsman, J. Lorenz, et al., *HistFitter software framework for statistical data analysis*, `arXiv:1410.1280 [hep-ex]`.

[180] *HistFitter package*, 2015. `https://twiki.cern.ch/twiki/bin/viewauth/AtlasProtected/SusyFitter`.

[181] ROOT Collaboration, K. Cranmer, G. Lewis, L. Moneta, A. Shibata, and W. Verkerke, *HistFactory: A tool for creating statistical models for use with RooFit and RooStats*, Tech. Rep. CERN-OPEN-2012-016, New York U., New York, Jan, 2012.

[182] *RooFit package*, 2015. `http://roofit.sourceforge.net/intro.html`.

[183] *RooStats package*, 2015. `https://twiki.cern.ch/twiki/bin/view/RooStats/WebHome`.

[184] J. Li, D. Liu, and J. Shu, *Towards the fate of natural composite Higgs model through single t' search at the 8 TeV LHC*, JHEP **1311** (2013) 047, `arXiv:1306.5841 [hep-ph]`.

[185] ATLAS Collaboration, *A search for $t\bar{t}$ resonances in the lepton plus jets final state using 20 fb^{-1} of pp collisions at $\sqrt{s} = 8$ TeV*, Tech. Rep. ATL-COM-PHYS-2014-003, CERN, Geneva, Jan, 2014.